ALMA MATER STUDIORUM - UNIVERSITÀ DI BOLOGNA

DOTTORATO DI RICERCA IN
INGEGNERIA STRUTTURALE ED IDRAULICA
CICLO XXV

Settore Concorsuale di afferenza: 08/B2
Settore Scientifico disciplinare: ICAR/08

Numerical methods for the dispersion analysis of Guided Waves

Presentata da: Matteo Mazzotti

Coordinatore Dottorato
Prof. Erasmo Viola

Relatore
Prof. Erasmo Viola

Correlatori
Dott. Alessandro Marzani
Dott. Ivan Bartoli

Esame finale anno 2013

To my family

Abstract

The use of guided ultrasonic waves (GUW) has increased considerably in the fields of non-destructive (NDE) testing and structural health monitoring (SHM) due to their ability to perform long range inspections, to probe hidden areas as well as to provide a complete monitoring of the entire waveguide. Guided waves can be fully exploited only once their dispersive properties are known for the given waveguide. In this context, well stated analytical and numerical methods are represented by the Matrix family methods and the Semi Analytical Finite Element (SAFE) methods. However, while the former are limited to simple geometries of finite or infinite extent, the latter can model arbitrary cross-section waveguides of finite domain only.

This thesis is aimed at developing three different numerical methods for modelling wave propagation in complex translational invariant systems.

First, a classical SAFE formulation for viscoelastic waveguides is extended to account for a three dimensional translational invariant static prestress state. The effect of prestress, residual stress and applied loads on the dispersion properties of the guided waves is shown.

Next, a two-and-a-half Boundary Element Method (2.5D BEM) for the dispersion analysis of damped guided waves in waveguides and cavities of arbitrary cross-section is proposed. The attenuation dispersive spectrum due to material damping and geometrical spreading of cavities with arbitrary shape is shown for the first time.

Finally, a coupled SAFE-2.5D BEM framework is developed to study the dispersion characteristics of waves in viscoelastic waveguides of arbitrary geometry embedded in infinite solid or liquid media. Dispersion of leaky and non- leaky guided waves in terms of speed and attenuation, as well as the radiated wavefields, can be computed.

The results obtained in this thesis can be helpful for the design of both actuation and sensing systems in practical application, as well as to tune experimental setup.

Contents

List of Figures

Nomenclature

α	attenuation
$\boldsymbol{\sigma}^0$, $\boldsymbol{\sigma}$	Cauchy stress tensors
$\boldsymbol{\varepsilon}$, $\boldsymbol{\epsilon}$	independent linear strains
$\boldsymbol{\varepsilon}_{NL}$, $\boldsymbol{\epsilon}_{NL}$	independent nonlinear strains
$\boldsymbol{\Xi}$	1st Piola-Kirchhoff stress tensor
$\boldsymbol{\xi}$	natural coordinates for bidimensional elements
δ_{ij}	Kronecker's delta
η	natural coordinate for monodimensional elements
λ, $\tilde{\lambda}$	Lamé's first constant
λ, $\tilde{\mu}$	Lamé's second constant
$\mathbf{E}$, $\mathbf{e}$	Green-Lagrange strain
$\mathbf{F}$	deformation gradient
$\mathbf{f}^0$, $\mathbf{f}_c$	volume forces vectors
$\mathbf{I}$	identity matrix
$\mathbf{J}$	Poynting vector
$\mathbf{k}_L$, κ_L	bulk longitudinal wavevector and wavenumber
$\mathbf{k}_S$, $\mathbf{k}_S$	bulk shear wavevector and wavenumber
$\mathbf{k}_z$, κ_z	axial wavevector and wavenumber
$\mathbf{k}_\alpha$, κ_α	radial bulk longitudinal wavevector and wavenumbers
$\mathbf{k}_\beta$, κ_β	radial bulk shear wavevector and wavenumbers
$\mathbf{n}$	outward normal
$\mathbf{N}$, $\mathcal{N}$	shape functions
$\mathbf{S}$	2nd Piola-Kirchhoff stress tensor

$\mathbf{s}^0$, $\mathbf{s}$	vectors of independent linear stress components
$\mathbf{t}^0$, $\mathbf{t}_c$, $\mathbf{t}_s$, $\mathbf{t}_b$, $\mathbf{t}$	tractions vectors
$\mathbf{t}_{nc}$	nonconservative surface load
$\mathbf{u}^0$, $\mathbf{u}$, $\mathbf{u}_c$	displacements vectors
$\mathbf{X}$	$= [x,\ y,\ z]^{\mathrm{T}}$ configuration of the material particle on V
$\mathbf{x}$	$= [x,\ y]^{\mathrm{T}}$ configuration of the material particle in the $x - y$ plane
$\mathbf{X}'$	$= [x',\ y',\ z']^{\mathrm{T}}$ source point on V
$\mathbf{x}'$	$= [x',\ y']^{\mathrm{T}}$ source point on the $x - y$ plane
$\mathbf{x}_c$	collocation point
$\mathcal{C}$, $\tilde{\mathbf{C}}$	fourth order tensors of viscoelastic moduli
$\mathcal{C}^0$, $\mathcal{C}$, $\mathcal{C}^t$	material configurations
$\mathscr{B}_{xy}$, $\mathscr{B}_z$	compatibility matrices
$\mathscr{K}$, $\mathscr{W}$, $\mathscr{V}_c$, $\mathscr{V}_{nc}$	energy quantities
$\mathscr{L}_x$, $\mathscr{L}_y$, $\mathscr{L}_z$	compatibility operators
∇	gradient operator
ν	Poisson's ratio
ω	circular frequency
Ω_b^{aux}, $\partial\Omega_b^{\mathrm{aux}}$	domain and boundary of the auxiliary problem
Ω_b, $\partial\Omega_b$	area and boundary of the solid BEM region on the $x - y$ plane
Ω_f, $\partial\Omega_f$	area and boundary of the fluid domain in the $x - y$ plane
Ω_s, $\partial\Omega_s$	area and boundary of the waveguide cross-section in the $x - y$ plane
$\partial p / \partial \mathbf{n}$	pressure flux
ρ	material density
c_e	energy velocity
c_g	group velocity
c_L, $\tilde{c}_L$	bulk longitudinal velocities
c_p	phase velocity
c_S, $\tilde{c}_S$	bulk shear velocities
c_∞	adimensional coefficient
c_{ij}, c_{ij}^{aux}, c_∞, c	free terms

$D_{\mathbf{u}}$	directional derivative in the direction of $\mathbf{u}$
E	Young's modulus
$H_n^{(1)}(\cdot)$, $H_n^{(2)}(\cdot)$	nth order Hankel function of the first and second kind
P^D, $\partial P^D/\partial \mathbf{n}$	fundamental pressures and fluxes of the 2.5D Helmholtz equation
P^S, $\partial P^S/\partial \mathbf{n}$	fundamental pressures and fluxes of the 2D Laplace equation
p_0, p	pressure in the acoustic domain
R, r, r_c	source-receiver distances
t	time
U_{ij}^D, T_{ij}^D	fundamental displacement and tractions for the 2.5D elastodynamic problem
U_{ij}^S, T_{ij}^S	fundamental displacement and tractions for the 2.5 plane strain problem
$u_{\mathbf{n}}$	$= \mathbf{u} \cdot \mathbf{n}$ normal displacement
V, ∂V	volume and boundary surface of the waveguide
i	imaginary unit

Chapter 1

Introduction

1.1 Sommario

Nel capitolo introduttivo vengono inizialmente descritte in modo sommario le potenzialità dei metodi basati su onde ultrasoniche di tipo guidato (GUW) nei campi delle indagini non distruttive, del monitoraggio strutturale e della caratterizzazione dei materiali. Poichè tali metodi richiedono un'accurata conoscenza dei parametri di dispersione per la specifica guida d'onda oggetto dell'indagine, l'attenzione viene in seguito focalizzata sulle tecniche analitiche e numeriche utilizzate in letteratura per il calcolo delle curve di dispersione, mettendone in luce i principali vantaggi e limitazioni.

Sono successivamente descritte le motivazioni che hanno guidato la ricerca ed hanno condotto alla stesura della presente tesi.

Infine, vengono brevemente illustrati gli aspetti innovativi introdotti e i principali risultati ottenuti in ogni capitolo.

1.2 Research motivations

Guided Ultrasonics Waves (GUW) are recognized as an effective diagnostic tool in the fields of nondestructive evaluation (NDE) testing, structural health monitoring (SHM) and materials characterization. The basic concept behind guided waves is that a structural component with invariant geometric and mechanical characteristics along one or more dimensions (waveguide), can be used as support to "drive" the wave propagation, thus providing a fundamental means for its inspection.

Compared with classical ultrasonic testing techniques, some advantages exist. First, the energy of the wave is carried for long distances over the waveguide, whereas in standard ultrasonic testings only small areas of the structural component can be investigated at once. As a consequence, operations times are also drastically reduced. The second advantage is that guided waves can provide a complete inspection of the entire waveguide cross-section. Additionally, guided waves have inherent potential to target particular defects. Unlike longitudinal and shear waves used in standard ultrasonic techniques, guided waves are multi modal, i.e. many modes can carry energy at a given frequency. This property allows one to select several modes having the greatest sensitivity with respect to a specific defect or a mechanical parameter that must be identified. Another advantage offered by GUW is the possibility to design permanent monitoring systems with relatively small hardware.

For the reasons above, the importance of GUW in civil, industrial and medical applications has increased considerably in recent years. For example, guided waves are widely used in the water and oil transportation industry for the detection of defects in pipelines. In the railroad industry they are used to monitoring the conditions of rails, with the aim to prevent failures that can cause disservices or compromise safety. In the aerospace industry, they are largely employed for the quality assessment of adhesively-bonded components. In the civil engineering field, guided waves have proven to be effective in the damage detection of bridge cables, inspections of foundation piles, weld inspections and characterization of the material constants in composite structural components.

All these applications require an accurate knowledge of the dispersive characteristics of guided waves. The concept of dispersion denotes a variation of the behaviour of guided waves as a function of the frequency, and is a consequence of the interaction of the wave propagation process with the structural geometry.

The fundamental dispersive parameters are the phase velocity, the attenuation, group velocity and attenuation. The phase velocity denotes the rate at which the crests of a particular guided mode propagate along the waveguide at a certain frequency. The attenuation expresses instead the amplitude decay per unit of distance traveled. This information is of great importance, especially in leaky systems, where attenuation mostly affects the length of inspection ranges. The group velocity indicates the rate at which packets of waves at infinitely close frequencies move along the waveguide. This feature gives an indication about how much dispersion occurs for a signal generated in a certain frequency range, i.e. how much the shape of the signal is distorted while it propagates along the waveguide. The energy velocity represents a generalization of the energy velocity concept for attenuative systems, and correspond to the rate at which the energy carried by the wave moves along the propagation direction.

In order to efficiently exploit guided waves, it is therefore necessary to chose the guided modes that maximize the inspection ranges with high sensitivity with respect to the defect or parameter to be identified. From the above considerations it clearly appears the need of mathematical tools able to extract dispersive data for waveguides with different geometries and materials, as well as to model the interaction of the waveguide with the surrounding environment.

To this purpose, different analytical and numerical methods are available in literature. The Transfer Matrix Method (TMM) [Haskell, 1953; Thomson, 1950] and the Global Matrix Method (GMM) [Knopoff, 1964; Lowe, 1992; Pavlakovic, 1998] represent the most widely adopted techniques in the context of analytical methods. These methods are able to extract the dispersion curves for plate-like and cylindrical waveguides that are immersed in vacuum or embedded in solid or fluid media. Their capability to handle multilayered waveguides and to provide very accurate solutions makes them very appealing for different wave propagation problems involving civil, mechanical and aerospace structures.

The Finite Element Methods (FEM) [Chen and Wilcox, 2007; Sorohan et al., 2011] and the Semi-Analytical Finite Element (SAFE) methods [Bartoli et al., 2006; Gavric, 1995; Hayashi et al., 2003; Hladky-Hennion, 1996; Shah et al., 2001] have instead the unique capability to model waveguides of complex geometries and materials, for which theoretical solutions are not available. Moreover, they generally lead to well posed problems, while Matrix Methods may result unstable when the waveguide presents a large number of layers, as in the case of composite laminates.

Although the above methods can model a large variety of problems, some situations that are often encountered in practice have not been investigated in the literature. These are, for example, the cases of prestressed viscoelastic waveguides and waveguides of complex geometry and materials that are embedded in solids or immersed in fluids.

In this thesis, three different numerical methods are presented for the solution of the above mentioned problems. The first is an extension of the Semi-Analytical Finite Element (SAFE) method for the extraction of the waves modal properties in viscoelastic prestressed waveguides. The main novelty introduced is the derivation of the wave equation, which is obtained in linearized incremental form within an Updated Lagrangian framework and by considering the influence of nonconservative loads. A modal formula for the wave energy velocity calculation is also proposed, which is based on the linearized incremental form of the Poynting theorem obtained by manipulating the energy balance principle expressed in material description.

The second numerical method developed is a two-and-a-half (2.5D) Boundary Element Method (BEM) able to predict the dispersion properties of damped guided waves in waveguides and cavities of arbitrary cross-section. In this formulation, the Cauchy Principal Value integrals and the boundary coefficients are treated by means of a regularization procedure. Unlike the SAFE formulations, where the dispersion analysis consists in solving a linear eigenvalue problem, the dispersive wave equation resulting from the regularized 2.5D BEM is configured as a nonlinear eigenvalue problem. This problem is solved by means of a recently developed Contour Integral Method. In relation to the singular characteristics and the multivalued feature of the Green functions, the properties of various Riemann sheets are investigated and a contour integration path is proposed, which takes into account the presence of the Sommerfeld branch cuts in the complex plane of the axial wavenumbers. By means of some numerical examples, a comparative analysis between the 2.5D BEM and the SAFE is performed, while some new results are obtained concerning the dispersive properties of surface guided waves along cavities of different geometries.

The third method proposed is a coupled SAFE-2.5D BEM approach for the dispersion analysis of leaky guided waves in viscoelastic waveguides of arbitrary cross-section that are embedded in viscoelastic isotropic media. So far, leaky guided waves have been essentially investigated for waveguides of simple geometries by means of analytical methods. Few studies have been proposed in literature in which are modeled using different approaches, such as absorbing regions [Castaings and Lowe, 2008; Fan et al., 2008], infinite elements [Jia et al., 2011] or Perfectly Matched Layers [Treyssède et al., 2012]. However, all the numerical methods above present some approximations in the description of the radiated wavefield, and the problem of how correctly model leaky guided waves in complex structures is still challenging.

In the proposed formulation, the energy radiation due to leakage of bulk waves is introduced in the SAFE model by converting the BEM impedance matrix into an equivalent dynamic stiffness matrix, which is manipulated as a single, wavenumber and frequency dependent, finite element of infinite extension. Due to singular characteristics of leaky modes, additional conditions are introduced in the Green functions in order to satisfy the Snell-Descartes law at the SAFE-BEM interface. The coupled SAFE-2.5D BEM formulation is also presented for waveguides immersed in fluids, in which the solution in the fluid region is assumed to satisfy the 2.5D Helmholtz equation.

The results obtained in this thesis and can be helpful for the design of both actuation and sensing systems in practical application, as well as to tune experimental setup.

1.3 Outline of the thesis

The thesis is organized as follows.

In Chapter 3, an extension to the Semi-Analytical Finite Element (SAFE) method is proposed in order to include the effect of a general state of initial stress on the dispersive behavior of damped guided waves. The wave equation is derived in linearized incremental form within an Updated Lagrangian framework. A modal formula for the wave energy velocity calculation is proposed, which is based on the linearized incremental form of the Poynting theorem in material description. New results not available in literature are discussed, which can be helpful in guided wave testing of loaded rails and pressurized pipelines.

In Chapter 3, a 2.5D Boundary Element formulation is developed to predict the dispersion properties of damped guided waves in waveguides and cavities of arbitrary cross-section. A regularization procedure is described to treat Cauchy Principal Value Integrals and boundary coefficients, while the resulting nonlinear eigenvalue problem is solved by using a recently developed Contour Integral Method. A Riemann surface analysis is also presented, and a contour integration path is described for the elastic and viscoelastic cases. The method is first validated against the SAFE method, while new results are discussed for cavities of different geometries.

Chapter 4 is dedicated to the study of leaky guided waves in viscoelastic waveguides of arbitrary cross-section embedded in viscoelastic media. The problem is solved by using a coupled SAFE-2.5D approach, in which the SAFE is used to model the embedded waveguide and the 2.5D BEM to represent the impedance of the surrounding medium. A single-valued analysis is presented for the resolvent stiffness operator, which is based on supplementary interface conditions introduced via the Snell-Descartes law. The proposed method is first validated against some results available in literature for simple geometries, while some new applications for complex geometries are proposed for the first time.

Chapter 5 describes a coupled SAFE-2.5D BEM model for the computation of the dispersion properties of leaky guided waves in waveguides immersed in ideal fluids. As in Chapter 3, a regularization procedure is adopted for the desingularization of the boundary integrals. To improve the numerical stability of the external Helmholtz problem, the so called CHIEF method is also implemented. The results obtained using the proposed procedure are first compared with those given by the GMM method. New results not available in literature are finally presented.

Finally, in Chapter 5 some brief conclusions are presented, with emphasis on the new contributions given in this study.

Chapter 2

Wave propagation in prestressed waveguides: SAFE method

2.1 Sommario

Un'estensione del metodo semi-analitico agli elementi finiti (SAFE method) viene proposta al fine di studiare l'effetto di uno stato pluriassiale di pretensione o predeformazione sul comportamento dispersivo di onde guidate che si propagano in guide d'onda dissipative. L'equazione del moto viene ricavata in un sistema di riferimento Lagrangiano aggiornato, nel quale la configurazione di pretensione viene assunta come configurazione di riferimento.

Poichè in applicazioni pratiche le deformazioni indotte nelle guide d'onda risultano di alcuni ordini di grandezza inferiori a quelle prodotte dai normali carichi di servizio, lo stato di deformazione iniziale può considerarsi finito in rapporto a quello generato dall'onda anche se la guida possiede, in questo stato, una riserva elastica.

In conformità a queste ipotesi, le equazioni di congruenza, costitutive e di equilibrio sono ricavate in forma incrementale linearizzata, includendo l'effetto di carichi di tipo non conservativo. L'equazione d'onda per il sistema semi-discretizzato conduce ad un problema polinomiale agli autovalori, dal quale i numeri d'onda e le associate forme modali vengono estratti per diverse fissate frequenze. Il set di soluzioni calcolato viene successivamente impiegato nell'estrazione dei parametri di dispersione: velocità di fase, attenuazione e velocità di gruppo. Mentre i primi due parametri possono essere estratti direttamente dal set di soluzioni calcolate, la velocità di gruppo richiede un'ulteriore elaborazione dei risultati. Una formula per il calcolo della velocità di gruppo è stata presentata e validata in letteratura per soli stati tensionali iniziali di tipo monoassiale. Nel presente studio questa formula viene pertanto estesa a stati di pretensione o predeformazione di tipo pluriassiale.

Tuttavia, il concetto di velocità di gruppo perde significato fisico nel caso di guide d'onda dissipative, essendo sostituito dal più generale concetto di velocità dell'energia. Poichè i modi attenuati sono di notevole interesse in ambito teorico ed applicato, viene proposta una formula modale per il calcolo della velocità dell'energia. Tale formula viene derivata in forza al teorema di Umov-Poynting stabilendo una legge di bilancio dell'energia in forma incrementale linearizzata.

La formulazione proposta viene dapprima validata comparando i risultati ottenuti con due casi noti in letteratura, una barra a sezione circolare ed un binario soggetto a variazioni termiche uniformi. Nuovi casi studio vengono proposti, riguardanti l'effetto delle tensioni residue derivanti dai processi di produzione dei binari e l'effetto di una pressione iniziale di tipo idrostatico sulla propagazione di onde guidate in condotte in mezzi fluidi.

In tutti i casi, l'effetto dovuto allo stato di pretensione iniziale risulta maggiormente evidente alle basse frequenze, dove il fenomeno di propagazione risulta più sensibile alle variazioni di rigidezza geometrica della guida. Ad alte frequenze il moto risulta quasi totalmente dominato dalla rigidezza meccanica della guida e l'effetto della pretensione diventa sostanzialmente trascurabile.

2.2 Introduction and literature review

A first rigorous mathematical treatment of wave propagation problems in solids with a predeformation or a prestress state has been provided by Biot [1957, 1940, 1965] and Hayes [1963]. Through the years, the problem has been subjected to an intensive research. Williams and Malvern [1969] used the harmonic analysis to get the phase-velocity dispersion curves for prestressed circular rods, flat plates and unbounded mediums considering both strain-rate-independent and strain-rate-dependent constitutive equations. The effect of tensile and compressive axial loads on the dispersive characteristic of elastic waves propagating in submerged beams was investigated by Cook and Holmes [1981]. More recently, Bhaskar [2003] studied the dispersion relations for propagative and evanescent modes with bending-torsion coupling, while Tanuma and Man [2006] considered Rayleigh waves propagating along the free surface of a prestressed anisotropic media, deriving a first-order perturbation formula for the phase velocity shift of Rayleigh waves from its comparative isotropic value. Frikha et al. [2011] have demonstrated that the effect of a compressive or tensile axial load on the elastic wave propagation in helical beams is significant for the four propagating modes in a low-frequency range.

The wave propagation problem in waveguide-like structures has been investigated in the literature using different mathematical approaches. In their work, Chen and Wilcox [2007] proposed a three-dimensional finite element based procedure to predict the effect of axial load on the dispersive properties of guided waves in elastic waveguides of arbitrary cross section such rods, plates and rails, validating the method at low frequencies by using analytical formulae for low order theories. Osetrov et al. [2000] applied the Transfer Matrix Method (TMM) to study Surface Acoustic Waves (SAW) propagating in anisotropic and hyperelastic layered systems under residual stress, including also changes in density, modification of the elastic stiffness tensor by residual strain and third-order stiffness constants. Lematre et al. [2006] applied matrix methods to predict Lamb, Shear Horizontal (SH) and SAW propagation in piezoelectric plates subjected to different stress profiles and to calculate the acoustoelastic effect on Lamb wave propagation in stressed thin-films as well as in multilayered heterostructures under biaxial residual stresses.

The prediction of dispersive characteristics of waves traveling along waveguides of arbitrary cross section represents a computationally expensive problem, especially when dispersive data is required at high frequencies. For waveguides of arbitrary but constant cross section the Semi Analytical Finite Element (SAFE) technique represents a very efficient tool, since it allows to discretize the waveguide cross section only, reducing drastically the dimension of the problem [Bartoli et al., 2006; Mu and Rose, 2008; Treyssède, 2008].

To date, Semi Analytical Finite Element (SAFE) formulations were predominantly exploited for axially-loaded waveguides of linear elastic materials only [Loveday, 2009]. In this work, Loveday included the effect of the axial load, resulting in a additional geometric stiffness matrix proportional to the mass matrix through the ratio between the axial stress and mass density. At low frequencies numerical results were shown to be in good agreement with those predicted by the Euler-Bernoulli beam theory. This extension has been used subsequently to evaluate the influence of axial load changes in rails by using sensitivity analysis and phase shift [Loveday and Wilcox, 2010] as well to support the development of a prototype aimed at predicting incipient buckling in Continuously Welded Rails (CWR) [Bartoli et al., 2010].

Experimental validations of the various formulations proposed in the literature can be found in different works. For instance, in their work, Chaki and Bourse [2009] applied simplified acoustoelastic formulations to calibrate a guided ultrasonic wave procedure for monitoring the stress level in seven-wire steel strands while Shen et al. [2008] used guided waves to localize defects in pipes bearing high pressure gases.

Since the use of guided waves for long range inspection applications is increasing, a further development of the SAFE formulation is necessary to extend it beyond the case of mono-axial prestress states. To this aim, the study presented in this chapter generalizes the SAFE formulations to viscoelastic waveguides subject to a three-dimensional state of prestress. The present extension allows thus to predict the effect of prestress on the guided waves group and energy velocity as well as the wave attenuation. In this context, Caviglia and Morro [1992, 1998] provided a rigorous mathematical treatment of the energy flux and dissipation of waves traveling in prestressed anisotropic viscoelastic solids. In their work, Degtyar and Rokhlin [1998] used a energy velocity formula to investigate the reflection/refraction problem for elastic wave propagation through a plane interface between two anisotropic stressed solids and between a fluid and a stressed anisotropic solid with arbitrary propagation directions and arbitrary incident wave type.

The present Chapter is organized in the following manner: the equilibrium equations of the incremental linearized theory are first reviewed including the general state of prestress, the viscoelastic properties of the material and the effect of nonconservative forces. The discretized system governing the wave propagation problem is then derived via application of the SAFE method. The group velocity formula proposed by Loveday

[2009] is updated to account for the new stiffness operators without including the viscoelastic effect, which is taken into account in the energy velocity formula derived from the energy balance principle recasted in incremental form. The scheme developed is sufficiently general to cover also prestressed waveguides of viscoelastic anisotropic materials.

2.3 Wave equation in linearized incremental form

The incremental equation of motion is derived in the Lagrangian framework depicted in Fig. 2.1 where $\mathcal{C}^0$ is a stress-free initial configuration in which the waveguide is not subjected to any static or dynamic loading process. The generic material particle is individuated in $\mathcal{C}^0$ by the position vector $\mathbf{X}^0 = [x^0,\ y^0,\ z^0]^{\mathrm{T}}$.

If a static load is applied to the stress free configuration $\mathcal{C}^0$, the particle $\mathbf{X}^0$ moves by a quantity $\mathbf{u}^0\left(\mathbf{X}\right) = \left[u_x^0,\ u_y^0,\ u_z^0\right]^{\mathrm{T}}$ and takes place in the configuration $\mathcal{C}$, which is indicated as the prestressed configuration. The volume and the boundary surface of the waveguide in $\mathcal{C}$ configuration are denoted with V and ∂V, respectively. The general particle at $\mathbf{X} = \mathbf{X}^0 + \mathbf{u}^0 = [x,\ y,\ z]^{\mathrm{T}}$ in the prestressed configuration is subjected to a stress field denoted by the Cauchy stress tensor $\boldsymbol{\sigma}^0\left(\mathbf{X}\right)$, which is assumed to satisfy the static equilibrium conditions with the external applied body and surface forces, denoted by $\mathbf{f}^0$ and $\mathbf{t}^0$, respectively.

The final configuration of the waveguide is denoted by $\mathcal{C}^t$ and is considered due to a displacement field resulting from the application of a dynamic pulse to the prestressed configuration. The current configuration vector at time t is given by $\mathbf{X}^t\left(\mathbf{u}\right) = \mathbf{X} + \mathbf{u} = [x^t,\ y^t,\ z^t]^{\mathrm{T}}$ and results from the superimposition of the (small) incremental time-dependent displacement field $\mathbf{u} = [u_x,\ u_y,\ u_z]^{\mathrm{T}}$ due to the mechanical waves on the prestressed configuration $\mathbf{X}$.

The equilibrium equations in incremental form can be obtained by following different approaches. Based on the coordinate systems chosen to describe the behavior of the body whose motion is under consideration, relevant quantities, such as deformations, constitutive relations and stresses can be described in terms of where the body was before any deformation due to externally applied loads or where it is during deformation; the former is called a *material description*, and the latter is called a *spatial description* [Bonet and Wood, 2008]. Alternatively, these are often referred to as *Lagrangian* and *Eulerian* descriptions respectively. Therefore, a material description refers to the behavior of a material particle, whereas a spatial description refers to the behavior at a spatial position. If the deformation state in the current configuration is described with respect to a coordinate system that does not correspond to the stress-free configuration, one refer in this case to the *Updated Lagrangian* description.

Although the Total Lagrangian (TL) description is widely used in the context of nonlinear solid mechanics, for the purpose of this study the Updated Lagrangian (UL) formulation results more convenient. According to the UL description, the $\mathcal{C}$ configuration is taken as reference and it can be computed from $\mathcal{C}^0$ considering the initial static displacement $\mathbf{u}_0$, which is assumed to be known, for example, from previous static analysis. Using this approach, the initial static displacement field $\mathbf{u}^0$ is accounted implicitly in the SAFE mesh that is used to discretize the cross-section of the waveguide in $\mathcal{C}$, thus without the need to include the static terms in the equilibrium equations. The TL description obviously still remains of general validity although the nonlinear compatibility relations would include in this case some additional high-order terms in $\mathbf{u}^0$, leading to more complicated equations [Bathe, 1996].

However, when deformations are superimposed on finite strains, the prestressed state is generally assumed identical or at most slightly deviated from the unstressed state and the TL and UL formulations can therefore be confused, i.e. one can assume $\mathbf{X}^0 \approx \mathbf{X}$. This simplification cannot be applied when large strains and stresses are involved since it requires the use of appropriate incremental kinematic and constitutive relations [Bathe, 1996; Bažant and Cedolin, 1991; Yang and Kuo, 1994]. Such cases are not considered in this study but are of great importance, especially when the stress level reaches the same order of magnitude of the incremental tangential moduli or, if the body is not thin, when the incremental material moduli shows high anisotropy [Bažant and Cedolin, 1991].

In finite deformation analysis that use FEM formulations, the Updated Lagrangian description is generally adopted to give a linearization of the equilibrium relations within a Newton method scheme [Bonet and Wood, 2008; Wriggers, 2008]. Following this scheme, the equilibrium configuration corresponding to a fixed load increment is found by subdividing first the load increment into different load steps and proceeding iteratively by solving a linearized system at each load step until convergence.

In reality, since only small pulses are applied on the waveguide, a fully nonlinear system of governing equations is not necessary.

In fact, the hypothesis of small incremental loads and small deformations is easily verified if one observes that in many practical applications waveguides can be treated as slender structures for which magnitudes of strains arising during their service state are generally included in the range of $10^{-4} \div 10^{-3}$, while guided waves generated by means of ultrasonic equipments generally produce strains in the order of 10^{-7} [Man, 1998; Rose, 2004]. This means that typical strains involved in slender structures can be considered “finite” if compared with ultrasonic strains even if the prestressed configuration posses an elastic reserve.

2.3.1 Linearized strain-displacement relations

The geometric nonlinearities associated with the initial stress enter the problem via the kinematic relations in force of the finite strains assumption.

A key quantity in finite deformation analysis is the deformation gradient $\mathbf{F}(\mathbf{u})$, which is involved in all equations relating quantities before deformation to corresponding quantities after (or during) deformation. The deformation gradient tensor enables the relative spatial position of two neighboring particles after deformation to be described in terms of their relative material position before deformation.

Denoting with $\mathbf{X}$ and $\mathbf{X}'$ the two position of a material particle in the prestressed and current configuration, respectively, the deformation gradient associated to the particle motion is expressed as

$$\begin{aligned}\mathbf{F}(\mathbf{u}) &= \frac{\partial \mathbf{X}^t(\mathbf{u})}{\partial \mathbf{X}} \\ &= \frac{\partial}{\partial \mathbf{X}}\left(\mathbf{X} + \mathbf{u}(\mathbf{X}, t)\right) \\ &= \mathbf{I} + \boldsymbol{\nabla}\mathbf{u},\end{aligned} \tag{2.1}$$

where $\mathbf{I}$ denotes the identity matrix and $\boldsymbol{\nabla}(\cdot)$ denotes the gradient with respect to the prestressed configuration $\mathcal{C}$. A general measure of the deformation in the material description is represented by the Green-Lagrange (GL) strain tensor, which can be expressed in terms of deformation gradient as [Bonet and Wood, 2008; Wriggers, 2008]

$$\mathbf{E}(\mathbf{u}) = \frac{1}{2}\left(\mathbf{F}^{\mathrm{T}}\mathbf{F} - \mathbf{I}\right), \tag{2.2}$$

or, by using the substitutions in Eq. (2.1), in terms of displacement gradient as

$$\mathbf{E}(\mathbf{u}) = \frac{1}{2}\left[\nabla\mathbf{u} + (\nabla\mathbf{u})^{\mathrm{T}} + (\nabla\mathbf{u})^{\mathrm{T}}\nabla\mathbf{u}\right]. \tag{2.3}$$

The Green-Lagrange can be conveniently decomposed into the sum of two tensors as $\mathbf{E}(\mathbf{u}) = \boldsymbol{\varepsilon}(\mathbf{u}) + \boldsymbol{\varepsilon}_{NL}(\mathbf{u})$, denoting $\boldsymbol{\varepsilon}(\mathbf{u})$ and $\boldsymbol{\varepsilon}_{NL}(\mathbf{u})$ the tensors of the strain components that are linear and nonlinear in the displacements $\mathbf{u}(\mathbf{X}, t)$, respectively. The linear strain tensor corresponds to the symmetric part of the GL strain tensor and is given by

$$\varepsilon(\mathbf{u}) = \mathrm{sym}(\mathbf{E}) = \frac{1}{2}\left[\nabla\mathbf{u} + \nabla(\mathbf{u})^{\mathrm{T}}\right], \tag{2.4}$$

while the tensor of nonlinear strains takes the form

$$\varepsilon_{NL}(\mathbf{u}) = \frac{1}{2}(\nabla\mathbf{u})^{\mathrm{T}}\nabla(\mathbf{u}). \tag{2.5}$$

In view of the Semi-Analytical Finite Element discretization, the independent components of the linear and nonlinear strain tensors in Eqs. (2.4) and (2.5) are collected in the 6×1 vector

$$\mathbf{e}(\mathbf{u}) = \boldsymbol{\epsilon}(\mathbf{u}) + \boldsymbol{\epsilon}_{NL}(\mathbf{u}), \tag{2.6}$$

where

$$\begin{aligned}\boldsymbol{\epsilon}(\mathbf{u}) &= \left[\varepsilon_{xx},\ \varepsilon_{yy},\ \varepsilon_{zz},\ \varepsilon_{yz},\ \varepsilon_{xz},\ \varepsilon_{xy}\right]^{\mathrm{T}}\\ &= \left[\mathscr{L}_x\frac{\partial}{\partial x} + \mathscr{L}_y\frac{\partial}{\partial y} + \mathscr{L}_z\frac{\partial}{\partial z}\right]\mathbf{u}\end{aligned} \tag{2.7}$$

is the vector of linear strain components and

$$\boldsymbol{\epsilon}_{NL}(\mathbf{u}) = \frac{1}{2}\left[\begin{array}{cccccc}\frac{\partial\mathbf{u}^{\mathrm{T}}}{\partial x}\frac{\partial\mathbf{u}}{\partial x} & \frac{\partial\mathbf{u}^{\mathrm{T}}}{\partial y}\frac{\partial\mathbf{u}}{\partial y} & \frac{\partial\mathbf{u}^{\mathrm{T}}}{\partial z}\frac{\partial\mathbf{u}}{\partial z} & 2\frac{\partial\mathbf{u}^{\mathrm{T}}}{\partial y}\frac{\partial\mathbf{u}}{\partial z} & 2\frac{\partial\mathbf{u}^{\mathrm{T}}}{\partial x}\frac{\partial\mathbf{u}}{\partial z} & 2\frac{\partial\mathbf{u}^{\mathrm{T}}}{\partial x}\frac{\partial\mathbf{u}}{\partial y}\end{array}\right]^{\mathrm{T}} \tag{2.8}$$

is the vector of nonlinear strain components. In Eqs. (2.7) and (2.8) the Voigt notation has been used, while the 6×3 compatibility operators $\mathscr{L}_i$ appearing in Eq. (2.7) are defined as [Bartoli et al., 2006]

$$\mathscr{L}_x = \begin{bmatrix}1&0&0\\0&0&0\\0&0&0\\0&0&0\\0&0&1\\0&1&0\end{bmatrix},\ \mathscr{L}_y = \begin{bmatrix}0&0&0\\0&1&0\\0&0&0\\0&0&1\\0&0&0\\1&0&0\end{bmatrix},\ \mathscr{L}_z = \begin{bmatrix}0&0&0\\0&0&0\\0&0&1\\0&1&0\\1&0&0\\0&0&0\end{bmatrix}. \tag{2.9}$$

Since the strain quantities defined in Eqs. (2.7) and (2.8) are nonlinear expressions in the displacement $\mathbf{u}(\mathbf{X}, t)$, they will lead to nonlinear governing equations. In force of the assumptions of small applied loads and small displacements, the governing equations can be recasted in a incremental linearized form. Assuming as incremental those quantities associated with the difference of motion between the current ($\mathcal{C}^t$) and the prestressed ($\mathcal{C}$) configurations, the linearized incremental strain-displacement relations can be obtained by means a first order Taylor series expansion in the neighborhood of the prestressed configuration, which reads

$$f\left(\mathbf{X}+\beta\mathbf{u}\right)-f\left(\mathbf{X}\right)=D_{\mathbf{u}}f\left(\mathbf{X}\right), \tag{2.10}$$

where

$$D_{\mathbf{u}}f\left(\mathbf{X}\right)=\left.\frac{\mathrm{d}}{\mathrm{d}\beta}\right|_{\beta=0}f\left(\mathbf{X}+\beta\mathbf{u}\right) \tag{2.11}$$

denotes the directional derivative at $\mathbf{X}$ in the direction of the incremental displacement $\mathbf{u}\left(\mathbf{X},t\right)$. Using Eq. (2.11), the linearizations of Eqs. (2.2) and (2.6) take the form

$$D_{\mathbf{u}}\mathbf{E}\left(\mathbf{u}\right)=\boldsymbol{\varepsilon}\left(\mathbf{u}\right), \tag{2.12}$$

$$D_{\mathbf{u}}\mathbf{e}\left(\mathbf{u}\right)=\boldsymbol{\epsilon}\left(\mathbf{u}\right), \tag{2.13}$$

while the linearizations of the first variations of Eqs. (2.2) and (2.6) are expressed as

$$D_{\mathbf{u}}\delta\mathbf{E}\left(\mathbf{u}\right)=\delta\boldsymbol{\varepsilon}_{NL}\left(\mathbf{u}\right), \tag{2.14}$$

$$D_{\mathbf{u}}\delta\mathbf{e}\left(\mathbf{u}\right)=\delta\boldsymbol{\epsilon}_{NL}\left(\mathbf{u}\right), \tag{2.15}$$

in which δ denotes the first variation with respect to $\mathbf{u}$.

2.3.2 Linearized stress-strain relations

The increment of stress related to any strain increment $\mathbf{E}\left(\mathbf{u}\right)$ results to be small as it depends on the small amplitude waves assumption. From an energetic point of view, the use of the 2nd Piola-Kirchhoff stress tensor $\mathbf{S}\left(\mathbf{u}\right)$ is required as work-conjugate of the GL strain tensor [Bažant and Cedolin, 1991; Bonet and Wood, 2008; Wriggers, 2008]. Because of only small amplitude waves are applied on the initial prestressed configuration, the state of stress in the current configuration will differ slightly from the prestressed state. As a consequence, the 2nd Piola-Kirchhoff stress tensor can be confused with the Cauchy stress tensor $\boldsymbol{\sigma}\left(\mathbf{u}\right)$. Making use of Eqs. (2.11) and (2.12), the above statement can be expressed in terms of linearized stress-strain relations as

$$\begin{aligned} D_{\mathbf{u}}\mathbf{S}\left(\mathbf{u}\right) &= \left.\frac{\partial\mathbf{S}\left(\mathbf{u}\right)}{\partial\mathbf{E}\left(\mathbf{u}\right)}\right|_{\mathbf{u}=0} : D_{\mathbf{u}}\mathbf{E}\left(\mathbf{u}\right) \\ &= \mathbf{C}\left(\mathbf{X}\right):\boldsymbol{\varepsilon}\left(\mathbf{u}\right) \\ &= \boldsymbol{\sigma}\left(\mathbf{u}\right) \end{aligned} \tag{2.16}$$

where $C_{ijkm}(\mathbf{X}) = \partial S_{ij}(\mathbf{u}) / \partial E_{km}(\mathbf{u})|_{\mathbf{u}=0}$ is the 6×6 fourth order symmetric tensor of tangential moduli of the material at point $\mathbf{X}$ in the prestressed configuration.

Since the linearized 2nd Piola-Kirchhoff stress tensor and the Cauchy stress tensor coalesce under the hypothesis of small displacements, their independent components can be uniquely collected in the 6×1 vector

$$\begin{aligned} \mathbf{s}(\mathbf{u}) &= [s_{xx},\ s_{yy},\ s_{zz},\ s_{yz},\ s_{xz},\ s_{xy}]^{\mathrm{T}} \\ &= [\sigma_{xx},\ \sigma_{yy},\ \sigma_{zz},\ \sigma_{yz},\ \sigma_{xz},\ \sigma_{xy}]^{\mathrm{T}}. \end{aligned} \tag{2.17}$$

Using Eqs. (2.7) and (2.17), the stress-strain relation in Eq. (2.16) can be reexpressed as

$$\mathbf{s}(\mathbf{u}) = \mathbf{C}(\mathbf{X})\,\boldsymbol{\epsilon}(\mathbf{u}). \tag{2.18}$$

If an isotropic material with linear viscoelastic behaviour is considered, the Boltzmann superposition principle can be used to express the incremental stress in force of the small amplitude waves. The linearized incremental stress vector in Eq. (2.18) can be rewritten in terms of convolution integral as [Christensen, 2010; Lee and Oh, 2005]

$$\mathbf{s}(\mathbf{u}) = \int_{-\infty}^{t} \mathbf{C}(\mathbf{X}, t-\tau)\, \frac{\partial \boldsymbol{\epsilon}\big(\mathbf{u}(\mathbf{X}, \tau)\big)}{\partial \tau} \mathrm{d}\tau \tag{2.19}$$

being now $\mathbf{C}(\mathbf{X}, t-\tau)$ the fourth order symmetric tensor of relaxation functions and t the current time instant.

2.3.3 Linearized incremental equilibrium equations

The equilibrium of the waveguide in incremental form is obtained by subtracting from the linearized equilibrium equations in the configuration $\mathcal{C}^t$ those written in the configuration $\mathcal{C}$. The equilibrium equations for both configurations can be obtained via application of the Hamilton's variational principle

$$\delta\mathscr{H}(\mathbf{u}, \delta\mathbf{u}) = \int_{t_1}^{t_2} \delta\big(\mathscr{K} - \mathscr{W} + \mathscr{V}_c + \mathscr{V}_{nc}\big)\mathrm{d}t = 0 \tag{2.20}$$

where $\mathscr{K}$ denotes the kinetic energy of the waveguide, $\mathscr{W}$ accounts for the stored stored elastic energy and the dissipated energy, $\mathscr{V}_c$ is the work done by the external conservative volume and surface forces and $\delta\mathscr{V}_{nc}$ is the nonconservative virtual work done by external deformation-dependent loads.

The various energetic terms at a generic point $\mathbf{X}^t$ in the configuration C^t can be expressed with respect to the configuration C as follows

$$
\begin{aligned}
\mathscr{K}\left(\mathbf{u}\right)|_{\mathcal{C}^t} &= \frac{1}{2}\int_V \rho\left(\mathbf{X}\right)\dot{\mathbf{u}}^2 \mathrm{d}v, && (2.21)\\
\mathscr{W}\left(\mathbf{u}\right)|_{\mathcal{C}^t} &= \frac{1}{2}\int_V \left(\boldsymbol{\epsilon}\left(\mathbf{u}\right)\right)^{\mathrm{T}}\mathbf{s}\left(\mathbf{u}\right)\mathrm{d}v, && (2.22)\\
\mathscr{V}_c\left(\mathbf{u}\right)|_{\mathcal{C}^t} &= \int_V \mathbf{u}^{\mathrm{T}}\left[\mathbf{f}_c^0\left(\mathbf{X}\right)+\mathbf{f}_c\left(\mathbf{X},t\right)\right]\mathrm{d}v + \int_{\partial V}\mathbf{u}^{\mathrm{T}}\left[\mathbf{t}_c^0\left(\mathbf{X}\right)+\mathbf{t}_c\left(\mathbf{X},t\right)\right]\mathrm{d}a, && (2.23)\\
\delta\mathscr{V}_{nc}\left(\mathbf{u}\right)|_{\mathcal{C}^t} &\simeq \int_{\partial V}\delta\mathbf{u}^{\mathrm{T}}\left[\mathbf{t}_{nc}^0\left(\mathbf{u}\right)+\mathbf{t}_{nc}\left(\mathbf{u}\right)\right]\mathrm{d}a, && (2.24)
\end{aligned}
$$

where $\mathbf{f}_c^0\left(\mathbf{X}\right)$ and $\mathbf{f}_c\left(\mathbf{X},t\right)$ are the vectors of initial and incremental conservative volume loads, respectively, $\mathbf{t}_c^0\left(\mathbf{X}\right)$ and $\mathbf{t}_c\left(\mathbf{X},t\right)$ denote the initial and incremental conservative traction loads, $\mathbf{t}_{nc}^0\left(\mathbf{u}\right)$ is the vector of nonconservative traction loads in the prestressed configuration and $\mathbf{t}_{nc}\left(\mathbf{u}\right)$ stands for a small displacement-dependent increment of the nonconservative traction loads. It should be remarked that the nonconservative external virtual work must be evaluated at the current configuration $\mathbf{X}^t\left(\mathbf{u}\right)$, which is unknown. Therefore, the spatial description should be used rigorously instead of the material description. However, if the increment in magnitude of the load is sufficiently small, the integration of the current load intensity can be performed with good accuracy over the surface of the prestressed configuration ∂V [Bathe, 1996].

The linearized variations of Eqs. (2.21)-(2.23) take the following representations

$$
\begin{aligned}
D_{\mathbf{u}}\delta\mathscr{K}\left(\mathbf{u},\delta\mathbf{u}\right) &= \int_V \delta\dot{\mathbf{u}}^{\mathrm{T}}\rho\left(\mathbf{X}\right)\dot{\mathbf{u}}\mathrm{d}v, && (2.25)\\
D_{\mathbf{u}}\delta\mathscr{W}\left(\mathbf{u},\delta\mathbf{u}\right) &= \int_V \left[D_{\mathbf{u}}\left(\delta\mathbf{e}\left(\mathbf{u}\right)\right)^{\mathrm{T}}\mathbf{s}\left(\mathbf{u}\right)|_{\mathbf{u}=0} + \left(\delta\mathbf{e}\left(\mathbf{u}\right)\right)^{\mathrm{T}}|_{\mathbf{u}=0}D_{\mathbf{u}}\mathbf{s}\left(\mathbf{u}\right)\right]\mathrm{d}v\\
&= \int_V \left[\left(\delta\boldsymbol{\epsilon}_{NL}\left(\mathbf{u}\right)\right)^{\mathrm{T}}\mathbf{s}^0\left(\mathbf{X}\right) + \left(\delta\boldsymbol{\epsilon}\left(\mathbf{u}\right)\right)^{\mathrm{T}}\mathbf{s}\left(\mathbf{u}\right)\right]\mathrm{d}v\\
&= \int_V \left(\delta\boldsymbol{\epsilon}_{NL}\left(\mathbf{u}\right)\right)^{\mathrm{T}}\mathbf{s}^0\left(\mathbf{X}\right)\mathrm{d}v\\
&\quad + \int_V\int_{-\infty}^{t}\left(\delta\boldsymbol{\epsilon}\left(\mathbf{u}\right)\right)^{\mathrm{T}}\mathbf{C}\left(\left(\mathbf{X}\right),t-\tau\right)\frac{\partial\boldsymbol{\epsilon}\left(\mathbf{u}\left(\mathbf{X},\tau\right)\right)}{\partial\tau}\mathrm{d}t\mathrm{d}v, && (2.26)\\
D_{\mathbf{u}}\delta\mathscr{V}_c\left(\mathbf{u},\delta\mathbf{u}\right) &= \int_V \delta\mathbf{u}^{\mathrm{T}}\mathbf{f}_c\left(\mathbf{X},t\right)\mathrm{d}v + \int_{\partial V}\delta\mathbf{u}^{\mathrm{T}}\mathbf{t}_c\left(\mathbf{X},t\right)\mathrm{d}a, && (2.27)
\end{aligned}
$$

in which $\mathbf{s}^0\left(\mathbf{X}\right) = \left[s_{xx}^0,\ s_{yy}^0,\ s_{zz}^0,\ s_{yz}^0,\ s_{xz}^0,\ s_{xy}^0\right]^{\mathrm{T}}$ is the vector collecting the independent components of the Cauchy stress tensor $\boldsymbol{\sigma}^0\left(\mathbf{X}\right)$ in the prestressed configuration. It is noted that Eq. (2.19) for the time-dependent stress-strain relations has been used in Eq. (2.26). In the rest of this chapter, it is assumed that the nonconservative forces applied to the system are of pressure type only, with no friction between the solid-fluid interfaces. In this case one can recognize that

$$\mathbf{t}_{nc}^{0}\left(\mathbf{u}\right) = -p_0 \mathbf{n}\left(\mathbf{u}\right), \tag{2.28}$$

$$\mathbf{t}_{nc}\left(\mathbf{u}\right) = -p \mathbf{n}\left(\mathbf{u}\right), \tag{2.29}$$

where p_0 and p are, respectively, the hydrostatic pressure acting on the waveguide in the prestressed configuration and the incremental pressures applied at the boundary, while $\mathbf{n}\left(\mathbf{u}\left(\mathbf{X}, t\right)\right)$ is the outward normal at the point $\mathbf{X}$ of the boundary surface ∂V. It is noted that, since $\mathbf{t}_{nc}^{0}\left(\mathbf{u}\right)$ and $\mathbf{t}_{nc}\left(\mathbf{u}\right)$ must represent a traction, the notation used in Eqs. (2.28) and ((2.29)) implies that the pressure is positive in compression. If the fluid-structure interaction is neglected, then the term $\mathbf{t}_{nc}\left(\mathbf{u}\right)$ on the right hand side of Eq. (2.24) vanishes, since in this case the magnitude of the pressure does not depend upon the deformation but only on the load direction $p\mathbf{n}\left(\mathbf{u}\right)$. As a consequence, the linearized external virtual work can be reexpressed as

$$D_{\mathbf{u}}\delta\mathscr{V}_{nc}\left(\mathbf{u}, \delta\mathbf{u}\right) = D_{\mathbf{u}}\delta\mathscr{V}_{p}\left(\mathbf{u}, \delta\mathbf{u}\right) = \int_{\partial\Omega_s} -p_0 \delta\mathbf{u}^{\mathrm{T}} \big(D_{\mathbf{u}}\mathbf{n}\left(\mathbf{u}\right)\big) \mathrm{d}a \tag{2.30}$$

where $D_{\mathbf{u}}\mathbf{n}\left(\mathbf{u}\right) = \frac{\partial \mathbf{n}(\mathbf{u})}{\partial \mathbf{u}}\mathbf{u}$ denotes the linearized change of orientation of the outward normal at $\mathbf{X}$ due to the displacement $\mathbf{u}\left(\mathbf{X}, t\right)$ at the same point.

In order to obtain the linearized incremental form of the equation of motion, Eq. (2.20) can be first substituted into Eq. (2.10) to give

$$D_{\mathbf{u}}\delta\mathscr{H}\left(\mathbf{u}, \delta\mathbf{u}\right) = 0, \tag{2.31}$$

which expresses that the directional derivative of the first variation of the Hamilton's functional must vanish for any given small displacement $\mathbf{u}\left(\mathbf{X}, t\right)$ applied at point $\mathbf{X}$ on the prestressed configuration must vanish. Making use of Eqs. (2.25), (2.26), (2.27) and (2.30), after some algebra the first variation of the Hamiltonian action in linearized incremental form is obtained

$$\begin{aligned}D_{\mathbf{u}}\delta\mathscr{H}\left(\mathbf{u},\delta\mathbf{u}\right)=&\int_{t_1}^{t_2}\int_V\Big(-\left(\delta\mathbf{u}\right)^{\mathrm{T}}\rho\left(\mathbf{X}\right)\ddot{\mathbf{u}}-\big(\delta\boldsymbol{\epsilon}_{NL}\left(\mathbf{u}\right)\big)^{\mathrm{T}}\mathbf{s}^0\left(\mathbf{X}\right)+\left(\delta\mathbf{u}\right)^{\mathrm{T}}\mathbf{f}_c\left(\mathbf{X},t\right)\Big)\mathrm{d}v\mathrm{d}t\\&-\int_{t_1}^{t_2}\int_V\int_{-\infty}^{t}\big(\delta\boldsymbol{\epsilon}\left(\mathbf{u}\right)\big)^{\mathrm{T}}\mathbf{C}\left(\mathbf{X},t-\tau\right)\frac{\partial\boldsymbol{\epsilon}\big(\mathbf{u}\left(\mathbf{X},\tau\right)\big)}{\partial\tau}\mathrm{d}\tau\mathrm{d}v\mathrm{d}t\\&+\int_{t_1}^{t_2}\int_{\partial V}\left(\delta\mathbf{u}\right)^{\mathrm{T}}\mathbf{t}_c\left(\mathbf{X},t\right)\mathrm{d}a\mathrm{d}t\\&-\int_{t_1}^{t_2}\int_{\partial V}\left(\delta\mathbf{u}\right)^{\mathrm{T}}p_0\frac{\partial\mathbf{n}\left(\mathbf{u}\right)}{\partial\mathbf{u}}\mathbf{u}\mathrm{d}a\mathrm{d}t\\&=0\end{aligned}\tag{2.32}$$

Eq. (2.32) represents the basic system governing the dynamic of small oscillations of a three dimensional viscoelastic body subjected to an initial generic stress field.

2.4 Equations in the wavenumber-frequency domain

Given the longitudinal invariance, or periodicity, of both material and geometric characteristics of the waveguide in direction z and considering a wavenumber-frequency dependence of the form

$$\exp\left[\mathrm{i}\left(\kappa_z z-\omega t\right)\right]\tag{2.33}$$

where κ_z denotes the wavenumber in the direction of propagation, ω is the angular frequency and i is the imaginary unit, any scalar or vectorial field can be contracted from the space-time domain to the wavenumber-frequency domain using the Fourier transforms

$$f\left(z,\omega\right)=\mathscr{F}\big[f\left(z,t\right)\big]\left(\omega\right)=\int_{-\infty}^{+\infty}f\left(z,t\right)\exp\left(-\mathrm{i}\omega t\right)\mathrm{d}t,\tag{2.34}$$

$$f\left(\kappa_z,t\right)=\mathscr{F}\big[f\left(z,t\right)\big]\left(\kappa_z\right)=\int_{-\infty}^{+\infty}f\left(z,t\right)\exp\left(-\mathrm{i}\kappa_z z\right)\mathrm{d}z.\tag{2.35}$$

Important consequences of this transformation convention concern the direction of positive wave propagation and decay and the location of poles for the dynamic system under consideration [Kausel, 2006]. These, in turn, relate to the principles of radiation and boundedness at infinity, which will be addressed in the next chapters. Since the Fourier transforms act only on the t and z dependent fields, each wavenumber $\kappa_z\left(\omega\right)$ (or, conversely, each angular frequency $\omega\left(\kappa_z\right)$) is projected on the $x-y$ plane and the corresponding waveform propagating in the z-direction can be captured in the $x-y$ plane by an in-plane mesh of the waveguide cross section.

The stress-strain relation in Eq. (2.19) can be contracted from the time to the frequency domain, yielding to the well known relation [Christensen, 2010]

$$\begin{aligned} D_{\mathbf{u}}\mathbf{s}\left(\mathbf{X},\omega\right) &= \int_{-\infty}^{+\infty}\int_{-\infty}^{t}\mathbf{C}\left(\mathbf{X},t-\tau\right)\frac{\partial\boldsymbol{\epsilon}\left(\mathbf{u}\left(\mathbf{X},t\right)\right)}{\partial\tau}\exp\left(-\mathrm{i}\omega t\right)\mathrm{d}\tau\mathrm{d}t \\ &= \tilde{\mathbf{C}}\left(\mathbf{X},\omega\right)\boldsymbol{\epsilon}\left(\mathbf{X},\omega\right), \end{aligned} \tag{2.36}$$

which states that the incremental stress relative to small deformations can be obtained in the frequency domain as in a linear elastic analysis, providing only the substitution of the real tensor of elastic moduli with the complex tensor of relaxation functions $\tilde{\mathbf{C}}\left(\omega\right) = \mathrm{Re}[\tilde{\mathbf{C}}\left(\omega\right)] + \mathrm{i}\mathrm{Im}[\tilde{\mathbf{C}}\left(\omega\right)]$, where Re $\left(\tilde{\mathbf{C}}[\omega\right)]$ is the so-called tensor of storage moduli and $\mathrm{Im}[\tilde{\mathbf{C}}\left(\omega\right)]$ denotes the tensor of loss moduli.

The versatility of the finite element formulation allows considering several types of visco-elastic rheological models, by simply assuming the opportune complex moduli matrix $\tilde{\mathbf{C}}\left(\omega\right)$. Generally, two different models are used in the literature to describe absorbing media. One of them, the Maxwell rheological model, expresses the dynamic behavior of the hysteretic stress-strain relationship

$$\mathrm{Re}\left[\tilde{\mathbf{C}}\left(\omega\right)\right] = \mathbf{D}, \quad \mathrm{Im}\left[\tilde{\mathbf{C}}\left(\omega\right)\right] = -\mathrm{i}\boldsymbol{\eta}, \tag{2.37}$$

where $\mathbf{D}$ is the well known tensor of elastic moduli while $\boldsymbol{\eta}$ is the viscosity tensor. Compared to a non-absorbing propagation model, the only modification is that the visco-elastic tensor becomes complex.

In contrast, the Kelvin-Voigt model assumes a linear dependence of $\mathrm{Im}[\tilde{\mathbf{C}}\left(\omega\right)]$ on the frequency:

$$\mathrm{Re}\left[\tilde{\mathbf{C}}\left(\omega\right)\right] = \mathbf{D}, \quad \mathrm{Im}\left[\tilde{\mathbf{C}}\left(\omega\right)\right] = -\mathrm{i}\omega\boldsymbol{\eta}. \tag{2.38}$$

In Eqs. (2.37) and (2.38), a negative loss modulus is considered according to the harmonic definition of the displacement field given in Eq. (2.33). In fact, depending on the sign of the temporal term ($\mathrm{i}\omega t$), the sign of the loss modulus can assume positive or negative value. When used in the equation of motion, the effect of the Kelvin-Voigt model, bringing out the frequency dependence of the tensor, requires the imaginary part of the visco-elastic tensor to be recalculated at each frequency. The impact of both models has been thoroughly investigated in [Neau, 2003] and [Rose, 2004]. It appears that the attenuation is proportional to the frequency times the imaginary part of the viscoelastic tensor and, being the loss per unit distance traveled, is a linear function of the frequency in the case of the hysteretic model and a quadratic function of the frequency in the case of the Kelvin-Voigt model. While in the case of hysteretic damping the complex part of the viscoelastic tensor usually is given without any reference to the frequency value for which the tensor itself is obtained, it is important to remind that in the case of Kelvin-Voigt model, such frequency has to be specified. Since the study of the different behaviours of guided waves under different rheological models is not the primary topic of this thesis, only hysteretic (Maxwell) rheological models will be considered.

Using the Fourier transforms in Eq. (2.34) along with the fundamental property $\mathscr{F}\left[\mathrm{d}^n f\left(z,t\right)/\mathrm{d}t^n\right](\omega) = (\mathrm{i}\omega)^n f\left(z,\omega\right)$ and Eq. (2.36), the variational statement in Eq. (2.32) can be reelaborated from the space-time to the space-frequency domain as

$$\begin{aligned} &\omega^2 \int_V \delta\mathbf{u}^{\mathrm{T}} \rho\left(\mathbf{X}\right) \mathbf{u} \mathrm{d}v - \int_V \left(\delta\boldsymbol{\epsilon}_{NL}\left(\mathbf{u}\right)\right)^{\mathrm{T}} \mathbf{s}^0\left(\mathbf{X}\right) \mathrm{d}v \\ &+ \int_V \delta\mathbf{u}^{\mathrm{T}} \mathbf{f}_c\left(\mathbf{X},\omega\right) \mathrm{d}v - \int_V \left(\delta\boldsymbol{\epsilon}\left(\mathbf{u}\right)\right)^{\mathrm{T}} \tilde{\mathbf{C}}\left(\mathbf{X},\omega\right) \boldsymbol{\epsilon}\left(\mathbf{u}\right) \mathrm{d}v \\ &+ \int_{\partial V} \delta\mathbf{u}^{\mathrm{T}} \mathbf{t}_c\left(\mathbf{X},\omega\right) \mathrm{d}a - \int_{\partial V} \delta\mathbf{u}^{\mathrm{T}} p_0 \frac{\partial\mathbf{n}\left(\mathbf{u}\right)}{\partial\mathbf{u}} \mathbf{u} \mathrm{d}a = 0. \end{aligned} \tag{2.39}$$

The above equation is used as the basic equation for the semi-analytical finite element discretization procedure, which is exposed in the next section.

2.5 Domain discretization using semi-isoparametric finite elements

The dimension of the problem represented by Eq. (2.39) can be reduced by one in the space domain by exploiting the translational invariance (or periodicity) of the geometric and mechanical properties of the waveguide. The volume and surface integrals are decomposed as follows

$$\int_V f\left(\mathbf{X},t\right) \mathrm{d}v = \int_{-\infty}^{+\infty} \int_{\Omega_s} f\left(\mathbf{x},z,t\right) \mathrm{d}x\mathrm{d}y\mathrm{d}z \tag{2.40}$$

$$\int_{\partial V} f\left(\mathbf{X},t\right) \mathrm{d}a = \int_{-\infty}^{+\infty} \int_{\partial\Omega_s} f\left(\mathbf{x},z,t\right) \mathrm{d}s\mathrm{d}z \tag{2.41}$$

where Ω_s and $\partial\Omega_s$ denote the area and boundary of the waveguide cross-section, respectively, and $\mathbf{x} = [x,\ y]^{\mathrm{T}}$ is the generic in-plane configuration vector for a material particle in the prestressed configuration. Substituting the positions in Eqs. (2.40) and (2.41) into Eq. (2.39) yields

$$\begin{aligned}
&\omega^2 \int_{-\infty}^{+\infty}\int_{\Omega_s} (\delta\mathbf{u})^{\mathrm{T}} \rho\left(\mathbf{x}, z\right) \mathbf{u} \mathrm{d}x\mathrm{d}y\mathrm{d}z \\
&- \int_{-\infty}^{+\infty}\int_{\Omega_s} \left(\delta\boldsymbol{\epsilon}_{NL}\left(\mathbf{u}\right)\right)^{\mathrm{T}} \mathbf{s}^0\left(\mathbf{x}, z\right) \mathrm{d}x\mathrm{d}y\mathrm{d}z \\
&+ \int_{-\infty}^{+\infty}\int_{\Omega_s} (\delta\mathbf{u})^{\mathrm{T}} \mathbf{f}_c\left(\mathbf{x}, z, \omega\right)\mathrm{d}x\mathrm{d}y\mathrm{d}z \\
&- \int_{-\infty}^{+\infty}\int_{\Omega_s} \left(\delta\boldsymbol{\epsilon}\left(\mathbf{u}\right)\right)^{\mathrm{T}} \tilde{\mathbf{C}}\left(\mathbf{x}, z, \omega\right) \boldsymbol{\epsilon}\left(\mathbf{u}\right) \mathrm{d}x\mathrm{d}y\mathrm{d}z \\
&+ \int_{-\infty}^{+\infty}\int_{\partial\Omega_s} (\delta\mathbf{u})^{\mathrm{T}} \mathbf{t}_c\left(\mathbf{x}, z, \omega\right) \mathrm{d}s\mathrm{d}z \\
&- \int_{-\infty}^{+\infty}\int_{\partial\Omega_s} (\delta\mathbf{u})^{\mathrm{T}} p_0 \frac{\partial\mathbf{n}\left(\mathbf{u}\right)}{\partial\mathbf{u}} \mathbf{u} \mathrm{d}s\mathrm{d}z = 0.
\end{aligned} \tag{2.42}$$

Since Eq. (2.42) holds for any virtual displacement $\delta\mathbf{u}$, the integrals over the longitudinal coordinate z vanish, and Eq. (2.42) is therefore equivalent to

$$\begin{aligned}
&\omega^2 \int_{\Omega_s} \delta\mathbf{u}^{\mathrm{T}} \rho\left(\mathbf{x}, z\right) \mathbf{u} \mathrm{d}x\mathrm{d}y - \int_{\Omega_s} \left(\delta\boldsymbol{\epsilon}_{NL}\left(\mathbf{u}\right)\right)^{\mathrm{T}} \mathbf{s}^0\left(\mathbf{x}, z\right) \mathrm{d}x\mathrm{d}y \\
&+ \int_{\Omega_s} \delta\mathbf{u}^{\mathrm{T}} \mathbf{f}_c\left(\mathbf{x}, z, \omega\right)\mathrm{d}x\mathrm{d}y - \int_{\Omega_s} \left(\delta\boldsymbol{\epsilon}\left(\mathbf{u}\right)\right)^{\mathrm{T}} \tilde{\mathbf{C}}\left(\mathbf{x}, z, \omega\right) \boldsymbol{\epsilon}\left(\mathbf{u}\right) \mathrm{d}x\mathrm{d}y \\
&+ \int_{\partial\Omega_s} \delta\mathbf{u}^{\mathrm{T}} \mathbf{t}_c\left(\mathbf{x}, z, \omega\right) \mathrm{d}s - \int_{\partial\Omega_s} \delta\mathbf{u}^{\mathrm{T}} p_0 \frac{\partial\mathbf{n}\left(\mathbf{u}\right)}{\partial\mathbf{u}} \mathbf{u} \mathrm{d}s = 0.
\end{aligned} \tag{2.43}$$

The integral Eq. (2.43) can be solved by a Fourier transform of the longitudinal coordinate z to the axial wavenumber κ_z. Making use of Eq. (2.35), Eq. (2.43) is transformed to the wavenumber domain as

$$\begin{aligned}
&\omega^2 \int_{\Omega_s} \delta\mathbf{u}^{\mathrm{T}} \rho\left(\mathbf{x}, \kappa_z\right) \mathbf{u} \mathrm{d}x\mathrm{d}y - \int_{\Omega_s} \left(\delta\boldsymbol{\epsilon}_{NL}\left(\mathbf{u}\right)\right)^{\mathrm{T}} \mathbf{s}^0\left(\mathbf{x}, \kappa_z\right) \mathrm{d}x\mathrm{d}y \\
&+ \int_{\Omega_s} \delta\mathbf{u}^{\mathrm{T}} \mathbf{f}_c\left(\mathbf{x}, \kappa_z, \omega\right)\mathrm{d}x\mathrm{d}y - \int_{\Omega_s} \left(\delta\boldsymbol{\epsilon}\left(\mathbf{u}\right)\right)^{\mathrm{T}} \tilde{\mathbf{C}}\left(\mathbf{x}, \kappa_z, \omega\right) \boldsymbol{\epsilon}\left(\mathbf{u}\right) \mathrm{d}x\mathrm{d}y \\
&+ \int_{\partial\Omega_s} \delta\mathbf{u}^{\mathrm{T}} \mathbf{t}_c\left(\mathbf{x}, \kappa_z, \omega\right) \mathrm{d}s - \int_{\partial\Omega_s} \delta\mathbf{u}^{\mathrm{T}} p_0 \frac{\partial\mathbf{n}\left(\mathbf{u}\right)}{\partial\mathbf{u}} \mathbf{u} \mathrm{d}s = 0.
\end{aligned} \tag{2.44}$$

The cross-section of the waveguide is discretized in the prestressed configuration $\mathcal{C}$

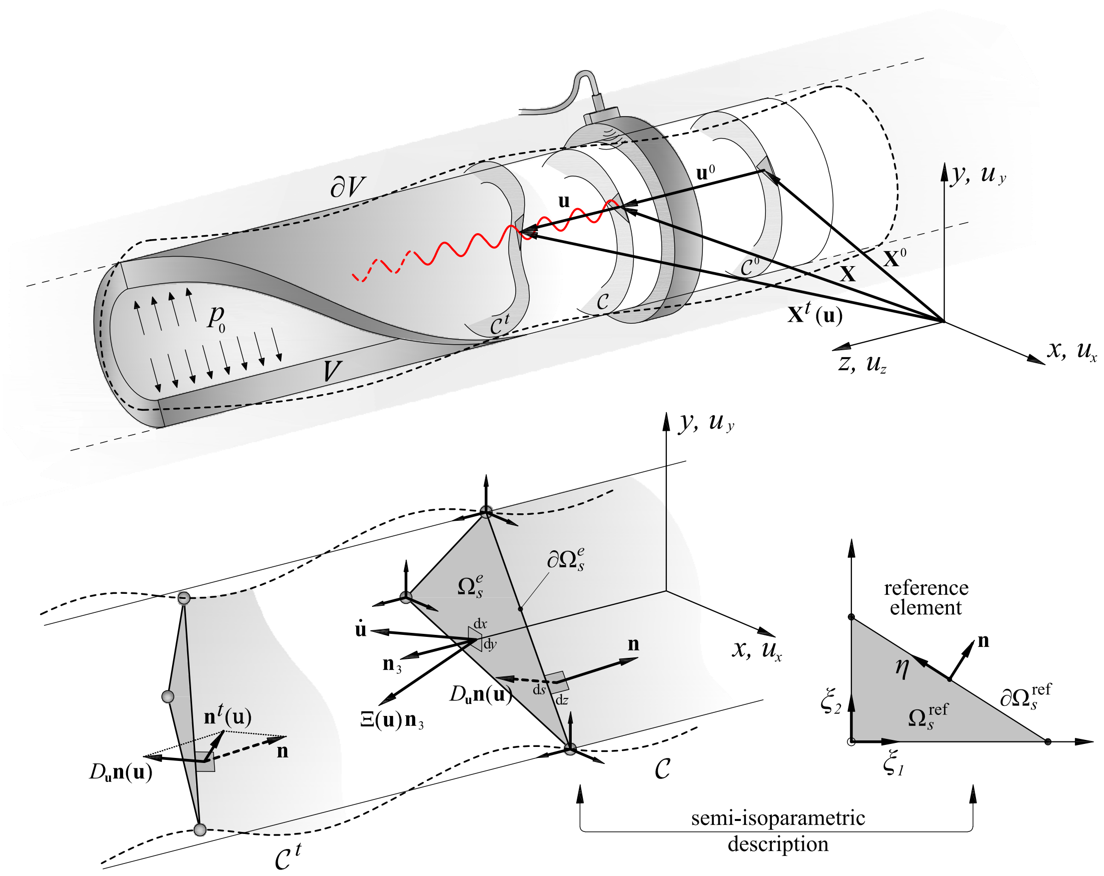

Figure 2.1: Fundamental configurations for the wave propagation problem in prestressed waveguides.

by means of a planar mesh of N_{el} bidimensional finite elements with area Ω_s^e, boundary $\partial\Omega_s^e$ and 3 degrees of freedom per node associated to the three displacements components u_i. Assuming an in-plane linear mapping from the reference element identified by the area Ω_s^{ref} and boundary $\partial\Omega_s^{\mathrm{ref}}$ to the corresponding area Ω_s^e and boundary $\partial\Omega_s^e$ of the generic eth element of the mesh (see Fig. 2.1), the semi-isoparametric representation results in an uncoupled description of the out-of-plane and in-plane motion. The displacement vector $\mathbf{u}(\mathbf{x}, z, t)$ within the eth element is approximated as

$$\mathbf{u}(\boldsymbol{\xi}, z, t) = \mathbf{N}(\boldsymbol{\xi})\,\mathbf{q}^e(z, t) \quad \text{on } \Omega_s^e \tag{2.45}$$

$$\mathbf{u}(\eta, z, t) = \boldsymbol{\mathcal{N}}(\eta)\,\mathbf{q}^e(z, t) \quad \text{on } \partial\Omega_s^e \tag{2.46}$$

where $\mathbf{N}(\boldsymbol{\xi})$ and $\boldsymbol{\mathcal{N}}$ are matrices containing the shape functions in the natural coordinates $\boldsymbol{\xi} = (\xi_1, \xi_2)$ and η on Ω_s^{ref} and $\partial\Omega_s^{\mathrm{ref}}$, respectively, while $\mathbf{q}^e(z, t)$ is the vector of nodal displacements (see Fig. 2.1).

Using the Fourier transforms in Eq. (2.34) and (2.35), the displacement vectors on Ω_s^e and $\partial\Omega_s^e$ in the wavenumber-frequency domain are rewritten as

$$\mathbf{u}\left(\boldsymbol{\xi},\kappa_z,\omega\right)=\mathbf{N}\left(\boldsymbol{\xi}\right)\mathbf{q}^e\left(\kappa_z,\omega\right)\quad\text{on }\Omega_s^e \tag{2.47}$$

$$\mathbf{u}\left(\eta,\kappa_z,\omega\right)=\boldsymbol{\mathcal{N}}\left(\eta\right)\mathbf{q}^e\left(\kappa_z,\omega\right)\quad\text{on }\partial\Omega_s^e \tag{2.48}$$

while the Fourier-transformed vectors corresponding to the increments of volume and surface loads become $\mathbf{f}_c\left(\boldsymbol{\xi},\kappa_z,\omega\right)$ and $\mathbf{t}_c\left(\eta,\kappa_z,\omega\right)$. The transformed kinematic relation given in Eq. (2.7) is

$$\boldsymbol{\epsilon}\left(\boldsymbol{\xi},\kappa_z,\omega\right)=\left[\mathscr{B}_{xy}\left(\boldsymbol{\xi}\right)+\mathrm{i}\kappa_z\mathscr{B}_z\left(\boldsymbol{\xi}\right)\right]\mathbf{q}^e\left(\kappa_z,\omega\right), \tag{2.49}$$

where

$$\mathscr{B}_{xy}\left(\boldsymbol{\xi}\right)=\left[\mathscr{L}_x\frac{\partial\mathbf{N}\left(\boldsymbol{\xi}\right)}{\partial\xi_i}\frac{\partial\xi_i}{\partial x}+\mathscr{L}_y\frac{\partial\mathbf{N}\left(\boldsymbol{\xi}\right)}{\partial\xi_i}\frac{\partial\xi_i}{\partial y}\right], \tag{2.50}$$

$$\mathscr{B}_z\left(\boldsymbol{\xi}\right)=\mathscr{L}_z\mathbf{N}\left(\boldsymbol{\xi}\right). \tag{2.51}$$

Finally, the vector of nonlinear strain components given in Eq. (2.8) transformed in the wavenumber-frequency domain takes the form

$$\boldsymbol{\epsilon}_{NL}\left(\boldsymbol{\xi},\kappa_z,\omega\right)=\frac{1}{2}\begin{bmatrix}\left(\mathbf{q}^e\right)^{\mathrm{T}}\left(\dfrac{\mathbf{N}\left(\boldsymbol{\xi}\right)}{\partial\xi_i}\dfrac{\partial\xi_i}{\partial x}\right)^{\mathrm{T}}\left(\dfrac{\mathbf{N}\left(\boldsymbol{\xi}\right)}{\partial\xi_i}\dfrac{\partial\xi_i}{\partial x}\right)\mathbf{q}^e\\ \left(\mathbf{q}^e\right)^{\mathrm{T}}\left(\dfrac{\mathbf{N}\left(\boldsymbol{\xi}\right)}{\partial\xi_i}\dfrac{\partial\xi_i}{\partial y}\right)^{\mathrm{T}}\left(\dfrac{\mathbf{N}\left(\boldsymbol{\xi}\right)}{\partial\xi_i}\dfrac{\partial\xi_i}{\partial y}\right)\mathbf{q}^e\\ -\kappa_z^2\left(\mathbf{q}^e\right)^{\mathrm{T}}\left(\mathbf{N}\left(\boldsymbol{\xi}\right)\right)^{\mathrm{T}}\mathbf{N}\left(\boldsymbol{\xi}\right)\mathbf{q}^e\\ 2\mathrm{i}\kappa_z\left(\mathbf{q}^e\right)^{\mathrm{T}}\left(\dfrac{\mathbf{N}\left(\boldsymbol{\xi}\right)}{\partial\xi_i}\dfrac{\partial\xi_i}{\partial y}\right)^{\mathrm{T}}\mathbf{N}\left(\boldsymbol{\xi}\right)\mathbf{q}^e\\ 2\mathrm{i}\kappa_z\left(\mathbf{q}^e\right)^{\mathrm{T}}\left(\dfrac{\mathbf{N}\left(\boldsymbol{\xi}\right)}{\partial\xi_i}\dfrac{\partial\xi_i}{\partial x}\right)^{\mathrm{T}}\mathbf{N}\left(\boldsymbol{\xi}\right)\mathbf{q}^e\\ 2\left(\mathbf{q}^e\right)^{\mathrm{T}}\left(\dfrac{\mathbf{N}\left(\boldsymbol{\xi}\right)}{\partial\xi_i}\dfrac{\partial\xi_i}{\partial x}\right)^{\mathrm{T}}\left(\dfrac{\mathbf{N}\left(\boldsymbol{\xi}\right)}{\partial\xi_i}\dfrac{\partial\xi_i}{\partial y}\right)\mathbf{q}^e\end{bmatrix}. \tag{2.52}$$

The discretized equations of motion can be derived for the translational invariant waveguide by observing that the relationship between an infinitesimal area $\mathrm{d}x\mathrm{d}y$ and the corresponding volume in the reference system $\mathrm{d}\xi_1\mathrm{d}\xi_2$ is given by $\mathrm{d}x\mathrm{d}y=J_s^e\left(\boldsymbol{\xi}\right)\mathrm{d}\xi_1\mathrm{d}\xi_2$, with $J_s^e\left(\boldsymbol{\xi}\right)=\det[\partial\mathbf{x}/\partial\boldsymbol{\xi}]$ denoting the Jacobian of the isoparametric mapping in the $x-y$ plane. Using these relations, one can compute the area integrals over finite elements as $\int_{\Omega_s^e}(\cdot)\,\mathrm{d}x\mathrm{d}y = \int_{\Omega_s^{\mathrm{ref}}}(\cdot)\,J_s^e(\boldsymbol{\xi})\,\mathrm{d}\xi_1\mathrm{d}\xi_2$.

Similarly, the relation between an infinitesimal surface area of the waveguide in the prestressed and reference configurations can be written as $\mathrm{d}s = J_s^e(\eta)\,\mathrm{d}\eta$, where the Jacobian of the in-plane transformation is now given by $J_s^e(\eta) = \|(\partial\mathbf{x}/\partial\eta)\times\mathbf{n}_3\|$, in which $\mathbf{n}_3$ denotes the unit vector along the z-direction. Therefore, each boundary integral can be written at the finite element level as $\int_{\partial\Omega_s^e}(\cdot)\,\mathrm{d}s = \int_{\partial\Omega_s^{\mathrm{ref}}}(\cdot)\,J_s^e(\eta)\,\mathrm{d}\eta$.

The linearized change of orientation of the surface normal due to the displacement $\mathbf{u}(\mathbf{x},t)$ can be obtained as the vector product between the tangential displacement at $\mathbf{x}$ in the $x-y$ plane and the unit vector in the z-direction. Introducing the linearization [Bonet and Wood, 2008; Wriggers, 2008]

$$D_{\mathbf{u}}\mathbf{n}(\mathbf{u}) = \frac{\partial\mathbf{n}(\mathbf{u})}{\partial\mathbf{u}}\mathbf{u} = \frac{\frac{\partial\mathbf{u}}{\partial\eta}\times\mathbf{n}_3}{\|\frac{\partial\mathbf{x}}{\partial\eta}\times\mathbf{n}_3\|}, \tag{2.53}$$

and using the relation $J_s^e(\eta) = \|(\partial\mathbf{x}/\partial\eta)\times\mathbf{n}_3\|$, one obtains

$$\frac{\partial\mathbf{n}(\mathbf{u})}{\partial\mathbf{u}}\mathbf{u} = \frac{1}{J_s^e(\eta)}\left(\frac{\partial\mathbf{u}}{\partial\eta}\times\mathbf{n}_3\right). \tag{2.54}$$

which allows to write the last boundary integral in Eq. (2.44) for the eth finite element as

$$\begin{aligned}&\int_{-\infty}^{+\infty}\int_{\partial\Omega_s^{\mathrm{ref}}} -p_0\,(\delta\mathbf{u})^{\mathrm{T}}\,\frac{\partial\mathbf{n}(\mathbf{u})}{\partial\mathbf{u}}\mathbf{u}J_s^e(\eta)\,\mathrm{d}\eta\mathrm{d}z\\ &= \int_{-\infty}^{+\infty}\int_{\partial\Omega_s^{\mathrm{ref}}} -p_0\,(\delta\mathbf{u})^{\mathrm{T}}\left(\frac{\partial\mathbf{u}}{\partial\eta}\times\mathbf{n}_3\right)\mathrm{d}z.\end{aligned} \tag{2.55}$$

As it can be noted, the final form of the surface integral in Eq. (2.55) is irrespective of the actual geometry of the element in the prestressed configuration.

Substituting Eqs. (2.47), (2.48), (2.49), (2.52) and (2.55) into Eq. (2.44), after some algebra the following linear system of M equations in the (κ_z,ω) domain is obtained

$$\begin{aligned}&\Big[\kappa_z^2\Big(\mathbf{K}_3+\mathbf{K}_{\sigma_{zz}^0}\Big)+\mathrm{i}\kappa_z\Big(\mathbf{K}_2-\mathbf{K}_2^{\mathrm{T}}+\mathbf{K}_{\sigma_{yz}^0}-\mathbf{K}_{\sigma_{yz}^0}^{\mathrm{T}}+\mathbf{K}_{\sigma_{xz}^0}-\mathbf{K}_{\sigma_{xz}^0}^{\mathrm{T}}\Big)\\ &+\mathbf{K}_1+\mathbf{K}_{\sigma_{xx}^0}+\mathbf{K}_{\sigma_{yy}^0}+\mathbf{K}_{\sigma_{xy}^0}+\mathbf{K}_{\sigma_{xy}^0}^{\mathrm{T}}-\mathbf{K}_p\Big]\mathbf{Q}(\kappa_z,\omega)\\ &=\mathbf{F}_v(\kappa_z,\omega)+\mathbf{F}_b(\kappa_z,\omega)\end{aligned} \tag{2.56}$$

where the dynamic stiffness matrices $\mathbf{K}_i$, the mass matrix $\mathbf{M}$ and the global vectors of nodal displacements $\mathbf{Q}(\kappa_z,\omega)$, volume forces $\mathbf{F}_v(\kappa_z,\omega)$ and surface forces $\mathbf{F}_b(\kappa_z,\omega)$

are expressed as

$$\mathbf{K}_3 = \bigcup_{e=1}^{N_{el}} \int_{\Omega_s^{\mathrm{ref}}} \mathscr{B}_z^{\mathrm{T}}\left(\boldsymbol{\xi}\right) \tilde{\mathbf{C}}^e\left(\boldsymbol{\xi},\omega\right) \mathscr{B}_z\left(\boldsymbol{\xi}\right) J_s^e\left(\boldsymbol{\xi}\right) \mathrm{d}\xi_1 \mathrm{d}\xi_2 \tag{2.57}$$

$$\mathbf{K}_2 = \bigcup_{e=1}^{N_{el}} \int_{\Omega_s^{\mathrm{ref}}} \left(\mathscr{B}_{xy}\left(\boldsymbol{\xi}\right)\right)^{\mathrm{T}} \tilde{\mathbf{C}}^e\left(\boldsymbol{\xi},\omega\right) \mathscr{B}_z\left(\boldsymbol{\xi}\right) J_s^e\left(\boldsymbol{\xi}\right) \mathrm{d}\xi_1 \mathrm{d}\xi_2 \tag{2.58}$$

$$\mathbf{K}_1 = \bigcup_{e=1}^{N_{el}} \int_{\Omega_s^{\mathrm{ref}}} \left(\mathscr{B}_{xy}\left(\boldsymbol{\xi}\right)\right)^{\mathrm{T}} \tilde{\mathbf{C}}^e\left(\boldsymbol{\xi},\omega\right) \mathscr{B}_{xy}\left(\boldsymbol{\xi}\right) J_s^e\left(\boldsymbol{\xi}\right) \mathrm{d}\xi_1 \mathrm{d}\xi_2 \tag{2.59}$$

$$\mathbf{M} = \bigcup_{e=1}^{N_{el}} \int_{\Omega_s^{\mathrm{ref}}} \rho_e \left(\mathbf{N}\left(\boldsymbol{\xi}\right)\right)^{\mathrm{T}} \mathbf{N}\left(\boldsymbol{\xi}\right) J_s^e\left(\boldsymbol{\xi}\right) \mathrm{d}\xi_1 \mathrm{d}\xi_2 \tag{2.60}$$

$$\mathbf{K}_{\sigma_{xx}^0} = \bigcup_{e=1}^{N_{el}} \int_{\Omega_s^{\mathrm{ref}}} \sigma_{xx}^0\left(\boldsymbol{\xi}\right) \left(\frac{\mathbf{N}\left(\boldsymbol{\xi}\right)}{\partial\xi_i}\frac{\partial\xi_i}{\partial x}\right)^{\mathrm{T}} \left(\frac{\mathbf{N}\left(\boldsymbol{\xi}\right)}{\partial\xi_i}\frac{\partial\xi_i}{\partial x}\right) J_s^e\left(\boldsymbol{\xi}\right) \mathrm{d}\xi_1 \mathrm{d}\xi_2 \tag{2.61}$$

$$\mathbf{K}_{\sigma_{yy}^0} = \bigcup_{e=1}^{N_{el}} \int_{\Omega_s^{\mathrm{ref}}} \sigma_{yy}^0\left(\boldsymbol{\xi}\right) \left(\frac{\mathbf{N}\left(\boldsymbol{\xi}\right)}{\partial\xi_i}\frac{\partial\xi_i}{\partial y}\right)^{\mathrm{T}} \left(\frac{\mathbf{N}\left(\boldsymbol{\xi}\right)}{\partial\xi_i}\frac{\partial\xi_i}{\partial y}\right) J_s^e\left(\boldsymbol{\xi}\right) \mathrm{d}\xi_1 \mathrm{d}\xi_2 \tag{2.62}$$

$$\mathbf{K}_{\sigma_{zz}^0} = \bigcup_{e=1}^{N_{el}} \int_{\Omega_s^{\mathrm{ref}}} \sigma_{zz}^0\left(\boldsymbol{\xi}\right) \left(\mathbf{N}\left(\boldsymbol{\xi}\right)\right)^{\mathrm{T}} \mathbf{N}\left(\boldsymbol{\xi}\right) J_s^e\left(\boldsymbol{\xi}\right) \mathrm{d}\xi_1 \mathrm{d}\xi_2 \tag{2.63}$$

$$\mathbf{K}_{\sigma_{yz}^0} = \bigcup_{e=1}^{N_{el}} \int_{\Omega_s^{\mathrm{ref}}} \sigma_{yz}^0\left(\boldsymbol{\xi}\right) \left(\frac{\mathbf{N}\left(\boldsymbol{\xi}\right)}{\partial\xi_i}\frac{\partial\xi_i}{\partial y}\right)^{\mathrm{T}} \mathbf{N}\left(\boldsymbol{\xi}\right) J_s^e\left(\boldsymbol{\xi}\right) \mathrm{d}\xi_1 \mathrm{d}\xi_2 \tag{2.64}$$

$$\mathbf{K}_{\sigma_{xz}^0} = \bigcup_{e=1}^{N_{el}} \int_{\Omega_s^{\mathrm{ref}}} \sigma_{xz}^0\left(\boldsymbol{\xi}\right) \left(\frac{\mathbf{N}\left(\boldsymbol{\xi}\right)}{\partial\xi_i}\frac{\partial\xi_i}{\partial x}\right)^{\mathrm{T}} \mathbf{N}\left(\boldsymbol{\xi}\right) J_s^e\left(\boldsymbol{\xi}\right) \mathrm{d}\xi_1 \mathrm{d}\xi_2 \tag{2.65}$$

$$\mathbf{K}_{\sigma_{xy}^0} = \bigcup_{e=1}^{N_{el}} \int_{\Omega_s^{\mathrm{ref}}} \sigma_{xy}^0\left(\boldsymbol{\xi}\right) \left(\frac{\mathbf{N}\left(\boldsymbol{\xi}\right)}{\partial\xi_i}\frac{\partial\xi_i}{\partial x}\right)^{\mathrm{T}} \left(\frac{\mathbf{N}\left(\boldsymbol{\xi}\right)}{\partial\xi_i}\frac{\partial\xi_i}{\partial y}\right) J_s^e\left(\boldsymbol{\xi}\right) \mathrm{d}\xi_1 \mathrm{d}\xi_2 \tag{2.66}$$

$$\mathbf{K}_p = \bigcup_{\substack{e=1\\(e\in\partial\Omega_s)}}^{N_{el}} \int_{\partial\Omega_s^e} -p_0 \left(\mathcal{N}\left(\eta\right)\right)^{\mathrm{T}} \begin{bmatrix} 0 & 1 & 0 \\ -1 & 0 & 0 \\ 0 & 0 & 0 \end{bmatrix} \frac{\partial\mathcal{N}}{\partial\eta} \mathrm{d}\eta \tag{2.67}$$

$$\mathbf{Q} = \bigcup_{e=1}^{N_{el}} \mathbf{q}^e\left(\kappa_z,\omega\right) \tag{2.68}$$

$$\mathbf{F}_v = \bigcup_{e=1}^{N_{el}} \int_{\Omega_s^e} \left(\mathbf{N}\left(\boldsymbol{\xi}\right)\right)^{\mathrm{T}} \mathbf{f}_c\left(\kappa_z,\omega\right) J_s^e\left(\boldsymbol{\xi}\right) \mathrm{d}\xi_1 \mathrm{d}\xi_2 \tag{2.69}$$

$$\mathbf{F}_b = \bigcup_{\substack{e=1\\(e\in\partial\Omega_s)}}^{N_{el}} \int_{\partial\Omega_s^e} \left(\mathcal{N}\left(\eta\right)\right)^{\mathrm{T}} \mathbf{t}_c\left(\kappa_z,\omega\right) J_s^e\left(\eta\right) \mathrm{d}\eta. \tag{2.70}$$

in which $\bigcup_{e=1}^{N_{el}}$ a finite element assembling procedure over the N_{el} elements of the mesh. The above integrals can be evaluated numerically using the Gauss-Legendre quadrature rule [Stroud and Secrest, 1996; Wriggers, 2008].

The algebraic system in Eq. (2.56) does not represents a complete general form of the possible load conditions since it has been derived making the assumption of invariant initial stresses and mechanical properties along the z direction, i.e.

$$\boldsymbol{\sigma}^0\left(\mathbf{x},\kappa_z\right)=\boldsymbol{\sigma}^0\left(\mathbf{x}\right), \tag{2.71}$$

$$\tilde{\mathbf{C}}\left(\mathbf{x},\kappa_z,\omega\right)=\tilde{\mathbf{C}}\left(\mathbf{x},\omega\right). \tag{2.72}$$

In some practical situations this statement may not be representative of the actual stress distribution in the waveguide. In these situations, the various operators defined in Eqs. (2.61)-(2.66) still remain formally unchanged but their positions inside the final system of Eq. (2.56) may vary.

Moreover, it can be noted that the particular case of closed boundary $\partial\Omega_s$ and constant hydrostatic pressure p_0 preserves the symmetry of $\mathbf{K}_p$, that is in general unsymmetric. In force of this property, one can assume an incremental pressure pseudo potential $D_{\mathbf{u}}\mathscr{V}_p=\frac{1}{2}\mathbf{Q}^{\mathrm{T}}\mathbf{K}_p\mathbf{Q}$ and $D_{\mathbf{u}}\delta\mathscr{V}_p=\delta\mathbf{Q}^{\mathrm{T}}\mathbf{K}_p\mathbf{Q}$, which is the particular case of nonconservative work considered in the rest of this chapter.

Considering only the free vibrations, i.e. $\mathbf{F}_v\left(\kappa_z,\omega\right)=\mathbf{0}$ and $\mathbf{F}_b\left(\kappa_z,\omega\right)=\mathbf{0}$, the application of the FE-discretized waveguide Eq. (2.56) yields the following M-dimensional homogeneous wave equation

$$\begin{aligned}&\Big[\kappa_z^2\Big(\mathbf{K}_3+\mathbf{K}_{\sigma^0_{zz}}\Big)+\mathrm{i}\kappa_z\Big(\mathbf{K}_2-\mathbf{K}_2^{\mathrm{T}}+\mathbf{K}_{\sigma^0_{yz}}-\mathbf{K}^{\mathrm{T}}_{\sigma^0_{yz}}+\mathbf{K}_{\sigma^0_{xz}}-\mathbf{K}^{\mathrm{T}}_{\sigma^0_{xz}}\Big)\\&+\mathbf{K}_1+\mathbf{K}_{\sigma^0_{xx}}+\mathbf{K}_{\sigma^0_{yy}}+\mathbf{K}_{\sigma^0_{xy}}+\mathbf{K}^{\mathrm{T}}_{\sigma^0_{xy}}-\mathbf{K}_p\Big]\mathbf{Q}\left(\kappa_z,\omega\right)=\mathbf{0}.\end{aligned} \tag{2.73}$$

Eq. (2.73) represents a twin parameter generalized eigenproblem in κ_z and ω, where for dissipative materials the stiffness matrices $\mathbf{K}_i$ result to be complex. The eigenvectors $\mathbf{Q}^m\left(\kappa_z,\omega\right)$, describe the cross sectional deformation of the wave whereas the wavenumbers, κ_z^m, describe the wave propagation and decay ($\kappa_z=\mathrm{Re}\left(\kappa_z\right)+\mathrm{i}\mathrm{Re}\left(\kappa_z\right)$). The frequency ω is assumed real and the frequency range is usually known. Consequently, complex valued wavenumbers and associated wavestructures are calculated as $\kappa_z\left(\omega\right)$ and $\mathbf{Q}\left(\kappa_z\left(\omega\right)\right)$.

For the sake of simplicity, Eq. (2.73) can be rewritten in a more compact form as

$$\Big[\kappa_z^2\mathbf{K}_3'+\mathrm{i}\kappa_z\mathbf{K}_2'+\mathbf{K}_1'-\omega^2\mathbf{M}\Big]\mathbf{Q}\left(\kappa_z,\omega\right)=\mathbf{0}, \tag{2.74}$$

where

$$\mathbf{K}_3' = \mathbf{K}_3 + \mathbf{K}_{\sigma_{zz}^0}, \tag{2.75}$$

$$\mathbf{K}_2' = \mathbf{K}_2 - (\mathbf{K}_2)^{\mathrm{T}} + \mathbf{K}_{\sigma_{yz}^0} - \left(\mathbf{K}_{\sigma_{yz}^0}\right)^{\mathrm{T}} + \mathbf{K}_{\sigma_{xz}^0} - \left(\mathbf{K}_{\sigma_{xz}^0}\right)^{\mathrm{T}}, \tag{2.76}$$

$$\mathbf{K}_1' = \mathbf{K}_1 + \mathbf{K}_{\sigma_{xx}^0} + \mathbf{K}_{\sigma_{yy}^0} + \mathbf{K}_{\sigma_{xy}^0} + \mathbf{K}_{\sigma_{xy}^0}^{\mathrm{T}} - \mathbf{K}_p \tag{2.77}$$

The second order eigenvalue problem in Eq. (2.74) can be recasted in the following eigensystem with first-order wavenumber κ_z by doubling its algebraic size (state-space solution)

$$\left[\mathbf{A} - \kappa_z \mathbf{B}\right] \bar{\mathbf{Q}} \left(\kappa_z, \omega\right) = \mathbf{0} \tag{2.78}$$

in which

$$\mathbf{A} = \begin{bmatrix} \mathbf{0} & \mathbf{K}_1' - \omega^2 \mathbf{M} \\ \mathbf{K}_1' - \omega^2 \mathbf{M} & -\mathrm{i}\mathbf{K}_2' \end{bmatrix}, \tag{2.79}$$

$$\mathbf{B} = \begin{bmatrix} \mathbf{K}_1' - \omega^2 \mathbf{M} & \mathbf{0} \\ \mathbf{0} & -\mathbf{K}_3' \end{bmatrix}, \tag{2.80}$$

are complex matrices of dimension $2M \times 2M$ and

$$\bar{\mathbf{Q}} = \begin{bmatrix} \mathbf{Q} \\ \kappa_z \mathbf{Q} \end{bmatrix} \tag{2.81}$$

is a complex vector of dimension $2M \times 1$.

2.6 Dispersion analysis

2.6.1 General solutions for lossy and lossless materials

The eigenvalue problem in Eq. (2.78) consists in finding the set of generally complex valued scalars $\kappa_z^m = a^m + \mathrm{i}b^m$ and the set of corresponding complex eigenvectors $\bar{\mathbf{Q}}^m = \bar{\mathbf{\Phi}}^m + \mathrm{i}\bar{\mathbf{\Psi}}^m$ for a given real frequency $\omega > 0$. The number of eigenvalues and corresponding eigenvectors is equal to $2M$. For an attenuating system in vacuum, i.e. viscoelastic materials are considered and the stress-strain relation is described by the complex moduli matrix $\tilde{\mathbf{C}}(\omega)$, all the solutions are complex $\kappa_z^m = \mathrm{Re}\left(\kappa_z^m\right) + \mathrm{iIm}\left(\kappa_z^m\right)$, indicating that all the possible guided modes, propagative and evanescent, are attenuated. The complex eigenvalues appear in the following two different types of pairs

$$\begin{aligned} \kappa_z^m &= \pm\left(a^m + \mathrm{i}b^m\right), \qquad \bar{\mathbf{Q}}^m = \pm\left(\bar{\mathbf{\Phi}}^m + \mathrm{i}\bar{\mathbf{\Psi}}^m\right), \\ \kappa_z^m &= \pm\left(c^m - \mathrm{i}d^m\right), \qquad \bar{\mathbf{Q}}^m = \pm\left(\bar{\mathbf{\Phi}}^m - \mathrm{i}\bar{\mathbf{\Psi}}^m\right), \end{aligned} \tag{2.82}$$

where a, b, c and d are positive arbitrary values. Substituting Eq. (2.82) into Eq. (2.33) allows to rewrite the wavenumber-frequency dependence in the form

$$\exp\left[\mathrm{i}\left(\kappa_z z - \omega t\right)\right] = \exp\left[\mathrm{i}\left(\left(\mathrm{Re}\left(\kappa_z\right) + \mathrm{i}\mathrm{Im}\left(\kappa_z\right)\right) z - \omega t\right)\right] \tag{2.83}$$

$$= \exp\left[\mathrm{i}\left(\mathrm{Re}\left(\kappa_z\right) z - \omega t\right)\right] \exp\left[-\mathrm{Im}\left(\kappa_z\right) z\right] \tag{2.84}$$

from which it possible to observe that the real part of any scalar or vectorial field represents the propagative part while the imaginary part is an exponential envelope of the wave. The propagative harmonic part of the field is described by a constant phase argument $\exp\left[\mathrm{i}\phi\right] = \exp\left[\mathrm{i}\left(\mathrm{Re}\left(\kappa_z\right) z - \omega t\right)\right]$. Thus for a given wavenumber and frequency, while t is increasing the value of z has to change in order to accommodate the property of constant phase ϕ. For example, for a wave with positive real part of the wavevector $\mathrm{re}\left(\kappa_z\right) > 0$, if the time increases the sign of z has to be positive and its value has to increase in order to maintain $\phi = \mathrm{cost}$.

based on these considerations, a positive $\mathrm{Re}\left(\kappa_z\right)$ indicate a wave traveling in the positive direction of the z-axis (right propagating wave), while a negative $\mathrm{Re}\left(\kappa_z\right)$ denotes a wave traveling in the negative direction (left propagating wave). Since the solution is symmetric, for any wave propagating in the positive direction a corresponding wave is propagating in the negative direction.

From the analysis of the solutions, one can observe that only the eigenvalues for which the exponential term $\exp[-\mathrm{i}\mathrm{Im}\left(\kappa_z\right)] < 1$ are of interest. In fact, since for thermodynamic reasons no energy is added to the system during the free propagation phenomena, all the solutions with $\exp[-\mathrm{i}\mathrm{Im}\left(\kappa_z\right)] > 1$ corresponding to waves increasing in magnitude while propagating are to be discarded because nonphysical. Thus, for waves propagating in the positive direction $(\mathrm{Re}\left(\kappa_z\right))$ for which $\mathrm{sign}(z) = +$, an acceptable physical solution requires $\mathrm{Im}\left(\kappa_z\right) \geq 0$, so that $\exp[-\mathrm{i}\mathrm{Im}\left(\kappa_z\right)] \leq 0$ describes a decaying $(\mathrm{Im}\left(\kappa_z\right) > 0)$ or a non-attenuated $(\mathrm{Im}\left(\kappa_z\right) = 0)$ wave.

In the opposite case, i.e. for a wave that propagates in the negative z-direction, a physical solution would require $\mathrm{Im}\left(\kappa_z\right) \leq 0$ in order to have an attenuated or wave or a wave with constant amplitude. Thus, among all the possible solutions Eqs. (2.83) and

(2.84)

$$\kappa_z^m = +\left(a^m + \mathrm{i}b^m\right) \quad \rightarrow \quad \exp\left[\mathrm{i}\left(a^m z - \omega t\right)\right]\exp\left[-b^m z\right] \quad \text{(attenuated wave),} \tag{2.85}$$

$$\kappa_z^m = -\left(a^m + \mathrm{i}b^m\right) \quad \rightarrow \quad \exp\left[\mathrm{i}\left(-a^m z - \omega t\right)\right]\exp\left[+b^m z\right] \quad \text{(attenuated wave),} \tag{2.86}$$

$$\kappa_z^m = +\left(c^m - \mathrm{i}d^m\right) \quad \rightarrow \quad \exp\left[\mathrm{i}\left(c^m z - \omega t\right)\right]\exp\left[+d^m z\right] \quad \text{(nonphysical),} \tag{2.87}$$

$$\kappa_z^m = -\left(c^m - \mathrm{i}d^m\right) \quad \rightarrow \quad \exp\left[\mathrm{i}\left(-c^m z - \omega t\right)\right]\exp\left[+d^m z\right] \quad \text{(nonphysical),} \tag{2.88}$$

$$\tag{2.89}$$

only the solutions of type Eq. (2.83) are physical, while the type in Eq. (2.84) have no physical meaning, since correspond to waves with amplitude that grows while propagating. Therefore, from the full set of eigensolutions $[\kappa_z^m(\omega), \bar{\mathbf{Q}}^m(\omega)]$ $(m = 1, 2, ..., 2M)$ obtained from Eq. (2.78), only those of type $\kappa_z^m(\omega) = \pm[\mathrm{Re}\,(k_z^m) + \mathrm{i}\mathrm{Im}\,(k_z^m)]$ are selected along with their corresponding eigenvectors.

For the situation in which elastic materials are considered, the stress-strain relation is governed only by the storage modulus $\tilde{\mathbf{C}} = \mathrm{Re}\,(\mathbf{C})$ since the loss moduli becomes null. In this case the wavenumbers can be real, imaginary or complex.

The real eigenvalues correspond to real eigenvectors. In such a case, the real scalars are the wavenumbers of propagative elastic waves $\kappa_z^m(\omega)$, while the upper part of the corresponding eigenvector $\bar{\mathbf{Q}}^m = [\mathbf{Q}^m,\ \kappa_z \mathbf{Q}^m]^{\mathrm{T}}$ describes the propagative modes of the cross section of the waveguide. The real eigenvalues appear in pairs of opposite sign, which indicates two waves propagating in opposite directions,

$$\kappa_z^m = \pm a, \qquad \bar{\mathbf{Q}}^m = \pm \mathbf{\Phi}^m. \tag{2.90}$$

The purely imaginary solutions for the wavenumber correspond to the exponentially decaying near fields, which generally do not transport any appreciable mechanical energy, unless the length of the waveguide is small. These evanescent modes are also known as *end modes*, referring to the fact that their presence is necessary to satisfy the condition of traction free in a boundary problem or in the study of wave reflection. They also appear in pairs of opposite sign. The corresponding eigenvectors are purely imaginary,

$$\kappa_z^m = \pm \mathrm{i}b, \qquad \bar{\mathbf{Q}}^m = \pm \mathrm{i}\bar{\mathbf{\Psi}}^m. \tag{2.91}$$

The complex wavenumbers and corresponding complex modes appear in groups of four and are the evanescent modes. Each of the waves has two components. The real part of the solution represents the propagative part of the field while the imaginary part is an exponential envelope of the wave,

$$\kappa_z^m = \pm\left(a \mp \mathrm{i}b\right), \qquad \bar{\mathbf{Q}}^m = \pm\bar{\mathbf{\Phi}}^m \mp \mathrm{i}\bar{\mathbf{\Psi}}^m. \tag{2.92}$$

Following what stated before in the general case, some of this solutions can be discarded because physically not acceptable.

2.6.2 Dispersive parameters

The solutions obtained from the eigenvalue problem in Eq. (2.78) are post-processed to extract the dispersive characteristics of guided modes for the given geometry and materials of the waveguide. Since the eigenproblem is solved in the axial wavenumbers and associated wavestructures for any fixed $\omega > 0$, the dispersion spectra are graphically represented as continuous or discontinuous lines which are plotted as a function of the frequency.

The dispersion spectra of more practical interest are those of the real wavenumber ($\mathrm{Re}\left[\kappa_z\left(\omega\right)\right]$), phase velocity ($c_p\left(\omega\right)$), attenuation ($\alpha\left(\omega\right)$), group velocity ($c_g\left(\omega\right)$) and energy velocity ($c_e\left(\omega\right)$). The first three do not necessitate post-processing operations since can be directly obtained from the real and imaginary parts of the computed wavenumbers. On the other hand, the group and energy velocity require further elaborations. In the following sections, each dispersion parameter is described from the mathematical and physical point of view. The following sections give a description of each fundamental dispersion parameter from both the mathematical and physical point of view. In particular, in sec: 2.6.2.5 the derivation of a new modal formula for the energy velocity extraction is proposed.

2.6.2.1 Real wavenumber

The real part of the axial wavenumber displays the relationship between the temporary and spatially varying wave characteristics of the guided mode along the direction of propagation, and is generally given in radians per meter [Pavlakovic, 1998]. The real wavenumber of the generic mth propagative mode is inversely related to its the wavelength by the equation

$$\mathrm{wavelength}^m\left(\omega\right) = \frac{2\pi}{\mathrm{Re}\left[\kappa_z^m\left(\omega\right)\right]}. \tag{2.93}$$

As can be noted, the frequency-real wavenumbers spectra can be traced from the full set of eigensolutions without the need of post-processing operations. Moreover, since these spectra appear as straight lines, they are generally used along their corresponding eigenvectors in mode sorting operations. A routine that is able to track the various modes is particularly useful, especially at high frequencies where an high number of modes is generally found and it becomes difficult to discriminate between various modes.

To effectively represent dispersion curves, a routine that is based on wavenumbers sorting and eigenvectors correlations has been used in this thesis to trace continuous dispersion curves.

2.6.2.2 Phase velocity

The phase velocity of a guided wave describes the rate at which individual crests of the wave move [Pavlakovic, 1998] and is related to the real part of the axial wavenumber through the relation

$$c_p^m(\omega) = \frac{\omega}{\mathrm{Re}\left[\kappa_z^m(\omega)\right]}. \tag{2.94}$$

Since the real part of the axial wavenumber appears in both Eqs. (2.93) and (2.94), the real wavenumber and phase velocity spectra show the same informations. However, the phase velocity view is more convenient to use for realistic ultrasonic testing, since it emphasizes the velocity changes due to the guided nature of the modes [Pavlakovic, 1998].

2.6.2.3 Attenuation

The attenuation parameter is expressed by the relationship

$$\alpha^m(\omega) = \mathrm{Im}\left[\kappa_z(\omega)\right] \tag{2.95}$$

and gives an information on the energy lost by the guided mode per unit distance traveled. This parameter is generally measured in Nepers per meter (Np/m) or, alternatively, in Decibels per meter, being the relation between the two: $\alpha^m_{[\mathrm{dB/m}]} = 20\log_{10}[\exp(\alpha^m_{[\mathrm{Np/m}]})]$.

Since the amplitude of the wave has an harmonic wavenumber-frequency dependence of type $\exp[\mathrm{i}(\kappa_z z - \omega t)]$, an attenuation of 1 Np/m denotes that the amplitude of the guided wave is reduced of $\exp(-\alpha)$ after traveling one meter.

The attenuation of guided mode can be related to various phenomena: if the waveguide is elastic and immersed in vacuum, then the attenuation is zero and the amplitude of the guided mode is constant along the direction of propagation. In case of dissipative materials, both the bulk and guided waves are attenuated along their corresponding propagation directions.

2.6.2.4 Group velocity

As stated in [Rose, 2004], the group velocity corresponds to the propagation velocity of a group (or packet) of waves having similar frequency. Mathematically, it is defined as derivative of the frequency-wavenumber dispersion relation

$$c_g\left(\omega\right) = \frac{\partial \omega}{\partial \kappa_z\left(\omega\right)} \tag{2.96}$$

and it may be numerically calculated by the values of wavenumbers and frequencies of two adjacent points in the spectra.

The knowledge of the group velocity in practical application is of fundamental importance, since it provides an information on the dispersion of a wave packet generated in the structure in a certain frequency range. The dispersion of the wave packet is directly related to the slope of the group velocity in the given frequency range. If the difference between the group velocity of each frequency component is large, then the packet is formed by waves that travels at different velocities, causing the signal to change shape while propagating in the structure. On the other hand, if the group velocities are similar, the shape of the wave packet is maintained, so that the signal recorded has the same shape of the signal generated at a certain distance.

A closed formula for the computation of group velocity in lossless media and for axial loads only ($\sigma^0_{zz} \neq 0$) has been already proposed in the literature [Loveday, 2009]. If the geometric stiffness terms related to the nonzero initial stress components σ^0_{yz} and σ^0_{xz} in Eqs. (2.64) and (2.65) are introduced to take into account for a complete three dimensional prestress field, the formula proposed by Loveday [2009] becomes

$$c_g^m\left(\omega\right) = \frac{\partial \omega}{\partial \kappa_z^m} = \frac{\left(\mathbf{Q}^m\right)^{\mathrm{T}} \left[\mathbf{T}^{\mathrm{H}} \left(\mathbf{K}_2 + \mathbf{K}_{\sigma^0_{yz}} + \mathbf{K}_{\sigma^0_{xz}}\right) \mathbf{T} + 2\kappa_z^m\left(\omega\right) \left(\mathbf{K}_3 + \mathbf{K}_{\sigma^0_{zz}}\right)\right] \mathbf{Q}}{2\omega \left(\mathbf{Q}^m\right)^{\mathrm{T}} \mathbf{M}\mathbf{Q}}, \tag{2.97}$$

whereas in the original formula only the geometric stiffness operator $\mathbf{K}_{\sigma^0_{zz}}$ was taken into account. Eq. (2.97) is still valid for the case of general initial stress, with the exception that the operator $\mathbf{K}_i$ inglobes also the geometric stiffness terms related to the nonzero initial stress components σ^0_{yz} and σ^0_{xz} defined in Eqs. (2.64) and (2.65). In Eq. (2.97) $\mathbf{T}$ is an $M \times M$ identity matrix with the imaginary unit substituted in correspondence of each degree of freedom in the z direction and H denotes the complex conjugate transpose (Hermitian).

As well stated in the literature [Achenbach, 1973; Brillouin, 1960; Whitam, 1974], the equivalence between the group velocity c_{gr} and the velocity of energy transportation c_e is guaranteed by the Lighthill theorem [Biot, 1957; Lighthill, 1965] only in the general case of dispersive uniform lossless media, for which the central wavenumber of the wave packets traveling at infinitely close frequencies is conserved. On the contrary, the dissipation mechanism in nonconservative systems leads to complex wavenumbers and, as a consequence, the group velocity loses significance and the meaningful parameter becomes the energy velocity [Davidovich, 2010; Gerasik and Stastna, 2010].

2.6.2.5 Energy velocity

The energy velocity is a real scalar that defines the velocity at which the energy carried by a wave packet at infinitely close frequencies travels down the structure. This concept correspond to a generalization of the group velocity and therefore the energy velocity also represents a generalization of the group velocity, being $c_e(\omega) = c_g(\omega)$ for non-attenuated modes [Achenbach, 1973; Davidovich, 2010; Gerasik and Stastna, 2010].

The rate of transfer of the energy is determined as the ratio between the energy flux density per unit of time and the total energy density of the system, which follows from the application of the energy conservation law [Chang and Ho, 1995; Holzapfel, 2000]

$$\frac{\mathrm{D}\mathscr{K}}{\mathrm{D}t} + \mathscr{P}_{\text{int}} + \mathscr{P}_{D} = \mathscr{P}^{v}_{\text{ext}} + \mathscr{P}^{s}_{\text{ext}} \tag{2.98}$$

where the stress power $\mathscr{P}_{\text{int}}$, the viscous power loss $\mathscr{P}_{D}$, the power supplied on the system by the external volume forces $\mathscr{P}^{v}_{\text{ext}}$ and the power supplied by the external surface forces, $\mathscr{P}^{s}_{\text{ext}}$, are expressed, in the order, as

$$\mathscr{P}_{\text{int}} + \mathscr{P}_{D} = \int_V \mathbf{\Xi}(\mathbf{u}) : \dot{\mathbf{F}}(\mathbf{u})\mathrm{d}x\mathrm{d}y\mathrm{d}z \tag{2.99}$$

$$\mathscr{P}^{v}_{\text{ext}} = \int_V \dot{\mathbf{u}}^{\mathrm{T}}\mathbf{f}_c\mathrm{d}x\mathrm{d}y\mathrm{d}z \tag{2.100}$$

$$\mathscr{P}^{s}_{\text{ext}} = \int_{\partial V} \dot{\mathbf{u}}^{\mathrm{T}}(\mathbf{t}_c - p\mathbf{n})\mathrm{d}s\mathrm{d}z \tag{2.101}$$

in which $\mathbf{\Xi}(\mathbf{u})$ denotes the 1st Piola-Kirchhoff stress tensor [Bonet and Wood, 2008; Wriggers, 2008]. Eq. (2.98) can be recasted in linear incremental form by introducing the positions in Eqs. (2.99)-(2.101) and applying the usual linearization concept. Using the power equivalence

$$\int_V \boldsymbol{\Xi}\left(\mathbf{u}\right) : \dot{\mathbf{F}}\left(\mathbf{u}\right)\mathrm{d}x\mathrm{d}y\mathrm{d}y = \int_V \mathbf{S}\left(\mathbf{u}\right) : \dot{\mathbf{E}}\left(\mathbf{u}\right)\mathrm{d}x\mathrm{d}y\mathrm{d}y \tag{2.102}$$

and considering a constant pressure $p = p_0$ applied to closed boundary conditions during the motion (i.e. no fluid-structure interaction), yields to

$$\frac{\partial}{\partial t}\Big(\mathscr{K} + D_{\mathbf{u}}\mathscr{W} - D_{\mathbf{u}}\mathscr{V}_p\Big) = \int_V \dot{\mathbf{u}}^{\mathrm{T}}\mathbf{f}_c\left(\mathbf{x}, z, t\right)\mathrm{d}x\mathrm{d}y\mathrm{d}y + \int_{\partial V} \dot{\mathbf{u}}^{\mathrm{T}}\mathbf{t}_c\left(\mathbf{x}, z, t\right)\mathrm{d}s\mathrm{d}z \tag{2.103}$$

which represents the incremental form of the balance of energy in material description. Looking at the second integral on the right hand side of Eq. (2.103) in terms of incremental equilibrium at the boundary surface of the solid, it can be recognized that

$$D_{\mathbf{u}}\boldsymbol{\Xi}\left(\mathbf{u}\right)\mathbf{n} = \mathbf{t}_c\left(\mathbf{x}, z, t\right) \tag{2.104}$$

where, in force of the relation [Bonet and Wood, 2008; Wriggers, 2008]

$$\boldsymbol{\Xi}\left(\mathbf{u}\right) = \mathbf{F}\left(\mathbf{u}\right)\mathbf{S}\left(\mathbf{u}\right) \tag{2.105}$$

the linearized incremental 1st Piola-Kirchhoff stress tensor can be computed as

$$\begin{aligned} D_{\mathbf{u}}\boldsymbol{\Xi}\left(\mathbf{u}\right) &= D_{\mathbf{u}}\left[\mathbf{F}\left(\mathbf{u}\right)\mathbf{S}\left(\mathbf{u}\right)\right] \\ &= \left(D_{\mathbf{u}}\mathbf{F}\left(\mathbf{u}\right)\right)\mathbf{S}\left(\mathbf{u}\right)\big|_{\mathbf{u}=0} + \mathbf{F}\left(\mathbf{u}\right)\big|_{\mathbf{u}=0} D_{\mathbf{u}}\mathbf{S}\left(\mathbf{u}\right), \end{aligned} \tag{2.106}$$

from which, substituting the following identities

$$D_{\mathbf{u}}\mathbf{F}\left(\mathbf{u}\right) = \nabla\mathbf{u},$$

$$\mathbf{S}\left(\mathbf{u}\right)\big|_{\mathbf{u}=0} = \boldsymbol{\sigma}^0\left(\mathbf{x}, z\right),$$

$$\mathbf{F}\left(\mathbf{u}\right)\big|_{\mathbf{u}=0} = \mathbf{I},$$

$$D_{\mathbf{u}}\mathbf{S}\left(\mathbf{u}\right) = \int_{-\infty}^{t} \mathbf{C}\left(\mathbf{x}, z, t-\tau\right) : \frac{\partial\mathbf{e}\big(\mathbf{u}\left(\mathbf{x}, z, \tau\right)\big)}{\partial\tau}\mathrm{d}\tau,$$

one obtains

$$D_{\mathbf{u}}\boldsymbol{\Xi}\left(\mathbf{u}\right) = \nabla\mathbf{u}\boldsymbol{\sigma}^{0}\left(\mathbf{x},z\right) + \int_{-\infty}^{t} \mathbf{C}\left(\mathbf{x},z,t-\tau\right) : \frac{\partial \mathbf{e}\big(\mathbf{u}\left(\mathbf{x},z,\tau\right)\big)}{\partial \tau}\mathrm{d}\tau. \tag{2.107}$$

Multiplication of Eq. (2.107) by $\mathbf{n}$ and substitution inside the boundary integral on the right hand side of Eq. (2.103) leads finally to the incremental form of the Poynting theorem in material description

$$\frac{\partial}{\partial t}\Big(\mathscr{K} + D_{\mathbf{u}}\mathscr{W} - D_{\mathbf{u}}\mathscr{V}_{p}\Big) + \int_{\partial V} -\big(D_{\mathbf{u}}\boldsymbol{\Xi}\left(\mathbf{u}\right)\big)^{\mathrm{T}}\dot{\mathbf{u}}\cdot\mathbf{n}\mathrm{d}a = \mathscr{P}^{v}_{\mathrm{ext}}, \tag{2.108}$$

where $-\big(D_{\mathbf{u}}\mathbb{P}\left(\mathbf{u}\right)\big)^{\mathrm{T}}\dot{\mathbf{u}}$ is the linearized incremental Poynting vector in material description. This entity expresses the energy flux in the current configuration $\mathcal{C}^{t}$ per unit of area in the prestressed configuration $\mathcal{C}$ when a small displacement $\mathbf{u}\left(\mathbf{x},z,t\right)$ is applied.

Given the harmonic behaviour of the wave process, the time derivative can be replaced by the average over a time period $[t, t+2\pi/\omega]$, leading to

$$\Big\langle \mathscr{K} + D_{\mathbf{u}}\mathscr{W} - D_{\mathbf{u}}\mathscr{V}_{p}\Big\rangle + \int_{\partial V}\Big\langle D_{\mathbf{u}}\mathbf{J}\left(\mathbf{u}\right)\cdot\mathbf{n}\Big\rangle\mathrm{d}a = \Big\langle \mathscr{P}^{v}_{\mathrm{ext}}\Big\rangle, \tag{2.109}$$

where $\langle\ \rangle = \frac{\omega}{2\pi}\int_{t}^{t+\frac{2\pi}{\omega}}\mathrm{d}t$ denotes the time average operation and the incremental Poynting vector $D_{\mathbf{u}}\mathbf{J}\left(\mathbf{u}\right) = -\big[D_{\mathbf{u}}\boldsymbol{\Xi}\left(\mathbf{u}\right)\big]^{\mathrm{T}}\dot{\mathbf{u}}$ in the wavenumber-frequency domain takes the form

$$D_{\mathbf{u}}\mathbf{J}\left(\mathbf{u}\right) = -\mathrm{i}\omega\Big[\boldsymbol{\sigma}^{0}\left(\mathbf{x},\kappa_{z}\right)\left(\nabla\mathbf{u}\right)^{\mathrm{T}} + \tilde{\mathbf{C}}\left(\mathbf{x},\kappa_{z},\omega\right):\mathbf{e}\left(\mathbf{u}\right)\Big]\,\mathbf{u}. \tag{2.110}$$

Once the wave solution is known from the eigenvalue problem of Eq. (2.74) in terms of $\kappa_{z}^{m}\left(\omega\right)$ and $\mathbf{Q}^{m}\left(\omega\right)$ for the mth propagating mode, the previous quantities are only function of the angular frequency ω. Based on the Umov's definition [Davidovich, 2010], the energy velocity for the mth propagating mode is then obtained as the ratio between the average energy flux component projected along the z-direction and the total energy density of the waveguide at the given angular frequency ω

$$c_{e}^{m}\left(\omega\right) = \frac{\displaystyle\int_{\Omega_{s}}\Big\langle D_{\mathbf{u}}\mathbf{J}^{m}\left(\omega\right)\cdot\mathbf{n}_{3}\Big\rangle\mathrm{d}\Omega_{s}}{\Big\langle \mathscr{K}^{m}\left(\omega\right) + D_{\mathbf{u}}\mathscr{W}^{m}\left(\omega\right)\Big\rangle\Big|_{\Omega_{s}} - \Big\langle D_{\mathbf{u}}\mathscr{V}_{p}^{m}\left(\omega\right)\Big\rangle\Big|_{\partial\Omega_{s}}}. \tag{2.111}$$

As shown in other works [Treyssède, 2008], Eq. (2.111) can be rewritten making use of the matrix operators previously defined in Eqs. (2.57)-(2.66). For the incremental energy flux in the z direction, using Eq. (2.110) and the compatibility operator $\mathscr{L}_{z}$, one obtains

$$
\begin{aligned}
&\Big\langle D_{\mathbf{u}}\mathbf{J}^m(\omega)\cdot\mathbf{n}_3\Big\rangle\\
&=\frac{\omega}{2}\mathrm{Im}\left[\left(\mathbf{u}^m\right)^{\mathrm{H}}\left(\sigma^0_{13}\frac{\partial\mathbf{u}^m}{\partial x}+\sigma^0_{23}\frac{\partial\mathbf{u}^m}{\partial y}+\mathrm{i}\kappa^m_z(\omega)\,\sigma^0_{33}\mathbf{u}^m+\mathscr{L}_z^{\mathrm{T}}\tilde{\mathbf{C}}\boldsymbol{\epsilon}^m\right)\right]
\end{aligned}
\tag{2.112}
$$

Substituting the expressions in Eq. (2.47) and recalling the operators in Eqs. (2.57), (2.58), (2.63), (2.64) and (2.65), the integral of the energy intensity flux over the waveguide cross section reads

$$
\begin{aligned}
&\int_{\Omega_s}\Big\langle D_{\mathbf{u}}\mathbf{J}^m(\omega)\cdot\mathbf{n}_3\Big\rangle\mathrm{d}\Omega_s\\
&=\frac{\omega}{2}\mathrm{Im}\left\{\left(\mathbf{Q}^m\right)^{\mathrm{H}}\left[\mathbf{K}^{\mathrm{T}}_{\sigma^0_{xz}}+\mathbf{K}^{\mathrm{T}}_{\sigma^0_{yz}}+\mathbf{K}^{\mathrm{T}}_2+\mathrm{i}\kappa^m_z(\omega)\left(\mathbf{K}_3+\mathbf{K}_{\sigma^0_{zz}}\right)\right]\mathbf{Q}^m\right\}
\end{aligned}
\tag{2.113}
$$

while the time average incremental kinetic energy, stored and dissipated energy, as well as the average nonconservative work are defined respectively as

$$
\langle\mathscr{K}^m(\omega)\rangle|_{\Omega_s}=\frac{\omega^2}{4}\mathrm{Re}\left[\left(\mathbf{Q}^m\right)^{\mathrm{H}}\mathbf{M}\mathbf{Q}^m\right],
\tag{2.114}
$$

$$
\begin{aligned}
\langle D_{\mathbf{u}}\mathscr{W}^m(\omega)\rangle|_{\Omega_s}&=\frac{1}{4}\mathrm{Re}\left\{\left(\mathbf{Q}^m\right)^{\mathrm{H}}\left[\left(\kappa^m_z(\omega)\right)^2\left(\mathbf{K}_3+\mathbf{K}_{\sigma^0_{zz}}\right)+\right.\right.\\
&\quad+\mathrm{i}\kappa^m_z(\omega)\left(\mathbf{K}_2-\mathbf{K}^{\mathrm{T}}_2+2\mathbf{K}_{\sigma^0_{yz}}+2\mathbf{K}_{\sigma^0_{xz}}\right)+\\
&\quad\left.\left.+\mathbf{K}_1+\mathbf{K}_{\sigma^0_{xx}}+\mathbf{K}_{\sigma^0_{yy}}+2\mathbf{K}_{\sigma^0_{xy}}\right]\mathbf{Q}^m\right\},
\end{aligned}
\tag{2.115}
$$

$$
\langle D_{\mathbf{u}}\mathscr{V}^m_p(\omega)\rangle|_{\partial\Omega_s}=\frac{1}{4}\mathrm{Re}\left[\left(\mathbf{Q}^m\right)^{\mathrm{H}}\mathbf{K}_p\mathbf{Q}^m\right].
\tag{2.116}
$$

Substituting Eqs. (2.113), (2.114), (2.115) and (2.116) into Eq. (2.111) provides the energy velocity for the assumed mth guided mode at given frequency ω. This relation holds for a generic 3D prestress field and linear elastic and viscoelastic materials. Moreover, it can be verified that Eq. (2.97) is exactly recovered by Eq. (2.111) for the case of lossless materials.

2.7 Numerical applications

2.7.1 Viscoelastic rail under thermal-induced axial stress

Residual stresses represent a fundamental issue in the railway production and maintenance since they affect negatively the rail resistance, compromise integrity and reduce

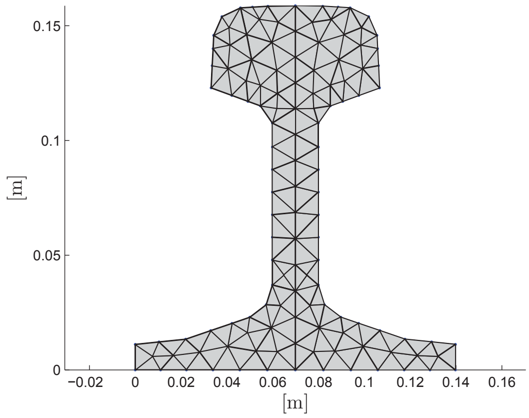

Figure 2.2: Finite element mesh used for the dispersion curves extraction in sections 2.7.1 and 2.7.2.

durability. While the presence of high compressive stresses is generally related to buckling problems, especially under hot temperatures, tensile stresses represent a vehicle for crack initiation and propagation. Moreover, some geometrical characteristics of the rail such as straightness and flatness of the running surface can be deteriorated with loss in comfort. Therefore, it is of great importance for railways companies to monitorize the state of stress of the generic cross section of the rail.

Some numerical investigations on the effect of a constant axial prestress σ^0_{zz} along with some proposed techniques based on guided waves for the stress magnitude measurement can be found in [Bartoli et al., 2010; Chen and Wilcox, 2007; Loveday, 2009; Loveday and Wilcox, 2010]. In these works only perfectly elastic materials are considered. The purpose of this numerical example is to show the effect of the material attenuation on the dispersive behaviour of guided waves propagating in the rail subjected to a positive axial elongation $\varepsilon^0_{zz} = 0.1\%$.

In the following examples a standard A113 rail is considered. The mesh used is represented in Fig. 2.2, which is composed of 125 nodes and 182 triangular elements with linear shape functions. The steel in the prestressed configuration is considered as a hysteretic linear viscoelastic material with mass density $\rho = 7800$ kg/m^3, longitudinal and shear bulk waves equal to $c_L = 6005$ m/s and $c_S = 3210$ m/s respectively, longitudinal bulk wave attenuation $\kappa_L = 0.003$ Np/λ and shear bulk wave attenuation $\kappa_S = 0.043$ Np/λ. Following Lowe [1992], the complex bulk velocities, Young's modulus and Poisson's ratio can be expressed as

$$\tilde{c}_{L,S} = c_{L,S}\left(1 + \mathrm{i}\frac{\kappa_{L,S}}{2\pi}\right)^{-1}, \tag{2.117}$$

$$\tilde{E} = \rho\tilde{c}_S\left(\frac{3\tilde{c}_L^2 - 4\tilde{c}_S^2}{\tilde{c}_L^2 - \tilde{c}_S^2}\right), \tag{2.118}$$

$$\tilde{\nu} = \frac{1}{2}\left(\frac{\tilde{c}_L^2 - 2\tilde{c}_S^2}{\tilde{c}_L^2 - \tilde{c}_S^2}\right), \tag{2.119}$$

from which one obtains the complex Lamè constants and the tensor of complex moduli

$$\tilde{\lambda} = \frac{\tilde{E}\tilde{\nu}}{\left(1+\tilde{\nu}\right)\left(1-2\tilde{\nu}\right)}, \tag{2.120}$$

$$\tilde{\mu} = \frac{\tilde{E}}{2\left(1+\tilde{\nu}\right)}, \tag{2.121}$$

$$\tilde{C}_{ijkm} = \tilde{\lambda}\delta_{ij}\delta_{km} + \tilde{\mu}\left(\delta_{ik}\delta_{jm} + \delta_{im}\delta_{jk}\right), \tag{2.122}$$

to be used into the incremental stress-strain relations in Eq. (2.36). It should be noted that the tensor of complex moduli remains independent from the angular frequency ω, in agreement with the assumed hysteretic behaviour of the material. Therefore, there is no need to update it at each frequency step performed in the eigenvalue problem of Eq. (2.73) and the matrices in Eqs. (2.57)-(2.67) can be computed once at the beginning of the analysis.

The dispersion results in the $0 \div 10$ kHz frequency range are depicted in Fig. 2.3 for the first five low order modes. The mode identification assumed here is the same adopted in [Bartoli et al., 2006], where the flexural-like modes $m1$ and $m4$ as well as the torsional-like mode $m2$ result to be antisymmetric with respect to the $x-z$ plane while the flexural-like mode $m3$ and the extensional-like mode $m5$ are symmetric. The three plots represented in the left hand side of Fig. 2.3 show the phase velocity, energy velocity and attenuation dispersion curves for the elastic and viscoelastic rail without applied loads. It can be noted that the phase velocity and the energy velocity of the first five modes are almost unaffected by the presence of the material attenuation. The three graphs on the right hand side of Fig. 2.3 report the variations of the corresponding quantities due to the applied axial stress $\sigma_{zz}^0 = 0.001\mathrm{Re}\left(\tilde{E}\right)$. As it can be seen, the presence of an axial load leads to an increase in the phase velocity for the two flexural-like modes $m1$ and $m3$ at very low frequencies, which corresponds to a decrease of about 40 m/s in the energy velocity. It is interesting nothing that the maximum shift in the attenuation is located at about 4.5 kHz for the $m1$ mode and 6.2 kHz for the $m3$ mode. This trend is in contrast with the one observed for the shift in phase and energy velocity of the two modes, which present their maximum for a frequency value approaching zero. Due to the decrease in attenuation, it follows that mode $m3$ at around 6 kHz could be a good candidate for revealing the state of σ_{zz}^0 prestress in the waveguide.

The torsional-like mode $m2$ shows a positive Δc_p along the entire frequency range considered due to the tensile σ_{zz}^0. However, its energy velocity shows both positive and negative variations. The frequency values in correspondence of the maximum and minimum shift in the attenuation for the $m2$ mode are approximatively those with minimum and maximum shift on the energy velocity. Similar behaviour can be observed also for the two flexural-like modes $m1$ and $m3$. Similarly to the previous modes, the flexural-like mode $m4$ presents an increase in the phase velocity for the entire frequency range, and an alternate trend for both energy velocity and attenuation. It can be noticed that while the flexural-like modes present their maximum shift in the phase velocity at very low frequency values (about 0 kHz for the $m1$ and $m3$ modes and in correspondence of the cutoff frequency for the $m4$ mode), the remaining two modes do not show this behaviour. This is particularly evident for the $m5$ extensional-like mode, which presents its maximum at about 6.7 kHz. Moreover, at the same frequency value of about 6.5 kHz, the mode shows the maximum increase in the energy velocity and the maximum decrease in the attenuation with respect to the unloaded case. The maximum negative shift in the attenuation is not shown in the frequency-Δatt spectra for representative reasons, and its value is -0.016 Np/m.

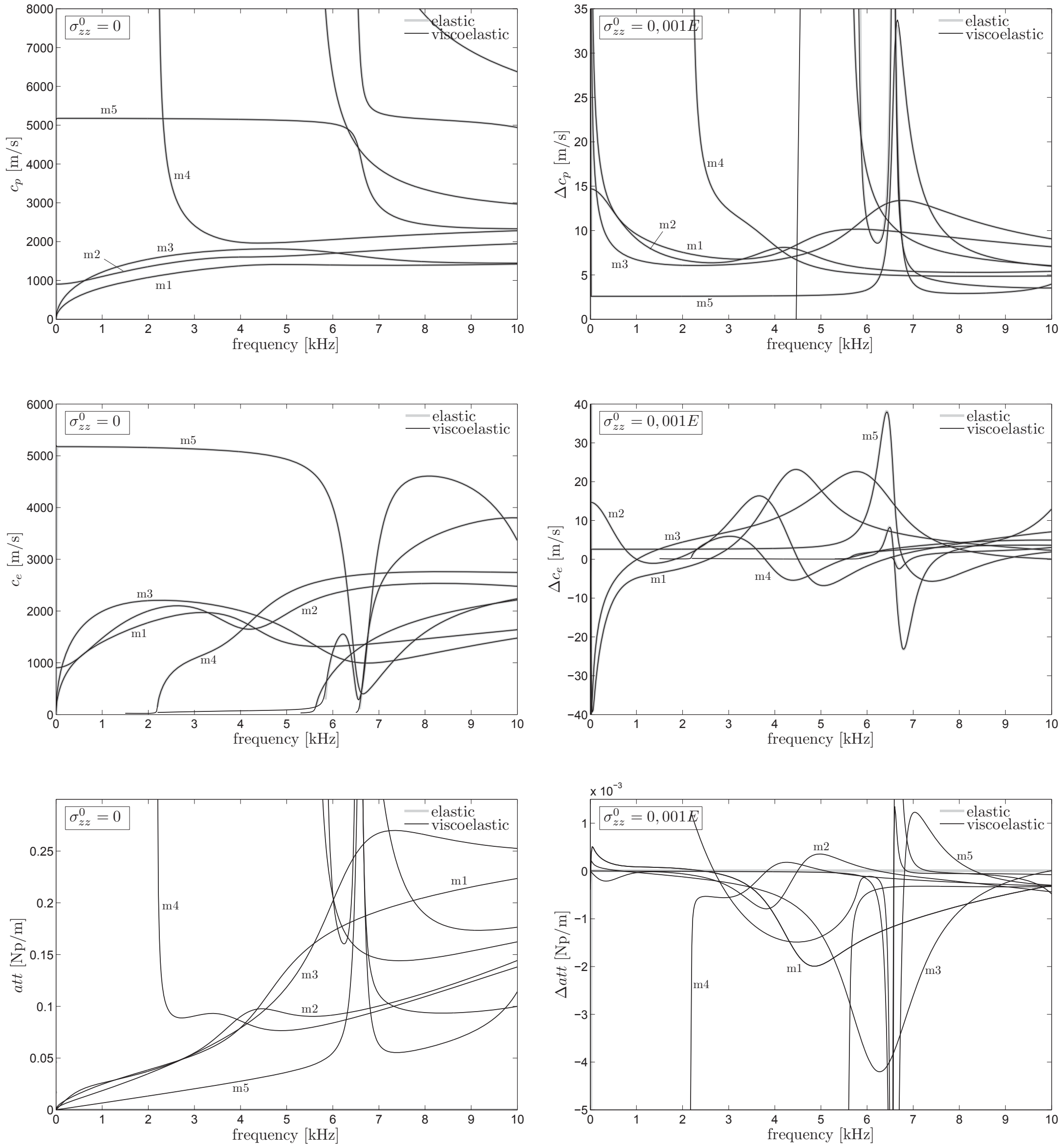

Figure 2.3: Phase velocity, energy velocity and attenuation for the loaded and unloaded cases. The first five modes m1, m2, m3, m4 and m5 are identified as in [Bartoli et al., 2006].

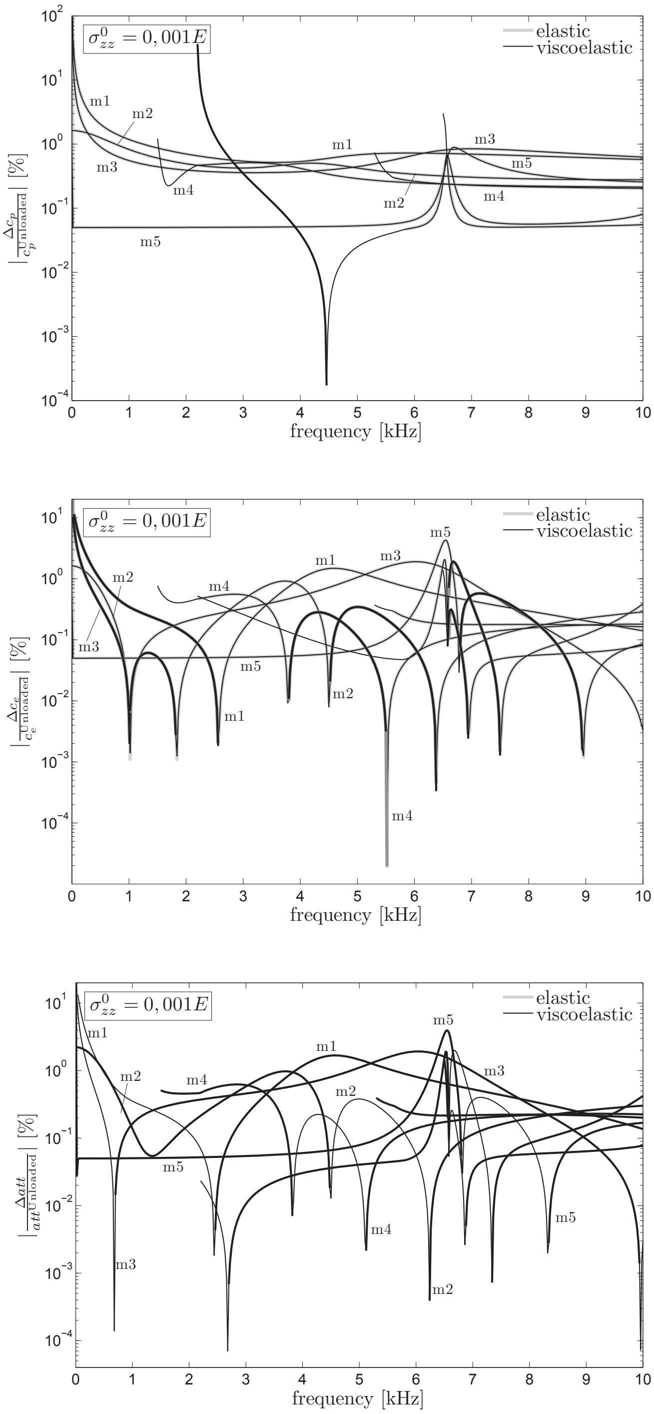

Figure 2.4: Percent variations between the loaded and unloaded cases for the axially loaded rail. Thin lines denote positive variations while thick lines denote negative variations.

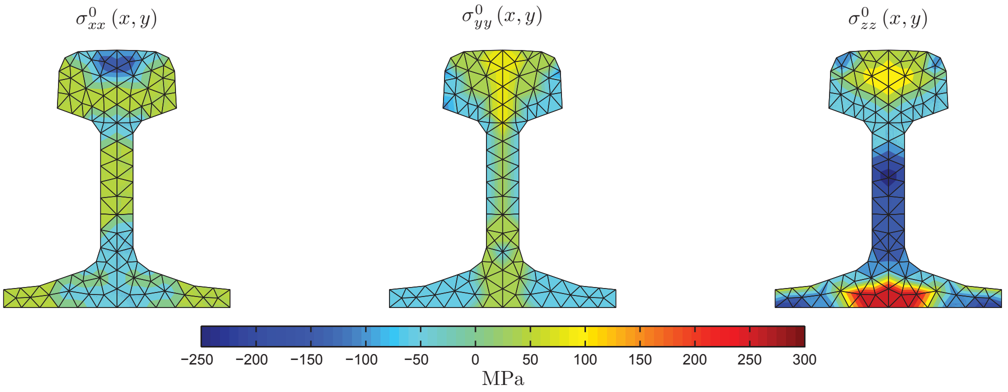

Figure 2.5: Reconstructed stress patterns for the roller straightened 113A standard profile in [Keller et al., 2003].

2.7.2 Guided waves propagation in a new roll-straightened viscoelastic rail

Residual stresses in rails do not depend only on the loads occouring during the service life, but also with those arising from welding or manufacturing processes, which can be very large. A principal source of residual stresses is represented by the roller straightening, which is generally the last stage of the production cycle of the rail.

The residual stress formation in rails due to roller straightening has been intensively investigated in the last years [Biempica et al., 2009; Keller et al., 2003; Ringsberg and Lindbäck, 2003; Schleinzer and Fischer, 2001] and non destructive techniques, such as guided waves, can be very useful to determine the state of stress. To show the effect induced by the residual stress on the dispersive behaviour in new roll-straightened rails, the stress patterns obtained by Keller et al. [Keller et al., 2003] for the standard 113A profile have been considered. In particular, transversal, vertical and longitudinal contours of the residual stress are shown in Fig. 2.5 along with the finite element mesh.

The nonzero initial stress components σ^0_{xx}, σ^0_{yy} and σ^0_{zz} are assumed to vary linearly over the generic finite element as a function of the stress value at each node, $\sigma^0_{ii}(\boldsymbol{\xi}) = \sum_{j=1}^{3} N_j(\boldsymbol{\xi})\left(\sigma^0_{ii}\right)_j$, with the jth nodal stress value $\left(\sigma^0_{ii}\right)_j$ depending on the position of the node itself inside a specific stress region. The remaining stress components are neglected since of low order of magnitude.

The effect of the stress patterns on the guided waves dispersive characteristics is presented in Fig. 2.6 in the frequency range $0 \div 10$ kHz.

As previously noticed for the axially loaded rail, the dispersive behaviour for the first five low order modes is only slightly influenced except for the $m2$ mode, which phase and energy velocity tend asymptotically to plus infinity and minus infinity for a frequency value tending to zero, respectively. At the same time, the mode attenuation decreases.

This particular behaviour is not observed in the axially loaded rail and is a consequence of the presence of the transverse and vertical stresses σ^0_{xx} and σ^0_{yy}.

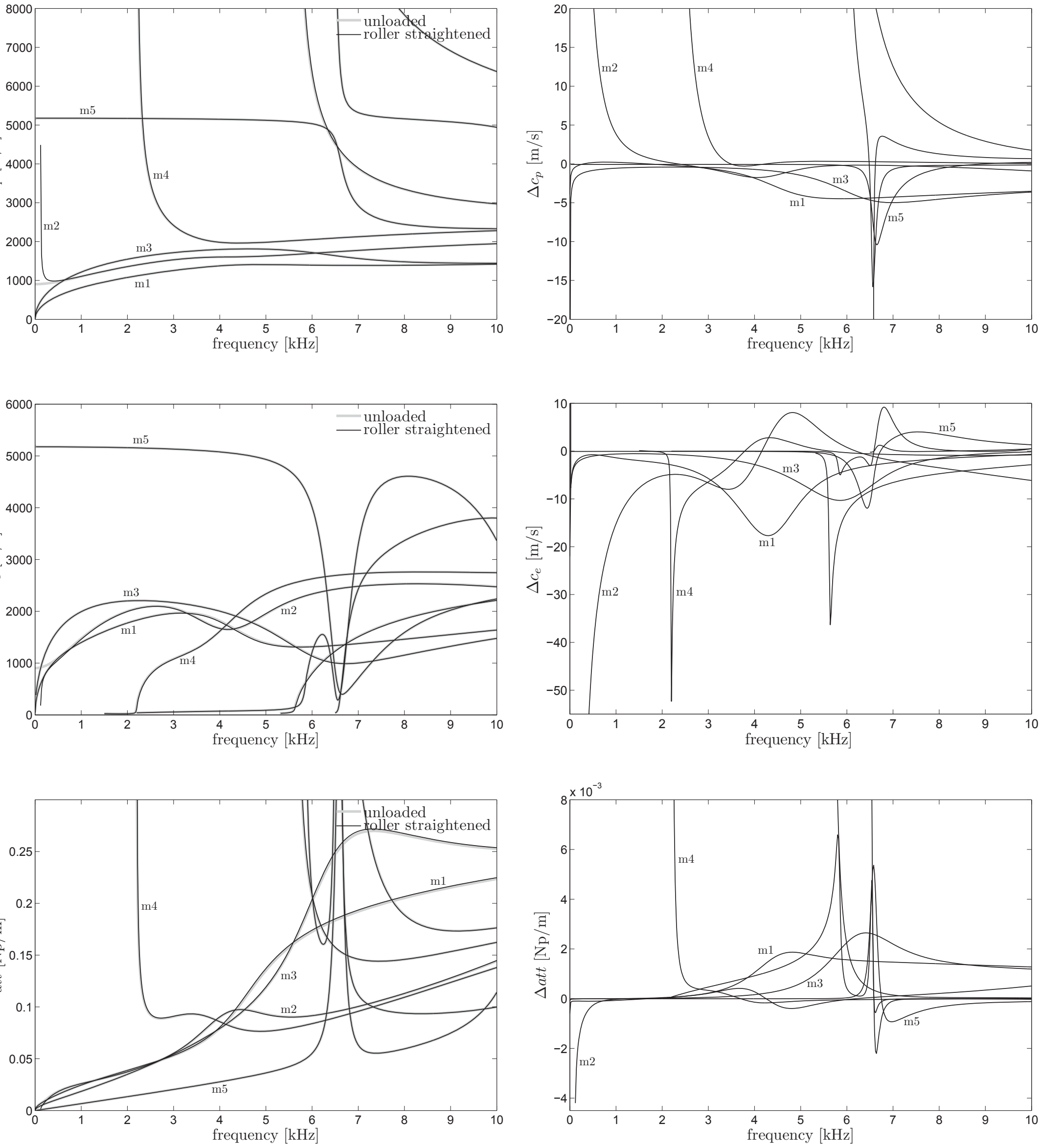

Figure 2.6: Phase velocity, energy velocity and attenuation for the unloaded rail and the roller straightened rail in [Keller et al., 2003].

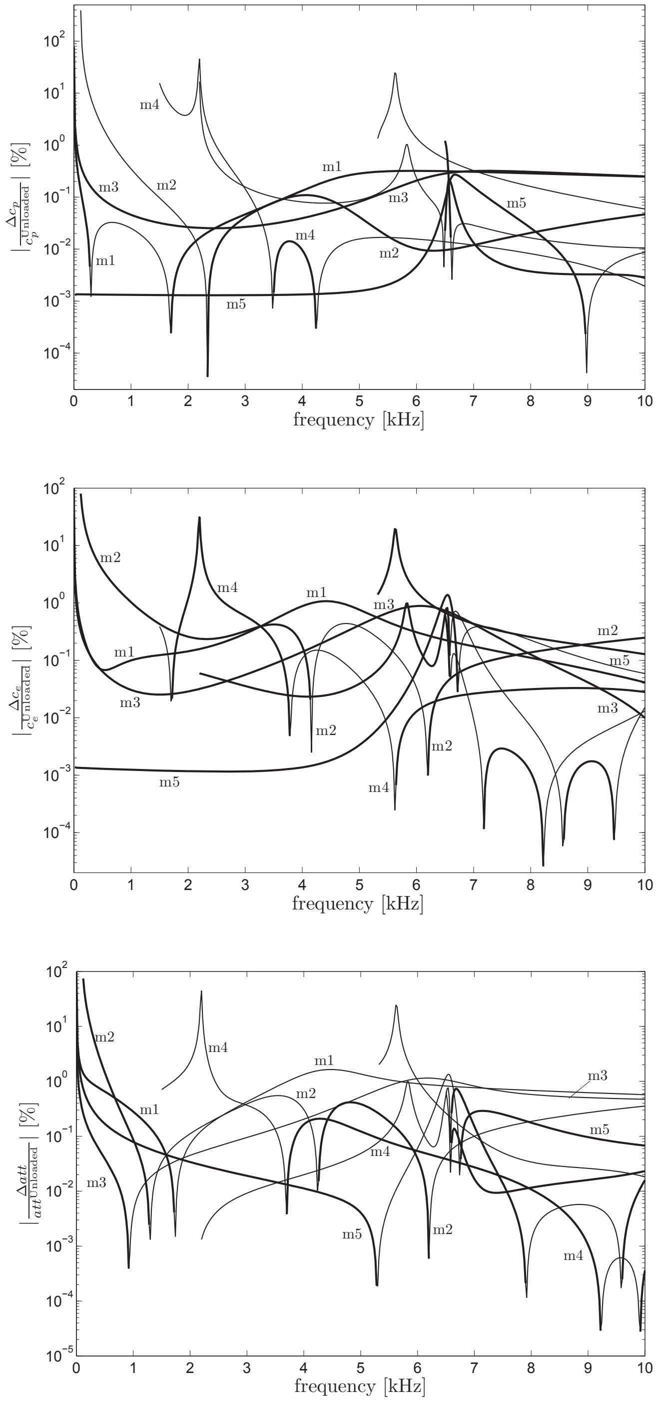

Figure 2.7: Percent variations between the loaded and unloaded case for the roller straightened rail. Thin lines denote positive variations while thick lines denote negative variations.

2.7.3 Pipe under initial pressure loading

In many practical situations the loads applied on the waveguide are dependent upon the deformation of the solid itself. This is the case, for instance, of a pressure acting at the inner and outer surfaces of a pipe when it undergoes to stress wave propagation, which is the case studied in this example.

The pressure fluctuations in the gas phase due to the solid-fluid interaction are neglected and the pressure is assumed to be constant during the motion. The pipe is considered sufficiently long to assume the cross-section in plain strain state in the prestressed configuration $\mathcal{C}$. For different inner and outer pressures p_i and p_e, the generic point (x_p, y_p) of the pipe cross section with center in $(x = 0, y = 0)$ is subjected to the following nonzero components of initial stress (see Fig. 2.8)

$$\begin{aligned} \sigma^0_{xx}, \sigma^0_{yy} &= \left[\frac{c_1}{x_p^2 + y_p^2} - c_2\right]\left(\frac{x_p^2, y_p^2}{x_p^2 + y_p^2}\right) + \left[-\frac{c_1}{x_p^2 + y_p^2} - c_2\right]\left(\frac{y_p^2, x_p^2}{x_p^2 + y_p^2}\right) \\ \sigma^0_{zz} &= \mathrm{Re}\big(\tilde{\nu}\big)\Big(\sigma^0_x + \sigma^0_y\Big) = -2\mathrm{Re}\big(\tilde{\nu}\big)\frac{p_e R_e^2 - p_i R_i^2}{R_e^2 - R_i^2} \end{aligned} \tag{2.123}$$

where $\tilde{\nu}$ is defined as in Eq. (2.119) and the constants c_1 and c_2 take the form

$$c_1 = \frac{R_i^2 R_e^2 \big(p_e - p_i\big)}{R_e^2 - R_i^2} \qquad c_2 = \frac{p_e^2 R_e^2 - p_i^2 R_i^2}{R_e^2 - R_i^2} \tag{2.124}$$

Positive values for the two pressures p_i and p_e produce compressive stresses σ^0_{xx} and σ^0_{yy}, which vary quadratically along the pipe wall thickness, while the axial stress σ^0_{zz} is constant for each point of the waveguide. The geometric stiffness matrices $\mathbf{k}^e_{\sigma^0_{xx}}$, $\mathbf{k}^e_{\sigma^0_{yy}}$ and $\mathbf{k}^e_{\sigma^0_{zz}}$ can be calculated by integrating via Gauss quadrature the stresses defined in Eq. (2.123) over each finite element. The numerical application considers an ASME 1-1/2 Schedule 160 steel pipe (outside radius $R_e = 24.15$ mm and inside radius $R_i = 17.01$ mm) subjected to a hydrostatic pressure gradient between the internal and the external surfaces.

The steel in the prestressed configuration is assumed as isotropic and hysteretic linear viscoelastic, having mass density $\rho = 7800$ kg/m^3, longitudinal and shear bulk waves equal to $c_L = 5963$ m/s and $c_S = 3187$ m/s respectively, longitudinal bulk wave attenuation $\kappa_L = 0.003$ Np/λ and shear bulk wave attenuation $\kappa_S = 0.008$ Np/λ.

The complex bulk velocities as well as the tensor of complex moduli are computed as in Eq. (2.117) and Eq. (2.122). In Fig. 2.9 solutions relative to five cases are represented considering the mesh of 112 nodes and 150 linear triangular elements depicted

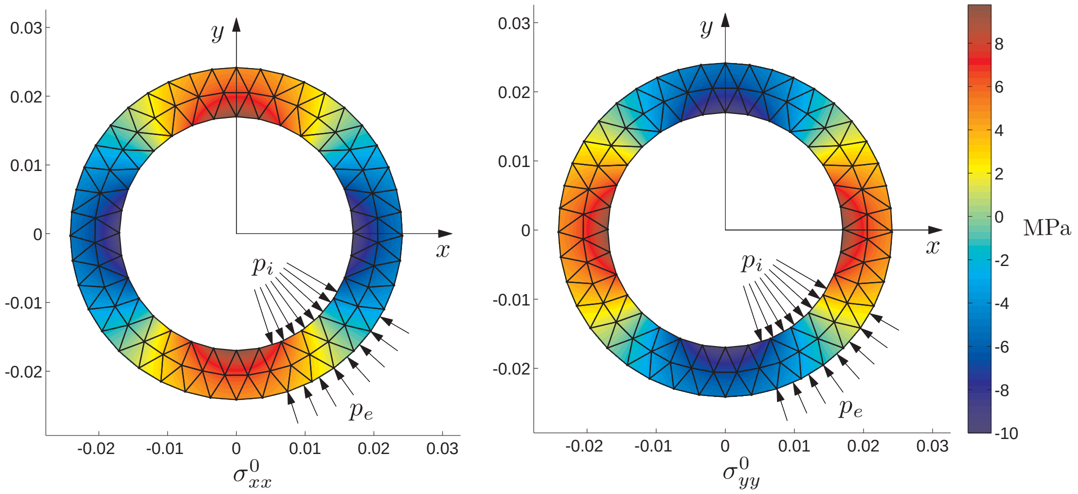

Figure 2.8: Finite element mesh of 112 nodes and 150 linear triangular elements for the ASME 1-1/2 Schedule 160 pipe. The transversal stress contours are relative to an inner pressure $p_i = 10$ MPa and an outer pressure $p_e = 5$ MPa (case 3). Negative values denote compressive stresses.

in Fig. 2.8. All the cases are studied by taking a reference pressure $p_{ref} = 5$ MPa. The continuous thick line denotes the stress free case (case 1), in which the pipe is not subjected to any pressure gradient. The solutions for the remaining four cases are obtained by varying the inner and outer pressures. In particular, the dashed line denotes an internal pressure $p_i = p_{ref}$ and $p_e = 0$ (case 2); the dotted line denotes that $p_i = 2p_{ref}$ and $p_e = p_{ref}$ (case 3); the dash dotted line refers to $p_i = 0$ and $p_e = p_{ref}$ (case 4), and finally, the continuous thin line indicates an internal pressure $p_i = p_{ref}$ and an external pressure $p_e = 2p_{ref}$ (case 5). As it can be seen in Fig. 2.9, the presence of a pressure gradient mostly affects the low order modes, essentially the torsional mode T(0,1) and the two flexural modes F(1,1). The most significant effect for this two modes is essentially related to changes in phase and energy velocities in the frequency range between 0 and 1000 Hz, which becomes larger if one assumes $p_{ref} > 5$ MPa.

The presence of an internal pressure only (case 2) produces a decrease of the phase velocity in the frequency range $0 \div 1000$ Hz for the torsional mode T(0,1), which become dispersive. At the same time, an increase of the phase velocity for the two flexural modes F(1,1) is observed in the frequency range $0 \div 50$ Hz, with a corresponding decrement in the energy velocity. This is principally due to the fact that an internal pressure produces a traction stress on the orthogonal direction z (see Eq. (2.124)), which translates into an additional geometric stiffness contribute and, as a consequence, into an increased flexural waves velocity (see also [Chen and Wilcox, 2007; Loveday, 2009]). Moreover, an increase of the wave attenuation is observed for the torsional mode T(0,1) in the frequency range $0 \div 500$ Hz, while a further drop in the wave attenuation for the longitudinal mode L(0,1) is observed in the range $0 \div 100$ Hz (phase and energy velocities for this mode result to be substantially unchanged).

Dispersion curves for the cases 3, 4 and 5 show a similar behaviour. In these cases the presence of an external pressure (lower than the internal pressure in the case 3 and higher in the cases 4 and 5) produces always a cutoff frequency and an increment in the phase velocity for the torsional mode T(0,1), which is limited to the frequency range $25 \div 250$ Hz for the case 3 and $190 \div 1500$ Hz and $240 \div 1500$ Hz for the cases 4 and 5, respectively. The related energy velocity is always increased for these cases.

In the same frequency ranges the wave attenuation of the T(0,1) mode is highly reduced by the presence of the prestress field and the phase velocity for the two flexural modes F(1,1) results to be lower than the stress-free case for each of the three cases considered. An interesting observation can be made by noting the behaviour of the flexural mode F(1,1) in case 2 and case 3. In fact, even if in both cases the axial stress σ_{zz}^0 is positive, in case 2 the effect of the internal pressure increases the mode phase velocity as a consequence of an increased geometric stiffness while in case 3 the extra external pressure reduces the mode phase velocity. As previously noticed for the case 2, only very small changes can be observed for the F(1,1) wave attenuation at very low frequencies, with a decrease on the attenuation values for the cases 3 and 4 and an increase for the case 5. However, an increment in the wave attenuation (very small for the case 3 and much higher for the cases 4 and 5) is observed for the longitudinal mode L(0,1) while its speed is not substantially affected by the presence of the pressure gradient.

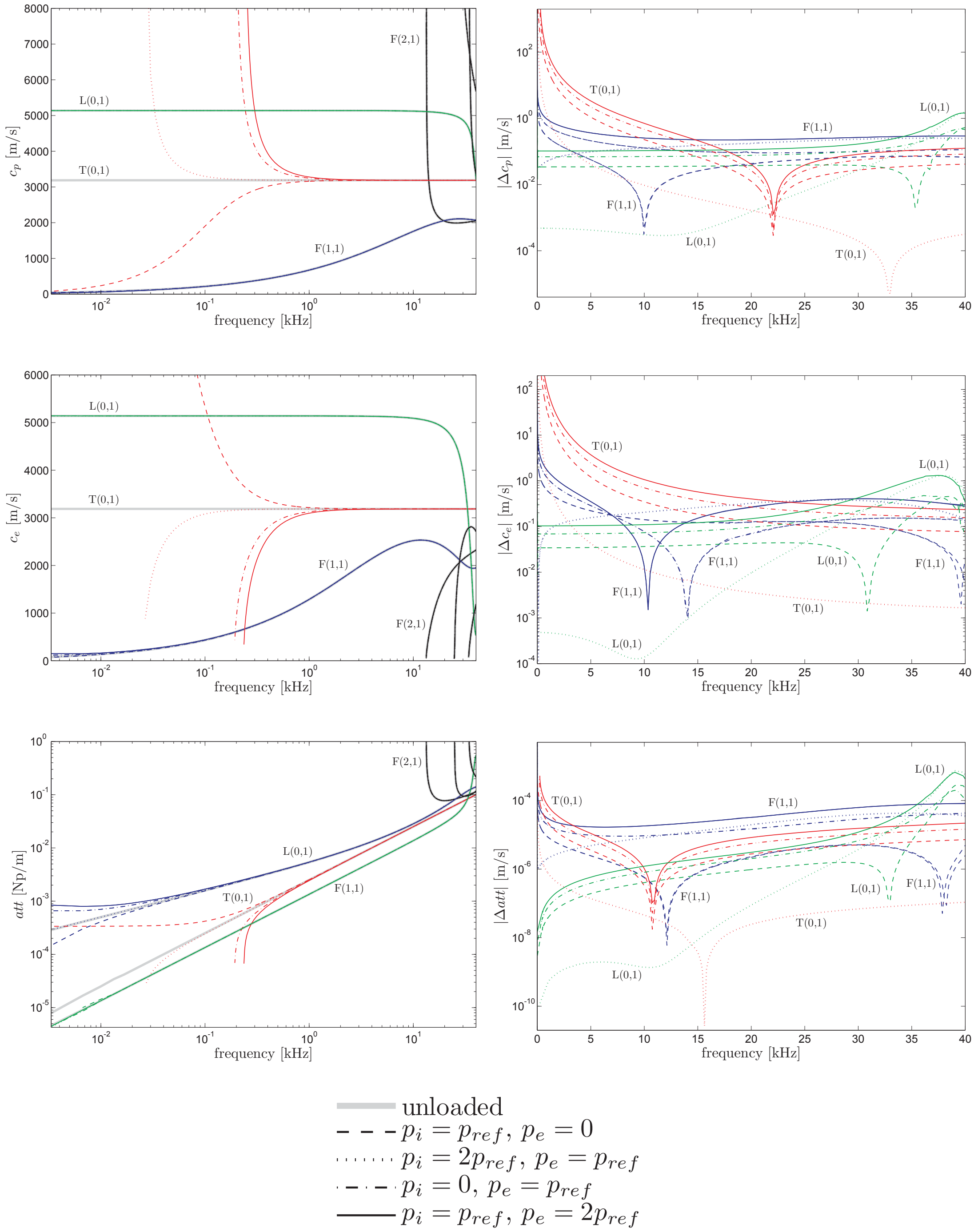

Figure 2.9: Phase velocity, energy velocity and attenuation for the ASME 1-1/2 Schedule 160 pipe under different pressure gradients.

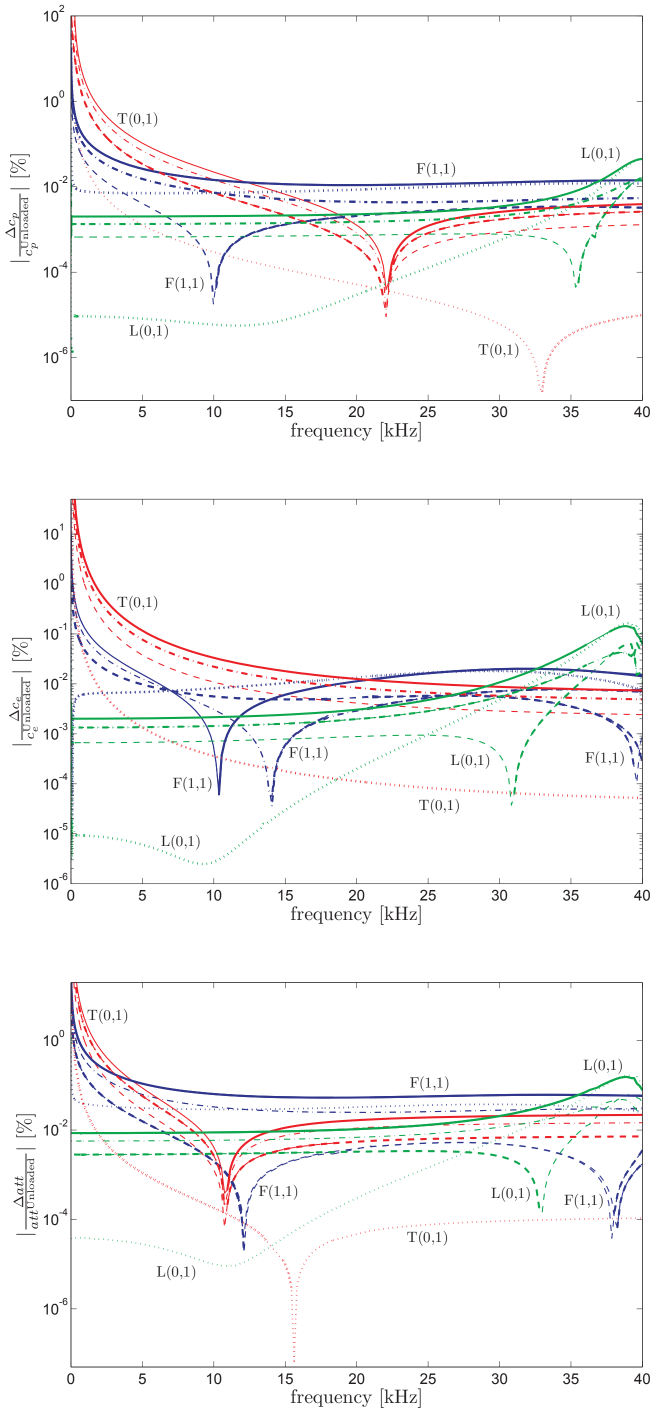

Figure 2.10: Percent variations between the loaded and unloaded cases for the pressurized pipe. Thin lines denote positive variations while thick lines denote negative variations.

2.8 Conclusions

An extension of the Semi Analytical Finite Element (SAFE) formulation has been proposed to include the effect of a three dimensional prestress field in viscoelastic waveguides. Based on a semi-isoparametric discretization, the formulation of the problem has been extended by taking into account high order terms in the strain-displacement relations and complex elastic constants in the incremental stress-strain relations. The energy velocity formula has been also revisited to include initial stress terms starting from the balance law of the mechanical energy in material description. Some numerical investigation have been conducted on a 113A standard rail, considering hysteretic materials.

The rail has been analyzed in the $0 \div 10$ kHz frequency range, but knowledge of high-frequency dispersion data (up to 100 kHz) can be very helpful for axial load measurement.

For the case of an axial load only, the first flexural modes in the low frequency range are the most influenced, showing generally an increase in the phase velocity and a corresponding decrease in the energy velocity when a tensile load is applied. The phase and energy velocities of the first modes are mostly sensitive in the very low frequency range, although this does not happen for their corresponding wave attenuation, which show the highest changes in magnitude for higher frequency values.

In the case of a roller-straightened rail, the simultaneous presence of both longitudinal and transversal stresses modifies significantly the behaviour of the fundamental torsional mode, while the sensitivity of the first flexural modes to the residual stress results to be highly mitigated with respect to the constant axial stress case. Although the analysis have been conducted in a low frequency range, the knowledge of high-frequency dispersion data (up to 100 kHz) can be very helpful for axial load measurement since some higher order modes remain considerable sensitive, providing useful informations in load detection schemes based on the measurement of the shift in phase produced by the load itself.

The dispersive characteristic of guided waves propagating in a hysteretic ASME 1-1/2 Schedule 160 pipe have been also analyzed by considering the effect of a pressure gradient between the inner and outer surfaces. Similarly to the roller-straightened rail, the presence of the transversal (radial and circumferential) initial stresses affects principally the first torsional modes, which becomes dispersive, while the principal flexural mode are slightly influenced by the axial load which arise by considering the pipe in plane stress state.

Finally, it appears that the influence of the initial stress on the dispersive characteristics of compact sections is large for low order modes at low frequencies while higher order modes are generally less influenced. The reason is that at high frequencies the geometric stiffness contribution becomes very small if compared with the elastic stiffness contribution and therefore the wave propagation behaviour mainly depends on the waveguide properties and it is slightly affected by the prestress state Chen and Wilcox [2007].

Based on the proposed numerical examples, the frequency values corresponding to the highest shift in the attenuation for the principal modes seem generally far to those at which the highest shift in the phase and energy velocity are observed. This particular behaviour could be deepened by assuming a different viscoelastic model as, for example, the Kelvin-Voigt model or the Linear Standard Solid.

The proposed formulation is sufficiently general to cover also prestressed waveguides of viscoelastic anisotropic materials and can be relevant in the design of several long range non-destructive techniques based on guided waves. In particular, it can be extremely helpful in the prediction of testing results for ultrasonic guided wave based screening of roller straightened rails, where the stress state has to be limited to prevent crack propagations and rail failures, as well as in pressurized pipelines carrying gases, where the distance of propagation of guided waves is of primary importance.

Chapter 3

Wave propagation in bounded and unbounded waveguides: 2.5D Boundary Element Method

3.1 Sommario

Nel presente capitolo viene descritta una formulazione basata sul metodo degli elementi di contorno (Boundary Element Method) per il calcolo delle caratteristiche di dispersione di onde guidate in guide d'onda con sezione trasversale di estensione finita ed infinita. La geometria dell'elemento longitudinale o della cavità si considera arbitraria, mentre il materiale della guida è assunto isotropo e viscoelastico lineare. L'attenuazione dell'onda guidata viene descritta in maniera spaziale attraverso la componente immaginaria del vettore d'onda e si considera dovuta unicamente a meccanismi di dissipazione interna del materiale.

La formulazione agli elementi di contorno viene ricavata dal caso elastodinamico tridimensionale mediante trasformate di Fourier nel tempo e nello spazio. La trasformazione dal dominio spazio-tempo a quello numero d'onda-frequenza consente di rappresentare il problema tridimensionale mediante una mesh di elementi al contorno monodimensionali, utilizzata per modellare il contorno della guida.

Come ben noto, gli integrali di contorno presentano delle singolarità legate alla natura delle funzioni di Green. Utilizzando una tecnica basata su moti di corpo rigido e sulla corrispondenza fra le singolarità delle funzioni di Green dinamiche e statiche, gli integrali non convergenti in senso classico sono regolarizzati, rendendo possibile l'utilizzo di tecniche convenzionali di quadratura numerica.

L'equazione d'onda si configura come un problema non lineare agli autovalori, il quale viene risolto nelle incognite numeri d'onda complessi per ogni fissata frequenza reale e positiva. Mediante l'utilizzo di un algoritmo basato su integrali di contorno (Contour Integral Method), il problema in parola viene trasformato in un problema olomorfico e lineare all'interno di una fissata regione nel piano complesso del numero d'onda assiale. Basandosi sul principio di radiazione di Sommerfeld e sulla natura del fenomeno di propagazione, viene dimostrato che le radici corrispondenti ai modi guidati reali giacciono su tre dei quattro possibili fogli di Riemann.

I risultati ottenuti con il metodo proposto per due differenti guide d'onda di sezione finita risultano in ottimo accordo con quelli ottenuti con il metodo SAFE. Mediante studi numerici condotti su cavità di due differenti geometrie, viene infine dimostrato che l'attenuazione dei modi guidati tende asintoticamente al valore di attenuazione dell'onda di Rayleigh per interfacce piane.

3.2 Introduction and literature review

In Guided Waves based nondestructive testing and structural health monitoring, the computation of the waves dispersion properties is indispensable for the design of both actuation and sensing systems, as well as to tune experimental set-up. To date, for the prediction of the dispersion properties several formulations are available.

Widely adopted numerical techniques are represented by analytical methods [Lowe, 1995] and semi-analytical methods [Bartoli et al., 2006; Gavric, 1995; Hayashi et al., 2003]. The analytical methods generally provide accurate solutions for problems involving energy losses due to both internal damping and leakage, but their application is generally restricted to waveguides of regular geometry. In addition, while looking for roots of the dispersive equation they suffer from numerical instabilities, missing roots and can require large computational time for multilayered waveguides (e.g. composite laminates). On the other hand, semi-analytical methods hardly handle problems involving unbounded domains. Moreover, at high frequency they become time consuming due to the large number of degrees of freedom involved to support accurate solutions.

The Boundary Element Method can enter in this context as a possible alternative for the dispersive data computation in both bounded and unbounded waveguides. Unlike FE-based formulations, which operate by discretizing the entire domain, the BEM can achieve a better accuracy by only discretizing the boundary of the waveguide, reducing the dimension of the problem. At the same time, some features of the analytical methods are conserved, in particular the potential to deal with problems involving unbounded mediums.

In the last years a large number of works have been published, in which different boundary element formulations have been proposed for the wave propagation problem in waveguide-like structures. This problem is sometimes referred in literature as the two-and-a-half (2.5D) problem [Costa et al., 2012; François et al., 2010; Godinho et al., 2003; Lu et al., 2008b; Rieckh et al., 2012; Sheng et al., 2005, 2006; Tadeu and Kausel, 2000], since the geometric and mechanical translational invariance allows a two dimensional description of the geometry, while the body motion still completely retains its three dimensional characteristic.

While most of these studies are focused on wave scattering problems [Cho and Rose, 2000, 1996; Galán and Abascal, 2005, 2004; Godinho et al., 2003; Pedersen et al., 1994; Wang et al., 2011; Zhao and Rose, 2003], vibrations induced problems [Costa et al., 2012; François et al., 2010; Rieckh et al., 2012; Sheng et al., 2005, 2006] or dynamic response problems [Lu et al., 2008b], minor attention has been dedicated to the study of dispersive characteristics of guided waves, especially when attenuation is involved. For such task, FE-based formulations are preferred to BEM due to (i) numerical difficulties with the treatment of the characteristic singularities of the fundamental solutions and (ii) complexities related to the solution of a nonlinear eigenvalue problem resulting from the boundary element modal analysis.

However, these two problems have been successfully tackled in different manners in recent years. In their work, Tadeu and Santos [2001] used a 2.5D boundary element formulation to extract the phase and group velocity dispersion curves for both slow and fast elastic formations by solving an eigenvalue problem in absence of an incident wavefield. The leaky modes poles have been found using complex frequencies, i.e. by describing decay in time, and no attenuation dispersion curves were provided. Godinho et al. [2003] used a similar 2.5D boundary element formulation to extract the phase velocity dispersion curves in cylindrical shell structures immersed in fluids. The dispersion curves were obtained by computing the response of the system for different values of the axial wavenumber at a given frequency and by considering a source and receiver line inside the cavity. It is well known that when the wavenumber approaches a modal wavenumber of the system, a peak in the system response is obtained [Wu, 2000], providing a tool to extract the dispersion curves. Unfortunately, attenuation information is generally difficult to obtain using this method.

Gunawan and Hirose [2005] proposed a boundary element formulation for waveguides of arbitrary cross-section, using discontinuous quadratic elements and subdividing the singular integrals into regular and singular parts, which were treated separately. To extract dispersion curves, they used a Newton's scheme where the eigensolutions, the real wavenumbers, were searched at different frequency steps by starting from the highest frequency of interest and proceeding backwards, exploiting the relative straightness of the axial wavenumbers dispersion curves. Moreover, their scheme was made more robust by using the group velocity extrapolation formula during the iterative search. The method has demonstrated to work properly for real wavenumbers. However, the extension of this approach for complex wavenumbers would imply a substantial increment of operations. In addition, the convergence of the method strongly depends on the initial guesses, which are difficult to estimate when attenuation is involved.

To account for attenuation, the modified bisection method proposed by Lowe [1995] represents an excellent variation into the curve tracking algorithms family; this approach is very robust, although its convergence rate is lower than that of a Newton-like method. The main limitations in using Newton-like methods and iterative methods are represented by the risk to follow the wrong curve when the spectrum is densely populated and by the fact that the solution at the previous step is needed as starting point to find the solution at the subsequent step. Therefore, for densely populated dispersion spectra, very small incremental steps are required. In addition, extraction of eigenvalues with multiplicity higher than one is generally complicated.

A substantially different method is represented by the Modified Matrix Pencil Algorithm proposed by Ekstrom [1995], who estimated dispersion data from borehole acoustic arrays. The method estimates dispersion properties by first performing a time Fourier transform of a space-time array resulting from multiple receivers. Then, at each temporal frequency, the complex wavenumbers are extracted using a forward/backward averaging matrix pencil method [Hua and Sarkar, 1990]. The method has been applied by Zengxi et al. [2007] for the dispersion parameters extraction in fluid-filled boreholes with irregular shapes using a 2.5D Boundary Element Formulation.

More recently, Badsar et al. [2010] used a half-power bandwidth method for the determination of the material damping ratio in shallow soil layers. This method uses computed or measured wavefields to extract the frequency-wavenumber and frequency-attenuation spectra. In particular, the wavenumber dispersion curves are derived from the peaks positions of the FFT-transformed wavefield, whereas the attenuation curves are derived from their width using the half-power bandwidth method.

In this chapter, a 2.5D regularized boundary element formulation [François et al., 2010; Lu et al., 2008b] is used to extract dispersion curves for homogeneous damped waveguides. The attenuation is spatially described through the imaginary part of the axial wavenumber [Bartoli et al., 2006; Lowe, 1995] and the dispersive parameters, i.e. complex wavenumbers, phase velocity and energy velocity, are computed by solving a nonlinear eigenvalue problem using a contour integral algorithm [Amako et al., 2008; Asakura et al., 2009; Beyn, 2012].

This algorithm does not require an initial guess of eigenvalues and eigenvectors. Moreover, this method is particularly suitable when the number of roots in the complex region of interest is much smaller than the eigenvalue problem dimension, as it appears in the dispersion curves extraction of fundamental modes. At low frequencies, in fact, few fundamental modes generally exist, while eigenvalue problems designed also for waves computation at high frequencies may be characterized by a large number of equations. A recent application of a contour integral algorithm in 2D-BEM acoustic problems can be found in the work of Gao et al. [2011].

The extraction of the energy velocity in post-processing is also discussed, and some numerical examples are presented, comparing the obtained results with those provided by the SAFE method [Bartoli et al., 2006].

The chapter is concluded with a study of the dispersion properties of cavities with arbitrary cross-section in unbounded linear isotropic viscoelastic mediums. The knowledge of surface waves dispersion properties in the vicinity of cavities can be useful in some practical applications such as, for example, geophysical and seismic prospecting techniques or in the study of vibrations in underground tunnels.

3.3 Problem statement

The problem under consideration consists in an isotropic viscoelastic waveguide of general shape which is interested by a wavefront propagating along its longitudinal axis (Fig. 3.1). The boundary of the waveguide is considered to be in contact with vacuum and, as a consequence, no energy losses due to radiation of bulk waves occur, since the generic bulk wave incident at the solid-vacuum interface is totally reflected and mode-converted. The wavenumber vector $\mathbf{k}_z = \mathbf{k}_z^{\mathrm{Re}} + \mathrm{i}\mathbf{k}_z^{\mathrm{Im}}$ associated to the guided wave results from the sum of the projections of the bulk wavenumbers $\mathbf{k}_L = \mathbf{k}_L^{\mathrm{Re}} + \mathrm{i}\mathbf{k}_L^{\mathrm{Im}}$ and $\mathbf{k}_S = \mathbf{k}_S^{\mathrm{Re}} + \mathrm{i}\mathbf{k}_S^{\mathrm{Im}}$ onto the z-direction, so that the guided wave represents the wavefront that propagates along the z-axis as a result of the superimposition of the bulk waves traveling obliquely and continuously reflected and mode-converted at the boundary of the waveguide.

Since the bulk waves travel at some incidence angle with respect to the z-axis, it can be recognized the presence of a wavefront in the $x - y$ plane, which wavenumber vector is intended as the sum of the projections of $\mathbf{k}_L$ and $\mathbf{k}_S$ to the generic z=cost plane. The associated radial components of the longitudinal and shear bulk wavenumber vectors are denoted with $\mathbf{k}_\alpha = \mathbf{k}_\alpha^{\mathrm{Re}} + \mathrm{i}\mathbf{k}_\alpha^{\mathrm{Im}}$ and $\mathbf{k}_\beta = \mathbf{k}_\beta^{\mathrm{Re}} + \mathrm{i}\mathbf{k}_\beta^{\mathrm{Im}}$ respectively.

Given a time-harmonic excitation and the translational invariance of geometric and mechanical characteristics along the z-axis, the wave propagation process is assumed with dependence

$$\exp\left[\mathrm{i}\left(\omega t - \kappa_z z\right)\right], \tag{3.1}$$

where the angular frequency ω is real and positive while, for a generic dissipative system, $\kappa_z = |\mathbf{k}_z^{\mathrm{Re}}| + \mathrm{i}|\mathbf{k}_z^{\mathrm{Im}}|$. The real component of the axial wavenumber represents the modulus of the harmonic propagation vector $\mathbf{k}_z^{\mathrm{Re}}$, while the imaginary component is the modulus of the spatial attenuation vector $\mathbf{k}_z^{\mathrm{Im}}$, which describes the exponential amplitude decay per unit of distance traveled.

Focusing only on guided waves propagating in the positive z-direction, it can be noted from Eq. (3.1) that, in order to have an amplitude decay for $z > 0$, the conditions

$\mathrm{Re}\left(\kappa_z\right) > 0$ and $\mathrm{Im}\left(\kappa_z\right) < 0$ must be satisfied for any fixed real positive frequency. In such case, and according to the Correspondence Principle [Christensen, 2010], the complex velocities for the longitudinal and shear bulk waves, $\tilde{c}_L\left(\omega\right)$ and $\tilde{c}_S\left(\omega\right)$, can be written in the following form [Luo and Rose, 2007]

$$\tilde{c}_{L,S}\left(\omega\right) = \frac{\omega}{\mathrm{Re}(\kappa_{L,S}) + \mathrm{i}\mathrm{Im}(\kappa_{L,S})} = \frac{c_{L,S}\left(\omega\right)}{1 - \mathrm{i}\alpha_{L,S}\left(\omega\right)/2\pi}, \tag{3.2}$$

where $\kappa_{L,S} = |\mathbf{k}^{\mathrm{Re}}_{L,S}| + \mathrm{i}|\mathbf{k}^{\mathrm{Im}}_{L,S}|$ are the complex moduli of the longitudinal and shear bulk wavevectors, while the bulk attenuation coefficients $\alpha_{L,S}\left(\omega\right) = -\mathrm{Im}(\kappa_{L,S})/\mathrm{Re}(\kappa_{L,S})$ represent the exponential amplitude decay of the wave after traveling one wavelength. If a linear viscoelastic Maxwell rheological model is adopted, $\tilde{c}_{L,S}$ result to be frequency independent [Christensen, 2010]. The corresponding complex material constants are evaluated as [Luo and Rose, 2007]

$$\tilde{\mu} = \tilde{c}_S^2\rho, \qquad \tilde{\lambda} = \left[\frac{2\tilde{\mu} - \tilde{E}}{\tilde{E}/\tilde{\mu} - 3}\right], \tag{3.3}$$

$$\tilde{E} = \left[\frac{3 - 4\left(\tilde{c}_S/\tilde{c}_L\right)^2}{1 - \left(\tilde{c}_S/\tilde{c}_L\right)^2}\right]\tilde{\mu}, \qquad \tilde{\nu} = \frac{\tilde{\lambda}}{2\left(\tilde{\lambda} + \tilde{\mu}\right)}, \tag{3.4}$$

where $\tilde{\lambda}$ and $\tilde{\mu}$ denote the first and second complex Lamé constants, ρ the material density, $\tilde{E}$ is the complex Young's modulus and $\tilde{\nu}$ the complex Poisson's ratio. To be consistent with Eq. (3.2) and the analysis of Lowe [1995], in the following it is assumed that the attenuation component of the wavenumber vectors is always parallel to the propagation component, i.e. the maximum amplitude decay due to material damping occurs along the propagation direction.

3.4 2.5D integral representation theorem

The integral representation theorem is first recalled in the 3D case for an isotropic linear viscoelastic body of volume V and external surface ∂V, with mechanical properties defined by the material density ρ and the complex Lamé constants $\tilde{\lambda}$ and $\tilde{\mu}$ (or, equivalently, the complex bulk velocities $\tilde{c}_L$ and $\tilde{c}_S$). The body is assumed to be either bounded or unbounded and allows for the presence of edges, corners and internal cavities.

The body is considered to be subjected to a unitary harmonic point load $p\left(\mathbf{X}', t\right) = \delta\left(\mathbf{X} - \mathbf{X}'\right)\exp(\mathrm{i}\omega t)$ applied at $\mathbf{X}' = [x',\ y',\ z']^{\mathrm{T}} \in V$, where $\delta\left(\cdot\right)$ denotes the Dirac

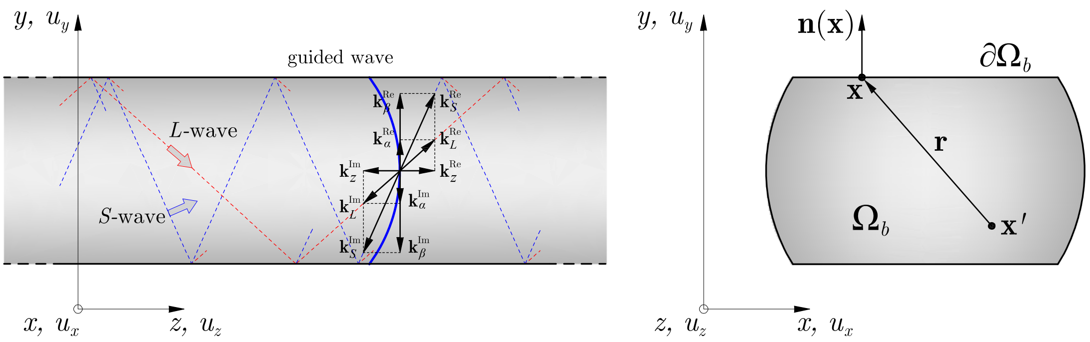

Figure 3.1: Analytical model of the bounded waveguide.

delta function. The spatial coordinate $\mathbf{X} = [x,\ y,\ z]^{\mathrm{T}} \in \partial V$ describes a receiver point located on the boundary. In this step, no distinctions are made on whether the body is bounded or unbounded. Denoting with $R = |\mathbf{X} - \mathbf{X}'|$ the spatial distance between the receiver point and the source point, the 3D integral representation theorem in the frequency domain is given by the well known relation [Andersen, 2006; Bonnet, 1999; Dominguez, 1993]

$$\begin{aligned} c_{ij}\left(\mathbf{X}'\right) u_j\left(\mathbf{X}', \omega\right) = &\int_{\partial V} U_{ij}^D\left(R, \omega\right) t_j\left(\mathbf{X}, \omega\right) \mathrm{d}a\left(\mathbf{X}\right) \\ &- \int_{\partial V} T_{ij}^D\left(R, \omega\right) u_j\left(\mathbf{X}, \omega\right) \mathrm{d}a\left(\mathbf{X}\right), \quad \mathbf{X}' \in V,\ \mathbf{X} \in \partial V \end{aligned} \tag{3.5}$$

which expresses the relation between the displacements $u_j\left(\mathbf{X}, \omega\right)$ and tractions $t_j\left(\mathbf{X}, \omega\right)$ at any $\mathbf{X}$ located on the boundary ∂V (state of unknown boundary variables) and the Green's functions for the displacements $U_{ij}^D\left(R, \omega\right)$ and tractions $T_{ij}^D\left(R, \omega\right)$ [Andersen, 2006; Bonnet, 1999; Dominguez, 1993] (known state of fundamental solutions). The fundamental displacements $U_{ij}^D\left(R, \omega\right)$ correspond to a second order tensor that satisfies the differential equation

$$\left(\tilde{\lambda} + \tilde{\mu}\right) \frac{\partial^2 U_{ij}^D\left(R, \omega\right)}{\partial x_k \partial x_i} + \tilde{\mu} \frac{\partial^2 U_{ij}^D\left(R, \omega\right)}{\partial x_i \partial x_i} + \delta_{kj} \delta\left(\mathbf{X} - \mathbf{X}'\right) = -\rho \omega^2 U_{kj}^D\left(R, \omega\right) \tag{3.6}$$

in the isotropic viscoelastic full space. The corresponding dynamic fundamental tractions $T_{ij}^D\left(R, \omega\right)$ at point $\mathbf{X} \in \partial V$ with outward normal $\mathbf{n}\left(\mathbf{X}\right) = [n_x,\ n_y,\ n_z]^{\mathrm{T}} \in \partial V$ are obtained from the fundamental displacements via constitutive relations.

The general subscript notation $(\cdot)_{ij}$, with $i, j = 1, 2, 3$, stands for the effect in the jth direction at the receiver point $\mathbf{X}$ when the unitary harmonic point load is acting at the source point $\mathbf{X}'$ in the ith direction. As usual, the subscripts $1, 2, 3$ are freely interchanged with x, y, z for convenience of representation. The coefficients $c_{ij}\left(\mathbf{X}'\right)$ in Eq. (3.5) take the values $C_{ij}\left(\mathbf{X}'\right) = \delta_{ij}$ if $\mathbf{X}' \in V$ and $C_{ij}\left(\mathbf{X}'\right) = 0$ if $\mathbf{X}' \notin V$, while Eq. (3.5) is not defined for $\mathbf{X}' \in \partial V$.

The derivation of the 2.5D integral representation theorem follows from the work of François et al. [2010]. To this end, the geometry and mechanical properties of the body are now assumed to be invariant in the z-direction and the intersections of V and ∂V with the $z = 0$ plane are denoted with Ω_b and $\partial\Omega_b$, respectively. Accordingly, the projection of the receiver point $\mathbf{X}$ and the source point $\mathbf{X}'$ on the $z = 0$ plane are denoted respectively with $\mathbf{x} = [x,\ y]^{\mathrm{T}}$ and $\mathbf{x}' = [x',\ y']^{\mathrm{T}}$. The point $\mathbf{x} \in \partial\Omega_b$ is understood as the intersection of an observer line infinitely extended along the z-direction with the $z = 0$ plane, while $\mathbf{x}' \in \Omega_b$ is intended as the intersection of a unitary harmonic line load with the same plane. Since the distance between the observer and source lines is constant throughout z, the spatial vector $\mathbf{R}$ is replaced by $\mathbf{r} = \mathbf{x} - \mathbf{x}'$, with $r = |\mathbf{x} - \mathbf{x}'|$ denoting the in-plane source-receiver distance. The line load is assumed to be harmonic in time and space and assumes the following representation

$$\mathfrak{p}\left(x', y', z', t\right) = \delta\left(x - x'\right)\delta\left(y - y'\right)\exp\left[\mathrm{i}\left(\omega t - \kappa_z z'\right)\right]. \tag{3.7}$$

where z' denotes the out-of-plane coordinate along the line of projection $\mathbf{x}$ on the $x - y$ plane. Given the longitudinal invariance, the surface integrals in Eq. (3.5) can be decomposed as

$$\int_{\partial V} (\cdot)\,\mathrm{d}a\left(\mathbf{X}\right) = \int_{-\infty}^{+\infty}\int_{\partial\Omega_b} (\cdot)\,\mathrm{d}s\left(\mathbf{x}\right)\mathrm{d}z \tag{3.8}$$

leading to the following integral representation

$$\begin{aligned} c_{ij}\left(\mathbf{x}'\right) u_j\left(\mathbf{x}', z', \omega\right) = &\int_{-\infty}^{+\infty}\int_{\partial\Omega_b} U_{ij}^{D}\left(r, z', z, \omega\right) t_j\left(\mathbf{x}, z, \omega\right)\mathrm{d}s\left(\mathbf{x}\right)\mathrm{d}z \\ &- \int_{-\infty}^{+\infty}\int_{\partial\Omega_b} T_{ij}^{D}\left(r, z', z, \omega\right) u_j\left(\mathbf{x}, z, \omega\right)\mathrm{d}s\left(\mathbf{x}\right)\mathrm{d}z, \end{aligned} \tag{3.9}$$

where $c_{ij}\left(\mathbf{x}'\right)$ are equal to δ_{ij} and 0 for $\mathbf{x}' \in \Omega_b$ and $\mathbf{x}' \notin \Omega_b$, respectively. Using the translational invariance property of the Green's functions [Andersen, 2006; Bonnet, 1999; Kobayashy, 1987], the source point of in-plane coordinates $\mathbf{x}'$ and out-of-plane coordinate z' can be shifted to the plane $z = 0$. Eq. (3.9) is then rewritten as

$$\begin{aligned} c_{ij}\left(\mathbf{x}'\right) u_j\left(\mathbf{x}', z', \omega\right) = & \int_{-\infty}^{+\infty} \int_{\partial\Omega_b} U_{ij}^{D}\left(r, 0, z - z', \omega\right) t_j\left(\mathbf{x}, z, \omega\right) \mathrm{d}s\left(\mathbf{x}\right) \mathrm{d}z \\ & - \int_{-\infty}^{+\infty} \int_{\partial\Omega_b} T_{ij}^{D}\left(r, 0, z - z', \omega\right) u_j\left(\mathbf{x}, z, \omega\right) \mathrm{d}s\left(\mathbf{x}\right) \mathrm{d}z. \end{aligned} \tag{3.10}$$

The spatial harmonic dependence assumed in Eq. (3.7) allows any scalar or vectorial field to be contracted in the wavenumber domain using the Fourier transform

$$f\left(\kappa_z\right) = \int_{-\infty}^{+\infty} f\left(z\right) \exp\left(\mathrm{i}\kappa_z z'\right) \mathrm{d}z, \tag{3.11}$$

which, applied to Eq. (3.10), leads to

$$\begin{aligned} c_{ij}\left(\mathbf{x}'\right) u_j\left(\mathbf{x}', z', \omega\right) = & \int_{-\infty}^{+\infty} \int_{-\infty}^{+\infty} \int_{\partial\Omega_b} U_{ij}^{D}\left(r, 0, z - z', \omega\right) t_j\left(\mathbf{x}, z, \omega\right) \mathrm{d}z \\ & \times \exp\left(\mathrm{i}\kappa_z z'\right) \mathrm{d}z \mathrm{d}s\left(\mathbf{x}\right) \mathrm{d}z' \\ & - \int_{-\infty}^{+\infty} \int_{-\infty}^{+\infty} \int_{\partial\Omega_b} T_{ij}^{D}\left(r, 0, z - z', \omega\right) u_j\left(\mathbf{x}, z, \omega\right) \\ & \times \exp\left(\mathrm{i}\kappa_z z'\right) \mathrm{d}z \mathrm{d}s\left(\mathbf{x}\right) \mathrm{d}z', \end{aligned} \tag{3.12}$$

Substituting the identity

$$\exp\left(\mathrm{i}\kappa_z z'\right) = \exp\left[-\mathrm{i}\kappa_z\left(z - z'\right)\right] \exp\left(\mathrm{i}\kappa_z z\right) \tag{3.13}$$

inside Eq. (3.12), the following expression is obtained

$$\begin{aligned} c_{ij}\left(\mathbf{x}'\right) u_j\left(\mathbf{x}', z', \omega\right) = & \int_{\partial\Omega_b} \int_{-\infty}^{+\infty} \left[\int_{-\infty}^{+\infty} \exp\left[-\mathrm{i}\kappa_z\left(z - z'\right)\right] U_{ij}^{D}\left(r, 0, z - z', \omega\right) \mathrm{d}z'\right] \\ & \times t_j\left(\mathbf{x}, z, \omega\right) \exp\left(\mathrm{i}\kappa_z z\right) \mathrm{d}z \mathrm{d}s\left(\mathbf{x}\right) \\ & - \int_{\partial\Omega_b} \int_{-\infty}^{+\infty} \left[\int_{-\infty}^{+\infty} \exp\left[-\mathrm{i}\kappa_z\left(z - z'\right)\right] T_{ij}^{D}\left(r, 0, z - z', \omega\right) \mathrm{d}z'\right] \\ & \times u_j\left(\mathbf{x}, z, \omega\right) \exp\left(\mathrm{i}\kappa_z z\right) \mathrm{d}z \mathrm{d}s\left(\mathbf{x}\right), \end{aligned} \tag{3.14}$$

where the terms inside the square brackets are recognized as the space Fourier transforms of the 3D Green's functions. These functions represent the fundamental solutions for the time and spatial harmonic line load problem of Eq. (3.7) in the isotropic linear viscoelastic full space. Denoting the 2.5D fundamental displacements with $U_{ij}^{D}\left(r,\kappa_z,\omega\right)$ and the corresponding fundamental tractions with $T_{ij}^{D}\left(r,\kappa_z,\omega\right)$, Eq. (3.53) is reelaborated as follows

$$\begin{aligned}
c_{ij}\left(\mathbf{x}'\right)u_j\left(\mathbf{x}',z',\omega\right) = &\int_{\partial\Omega_b} U_{ij}^{D}\left(r,-\kappa_z,\omega\right)\\
&\times\left[\int_{-\infty}^{+\infty} t_j\left(\mathbf{x},z,\omega\right)\exp\left(\mathrm{i}\kappa_z z\right)\mathrm{d}z\right]\mathrm{d}s\left(\mathbf{x}\right)\\
&-\int_{\partial\Omega_b} T_{ij}^{D}\left(r,-\kappa_z,\omega\right)\\
&\times\left[\int_{-\infty}^{+\infty} u_j\left(\mathbf{x},z,\omega\right)\exp\left(\mathrm{i}\kappa_z z\right)\mathrm{d}z\right]\mathrm{d}s\left(\mathbf{x}\right),
\end{aligned}\tag{3.15}$$

where the terms in the square brackets represent the space Fourier transforms of the displacements and tractions on the boundary, denoted with $u_j\left(\mathbf{x},\kappa_z,\omega\right)$ and $t_j\left(\mathbf{x},\kappa_z,\omega\right)$, respectively. Eq. (3.15) is finally recasted in the following form

$$\begin{aligned}
c_{ij}\left(\mathbf{x}'\right)u_j\left(\mathbf{x}',\kappa_z,\omega\right) = &\int_{\partial\Omega_b} U_{ij}^{D}\left(r,-\kappa_z,\omega\right)t_j\left(\mathbf{x},\kappa_z,\omega\right)\mathrm{d}s\left(\mathbf{x}\right)\\
&-\int_{\partial\Omega_b} T_{ij}^{D}\left(r,-\kappa_z,\omega\right)u_j\left(\mathbf{x},\kappa_z,\omega\right)\mathrm{d}s\left(\mathbf{x}\right),\\
&\mathbf{x}'\in\Omega_b,\ \mathbf{x}\in\partial\Omega_b
\end{aligned}\tag{3.16}$$

which corresponds to the 2.5D integral domain representation theorem. This result has also been found by Sheng et al. [2005] and Lu et al. [2008b] using the 2.5D reciprocal theorem for the cases of isotropic elastic and poroelastic materials, respectively.

3.5 Green's functions

The dynamic fundamental solutions for the 2.5D elastodynamic problem have been presented in recent years by different authors. Pedersen et al. [1994] and Sheng et al. [2005] derived the 2.5D Green's functions for an unbounded medium considering an harmonic load moving along the propagation direction. These functions also recover the stationary case when the velocity of the moving load is set to zero and can be applied to both isotropic linear elastic and viscoelastic media. The 2.5D Green's functions for a stationary line load in the full space have been derived by Li et al. [1992] and Tadeu and Kausel [2000] for linear viscoelastic isotropic media and by Tadeu et al. [2001] for an isotropic linear viscoelastic half space. In their work, Lu et al. [2008a] derived the Green's function for the 2.5D problem involving stationary line loads applied on poroelastic media. The Green's functions adopted here are those proposed by Tadeu and Kausel [2000] for a infinite homogeneous medium by using the method of potentials. Considering the line load in Eq. (3.7) passing through the point $\mathbf{x}'$ on the $x-y$ plane and extending along the z-direction, the displacement components at a receiver point $\mathbf{x}$ on the $x-y$ plane are given by [Kausel, 2006; Tadeu and Kausel, 2000]

$$\begin{aligned}
U_{11}^{D}(r,\kappa_z,\omega) &= A\left[\kappa_S^2 H_{0\beta} - \frac{1}{r}B_1 + \gamma_1^2 B_2\right]\\
U_{22}^{D}(r,\kappa_z,\omega) &= A\left[\kappa_S^2 H_{0\beta} - \frac{1}{r}B_1 + \gamma_2^2 B_2\right]\\
U_{33}^{D}(r,\kappa_z,\omega) &= A\left[\kappa_S^2 H_{0\beta} - \kappa_z^2 B_0\right]\\
U_{12}^{D}(r,\kappa_z,\omega) &= U_{21}^{D} = \gamma_1\gamma_2 A B_2\\
U_{13}^{D}(r,\kappa_z,\omega) &= U_{31}^{D} = \mathrm{i}\kappa_z\gamma_1 A B_1\\
U_{23}^{D}(r,\kappa_z,\omega) &= U_{32}^{D} = \mathrm{i}\kappa_z\gamma_2 A B_1
\end{aligned} \tag{3.17}$$

where the various terms take the following expressions

$$r = \sqrt{(x_1-x_1')^2 + (x_2-x_2')^2} \quad \text{source-receiver distance in the } x-y \text{ plane,} \tag{3.18}$$

$$A = \frac{1}{4\mathrm{i}\rho\omega^2} \quad \text{amplitude,} \tag{3.19}$$

$$\gamma_i = \frac{\partial r}{\partial x_i} = \frac{x_i - x_i'}{r} \quad \text{direction cosines in the } x-y \text{ plane,} \tag{3.20}$$

$$B_n = \kappa_\beta^n H_{n\beta} - \kappa_\alpha^n H_{n\alpha} \quad \text{composition of Hankel functions,} \tag{3.21}$$

$$H_{n\alpha} = H_n^{(2)}(\kappa_\alpha r) \quad n\text{th order Hankel function of the 2nd kind,} \tag{3.22}$$

$$H_{n\beta} = H_n^{(2)}(\kappa_\beta r) \quad n\text{th order Hankel function of the 2nd kind,} \tag{3.23}$$

$$\kappa_\alpha = \pm\sqrt{\kappa_L^2 - \kappa_z^2} \quad \text{radial longitudinal wavenumber,} \tag{3.24}$$

$$\kappa_\beta = \pm\sqrt{\kappa_S^2 - \kappa_z^2} \quad \text{radial shear wavenumber,} \tag{3.25}$$

$$\kappa_L = \frac{\omega}{\tilde{c}_L} \quad \text{longitudinal bulk wavenumber,} \tag{3.26}$$

$$\kappa_S = \frac{\omega}{\tilde{c}_S} \quad \text{shear bulk wavenumber.} \tag{3.27}$$

The solution along the observer line at a coordinate $z \neq 0$ in the (κ_z, ω) domain is obtained by multiplying Eq. (3.17) for Eq. (3.1), while the corresponding solution in the (z,t) domain can be recovered by means of the inverse Fourier transforms in space and time. The presence of the double sign ± in Eqs. (3.24) and (3.25) has a precise meaning: since the interest is focused on waves with amplitude decay in space due to both material attenuation and geometric spreading, it is required, coherently with the assumption in Eq. (3.1), that $\mathrm{Im}(\kappa_\alpha) \leqslant 0$ and $\mathrm{Im}(\kappa_\beta) \leqslant 0$. This requirement follows directly from the condition of zero amplitude at infinite distance ($r \to \infty$) from the origin, which must reflect the fact that no sources are located at infinity. This condition is also known as the Sommerfeld radiation condition [Bonnet, 1999].

Given the harmonic behaviour in time ($\exp(\mathrm{i}\omega t)$) and space ($\exp(-\mathrm{i}\kappa_z z)$) the Hankel functions $H_n^{(2)}(\kappa_\alpha r)$ and $H_n^{(2)}(\kappa_\alpha r)$ physically represent wavefronts that propagate away from the origin. Thus, the negativeness of the imaginary part of the radial wavenumbers ensures that the Hankel function of the second kind $H_n^{(2)}(\cdot)$ behave asymptotically as complex exponential ($\exp(-\mathrm{i}\kappa_z z)$), approaching zero as its argument approaches infinity.

However, this condition is not automatically ensured in a numerical implementation, but it must be guaranteed by an appropriate choice of the phase of the complex arguments $\kappa_\alpha r$ and $\kappa_\beta r$, which depends on the nature of the wave. This aspect is discussed in Sec. 3.8.2.

The second set of fundamental solutions, the tractions Green's functions $T_{ij}^D(r, \kappa_z, \omega)$, are obtained as

$$T_{ij}^D(r, \kappa_z, \omega) = \sigma_{ijk}^D(r, \kappa_z, \omega)\, n_k(\mathbf{x}), \quad i, j, k = 1, 2, 3 \tag{3.28}$$

being $n_k(\mathbf{x})$ the kth component of the external normal $\mathbf{n}(\mathbf{x}) = [n_1,\ n_2]^{\mathrm{T}}$ at $\mathbf{x} \in \partial\Omega_b$, while

$$\sigma_{ijk}^D(r, \kappa_z, \omega) = \tilde{\lambda}(\omega)\, \varepsilon_{i\mathrm{vol}}^D(r, \kappa_z, \omega)\, \delta_{jk} + 2\tilde{\mu}(\omega)\, \varepsilon_{ijk}^D(r, \kappa_z, \omega), \quad i, j, k = 1, 2, 3 \tag{3.29}$$

is the third order tensor of fundamental stresses, i.e. the jkth stress component at $\mathbf{x}$ when the line load is acting at $\mathbf{x}'$ in the ith direction. It is noted that the stress-strain relation in Eq. (3.29) is equivalent to Eq. (2.36) with the substitutions given in Eq. (2.122) and the replacement of the linearized second order strain tensor $\varepsilon_{ij}(\mathbf{x}, \kappa_z, \omega)$ with $\varepsilon_{ijk}^D(r, \kappa_z, \omega)$.

Applying the definition in Eq. (2.4), the third order tensor of fundamental linear strains $\varepsilon_{ijk}^D(r, \kappa_z, \omega)$ can be expressed in terms of fundamental displacements $U_{ij}^D(r, \kappa_z, \omega)$

as follows [Kausel, 2006; Tadeu and Kausel, 2000]

$$\begin{aligned}\varepsilon_{ijk}^{D}\left(r,\kappa_z,\omega\right) &= \frac{1}{2}\left[\frac{\partial U_{ij}^{D}\left(r,\kappa_z,\omega\right)}{\partial x_k}+\frac{\partial U_{ik}^{D}\left(r,\kappa_z,\omega\right)}{\partial x_j}\right]\\ &= \frac{1}{2}k_S^2 A\left(\delta_{jl}\frac{H_{0\beta}}{\partial x_k}+\delta_{kl}\frac{H_{0\beta}}{\partial x_j}\right)+A\frac{\partial^3 B_0}{\partial x_l \partial x_j \partial x_k}. \quad i,j,k=1,2,3\end{aligned} \tag{3.30}$$

Substituting Eqs. (3.18)-(3.27) into Eq. (3.30) leads to the following fundamental strains for the harmonic line load acting in the $x-y$ plane [Kausel, 2006; Tadeu and Kausel, 2000]

$$\begin{aligned}&\varepsilon_{i\mathrm{vol}}^{D}\left(r,\kappa_z,\omega\right)=\gamma_i A\left(-\kappa_S^2\kappa_\beta H_{1\beta}+\kappa_z^2 B_1+\frac{4}{r}B_2-B_3\right)\\ &\varepsilon_{i11}^{D}\left(r,\kappa_z,\omega\right)=\gamma_i A\left[\left(\frac{2}{r}B_2-\kappa_S^2\kappa_\beta H_{1\beta}\right)\delta_{1i}+\frac{B_2}{r}-\gamma_1^2 B_3\right]\\ &\varepsilon_{i22}^{D}\left(r,\kappa_z,\omega\right)=\gamma_i A\left[\left(\frac{2}{r}B_2-\kappa_S^2\kappa_\beta H_{1\beta}\right)\delta_{2i}+\frac{B_2}{r}-\gamma_2^2 B_3\right]\\ &\varepsilon_{i33}^{D}\left(r,\kappa_z,\omega\right)=\gamma_i\kappa_z^2 A B_1\\ &\varepsilon_{i12}^{D}\left(r,\kappa_z,\omega\right)=A\left[\left(\frac{B_2}{r}-\frac{1}{2}\kappa_S^2\kappa_\beta H_{1\beta}\right)\left(\delta_{1i}\gamma_2-\delta_{2i}\gamma_1\right)-\gamma_1\gamma_2\gamma_i B_3\right]\\ &\varepsilon_{i13}^{D}\left(r,\kappa_z,\omega\right)=\mathrm{i}\kappa_z A\left[\left(\frac{B_1}{r}-\frac{1}{2}\kappa_S^2 H_{0\beta}\right)\delta_{1i}-\gamma_1\gamma_i B_2\right]\\ &\varepsilon_{i23}^{D}\left(r,\kappa_z,\omega\right)=\mathrm{i}\kappa_z A\left[\left(\frac{B_1}{r}-\frac{1}{2}\kappa_S^2 H_{0\beta}\right)\delta_{2i}-\gamma_2\gamma_i B_2\right]\\ &\qquad i=1,2\end{aligned} \tag{3.31}$$

while for the line load acting in the z-direction ($i=3$) one has

$$\begin{aligned}
\varepsilon_{3\mathrm{vol}}^{D}\left(r,\kappa_z,\omega\right) &= \mathrm{i}\kappa_z A\left(-\kappa_S^2 H_{0\beta}+\kappa_z^2 B_0+\frac{2}{r}B_1-B_2\right)\\
\varepsilon_{311}^{D}\left(r,\kappa_z,\omega\right) &= \mathrm{i}\kappa_z A\left(\frac{B_1}{r}-\gamma_1^2 B_2\right)\\
\varepsilon_{322}^{D}\left(r,\kappa_z,\omega\right) &= \mathrm{i}\kappa_z A\left(\frac{B_1}{r}-\gamma_2^2 B_2\right)\\
\varepsilon_{333}^{D}\left(r,\kappa_z,\omega\right) &= \mathrm{i}\kappa_z A\left(-\kappa_S^2 H_{0\beta}+\kappa_z^2 B_0\right)\\
\varepsilon_{312}^{D}\left(r,\kappa_z,\omega\right) &= -\mathrm{i}\kappa_z\gamma_1\gamma_2 A B_2\\
\varepsilon_{313}^{D}\left(r,\kappa_z,\omega\right) &= \gamma_1 A\left(-\frac{1}{2}\kappa_S^2\kappa_\beta H_{1\beta}+\kappa_z^2 B_1\right)\\
\varepsilon_{323}^{D}\left(r,\kappa_z,\omega\right) &= \gamma_2 A\left(-\frac{1}{2}\kappa_S^2\kappa_\beta H_{1\beta}+\kappa_z^2 B_1\right).
\end{aligned}\tag{3.32}$$

Eqs. (3.31) and (3.32) can be finally substituted into Eq. (3.29) and then into Eq. (3.28) to evaluate the fundamental tractions. Alternatively, the following compact form has been presented by Castro and Tadeu [2012]

$$\begin{aligned}
T_{i1}^{D}\left(r,\kappa_z,\omega\right) &= 2\tilde{\mu}\left[\chi U_{i1,1}^{D}+(\chi-1)\left(U_{i2,2}^{D}+U_{i3,3}^{D}\right)\right]n_1+\tilde{\mu}\left(U_{i2,1}^{D}+U_{i1,2}^{D}\right)n_2\\
T_{i2}^{D}\left(r,\kappa_z,\omega\right) &= 2\tilde{\mu}\left[(\chi-1)\left(U_{i1,1}^{D}+U_{i3,3}^{D}\right)+\chi U_{i2,2}^{D}\right]n_2+\tilde{\mu}\left(U_{i2,1}^{D}+U_{i1,2}^{D}\right)n_1\\
T_{i3}^{D}\left(r,\kappa_z,\omega\right) &= \tilde{\mu}\left(U_{i1,3}^{D}+U_{i3,1}^{D}\right)n_1+\tilde{\mu}\left(U_{i2,3}^{D}+U_{i3,2}^{D}\right)n_2,\quad i=1,2,3
\end{aligned}\tag{3.33}$$

where $\chi=\tilde{c}_L^2/2\tilde{c}_S^2$.

When the source point approaches the receiver point, Eqs. (3.17) and (3.33) become singular. In particular, the asymptotic expressions of the Green's displacements and tractions for $\omega\neq 0$, $\kappa_z\neq 0$ and $r\to 0$ are

$$U_{ij}^{D}\left(\kappa_z,\omega\right)\xrightarrow[(\omega\neq 0,\ \kappa_z\neq 0)]{r\to 0}\ln\frac{1}{r},\tag{3.34}$$

$$T_{ij}^{D}\left(\kappa_z,\omega\right)\xrightarrow[(\omega\neq 0,\ \kappa_z\neq 0)]{r\to 0}\frac{1}{r}.\tag{3.35}$$

Based on Eqs. (3.34) and (3.35), the first integral on the right hand side of Eq. (3.16) becomes weakly singular when $\mathbf{x}'\to\mathbf{x}$, while the second integral has a strong singularity. This singularity needs a special treatment when the source points are taken on the boundary $\partial\Omega_b$, which is the problem addressed in Sec. 3.6.

For $\omega\neq 0$, $r\neq 0$ and $\kappa_z=0$, the Green's functions in Eqs. (3.17) and (3.33) recover those of the line load problem in plane-strain. Therefore, these expressions satisfy the plane-strain model as special case [Tadeu and Kausel, 2000].

3.6 Regularized 2.5D boundary integral equation

3.6.1 Limiting process

The integral representation theorem in Eq. (3.16) allows to calculate the displacements $u_i\left(\mathbf{x}', \kappa_z, \omega\right)$ at any $\mathbf{x}' \in \Omega_b$ once the displacements $u_j\left(\mathbf{x}, \kappa_z, \omega\right)$ and tractions $t_j\left(\mathbf{x}, \kappa_z, \omega\right)$ are known at any $\mathbf{x} \in \partial\Omega_b$. However, due to the possible unique assignment of either $u_j\left(\mathbf{x}, \kappa_z, \omega\right)$ (Dirichlet boundary conditions) or $t_j\left(\mathbf{x}, \kappa_z, \omega\right)$ (Neumann boundary conditions) at $\mathbf{x}$, the boundary conditions are half-determined. The remaining boundary variables are computed by extending Eq. (3.16) to $\partial\Omega_b$, which is usually accomplished by performing a limiting process $\mathbf{x}' \in \Omega_b \rightarrow \mathbf{x}' \in \partial\Omega_b$.

As stated in Sec. 3.5, this operation necessarily introduces singularities into the boundary integrals when the source point $\mathbf{x}'$ approaches the receiver point $\mathbf{x}$, since $U_{ij}^D\left(r, \kappa_z, \omega\right) \sim \ln\left(1/r\right)$ and $T_{ij}^D\left(r, \kappa_z, \omega\right) \sim 1/r$ for $r \rightarrow 0$. The first singularity is a weak singularity, and therefore the integrals involving the fundamental displacements converge in the ordinary sense. The second singularity can be studied by introducing a circular neighborhood $\Omega_\varepsilon\left(\mathbf{x}'\right)$ of $\mathbf{x}'$ as shown in Fig. 3.2, and subdividing the integral involving the fundamental tractions as follows

$$\begin{aligned}\int_{\partial\Omega_b} & T_{ij}^D\left(r, -\kappa_z, \omega\right) u_j\left(\mathbf{x}, \kappa_z, \omega\right) \mathrm{d}s\left(\mathbf{x}\right) \\ &= \int_{\partial\Omega_b - e_\varepsilon\left(\mathbf{x}'\right)} T_{ij}^D\left(r, -\kappa_z, \omega\right) u_j\left(\mathbf{x}, \kappa_z, \omega\right) \mathrm{d}s\left(\mathbf{x}\right) \\ &+ \int_{\partial\Omega_\varepsilon\left(\mathbf{x}'\right)} T_{ij}^D\left(r, -\kappa_z, \omega\right) u_j\left(\mathbf{x}, \kappa_z, \omega\right) \mathrm{d}s\left(\mathbf{x}\right),\end{aligned} \tag{3.36}$$

where $e_\varepsilon\left(\mathbf{x}'\right) = \partial\Omega_b \cap \Omega_\varepsilon\left(\mathbf{x}'\right)$ and $\partial\Omega_\varepsilon\left(\mathbf{x}'\right) = \Omega_b \cap \partial\Omega_\varepsilon\left(\mathbf{x}'\right)$. Taking the limit $\varepsilon \rightarrow 0$ in the representation formula Eq. (3.16), leads to [Bonnet, 1999]

$$\begin{aligned}c_{ij}\left(\mathbf{x}'\right) u_j\left(\mathbf{x}', \kappa_z, \omega\right) = & \int_{\partial\Omega_b} U_{ij}^D\left(r, -\kappa_z, \omega\right) t_j\left(\mathbf{x}, \kappa_z, \omega\right) \mathrm{d}s\left(\mathbf{x}\right) \\ & - C.P.V. \int_{\partial\Omega_b} T_{ij}^D\left(r, -\kappa_z, \omega\right) u_j\left(\mathbf{x}, \kappa_z, \omega\right) \mathrm{d}s\left(\mathbf{x}\right),\end{aligned} \tag{3.37}$$

where

$$C.P.V. \int_{\partial\Omega_b} \left(\cdot\right) \mathrm{d}s\left(\mathbf{x}\right) = ⨍_{\partial\Omega_b} \left(\cdot\right) \mathrm{d}s\left(\mathbf{x}\right) = \lim_{\epsilon \rightarrow 0} \int_{\partial\Omega_b - e_\varepsilon\left(\mathbf{x}'\right)} \left(\cdot\right) \mathrm{d}s\left(\mathbf{x}\right) \tag{3.38}$$

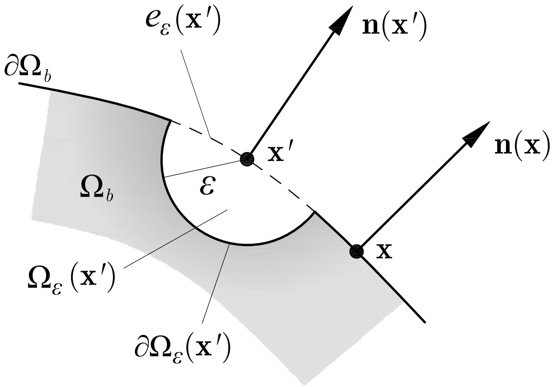

Figure 3.2: Exclusion neighborhood used for the limiting process $\varepsilon \to 0$.

is the Cauchy Principal Value of the integral over $\partial\Omega_b$. From the limiting process, the free term $c_{ij}(\mathbf{x}')$ is also determined, which assumes the following expression

$$c_{ij}\left(\mathbf{x}'\right) = \lim_{\epsilon\to 0}\int_{\partial\Omega_\varepsilon(\mathbf{x}')} T_{ij}^{D}\left(r, -\kappa_z, \omega\right) \mathrm{d}s\left(\mathbf{x}\right) \in \partial\Omega_b. \tag{3.39}$$

For $\mathbf{x}' \in \partial\Omega_b$ and $i = j$, the free term represents the ratio between the angle subtended by $\partial\Omega_\varepsilon$ and the angle of a complete circle when $\varepsilon \to 0$ [Bonnet, 1999; Brebbia and Dominguez, 1989; Zimmerman and Stern, 1993]. In the special case for which the boundary $\partial\Omega_b$ is smooth at $\mathbf{x}'$, Eq. (3.39) simplifies to $c_{ij}(\mathbf{x}') = 1/2\delta_{ij}$.

3.6.2 Regularization procedure

The analytical treatment of Cauchy Principal Value integrals in Eqs. (3.37) and (3.39) may result difficult due to (i) the analytical treatment of the strong singularity in the fundamental tractions, (ii) the presence of boundary corners, where the external normal is not uniquely defined and (iii) the shape functions used to interpolate the unknown boundary displacements.

Lately, researchers have proposed special integration methods to account for singularities in the integral kernels [Sheng et al., 2005] or to simplify the treatment of the corners at the discretization level by using discontinuous boundary elements [Gunawan and Hirose, 2005]. To overcome analytical and implementation difficulties, in this study the singular integrals and free terms are evaluated making use of the so-called rigid body motion technique [Banerjee, 1981; Brebbia and Dominguez, 1989; Dominguez, 1993]. This technique has been extended to the 2.5D case by [Lu et al., 2008b] for wave propagation problems involving poroelastic materials, and by François et al. [2010] for sound radiation problems involving translation invariant structures embedded in elastic and viscoelastic layered media.

The basic idea is to identify a second boundary value problem which uses simple fundamental solutions with the same asymptotic behaviour of the original boundary value problem when $r \to 0$. Then, if the solution of the second problem is adjusted so that the singular coefficients $c_{ij}(\mathbf{x}')$ have the same value at $\mathbf{x} = \mathbf{x}'$, the equations of the two problems can be subtracted and the singularity removed. For the dynamic problem under consideration, this can be accomplished by (i) choosing the domain of the auxiliary problem Ω_b^{aux} as complementary to the original domain to $\mathbb{R}^2$, i.e. $\Omega_b^{\mathrm{aux}} = \mathbb{R}^2 - \Omega_b$ and $\partial\Omega_b^{\mathrm{aux}} = \partial\Omega_b$, and (ii) applying a rigid body displacement u^0 on $\partial\Omega_b^{\mathrm{aux}}$.

Since the auxiliary volume $V^{\mathrm{aux}} = \mathbb{R}^3 - V$ is translational invariant, a constant displacement applied on Ω_b^{aux} can be understood as a time and spatial harmonic displacement with infinite wavelength in z-direction ($\kappa_z = 0$), and represents therefore a constant solution for the entire three dimensional domain. In this case, the original dynamic problem reduces to a combination of a static plane-strain line load problem $p(\mathbf{x}') = \delta(\mathbf{x} - \mathbf{x}')$ with fundamental solutions

$$\begin{aligned} U_{ij}^S(r) =& \frac{1}{8\pi \mathrm{Re}(\tilde{\mu})(1 - \mathrm{Re}(\tilde{\nu}))}\left[(3 - 4\mathrm{Re}(\tilde{\mu}))\ln\frac{1}{r}\delta_{ij} + \gamma_i\gamma_j\right] \\ T_{ij}^S(r) =& -\frac{1}{4\pi(1 - \mathrm{Re}(\tilde{\mu}))r}\left\{\gamma_k n_k\left[(2\mathrm{Re}(\tilde{\mu})\delta_{ij} + 2\gamma_i\gamma_j)\right.\right. \\ & \left.\left. -\ (1 - 2\mathrm{Re}(\tilde{\mu}))(\gamma_i n_j - \gamma_j n_i)\right]\right\}, \quad i,j,k = 1,2 \end{aligned} \tag{3.40}$$

and an anti-plane line load problem $p(z') = \delta(z - z')$ with fundamental solutions

$$\begin{aligned} U_{33}^S(r) &= \frac{1}{2\pi\mathrm{Re}(\tilde{\mu})}\ln\frac{1}{r} \\ T_{33}^S(r) &= -\frac{1}{2\pi r}\gamma_k n_k. \quad k = 1,2 \end{aligned} \tag{3.41}$$

The asymptotic expressions of the fundamental displacements and tractions in Eqs. (3.40) and (3.41) when the source point approaches the receiver point are

$$U_{ij}^S,\ U_{33}^S \xrightarrow{r\to 0} \ln\frac{1}{r}, \quad i,j = 1,2 \tag{3.42}$$

$$T_{ij}^S,\ T_{33}^S \xrightarrow{r\to 0} \frac{1}{r}, \quad i,j = 1,2 \tag{3.43}$$

which correspond to those in Eq. (3.34) and Eq. (3.35) for the 2.5D elastodynamic

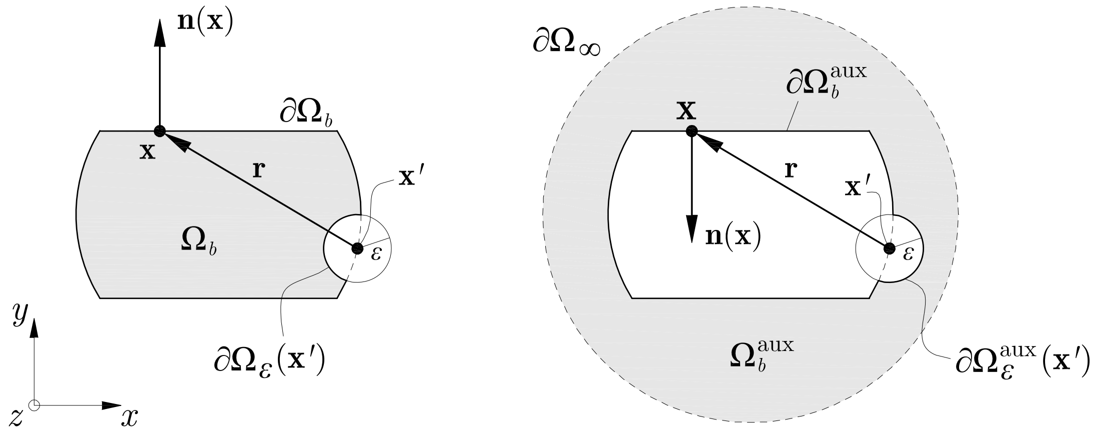

Figure 3.3: Auxiliary domain for a bounded waveguide.

problem. The rigid body displacement $u^0\left(\mathbf{x}, \kappa_z = 0, \omega = 0\right) = u^0\left(\mathbf{x}\right)$ is now considered to be applied at the boundary $\partial\Omega_b^{\mathrm{aux}}$ of an auxiliary domain Ω_b^{aux} corresponding to an infinite space bounded by $\partial\Omega_\infty$ at infinite distance from $\partial\Omega_b^{\mathrm{aux}}$ (see Fig. 3.3). Observing that for a rigid body motion $t_j\left(\mathbf{x}, \kappa_z = 0, \omega = 0\right) = 0$ and taking into account the equivalences $U_{ij}^D\left(r, \kappa_z = 0, \omega = 0\right) = U^S\left(r\right)$ and $T_{ij}^D\left(r, \kappa_z = 0, \omega = 0\right) = T^S\left(r\right)$, the application of Eq. (3.37) for the auxiliary domain results in the following expression

$$c_{ij}^{\mathrm{aux}}\left(\mathbf{x}'\right) u^0\left(\mathbf{x}'\right) = -u^0\left(\mathbf{x}\right)\left[\fint_{\partial\Omega_b} T_{ij}^S\left(r\right) \mathrm{d}s\left(\mathbf{x}\right) + \int_{\partial\Omega_\infty} T_{ij}^S\left(r\right) \mathrm{d}s\left(\mathbf{x}\right)\right], \tag{3.44}$$

where the boundary integral involving the fundamental displacements is vanished while the boundary integral involving the fundamental tractions has been extended in order to include $\partial\Omega_\infty$. Since the rigid displacement is arbitrary, Eq. (3.44) still holds for the particular choice $u^0\left(\mathbf{x}\right) = u_j\left(\mathbf{x}', \kappa_z, \omega\right)$, leading to

$$\begin{aligned} c_{ij}^{\mathrm{aux}}\left(\mathbf{x}'\right) u_j\left(\mathbf{x}', \kappa_z, \omega\right) = &- u_j\left(\mathbf{x}', \kappa_z, \omega\right)\left[\fint_{\partial\Omega_b} T_{ij}^S\left(r\right) \mathrm{d}s\left(\mathbf{x}\right)\right.\\ &\left. + \int_{\partial\Omega_\infty} T_{ij}^S\left(r\right) \mathrm{d}s\left(\mathbf{x}\right)\right]. \end{aligned} \tag{3.45}$$

Considering now that the unitary static force $p\left(\mathbf{x}', z'\right) = \delta\left(\mathbf{x} - \mathbf{x}'\right)\delta\left(z - z'\right)$ at the source point $\mathbf{x}' \in \partial\Omega_b^{\mathrm{aux}}$ must form an equilibrated system with the reaction forces distributed along $\partial\Omega_\infty$, it follows from equilibrium considerations that the integral of the fundamental tractions over $\partial\Omega_\infty$ results in an opposite force of the same unitary magnitude [Andersen, 2006; Brebbia and Dominguez, 1989]. The second integral in the right hand side of Eq. (3.45) becomes

$$\int_{\partial\Omega_\infty} T_{ij}^{S}\left(r\right) \mathrm{d}s\left(\mathbf{x}\right) = -\delta_{ij} \tag{3.46}$$

Substituting Eq. (3.46) into Eq. (3.45) gives

$$c_{ij}^{\mathrm{aux}}\left(\mathbf{x}'\right) u_j\left(\mathbf{x}', \kappa_z, \omega\right) = -u_j\left(\mathbf{x}', \kappa_z, \omega\right) \left[-\!\!\!\!\!\!\int_{\partial\Omega_b} T_{ij}^{S}\left(r\right) \mathrm{d}s\left(\mathbf{x}\right) - \delta_{ij}\right]. \tag{3.47}$$

Taking into account the opposite sign of the outward normals between the original and the auxiliary problems at $\mathbf{x}$, i.e. $\mathbf{n}\left(\mathbf{x}\right)|_{\partial\Omega_b} = -\mathbf{n}\left(\mathbf{x}\right)|_{\partial\Omega_b^{\mathrm{aux}}}$, the signs inside the square brackets in Eq. (3.47) can be reversed, leading to

$$\left[c_{ij}^{\mathrm{aux}}\left(\mathbf{x}'\right) - \delta_{ij}\right] u_j\left(\mathbf{x}', \kappa_z, \omega\right) = u_j\left(\mathbf{x}', \kappa_z, \omega\right) -\!\!\!\!\!\!\int_{\partial\Omega_b} T_{ij}^{S}\left(r\right) \mathrm{d}s\left(\mathbf{x}\right). \tag{3.48}$$

If Ω_b correspond to an unbounded domain, the second integral in the right-hand side of Eq. (3.44) vanishes since $\Omega_b^{\mathrm{aux}} = \mathbb{R}^2 - \Omega_b$ is bounded. In this case Eq. (3.49) reduces to

$$c_{ij}^{\mathrm{aux}}\left(\mathbf{x}'\right) u_j\left(\mathbf{x}', \kappa_z, \omega\right) = u_j\left(\mathbf{x}', \kappa_z, \omega\right) -\!\!\!\!\!\!\int_{\partial\Omega_b} T_{ij}^{S}\left(r\right) \mathrm{d}s\left(\mathbf{x}\right). \tag{3.49}$$

Generalizing the results in Eqs. (3.48) and (3.49) as proposed by Lu et al. [2008b] results in the following expression

$$\left[c_{ij}^{\mathrm{aux}}\left(\mathbf{x}'\right) - c_\infty\delta_{ij}\right] u_j\left(\mathbf{x}', \kappa_z, \omega\right) = u_j\left(\mathbf{x}', \kappa_z, \omega\right) -\!\!\!\!\!\!\int_{\partial\Omega_b} T_{ij}^{S}\left(r\right) \mathrm{d}s\left(\mathbf{x}\right), \tag{3.50}$$

where c_∞ is a coefficient equal to 1 if Ω_b is bounded and 0 if Ω_b is unbounded. Eq. (3.50) can be added to Eq. (3.37) without altering the original problem, since the rigid body motion does not involve physical tractions on the auxiliary domain.. As result, the following relation is obtained

$$\begin{aligned}
&\left[c_{ij}\left(\mathbf{x}'\right) + c_{ij}^{\mathrm{aux}}\left(\mathbf{x}'\right) - c_\infty\delta_{ij}\right] u_j\left(\mathbf{x}', \kappa_z, \omega\right) = \\
&= \int_{\partial\Omega_b} U_{ij}^{D}\left(r, -\kappa_z, \omega\right) t_j\left(\mathbf{x}, \kappa_z, \omega\right) \mathrm{d}s\left(\mathbf{x}\right) + \\
&- \int_{\partial\Omega_b} \left[T_{ij}^{D}\left(r, -\kappa_z, \omega\right) u_j\left(\mathbf{x}, \kappa_z, \omega\right) - T_{ij}^{S}\left(r\right) u_j\left(\mathbf{x}', \kappa_z, \omega\right)\right] \mathrm{d}s\left(\mathbf{x}\right).
\end{aligned} \tag{3.51}$$

Recalling Eq. (3.39), the sum of the free terms $c_{ij}\left(\mathbf{x}'\right) + c_{ij}^{\mathrm{aux}}\left(\mathbf{x}'\right)$ can be expressed as follows [Brebbia and Dominguez, 1989; Zimmerman and Stern, 1993]

$$\begin{aligned} c_{ij}\left(\mathbf{x}'\right) + c_{ij}^{\mathrm{aux}}\left(\mathbf{x}'\right) = &\lim_{\epsilon \to 0} \left[\int_{\partial\Omega_{\varepsilon}(\mathbf{x}')} T_{ij}^{D}\left(r, -\kappa_z, \omega\right) \mathrm{d}s\left(\mathbf{x}\right) \in \partial\Omega_b \right. \\ &+ \left. \int_{\partial\Omega_{\varepsilon}^{\mathrm{aux}}(\mathbf{x}')} T_{ij}^{D}\left(r, -\kappa_z, \omega\right) \mathrm{d}s\left(\mathbf{x}\right) \in \partial\Omega_b \right] \\ &= \delta_{ij}, \end{aligned} \tag{3.52}$$

where $\partial\Omega_{\varepsilon}^{\mathrm{aux}}\left(\mathbf{x}'\right)$ is defined as in Fig. 3.3. Substitution of the fundamental property in Eq. (3.52) into Eq. (3.51) cancels out the free term, and the regularized 2.5D boundary integral equation becomes

$$\begin{aligned} &\left(1 - c_{\infty}\right) u_i\left(\mathbf{x}', \kappa_z, \omega\right) = \int_{\partial\Omega_b} U_{ij}^{D}\left(r, -\kappa_z, \omega\right) t_j\left(\mathbf{x}, \kappa_z, \omega\right) \mathrm{d}s\left(\mathbf{x}\right) + \\ &- \int_{\partial\Omega_b} \left[T_{ij}^{D}\left(r, -\kappa_z, \omega\right) u_j\left(\mathbf{x}, \kappa_z, \omega\right) - T_{ij}^{S}\left(r\right) u_j\left(\mathbf{x}', \kappa_z, \omega\right) \right] \mathrm{d}s\left(\mathbf{x}\right), \\ &\left(\mathbf{x}, \mathbf{x}'\right) \in \partial\Omega_b \end{aligned} \tag{3.53}$$

in which the first integral on the right hand side contains a weak, integrable, singularity of order $\ln\left(1/r\right)$, while the strong singularity of order $1/r$ in the second boundary integral has been removed. The first and second integrals in Eq. (3.53) can therefore be evaluated numerically in a boundary element discretization scheme by using the Gauss-Laguerre and the Gauss-Legendre quadrature formulae, respectively [Stroud and Secrest, 1996]. However, as pointed out by Lu et al. [2008b], due to the presence of the Hankel function the Gauss-Laguerre quadrature formula for the integral involving $U_{ij}^{D}\left(r, -\kappa_z, \omega\right)$ may result inaccurate. Since the order of the singularities in both fundamental dynamic and static displacements is the same, Eq. (3.53) can be further modified using the addition-subtraction technique proposed by Lu et al. [2008b], leading to

$$\begin{aligned} &\left(1 - c_{\infty}\right) u_i\left(\mathbf{x}', \kappa_z, \omega\right) = \int_{\partial\Omega_b} \left[U_{ij}^{D}\left(r, -\kappa_z, \omega\right) - U_{ij}^{S}\left(r\right) \right] t_j\left(\mathbf{x}, \kappa_z, \omega\right) \mathrm{d}s\left(\mathbf{x}\right) \\ &+ \int_{\partial\Omega_b} U_{ij}^{S}\left(r\right) t_j\left(\mathbf{x}, \kappa_z, \omega\right) \mathrm{d}s\left(\mathbf{x}\right) \\ &- \int_{\partial\Omega_b} \left[T_{ij}^{D}\left(r, -\kappa_z, \omega\right) u_j\left(\mathbf{x}, \kappa_z, \omega\right) - T_{ij}^{S}\left(r\right) u_j\left(\mathbf{x}', \kappa_z, \omega\right) \right] \mathrm{d}s\left(\mathbf{x}\right), \\ &\left(\mathbf{x}, \mathbf{x}'\right) \in \partial\Omega_b \end{aligned} \tag{3.54}$$

where the first and third integral can be evaluated using the Gauss-Legendre quadrature formula while the second integral can now be evaluated analytically or via the Gauss-Laguerre quadrature formula.

It is remarked that Eq. (3.54) holds only for source points belonging to the boundary $\partial\Omega_b$. Once the solution is found in terms of displacements and tractions at any $\mathbf{x} \in \partial\Omega_b$, the complete displacement wavefield inside the domain Ω_b is readily obtained from Eq. (3.16) by posing $c_{ij}(\mathbf{x}') = \delta_{ij}$. The remaining quantities, i.e. strains and stresses, can be recovered from Eq. (3.16) via compatibility and constitutive relations.

3.7 Boundary discretization using semi-isoparametric boundary elements

The boundary $\partial\Omega_b$ is subdivided into N_b mono-dimensional boundary elements. The generic qth element of domain $\partial\Omega_b^q$ is assumed to be isoparametric in the plane of the domain Ω_b, i.e. the in-plane components of both u_j and t_j are interpolated with the same polynomial functions used to interpolate the cross-section geometry of the boundary.

Assuming an in-plane linear mapping from the two-nodes reference element identified by $\partial\Omega_b^{\text{ref}}$ to the corresponding two-nodes generic element $\partial\Omega_b^q$ as shown in Fig. 3.4, the semi-isoparametric representation of both displacements and tractions at the generic boundary point $\mathbf{x} \in \partial\Omega_b^q$ results in an uncoupled description of the out-of-plane from the in-plane motion of the form

$$\left.\begin{aligned} \mathbf{u}(\eta, \kappa_z, \omega) &= \mathbf{N}(\eta)\,\mathbf{q}^q(\kappa_z, \omega) \\ \mathbf{t}(\eta, \kappa_z, \omega) &= \mathbf{N}(\eta)\,\mathbf{h}^q(\kappa_z, \omega) \end{aligned}\right\} \text{ at } \mathbf{x}(\eta) = \mathbf{N}(\eta)\,\mathbf{x}^q \in \partial\Omega_b^q \tag{3.55}$$

where $\mathbf{N}(\eta)$ is the 3×6 matrix containing the linear shape functions in the natural coordinate $\eta \in \partial\Omega_b^{\text{ref}}$, while $\mathbf{x}^q$, $\mathbf{q}^q(\kappa_z, \omega)$ and $\mathbf{h}^q(\kappa_z, \omega)$ are the 6×1 vectors of nodal coordinates, displacements and tractions, respectively.

The discretized global system of algebraic equations is constructed from Eq. (3.54) by applying a point collocation scheme where the collocation points $\mathbf{x}'$ are assumed to be coincident with the nodes of the boundary element mesh [Brebbia and Dominguez, 1989].

Denoting by $\mathbf{x}_c$ the cth collocation node of the boundary element mesh and using Eqs. (3.55), the recursive collocation procedure over the total number of nodes $N_n = N_b$

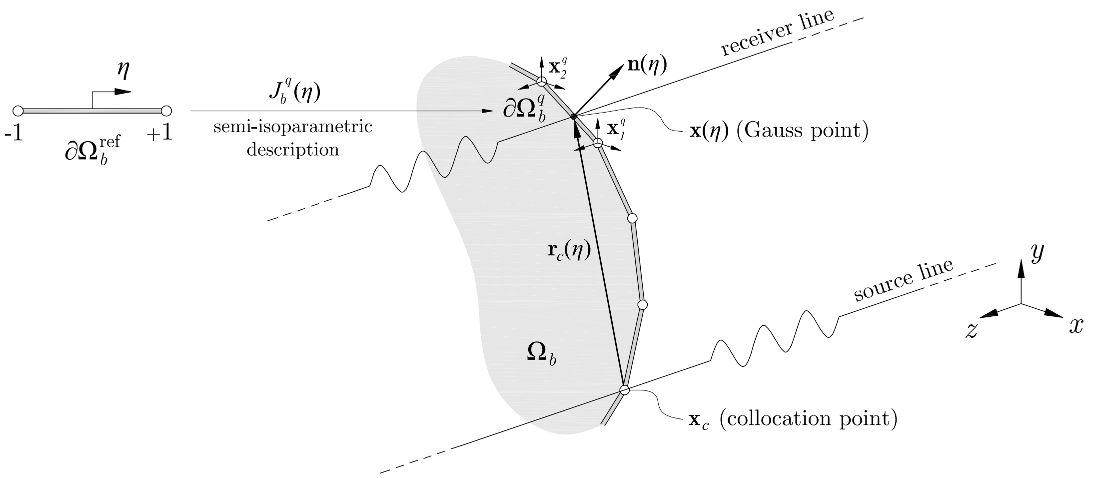

Figure 3.4: Semi-isoparametric discretization using mono-dimensional elements with linear shape functions.

allows to rewrite Eq. (3.54) in the following discrete form

$$
\begin{aligned}
&\bigcup_{c=1}^{N_n} (1 - c_\infty)\, \mathbf{u}_c(\kappa_z, \omega) \\
&= \bigcup_{c=1}^{N_n} \left\{ \bigcup_{q=1}^{N_b} \left[\mathbf{U}_1^q(r_c(\eta), \kappa_z, \omega) - \mathbf{U}_2^q(r_c(\eta)) \right] \mathbf{h}^q(\kappa_z, \omega) \right. \\
&- \bigcup_{\substack{q=1 \\ \left(\mathbf{x}_c \notin \partial\Omega_b^q\right)}}^{N_b} \left[\mathbf{T}_1^q(r_c(\eta), \kappa_z, \omega)\, \mathbf{q}^q(\kappa_z, \omega) \right] \\
&- \bigcup_{\substack{q=1 \\ \left(\mathbf{x}_c \in \partial\Omega_b^q\right)}}^{N_b} \left[\mathbf{T}_2^q(r_c(\eta), \kappa_z, \omega)\, \mathbf{q}^q(\kappa_z, \omega) \right] \\
&+ \left. \bigcup_{\substack{q=1 \\ \left(\mathbf{x}_c \notin \partial\Omega_b^q\right)}}^{N_b} \left[\mathbf{T}_3^q(r_c(\eta))\, \mathbf{u}_c(\kappa_z, \omega) \right] \right\}
\end{aligned}
\tag{3.56}
$$

where $r_c(\eta) = |\mathbf{x}(\eta) - \mathbf{x}_c|$ denotes the in-plane distance between the collocation point and the integration point, $\mathbf{u}_c(\kappa_z, \omega)$ is the 3×1 vector of boundary displacements at point $\mathbf{x}_c$ and $\bigcup$ stands for the assembling operation over the nodes (subscript c) and the elements (subscript q) of the mesh. The operators in Eq. (3.56) are defined as

$$\mathbf{U}_1^e\left(r_c\left(\eta\right),\kappa_z,\omega\right) = \int_{\partial\Omega_b^q}\Big[\mathbf{U}^D\left(r_c\left(\eta\right),-\kappa_z,\omega\right) - \mathbf{U}^S\left(r_c\left(\eta\right)\right)\Big]\mathbf{N}\left(\eta\right)J_b^q\left(\eta\right)\mathrm{d}\eta \tag{3.57}$$

$$\mathbf{U}_2^q\left(r_c\left(\eta\right)\right) = \int_{\partial\Omega_b^q}\mathbf{U}^S\left(r_c\left(\eta\right)\right)\mathbf{N}\left(\eta\right)J_b^q\left(\eta\right)\mathrm{d}\eta \tag{3.58}$$

$$\mathbf{T}_1^q\left(r_c\left(\eta\right),\kappa_z,\omega\right) = \int_{\partial\Omega_b^q}\mathbf{T}^D\left(r_c\left(\eta\right),-\kappa_z,\omega\right)\mathbf{N}\left(\eta\right)J_b^q\left(\eta\right)\mathrm{d}\eta \tag{3.59}$$

$$\mathbf{T}_2^q\left(r_c\left(\eta\right),\kappa_z,\omega\right) = \int_{\partial\Omega_b^q}\Big[\mathbf{T}^D\left(r_c\left(\eta\right),-\kappa_z,\omega\right)\mathbf{N}\left(\eta\right) - \mathbf{T}^S\left(r_c\left(\eta\right)\right)\mathbf{L}\Big]J_b^q\left(\eta\right)\mathrm{d}\eta \tag{3.60}$$

$$\mathbf{T}_3^q\left(r_c\left(\eta\right)\right) = \int_{\partial\Omega_b^q}\mathbf{T}^S\left(r_c\left(\eta\right)\right)J_b^q\left(\eta\right)\mathrm{d}\eta \tag{3.61}$$

where $J_b^q\left(\eta\right) = \left|\partial\mathbf{x}\left(\eta\right)/\partial\eta\right|$ is the Jacobian of the semi-isoparametric transformation.

The 3×3 displacement and traction Green's tensors in Eq. (3.57)-(3.61) are defined as

$$\mathbf{U}^D = \begin{bmatrix} U_{11}^D & U_{12}^D & U_{13}^D \\ U_{21}^D & U_{22}^D & U_{23}^D \\ U_{31}^D & U_{32}^D & U_{33}^D \end{bmatrix} \qquad \mathbf{T}^D = \begin{bmatrix} T_{11}^D & T_{12}^D & T_{13}^D \\ T_{21}^D & T_{22}^D & T_{23}^D \\ T_{31}^D & T_{32}^D & T_{33}^D \end{bmatrix} \tag{3.62}$$

$$\mathbf{U}^S = \begin{bmatrix} U_{11}^S & U_{12}^S & 0 \\ U_{21}^S & U_{22}^S & 0 \\ 0 & 0 & U_{33}^S \end{bmatrix} \qquad \mathbf{T}^S = \begin{bmatrix} T_{11}^S & T_{12}^S & 0 \\ T_{21}^S & T_{22}^S & 0 \\ 0 & 0 & T_{33}^S \end{bmatrix}. \tag{3.63}$$

where the entries of the 2×2 blocks in the static Green's tensors (identified by the first and second rows and columns) correspond to the fundamental solutions of the two-dimensional plane-strain line load problem given in Eq. (3.40) while the remaining nonzero terms correspond to the fundamental solutions for the case of the elastic anti-plane line load given in Eq. (3.41).

The 3×6 operator $\mathbf{L}$ is introduced to collocate the static Green's tractions tensor $\mathbf{T}^S\left(r_c\left(\eta\right)\right)$ on the 3×3 diagonal blocks of the global system, which contain singular terms. Such operator varies according to the position of the collocation node $\mathbf{x}_c$ inside the element and is denoted by

$$\mathbf{L} = \left[\,\beta_1\mathbf{I}_{3\times3},\ \beta_2\mathbf{I}_{3\times3}\,\right],\ \text{with}\ \left\{\begin{array}{lll} \beta_1 = 1, \beta_2 = 0 & \text{if} & \mathbf{x}_c \equiv \mathbf{x}_1^q \\ \beta_1 = 0, \beta_2 = 1 & \text{if} & \mathbf{x}_c \equiv \mathbf{x}_2^q \end{array}\right., \tag{3.64}$$

where $\mathbf{x}_1^q$ and $\mathbf{x}_2^q$ are, respectively, the coordinate vectors for the first and second node of the element including the collocation node $\mathbf{x}_c$ ($\mathbf{x} = [\mathbf{x}_1^q,\ \mathbf{x}_2^q]^{\mathrm{T}}$).

From Eq. (3.56), by grouping the local displacement and traction operators into the global influence operators according to the mesh topology

$$\mathbf{U}_b\left(\kappa_z, \omega\right) = \bigcup_{c=1}^{N_n} \bigcup_{q=1}^{N_b} \sum_{i=1}^{2} \mathbf{U}_i^q\left(r_c, \kappa_z, \omega\right), \tag{3.65}$$

$$\mathbf{T}_b\left(\kappa_z, \omega\right) = \bigcup_{c=1}^{N_n} \bigcup_{q=1}^{N_b} \sum_{i=3}^{2} \mathbf{T}_i^q\left(r_c, \kappa_z, \omega\right), \tag{3.66}$$

and by assembling the local displacement and tractions vectors into the global vectors

$$\mathbf{Q}_b\left(\kappa_z, \omega\right) = \bigcup_{q=1}^{N_b} \mathbf{q}^q\left(\kappa_z, \omega\right), \tag{3.67}$$

$$\mathbf{H}_b\left(\kappa_z, \omega\right) = \bigcup_{q=1}^{N_b} \mathbf{h}^q\left(\kappa_z, \omega\right), \tag{3.68}$$

the following set of linear algebraic equations is obtained

$$\left[\mathbf{T}_b\left(\kappa_z, \omega\right) + \left(1 - c_\infty\right)\mathbf{I}\right]\mathbf{Q}_b\left(\kappa_z, \omega\right) = \mathbf{U}_b\left(\kappa_z, \omega\right)\mathbf{H}_b\left(\kappa_z, \omega\right) \tag{3.69}$$

where $\mathbf{I}$ denotes the identity matrix. If no tractions discontinuities exist at a generic node, the operators in Eq. (3.69) have dimension $N \times N$, with $N = N_n \times 3$ denoting the total number of displacement variables, while the global vectors $\mathbf{Q}_b\left(\kappa_z, \omega\right)$ and $\mathbf{H}_b\left(\kappa_z, \omega\right)$ have dimension $N \times 1$.

Once Eq. (3.69) is formed, the boundary conditions must be imposed in terms of displacements and tractions on the discretized boundary nodes. Since only one between the Dirichlet $u_j\left(\kappa_z, \omega\right)$ and Neumann $t_j\left(\kappa_z, \omega\right)$ boundary conditions can be imposed at any $\mathbf{x}_c$, the effective system takes generally the form of a mixed linear system in which the rows of the matrix operators corresponding to the unknown variables are rearranged to form the matrix of coefficients, while the rows of the matrix operators corresponding to the assigned boundary conditions are selected to form the vector of constant terms.

After the above system has been solved for all the unknown boundary variables, the solution over $\partial\Omega_b$ is fully determined and the wavefield at a generic point $\mathbf{x}' \in \Omega_b$ can be computed by using Eq. (3.16), with $c_{ij}\left(\mathbf{x}'\right) = \delta_{ij}$. Since the integrals in Eq. (3.16) are not singular, the standard Gauss-Legendre quadrature formula can be used for their evaluation. The discretized representation of Eq. (3.16) reads

$$\mathbf{u}_d\left(\mathbf{x}', \kappa_z, \omega\right) = \mathbf{U}_d\left(\kappa_z, \omega\right) \mathbf{H}_b\left(\kappa_z, \omega\right) - \mathbf{T}_d\left(\kappa_z, \omega\right) \mathbf{Q}_b\left(\kappa_z, \omega\right) \tag{3.70}$$

where

$$\mathbf{U}_d\left(\kappa_z, \omega\right) = \bigcup_{q=1}^{N_b} \int_{\partial\Omega_b^q} \mathbf{U}^D\left(r\left(\eta\right), -\kappa_z, \omega\right) \mathbf{N}\left(\eta\right) J_b^q\left(\eta\right) \mathrm{d}\eta \tag{3.71}$$

$$\mathbf{T}_d\left(\kappa_z, \omega\right) = \bigcup_{q=1}^{N_b} \int_{\partial\Omega_b^q} \mathbf{T}^D\left(r\left(\eta\right), -\kappa_z, \omega\right) \mathbf{N}\left(\eta\right) J_b^q\left(\eta\right) \mathrm{d}\eta, \tag{3.72}$$

in which $r = \left|\mathbf{x}\left(\eta\right) - \mathbf{x}'\right|$, while $\mathbf{Q}_b\left(\kappa_z, \omega\right)$ and $\mathbf{H}_b\left(\kappa_z, \omega\right)$ are the vectors of displacements and tractions for the boundary nodes obtained as solution of Eq. (3.69). It is noted that the linear system in Eq. (3.70) is valid only for $\mathbf{x}' \in \Omega_b$ and the operators $\mathbf{U}_d\left(\kappa_z, \omega\right)$ and $\mathbf{T}_d\left(\kappa_z, \omega\right)$ have dimension $3 \times N$.

3.8 Nonlinear eigenvalue problem

The dispersion characteristics for each normal mode are determined from the wave equation of the external traction-free problem. Thus, by imposing homogeneous Neumann boundary conditions on the system Eq. (3.69), i.e. $\mathbf{H}_b\left(\kappa_z, \omega\right) = \mathbf{0}$, the following eigenvalue problem is obtained.

$$\mathbf{Z}\left(\kappa_z, \omega\right) \mathbf{Q}_b\left(\kappa_z, \omega\right) = \mathbf{0}, \tag{3.73}$$

where

$$\mathbf{Z}\left(\kappa_z, \omega\right) = \mathbf{U}_b^{-1}\left(\kappa_z, \omega\right) \left[\mathbf{T}_b\left(\kappa_z, \omega\right) + \left(1 - c_\infty\right) \mathbf{I}\right]. \tag{3.74}$$

corresponds to the dynamic stiffness matrix of the bounded ($c_\infty = 1$) or unbounded ($c_\infty = 0$) waveguide. For any fixed positive real frequency ω, the nonlinear eigenvalue problem Eq. (3.73) can be solved in the complex wavenumbers $\kappa_z\left(\omega\right)$ by using algorithms of the contour integral family [Amako et al., 2008; Asakura et al., 2009; Beyn, 2012]. These algorithms can extract the roots of the nonlinear problem Eq. (3.73) without the need of an initial guess for the eigensolutions, which is a limiting property of more classical algorithms such those of the Newton-Raphson family.

To solve the eigenvalue problem Eq. (3.73), the contour integral method proposed by Beyn [2012] is adopted. The method is able to compute all the eigenvalues and associated eigenvectors for an holomorphic eigenvalue problem that lies within a given close contour in the complex plane, including eigenvalues with multiplicity higher than one.

The algorithm proposed by Beyn [2012], in the form where the sum of the algebraic multiplicities of the eigenvalues does not exceed the system dimension, is recalled in Sec. 3.8.1. The singular and multivalued character of the operator $\mathbf{Z}(\kappa_z, \omega)$ are also discussed. Such properties are of fundamental importance in the definition of the region in the complex κ_z-plane where the roots of the fundamental modes must be sought.

3.8.1 Contour integral method

The algorithm is initialized by computing the two moment matrices

$$\mathbf{A}_0 = \frac{1}{2\pi \mathrm{i}} \oint_{\Gamma(\kappa_z)} \mathbf{Z}^{-1}(\kappa_z, \omega)\, \mathcal{V} \mathrm{d}\kappa_z \ \in \mathbb{C}^{N,L} \tag{3.75}$$

$$\mathbf{A}_1 = \frac{1}{2\pi \mathrm{i}} \oint_{\Gamma(\kappa_z)} \kappa_z \mathbf{Z}^{-1}(\kappa_z, \omega)\, \mathcal{V} \mathrm{d}\kappa_z \ \in \mathbb{C}^{N,L} \tag{3.76}$$

over the simple closed curve $\Gamma(\kappa_z)$ (Jordan curve) defined in the complex κ_z-plane. In Eqs. (3.75) and (3.76), $\mathcal{V} \in \mathbb{C}^{N,L}$ is chosen randomly. The positive integer L is chosen to satisfy the requirement $K \leqslant L \leqslant N$, denoting K the supposed number of eigenvalues inside the contour.

The integrals Eqs. (3.75) and (3.76) are evaluated numerically by discretizing the complex contour into N_p integration points and applying the trapezoidal rule.

Once the two moment matrices in Eqs. (3.75) and (3.76) are formed, a Singular Value Decomposition (SVD)

$$\mathbf{A}_0 = \mathbf{V} \mathbf{\Sigma} \mathbf{W}^{\mathrm{H}} \tag{3.77}$$

is computed, where $\mathbf{V}$ is a $N \times N$ complex unitary matrix, $\mathbf{\Sigma}$ is $N \times L$ is a diagonal matrix with non-negative entries along the diagonal and $\mathbf{W}^{\mathrm{H}}$ is a $L \times L$ complex unitary matrix. Since small singular values σ_l $(l = 1, ..., L)$ of the diagonal matrix $\mathbf{\Sigma}$ determine a bad conditioning of the eigenvalues computation, a rank test is then performed and only the first M singular values higher than a fixed tolerance tol_{rank} are retained. The remaining singular values are eliminated from $\mathbf{\Sigma}$ along with their corresponding columns in $\mathbf{V}$ and $\mathbf{W}$. After the rank test has been performed, the following operator is constructed

$$\mathbf{B} = \mathbf{V}_0^{\mathrm{H}} \mathbf{A}_1 \mathbf{W}_0 \mathbf{\Sigma}_0^{-1} \ \in \mathbb{C}^{M,M} \tag{3.78}$$

where

$$\mathbf{\Sigma}_0 = \operatorname{diag}\left(\sigma_1, ..., \sigma_M\right), \tag{3.79}$$

$$\mathbf{V}_0 = \mathbf{V}\left(1 : N, 1 : M\right), \tag{3.80}$$

$$\mathbf{W}_0 = \mathbf{W}\left(1 : L, 1 : M\right). \tag{3.81}$$

The operator $\mathbf{B}$ in Eq. (3.78) is diagonalizable and has as eigenvalues the eigenvalues of $\mathbf{Z}\left(\kappa_z, \omega\right)$ inside $\Gamma\left(\kappa_z\right)$ [Beyn, 2012]. Solving a standard linear eigenvalue problem for $\mathbf{B}$ leads to a set of eigenvalues $\kappa_z^m\left(\omega\right)$ and corresponding eigenvectors $\mathbf{y}^m\left(\omega\right)$ $(m = 1, 2, .., M)$ where, due to the choice of tol_{rank} and N_p, generally results $K \leqslant M \leqslant L$. Of the remaining $M - K$ spurious eigensolutions, those lying outside the contour are directly discarded, while the remaining are filtered out by establish first a suitable threshold value tol_{res} that is used next to perform the following relative residual test

$$\frac{\left\|\mathbf{Z}\left(\kappa_z^m\left(\omega\right), \omega\right)\mathbf{Q}_b^m\left(\omega\right)\right\|_\infty}{\left\|\mathbf{Z}\left(\kappa_z^m\left(\omega\right), \omega\right)\right\|_\infty \left\|\mathbf{Q}_b^m\left(\omega\right)\right\|_\infty} \leqslant \text{tol}_{\text{res}} \tag{3.82}$$

where $\mathbf{Q}_b^m\left(\omega\right) = \mathbf{V}_0\mathbf{y}^m\left(\omega\right)$ is the approximative eigenvector associated to $\kappa_z^m\left(\omega\right)$ and $\left\|\cdot\right\|_\infty$ denotes the infinity norm. Since the matrix $\mathbf{B}$ also retains the complete multiplicity structure of eigenvalues inside the contour $\Gamma\left(\kappa_z\right)$, some eigenvalues may result ill-conditioned with the corresponding eigenvectors. In this case, a Schur decomposition

$$\mathbf{BQ} = \mathbf{QR} \tag{3.83}$$

is performed, with $\mathbf{R}$ block-diagonalized such that the diagonal blocks belong to different eigenvalues. Then, the eigenvectors $\mathbf{y}^m\left(\omega\right)$ are selected from the first column of each mth diagonal-block in $\mathbf{R}$ to compute the associated true eigenvector $\mathbf{Q}_b^m\left(\omega\right)$.

The eigenpairs $\left[\kappa_z^m\left(\omega\right), \mathbf{Q}_b^m\left(\omega\right)\right]$ that satisfy the inequality Eq. (3.82) are then accepted as final solution.

3.8.2 Definition of the integral path and permissible Riemann sheets

The procedure proposed by Beyn [2012] and reported in Sec. 3.8.1 allows to extract all the eigenvalues for the holomorphic problem $\mathbf{Z}\left(\kappa_z, \omega\right) \in H\left(\Omega^*, \mathbb{C}^{K,K}\right)$, where Ω^* denotes the region of the complex κ_z-plane enclosed by $\Gamma\left(\kappa_z\right)$. From the inspection of

Eqs. (3.22)-(3.27) it appears that, due to the presence of the radial wavenumbers

$$\kappa_\alpha = \pm\sqrt{\kappa_L^2 - \kappa_z^2}, \qquad \kappa_\beta = \pm\sqrt{\kappa_S^2 - \kappa_z^2}. \tag{3.84}$$

in the arguments of the Hankel functions, the operator $\mathbf{Z}(\kappa_z, \omega)$:

- results to be singular at points $\kappa_z = \pm\kappa_L$ and $\kappa_z = \pm\kappa_S$, since the Hankel function is not defined as its argument $\kappa_{\alpha,\beta} r$ becomes zero;
- is multivalued due to the signs ± of κ_α and κ_β for any fixed couple (κ_z, ω).

To fulfill the holomorphicity requirement inside Ω^*, the operator $\mathbf{Z}(\kappa_z, \omega)$ must be made single-valued and the points of the complex plane corresponding to singularities and discontinuities must be excluded.

Firstly, it is recalled that, in order to have a wave that is attenuated in the direction of propagation, the imaginary component of its wavenumber must be negative in accordance with the position in Eq. (3.1). Then, the single valued definition of $\mathbf{Z}(\kappa_z, \omega)$ follows directly from the the imposition of the Sommerfeld radiation condition

$$\mathrm{Im}(\kappa_\alpha) < 0, \quad \mathrm{Im}(\kappa_\beta) < 0, \quad \forall \kappa_z \in \mathbb{C} \quad (\mathrm{Re}(\kappa_z) > 0,\ \mathrm{Im}(\kappa_z) \le 0) \tag{3.85}$$

which ensures that $H_n^{(2)}(\kappa_{\alpha,\beta} r) \to 0$ for $r \to \infty$, i.e. the amplitude of the outgoing radial waves becomes zero at infinite radial distance from the origin. Imposition of the Sommerfeld radiation condition determines the correct choice of the permissible Riemann sheets, i.e. the portions of the Riemann surface on which the physical solutions are located [He and Hu, 2009, 2010; van Dalen et al., 2010; Zhang et al., 2009]. On the Riemann surface, the operator $\mathbf{Z}(\kappa_z, \omega)$ is analytic and single-valued everywhere, except in correspondence of the poles of guided modes. Since the Riemann sheets are defined on the κ_z-plane by the possible combinations of signs $(\pm, \pm)$ for $(\kappa_\alpha, \kappa_\beta)$, the whole Riemann surface for the isotropic case is composed of four sheets [Ewing et al., 1957]. However, the poles of the function $\mathbf{Z}(\kappa_z, \omega)$ corresponding to the physical solutions must be searched only on the permissible sheets, which are selected according to the requirements in Eq. (3.85).

The choice of the signs for each region of the κ_z-plane enclosed by the contour is shown in Fig. 3.5. It can be noted that these assumptions result into a discontinuity of the operator $\mathbf{Z}(\kappa_z, \omega)$ along two hyperbolic trajectories that depart from κ_L and κ_S and extend to infinity along the negative imaginary axis. These hyperbolas can be determined by letting vanish the imaginary component of the radial wavenumbers.

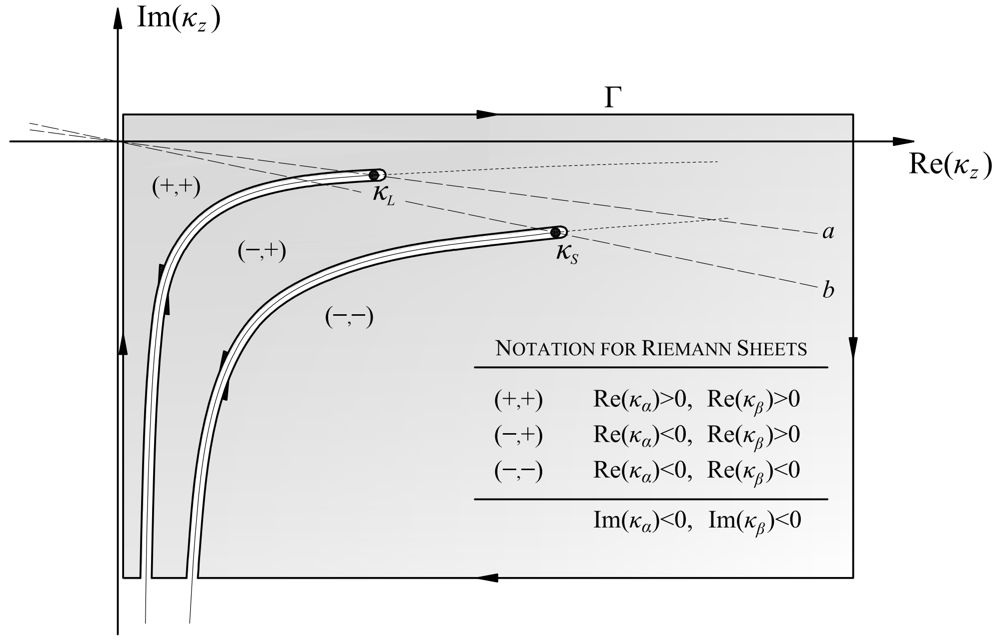

Figure 3.5: Complex κ_z-plane with branch points, branch cuts and integration path $\Gamma\left(\kappa_z\right)$. The notation $(\cdot,\cdot)$ stands for the choice of the signs in Eq. (3.84) for κ_α and κ_β respectively.

From Eq. (3.84), by posing $\operatorname{Im}\left(\kappa_\alpha\right)=0$ and $\operatorname{Im}\left(\kappa_\beta\right)=0$, one obtains

$$\operatorname{Im}\left(\kappa_z\right)=\frac{\operatorname{Re}\left(\kappa_L\right)\operatorname{Im}\left(\kappa_L\right)}{\operatorname{Re}\left(\kappa_z\right)}, \qquad \operatorname{Im}\left(\kappa_z\right)=\frac{\operatorname{Re}\left(\kappa_S\right)\operatorname{Im}\left(\kappa_S\right)}{\operatorname{Re}\left(\kappa_z\right)}, \tag{3.86}$$

which delimitate zone of the complex plane in which the phase of the radial wavenumbers satisfying at the Sommerfeld radiation condition Eq. (3.85) has a shift in phase of π radians. In fact, for any fixed $\operatorname{Re}\left(\kappa_z\right)\in\left[0,\operatorname{Re}\left(\kappa_{L,S}\right)\right]$ and $\operatorname{Im}\left(\kappa_z\right)\in\left[-\infty,+\infty\right]$, the shift in phase is not a continuous function if the conditions in Eq. (3.85) are imposed, but shows a jump when it crosses the hyperbolic trajectories in Eq. (3.86). Therefore, along these line the stiffness operator $\mathbf{Z}\left(\kappa_z,\omega\right)$ does not satisfy the requirement of holomorphicity.

The strategy to remove these discontinuities is to perform two cuts and closing the contour around the branches as shown in Fig. 3.5 (note that the total number of cuts is four since there are two other symmetric branches in the second quadrant of the complex plane, with branch points $-\kappa_L$ and $-\kappa_S$). These cuts are generally indicated as Sommerfeld (or fundamental) branch cuts [Ewing et al., 1957; van Dalen et al., 2010; Zhang et al., 2009] and vary in the κ_z-plane with $\kappa_\alpha\left(\omega\right)$ and $\kappa_\beta\left(\omega\right)$, which move along the lines a and b, respectively, while the frequency ω increases or decreases. Along the generic qth branch cut ($q = \alpha, \beta$), $\mathrm{Re}(\kappa_q) > 0$ on the left side and $\mathrm{Re}(\kappa_q) < 0$ on the right side, while $\mathrm{Im}(\kappa_q) < 0$ on both sides.

The two signs in each area in Fig. 3.5 represent the chosen Riemann sheet and correspond to the sign of the real part of the two radial wavenumbers $(\kappa_\alpha, \kappa_\beta)$ necessary to satisfy the condition in Eq. (3.85). It can be noted that the second Riemann sheet, denoted by $(+, -)$, is excluded from the search space, since it does not satisfy the Sommerfeld radiation condition.

If an elastic medium is considered, the bulk wavenumbers become real quantities, so that a and b rotate around the origin to overlap the real axis. In this case, the two branch cuts collapse on the negative imaginary axis and the portion of the real axis between the origin and the two corresponding bulk wavenumbers, becoming in fact a single branch cut. Since for the elastic case the poles of the normal modes lie on the real axis, it should be noted that the roots included in the range $0 \leqslant \kappa_z \leqslant \kappa_S$ are excluded from the contour region. However, due to the conditions in Eq. (3.85), the elastic case can only be treated by adding a small value of material attenuation (numerical attenuation) for both the bulk waves, so that the same considerations for the viscoelastic case can be applied.

As final remark, it is noted that the only other branch cut in the complex plane is represented by the negative real axis, which is a branch cut of the Hankel function as it presents a discontinuity along this axis. However, if only wavenumbers with strictly positive real part (right-propagating waves) are considered, this branch cut is unnecessary and can be directly avoided by assuming the integration path as in Fig. 3.5.

3.9 Dispersion characteristics extraction

Once the complete set of eigensolutions $[\kappa_z^m(\omega), \mathbf{Q}_b^m(\omega)]$ has been determined from Eq. (3.73) for the frequency of interest, the dispersion characteristics

$$c_p^m(\omega) = \frac{\omega}{\mathrm{Re}(\kappa_z^m(\omega))} \qquad \text{phase velocity,} \tag{3.87}$$

$$\alpha^m(\omega) = -\mathrm{Im}(\kappa_z^m(\omega)) \qquad \text{attenuation,} \tag{3.88}$$

$$c_e^m(\omega) = \frac{\int_{\Omega_b} \langle \mathbf{J}^m(\omega) \cdot \mathbf{n}_3 \rangle \mathrm{d}x \mathrm{d}y}{\int_{\Omega_b} \langle \mathscr{K}^m(\omega) + \mathscr{W}^m(\omega) \rangle \mathrm{d}x \mathrm{d}y} \qquad \text{energy velocity,} \tag{3.89}$$

for the mth propagating or evanescent normal mode can be extracted. It can be noted that the phase velocity and attenuation in Eqs. (3.87) and (3.88) are directly

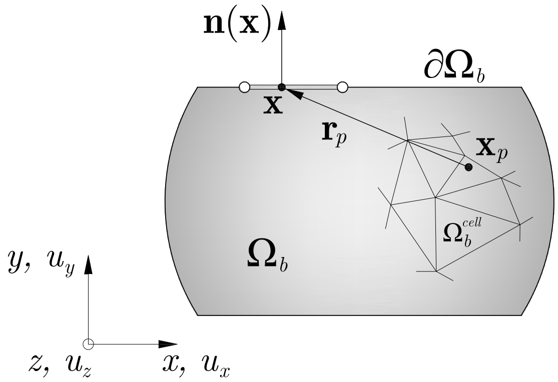

Figure 3.6: Subdivision of the domain Ω_b by means of integration cells.

derived from the obtained set of eigensolutions, while the energy velocity Eq. (3.89) is computed in post-processing. The various terms that appear in Eq. (3.89) are the acoustic Poynting vector $\mathbf{J}^m(\omega)$, the kinetic energy $\mathscr{K}^m(\omega)$ and the pseudo-potential energy $\mathscr{W}^m(\omega)$, which includes both the energy stored and dissipated via internal damping mechanisms. Their definitions have been given in Sec. 2.6.2.5, while their expressions are

$$J_i^m(\omega) = -\mathrm{i}\omega\sigma_{ji}^m(\omega)\, u_j^m(\omega) \tag{3.90}$$

$$\mathscr{K}^m(\omega) = \frac{\omega^2}{2}\rho u_i^m(\omega)\,\mathrm{conj}\left(u_i^m(\omega)\right) \tag{3.91}$$

$$\mathscr{W}^m(\omega) = \frac{1}{2}\sigma_{ij}^m(\omega)\,\mathrm{conj}\left(\varepsilon_{ij}^m(\omega)\right). \tag{3.92}$$

Since it is generally difficult to obtain a boundary integral representation of these quantities, the integrals in Eq. (3.89) can be evaluated by partitioning the domain Ω_b into an arbitrary number N_{cells} of integration cells as shown in Fig. 3.6. The shape of a single cell is defined as the mapping of a parent cell which is geometrically suitable to support a Gaussian quadrature scheme. Assuming an internal quadrature rule as shown in Fig. 3.1, the displacement field can be obtained at any quadrature point $\mathbf{x}_p \in \Omega_b$ using Eqs. (3.70) and (3.72), which yield the following $3 \times N$ linear system

$$\mathbf{u}_p^m(\omega) = -\left[\bigcup_{q=1}^{N_b} \int_{\partial\Omega_b^q} \mathbf{T}^D\left(r_p(\eta), -\kappa_z^m(\omega), \omega\right) \boldsymbol{\mathcal{N}}(\eta)\, J_b^q(\eta)\, \mathrm{d}\eta\right] \mathbf{Q}_b^m(\omega), \tag{3.93}$$

where $r_p(\eta) = |\mathbf{x}(\eta) - \mathbf{x}_p|$. It can be noted that in Eq. (3.93) the term involving the fundamental displacements has dropped since $\mathbf{H}_b^m(\kappa_z, \omega) = \mathbf{0}$.

The derived field variables at point $\mathbf{x}_p$ are denoted with the 6×1 vectors collecting the independent components of the Cauchy stress tensor expressed in Voigt notation, $\mathbf{s}_p^m(\omega) = [\sigma_{11}^m,\ \sigma_{22}^m\ \sigma_{33}^m,\ \sigma_{23}^m,\ \sigma_{13}^m,\ \sigma_{12}^m]^{\mathrm{T}}$, and the corresponding symmetric linear strain components, $\boldsymbol{\epsilon}_p^m(\omega) = [\varepsilon_{11}^m,\ \varepsilon_{22}^m\ \varepsilon_{33}^m,\ \varepsilon_{23}^m,\ \varepsilon_{13}^m,\ \varepsilon_{12}^m]^{\mathrm{T}}$ (cf. Sec. 2.3). The compatibility and constitutive relations can be rearranged in the general compact form

$$\boldsymbol{\epsilon}_p^m(\omega) = \mathscr{B}^m(\omega)\,\mathbf{u}_p^m(\omega)\,, \qquad \mathbf{s}_p^m(\omega) = \tilde{\mathbf{C}}\boldsymbol{\epsilon}_p^m(\omega)\,, \tag{3.94}$$

where the 6×3 compatibility operator $\mathbf{B}^m(\omega)$ and the 6×6 fourth order tensor of viscoelastic moduli $\tilde{C}_{ijkm}$ are expressed by

$$\begin{aligned} \mathscr{B}^m(\omega) &= \left[\mathscr{L}_x \frac{\partial}{\partial x} + \mathscr{L}_y \frac{\partial}{\partial y} - \mathrm{i}\kappa_z^m(\omega)\,\mathscr{L}_z\right], \\ \tilde{C}_{ijkm} &= \tilde{\lambda}\delta_{ij}\delta_{km} + \tilde{\mu}\left(\delta_{ik}\delta_{jm} + \delta_{im}\delta_{jk}\right), \end{aligned} \tag{3.95}$$

in which the $\mathscr{L}_i$ operators are defined as in Eq. (2.9). Substituting Eq. (3.93) into Eq. (3.94), the following $6 \times N$ linear systems are obtained for the strain and stress vectors at $\mathbf{x}_p$

$$\boldsymbol{\epsilon}_p^m(\omega) = -\left[\bigcup_{q=1}^{N_b} \int_{\partial\Omega_b^q} \mathscr{B}^m(\omega)\,\mathbf{T}^D\left(r_p(\eta), -\kappa_z^m(\omega), \omega\right)\mathbf{N}(\eta)\,J_b^q(\eta)\,\mathrm{d}\eta\right]\mathbf{Q}_b^m(\omega) \tag{3.96}$$

$$\mathbf{s}_p^m(\omega) = -\left[\bigcup_{q=1}^{N_b} \int_{\partial\Omega_b^q} \tilde{\mathbf{C}}\mathscr{B}^m(\omega)\,\mathbf{T}^D\left(r_p(\eta), -\kappa_z^m(\omega), \omega\right)\mathbf{N}(\eta)\,J_b^q(\eta)\,\mathrm{d}\eta\right]\mathbf{Q}_b^m(\omega) \tag{3.97}$$

where the compatibility operator $\mathscr{B}^m(\omega)$ applies only on the fundamental solutions $\mathbf{T}^D\left(r_p(\eta), -\kappa_z^m(\omega), \omega\right)$, since the derivative is intended as a variation around the point $\mathbf{x}_p$ [Dominguez, 1993].

The different operators in Eqs. (3.90)-(3.92) are integrated over the cross-section by considering the contribute of each cell. The time-averaged Poynting vector polarized in the z-direction, the pseudo-potential energy and the kinetic energy for the waveguide cross-section are obtained as follows

$$\int_{\Omega_b} \langle \mathbf{J}^m(\omega) \cdot \mathbf{n}_3 \rangle \mathrm{d}x\mathrm{d}y = \frac{\omega}{2}\mathrm{Im}\left\{\sum_{s=1}^{N_{cells}} \sum_{p=1}^{N_{Gp}} J_c^s(\boldsymbol{\xi}_p)\,w_p\left[\mathbf{u}_p^m(\omega)\right]^{\mathrm{H}} \mathscr{L}_z^{\mathrm{T}}\mathbf{s}_p^m(\omega)\right\} \tag{3.98}$$

$$\int_{\Omega_b} \langle \mathscr{K}^m(\omega) \rangle \mathrm{d}x\mathrm{d}y = \rho\frac{\omega^2}{4}\mathrm{Re}\left\{ \sum_{s=1}^{N_{cells}} \sum_{p=1}^{N_{G_p}} J_c^s(\boldsymbol{\xi}_p)\, w_p \left[\mathbf{u}_p^m(\omega)\right]^{\mathrm{H}} \mathbf{u}_p^m(\omega) \right\} \tag{3.99}$$

$$\int_{\Omega_b} \langle \mathscr{W}^m(\omega) \rangle \mathrm{d}x\mathrm{d}y = \frac{1}{4}\mathrm{Re}\left\{ \sum_{s=1}^{N_{cells}} \sum_{p=1}^{N_{G_p}} J_c^s(\boldsymbol{\xi}_p)\, w_p \left[\boldsymbol{\epsilon}_p^m(\omega)\right]^{\mathrm{H}} \mathbf{s}_p^m(\omega) \right\} \tag{3.100}$$

where N_{G_p} is the total number of Gauss points for the sth cell, $\boldsymbol{\xi}_p$ and $J_c^s(\boldsymbol{\xi}_p)$ are the natural coordinates and the Jacobian of the in-plane mapping for the sth cell at point p, respectively, w_p is the corresponding integration weight and the expressions for $\mathbf{u}_p^m(\omega)$, $\boldsymbol{\epsilon}_p^m(\omega)$ and $\mathbf{s}_p^m(\omega)$ are given by Eqs. (3.93), (3.96) and (3.97), respectively. Substitution of Eqs. (3.98)-(3.100) into Eq. (3.89) allows to compute the energy velocity for the mth normal mode.

3.10 Numerical analyses of bounded waveguides

To show the capability of the 2.5D BEM formulation, the dispersion curves obtained for a standard 113A rail section and a square section are compared with those extracted using the Semi-Analytical Finite Element (SAFE) method. In both the examples, the waveguides are considered to be made of steel with mass density $\rho = 7800$ Kg/m^3, longitudinal and shear bulk wave velocities equal to $c_L = 5744.7$ m/s and $c_S = 3224.6$ m/s, respectively, longitudinal wave attenuation $\kappa_L = 0.003$ Np/wavelength and shear bulk wave attenuation $\kappa_S = 0.008$ Np/wavelength.

Since the accuracy of the eigensolutions is strongly dependent on the number of integration points and the extension of the region enclosed by the curve $\Gamma(\kappa_z)$, an adaptive scheme has been implemented for the contour algorithm. The extension of the contour region, as well as the number of integration points, can be chosen by observing that at low frequencies only the first low order modes with small wavenumbers are expected, which allows to reduce the dimension of the complex contour and the number of integration points.

When frequency increases, the extension of the spectrum including propagative modes increases and the contour has to be adjusted in order to capture the complete set of roots. As the region enlarges, an increased number of integration points is needed, thus making the algorithm computationally more expensive at high frequencies. The rank and residual tolerances have been chosen on the bases of convergence tests in which the number of integration points has been increased until a stable trend was observable on the separation of singular values as well as the relative residuals given in Eq. (3.82).

3.10.1 Standard BS11-113A rail

In the first numerical application, the dispersion curves for a standard 113A rail are compared with those obtained using the SAFE method. The boundary element mesh used for the numerical test is illustrated in Fig. 3.7(a). It is composed of 146 semi-isoparametric linear elements and 146 nodes, corresponding to a total of 438 degrees of freedom. The numerical integrations have been carried out at the element level using 10 quadrature points, while the internal wavefield and its derivatives have been computed using a subdivision of the internal area into 1158 cells. Each cell is represented by a 3-nodes triangular element with linear shape functions. The SAFE solution has been obtained by using a mesh of 1496 semi-isoparametric linear triangular elements and 835 nodes (2505 dof) of Fig. 3.7(b). Both the boundary element mesh and the finite element mesh have been chosen from a convergence test performed over a frequency range of $0 \div 10$ kHz, decreasing the mesh size until a stable dispersion solution was reached.

The contour $\Gamma(\kappa_z)$ has been defined as in Fig. 3.5, with $L = 40$, a fixed vertical range of $-3.0 \leq \mathrm{Im}(\kappa_z) \leq +1.0$ and a horizontal range varying linearly with frequency, with constant minimum value of $\mathrm{Re}(\kappa_z) = 0.001$ and maximum varying between 20.0 ($f = 0$ kHz) and 50.0 ($f = 10.0$ kHz).

The singular values separation after 50 frequency steps can be observed in Fig. 3.8, where σ_i denotes the ith singular value and $\sigma_{\max}$ represents the maximum singular value at the current frequency step. For the first frequency, a total number of 500 integration points was used for the trapezoidal rule, then linearly increased to 1400 for the maximum frequency.

As it can be noted, the gap is generally included in the range $-2.0 \leq (\sigma_i/\sigma_{\max}) \leq -4.0$, although it becomes smaller at around $f = 2.0$ kHz and in the range $5.0 \div 6.0$ kHz, where cutoffs of the modes $m4$, $m6$, $m7$ and $m8$ occur. The term cutoff is used to indicate the frequency value corresponding to a noticeable increase of real part of the axial wavenumber, bearing in mind that the concept of cutoff does not have meaning in the viscoelastic case.

In order to minimize the negative effect of spurious solutions in the computation of the linear eigenvalue problem Eq. (3.78), the rank tolerance has been chosen equal to $\mathrm{tol}_{rank} = -2.0$, while the tolerance for the residual test Eq. (3.82) has been assumed

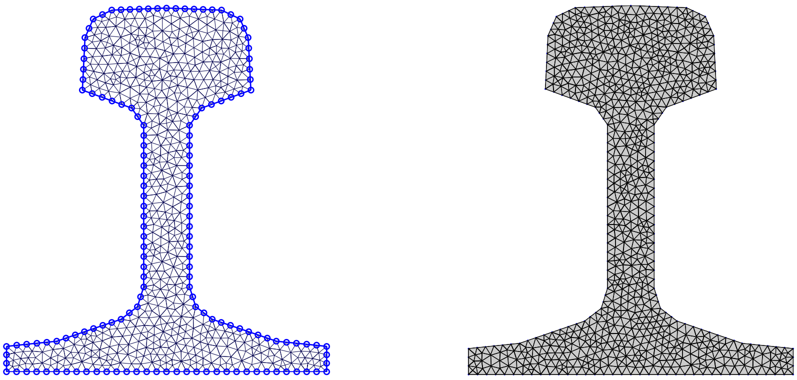
(a) (b)

Figure 3.7: (a) Boundary element mesh with internal cells subdivision and (b) SAFE mesh of the BS11-113A rail.

equal to $\text{tol}_{res} = 1.0 \times 10^{-6}$.

As observed in Figs. 3.9-3.12, the BEM solution (continuous lines) is in very good agreement with the SAFE solution (dots). Considerations on the dispersion characteristics of the various m modes can be found in a number of works (see, for example, [Bartoli et al., 2006; Gavric, 1995; Hayashi et al., 2003]) and are not repeated here.

The attenuation for all the guided modes are in very good agreement with those provided by the SAFE method (Fig. 3.11), although the $m5$ and $m7$ modes exhibit a slightly unstable behaviour in the $5.0 \div 5.6$ kHz and the $6.0 \div 7.0$ kHz frequency range, respectively. It is noted that, that attenuation curves for the viscoelastic rail have been found in literature only by means of Finite Element-based analyses.

The comparison between the BEM and the SAFE method for the energy velocity ((Fig. 3.12)) also indicates a good correspondence. The only noticeable differences are represented by the $m3$ mode in the $1.0 \div 4.0$ kHz frequency range and the $m8$ mode for its entire frequency range.

3.10.2 Square bar

The second numerical test is performed on a square bar with 20 mm side length. The dispersion curves have been extracted in the $0 \div 200.0$ kHz frequency range. The goal of this numerical test is to verify the performances of the method when the spectra are densely populated and in the presence of eigenvalues with multiplicity higher than one. After a convergence test, a boundary mesh of 148 semi-isoparametric linear elements and 148 nodes has been chosen, along with an internal subdivision into 4418 triangular

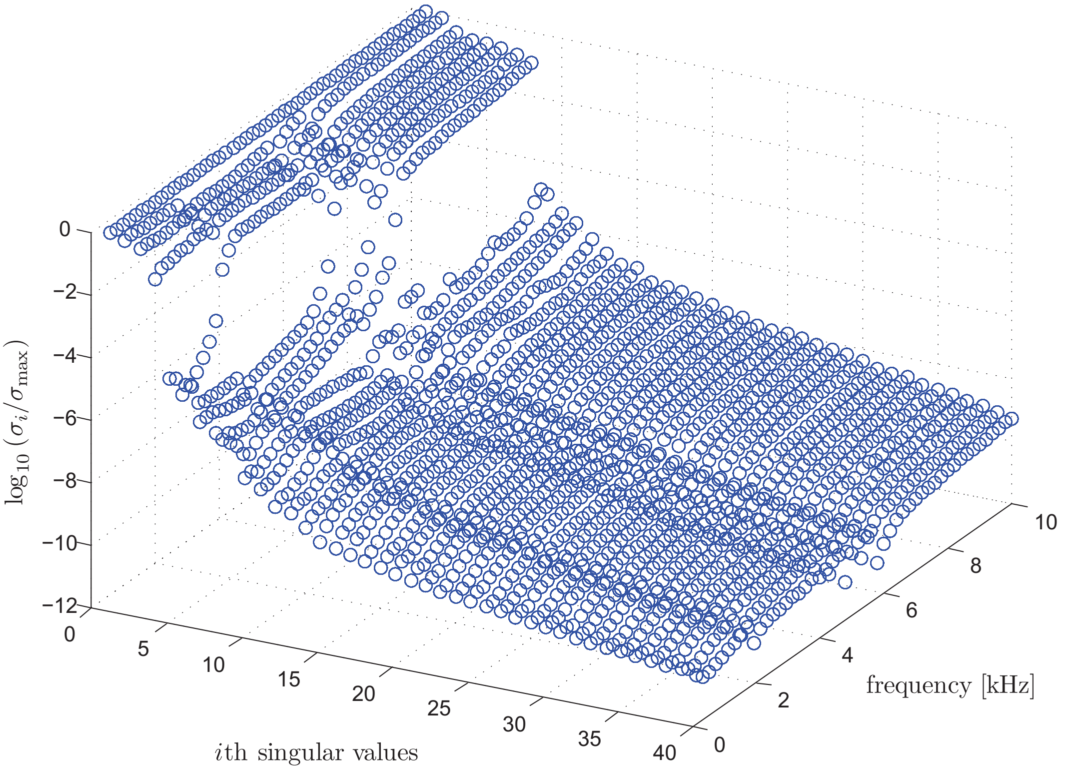

Figure 3.8: Singular values distribution after 50 frequency steps for the standard 113A rail in Sec. 3.10.1.

cells with associated linear shape functions (see Fig. 3.13(a)). As comparison, the square section has been analyzed using the SAFE method with a mesh of 4096 semi-isoparametric linear triangular elements and 2113 nodes (see Fig. 3.13(b)), which also gave a convergent solution in the considered frequency range.

The separation of singular values after 50 frequency steps can be observed in Fig. 3.14. For the eigenvalues computation, a dynamically adaptive contour window $\Gamma(\kappa_z)$ has been used as previously illustrated for the rail example. The number of integration point has been linearly increased from a minimum of 500 at the first frequency step to a maximum of 1500 at the last frequency step. As already noted, the jump in the singular values is strongly reduced at cutoff frequencies, where the solution appears more prone to numerical instabilities.

The comparison between the dispersion curves obtained via BEM and those extracted using the SAFE method is shown in Figs. 3.15-3.18. As can be noted, the solutions in terms of real part of the axial wavenumbers and energy velocity are in very good agreement. The solutions in terms of attenuation show some discrepancies for the

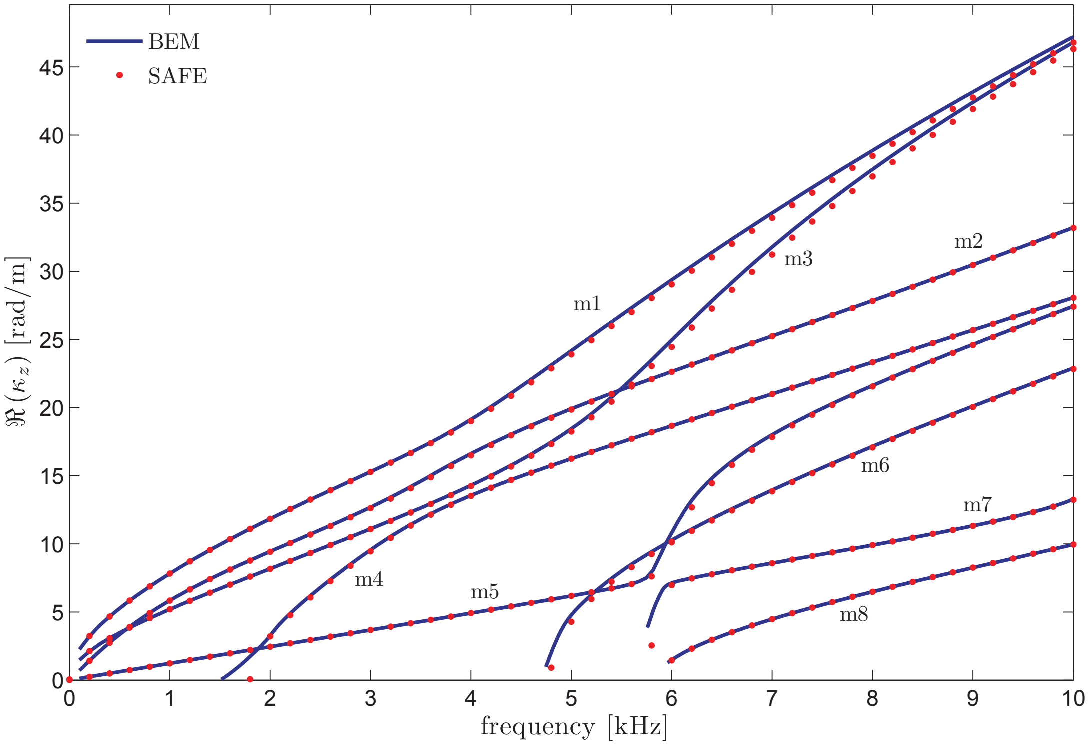

Figure 3.9: Real wavenumber dispersion curves for the viscoelastic steel BS11-113A rail.

flexural mode F_2 in the frequency range $85.0 \div 105.0$ kHz, for the flexural mode F_3 in the $115.0 \div 150.0$ kHz range and the longitudinal mode L_2 in the $150.0 \div 165.0$ kHz range. Larger discrepancies are observed for the attenuation of the screw S_3^1 mode for its entire frequency range. Small differences can be observed also in the attenuation curve for the L_3 mode.

It is finally emphasized that the contour algorithm correctly identifies the eigenvalues with multiplicity 2, corresponding to the flexural F_i modes.

3.11 Surface waves along cavities of arbitrary cross-section

A first investigation of surface dispersion characteristics for axially symmetric modes in cylindrical cavities of circular cross-section can be found in the work of Biot [1952], that demonstrated the existence of a cutoff for all the pseudo-Rayleigh modes with wavelength corresponding to the bulk shear wavelength. The existence of the first flexural mode at all frequencies has been proved analytically by Boström and Burden

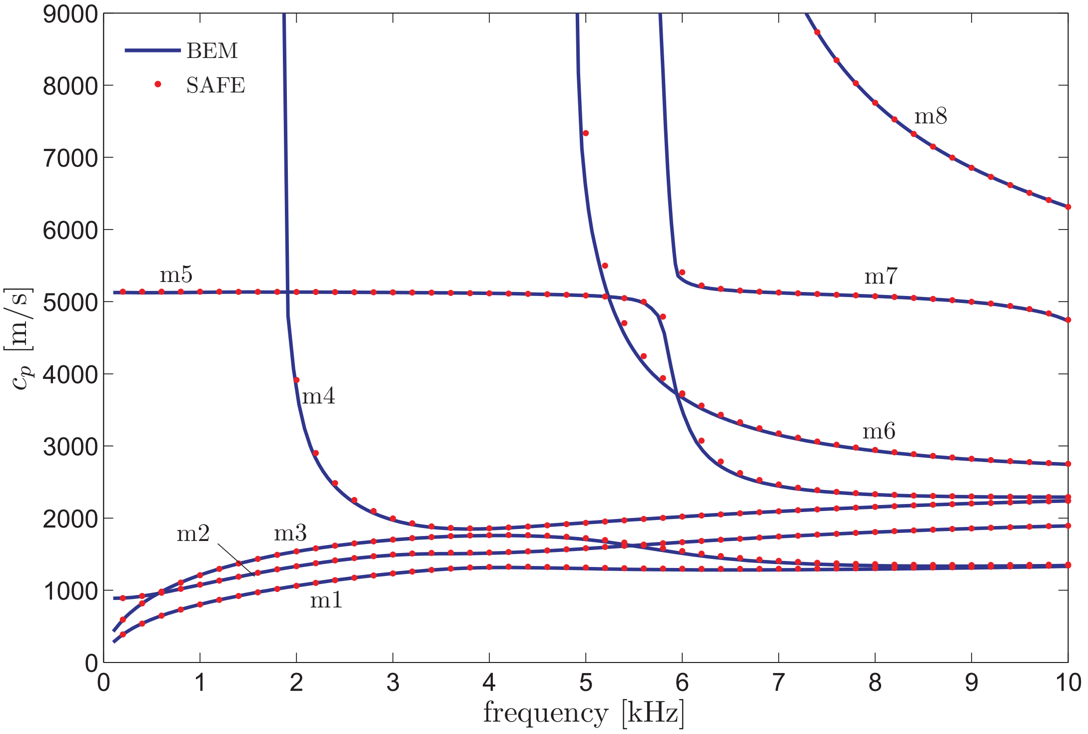

Figure 3.10: Phase velocity dispersion curves for the viscoelastic steel BS11-113A rail.

[1982] in cylindrical cavities of circular cross-section and by Burden [1985a,b] for cavities with circular indented, hyperelliptical and elliptical cross-section. However, in these works only elastic mediums are considered.

More recently, Tadeu et al. [2002b] used a 2.5D boundary element formulation to study borehole cavities of different cross-sections in elastic mediums, extracting the phase velocity spectra from the response of the system to a blast load in the frequency-wavenumber domain. Degrande et al. [2006] used a coupled boundary element-finite element formulation for the prediction of vibrations in the free field from excitations due to metro trains in tunnels, extracting the slowness dispersion curves for a layered soil medium with a cylindrical cavity.

In this section it is shown that for $\kappa_z > \kappa_S$ (non radiating region) the attenuation curves of surface normal modes approach asymptotically the attenuation of the Rayleigh wave.

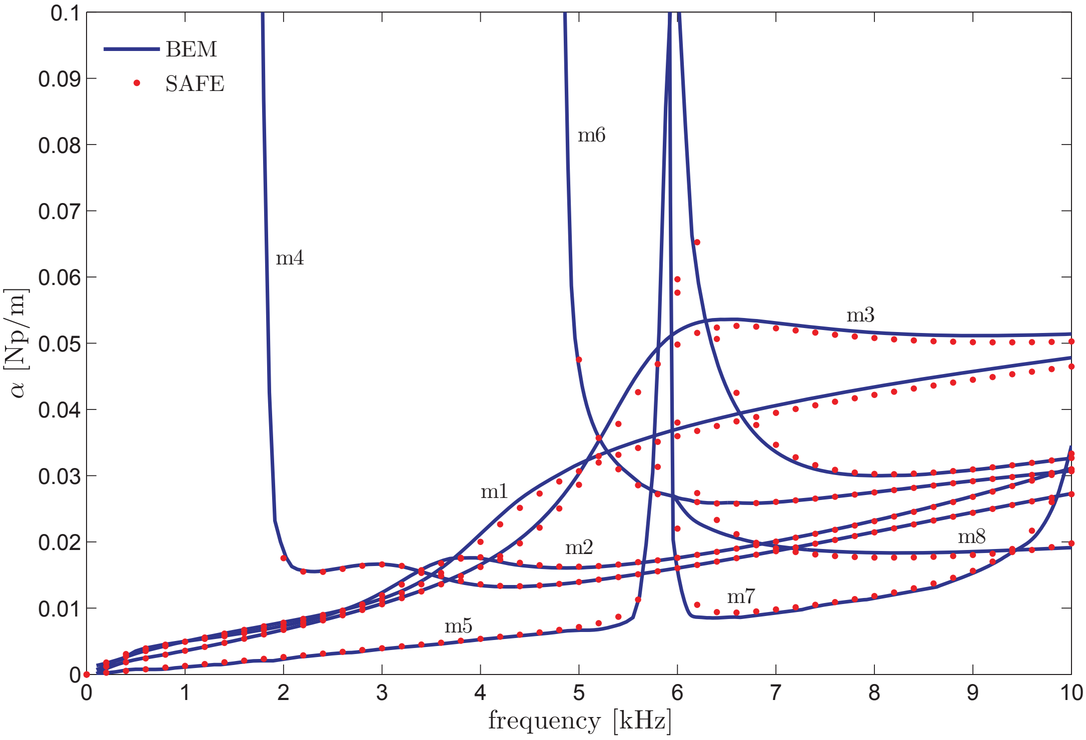

Figure 3.11: Attenuation dispersion curves for the viscoelastic steel BS11-113A rail.

3.11.1 Circular cavity in viscoelastic full-space

In the following numerical example, a cylindrical cavity with circular cross-section of radius $a = 1$ m and immersed in a viscoelastic medium is studied. As demonstrated by Biot [1952] and Boström and Burden [1982], surface waves in cylindrical cavities propagate with phase velocity varying between the shear wave speed c_S and the Rayleigh wave speed c_R. Following Biot [1952], the normal modes ranging between these velocities are classified as pseudo-Rayleigh waves, that do not exhibit attenuation if the medium is elastic. On the other hand, any disturbance propagating at the surface with wavelength longer than the shear wavelength causes shear waves to be radiated, and the energy carried by the surface waves is therefore geometrically attenuated [Botter and van Arkel, 1982]. As a consequence, a cutoff occurs when the axial wavenumbers of the propagating modes become equal to the shear wavenumber.

Since surface waves are characterized by a displacement amplitude decreasing with increasing depth, the corresponding axial wavenumbers κ_z must be larger than the shear wavenumber κ_S, so that the second Hankel functions give the typical exponential decay in the radial direction. As the inferior speed limit at which surface

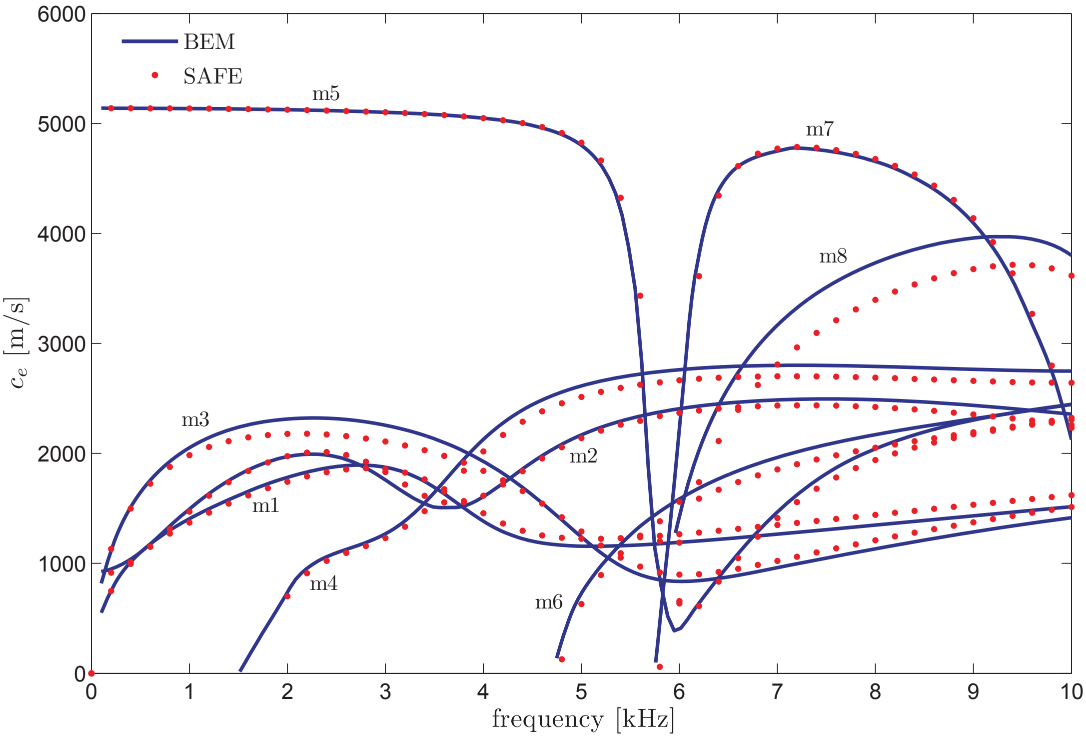

Figure 3.12: Energy velocity dispersion curves for the viscoelastic steel BS11-113A rail.

waves propagate without geometric attenuation is given by the Rayleigh wave speed c_R [Biot, 1952], the associated dispersion curves can be obtained by choosing the contour $\Gamma(\kappa_z)$ such that the real part of the axial wavenumber is always included in the range $\mathrm{Re}(\kappa_S) \leq \mathrm{Re}(\kappa_z) \leq \mathrm{Re}(\kappa_R)$, where $\kappa_R \approx \kappa_S (0.87 + 1.12\tilde{\nu}) / (1 + \tilde{\nu})$ denotes the Rayleigh wavenumber [Rose, 2004].

Note that, for this particular choice, the only singular point in the κ_z-plane is given by the shear wavenumber κ_S, which can be easily excluded from the complex region with an appropriate deformation of the contour $\Gamma(\kappa_z)$, while the operator $\mathbf{Z}(\kappa_z, \omega)$ does not present discontinuities in the included complex region. Moreover, only a small number of integration points is required, since for $\mathrm{Re}(\kappa_z) > \mathrm{Re}(\kappa_S)$ both the real and imaginary part of the displacement Green's functions are strongly attenuated with the amplitude approaching zero, so that in this subregion the matrix $\mathbf{Z}(\kappa_z, \omega)$ is almost constant, except near the bulk shear wavenumber.

The normalized dispersion curves in Fig. 3.19(a) and 3.19(b) have been extracted using a mesh of 150 boundary elements and a rectangular contour with a total of 120 integration points and limited by $1.0 \leq \kappa_z/\kappa_S \leq 1.1$. The rank and residual tolerances

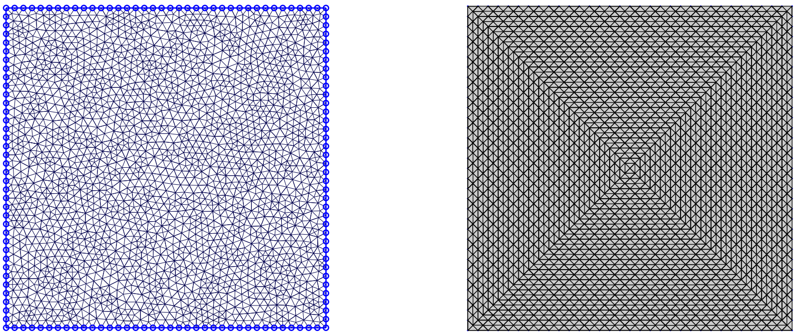
(a) (b)

Figure 3.13: (a) Boundary element mesh with internal cells subdivision and (b) SAFE mesh of the square bar.

have been set to $\mathrm{tol}_{rank} = -4.0$ and $\mathrm{tol}_{res} = 5.0 \times 10^{-5}$. The viscoelastic medium is defined through its complex Poisson's ratio $\tilde{\nu} = 0.3 - \mathrm{i}4.5 \times 10^{-4}$.

As discussed by Boström and Burden [1982], the flexural mode $m = 1$ is the only one existing in the whole frequency range, while the longitudinal mode $m = 0$ and the flexural modes $m = 2, 3, 4$ have a cutoff at $\kappa_z = \kappa_S$. From this value, each mode approaches asymptotically the Rayleigh wavenumber $\mathrm{Re}\left(\kappa_R\right)$ which, for the case $\mathrm{Re}\left(\tilde{\nu}\right) = 0.3$ is $\mathrm{Re}\left(\kappa_R\right)/\mathrm{Re}\left(\kappa_z\right) = 1.0779$. The dispersion curves for the real part of the axial wavenumber agree with those presented by Boström and Burden [1982], while the corresponding attenuation curves due to material damping are reported in Fig. 3.19(b). At the best of the authors knowledge, these curves were not previously reported in the literature. As expected, the attenuations of the various modes approach asymptotically the attenuation of the Rayleigh wave, which is approximately $\alpha_R/\alpha_S = 1.0178$.

It is worth noting that, despite the exclusion of the shear wavenumber from the contour region, the algorithm is able to extract a root which is very close to the shear wavenumber itself when $\mathrm{Re}\left(\kappa_S\right) a < 1$, although it is not shown in Fig. 3.19(a) and 3.19(b). In fact, for these values of the dimensionless frequency, the solution for the $m = 1$ is very close to the shear wavenumber and it is correctly detected by the algorithm. However, since the root lies in proximity of a singular point, its residual given by Eq. (3.82) is poor, and the root itself is consequently discarded by the residual test.

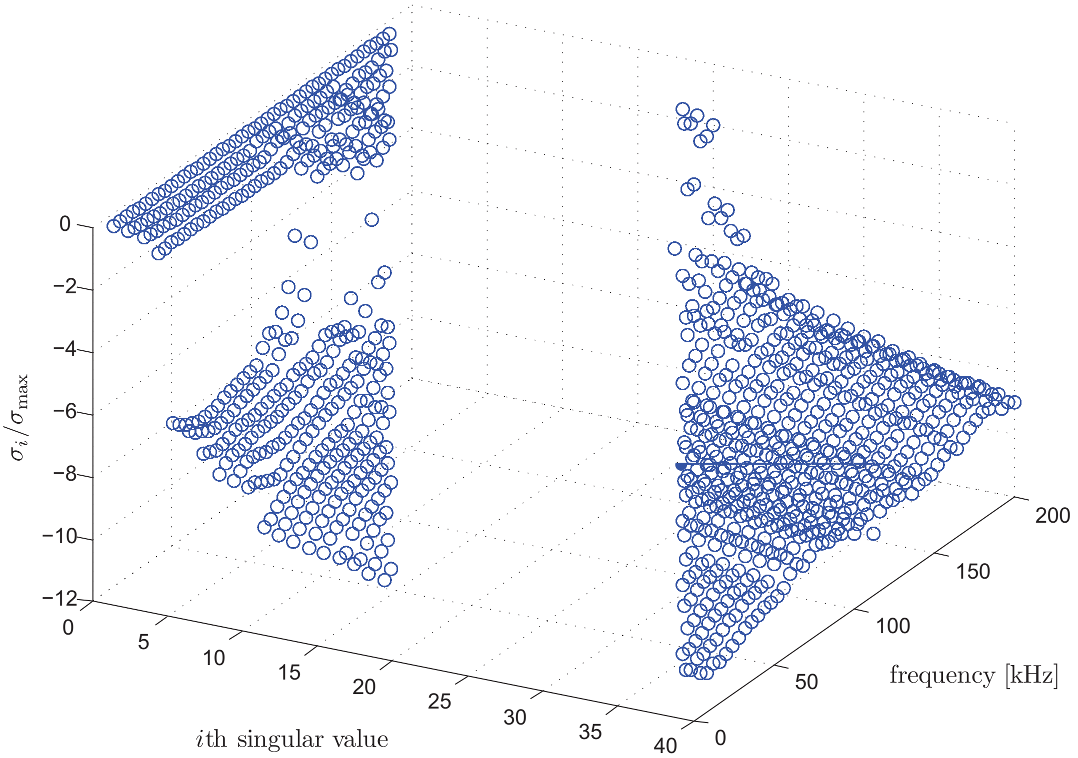

Figure 3.14: Singular values distribution after 50 frequency steps for the square bar in Sec. 3.10.2.

3.11.2 Square cavity in a viscoelastic full-space

In this numerical example, a square cavity with side length equal to $2a$ is considered. The cavity is immersed in a viscoelastic medium with complex Poisson's ratio $\tilde{\nu} = 0.3 - \mathrm{i}4.5 \times 10^{-4}$. The dispersion curves for the real part of the axial wavenumber and the attenuation are depicted in Fig. 3.20(a) and 3.20(b), respectively. The curves have been obtained using a mesh of 146 semi-isoparametric linear elements, while the scheme used for the contour algorithm is the same of Sec. 3.11.1.

As expected, the dispersive behaviour of the guided modes is very similar to that observed for the circular cavity for both the real part of the axial wavenumber and the attenuation. Furthermore, all the normal modes approach asymptotically with their real and imaginary parts the Rayleigh wavenumber. The normal modes appear as grouped in separate families. The first family is formed by the first flexural mode F_1, which does not have a cutoff, the first longitudinal mode L_1 and the first screw mode S_1^1. The second family is formed by the screw mode S_1^2, the flexural mode F_2

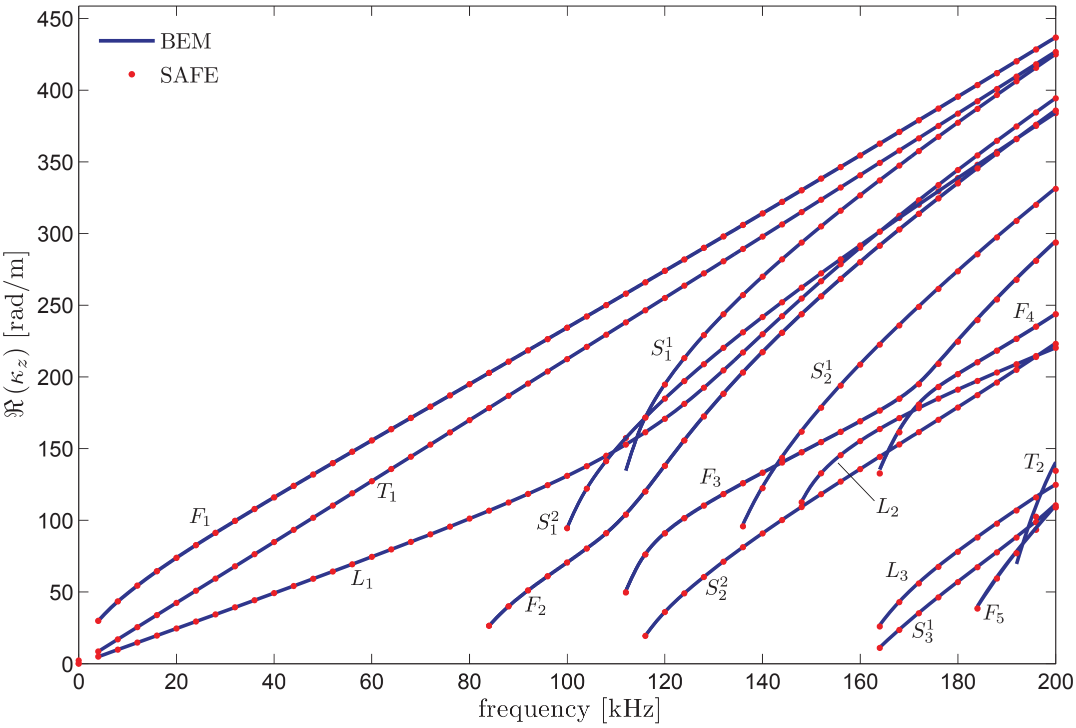

Figure 3.15: Real wavenumber dispersion curves for the viscoelastic steel square bar of 2.0 mm side length.

and the first torsional mode T_1. Finally, the third family includes the screw mode S_2^2, the flexural mode F_3 and the screw mode S_1^2.

As previously observed for the rail and the square bar, the separation reduces at the cutoff frequencies. In these cases, some eigensolutions may result slightly less accurate (see mode F_3). Finally, a moderate numerical instability in the attenuations can be observed for the first family of normal modes in the dimensionless frequency range $8.0 \div 9.0$. Note that this frequency range corresponds in fact to the cutoffs for the modes S_2^2 and F_3.

3.12 Conclusions

in this chapter, a 2.5D regularized Boundary Element formulation has been proposed to compute the dispersion curves for isotropic linear viscoelastic waveguides of arbitrary cross-section. The attenuation has been taken into account by adding an imaginary part to the axial wavenumber vector, which has been considered parallel to the real (propagative) component. The dispersive parameters have been extracted by solving a

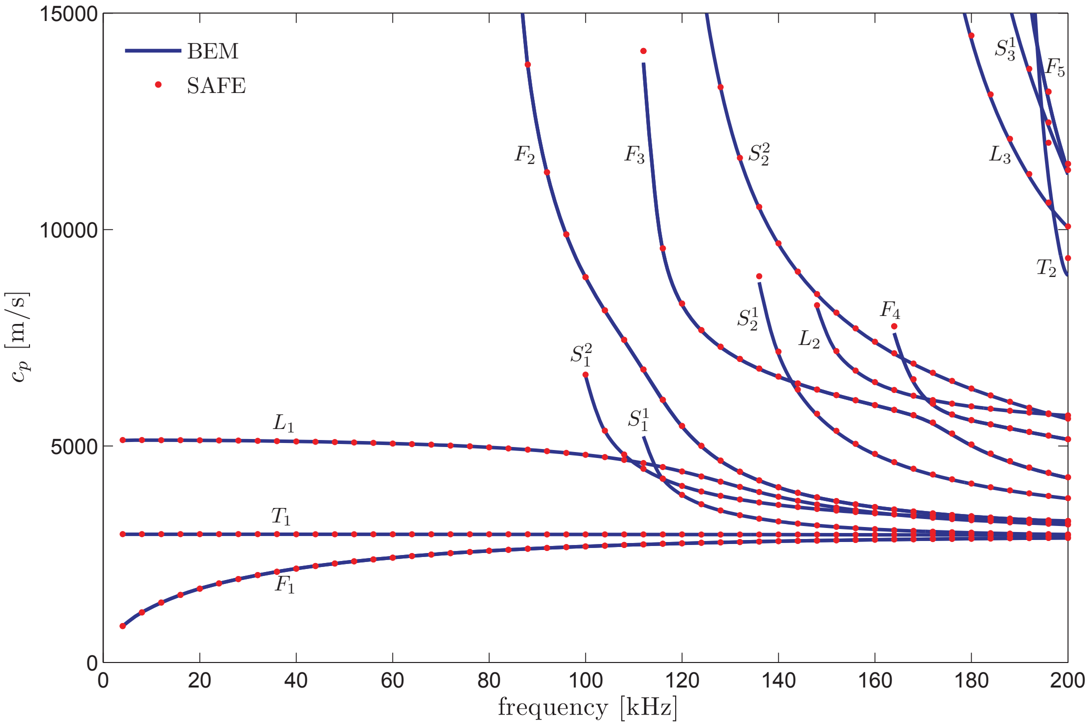

Figure 3.16: Phase velocity dispersion curves for the viscoelastic steel square bar of 2.0 mm side length.

nonlinear eigenvalue problem in absence of external applied tractions using the contour integral algorithm proposed by Beyn [2012]. The energy velocity has been obtained in post-processing using the method of the cells. Due to the singular characteristics and the multivalued nature of the Green's functions, the Sommerfeld branch cuts have been introduced and the signs for the real and imaginary parts of the axial wavenumber have been selected in order to satisfy both the Sommerfeld radiation condition and the holomorphicity requirement for the resolvent operator inside the complex region enclosed by the contour. Numerical tests performed on a rail cross-section and a square cross-section have shown that the real part of the eigensolution always matches the corresponding solution obtained via the SAFE method, while some larger discrepancies have been observed for both the attenuation and the energy velocity.

The dispersion data extracted for surface normal modes propagating along cylindrical cavities of circular cross-section are in very good agreement with those available in the literature. As expected with the introduction of the material damping, the attenuation dispersion curves of the surface normal modes approach the value of the attenuation of the non-dispersive Rayleigh waves. A similar behaviour has been ob-

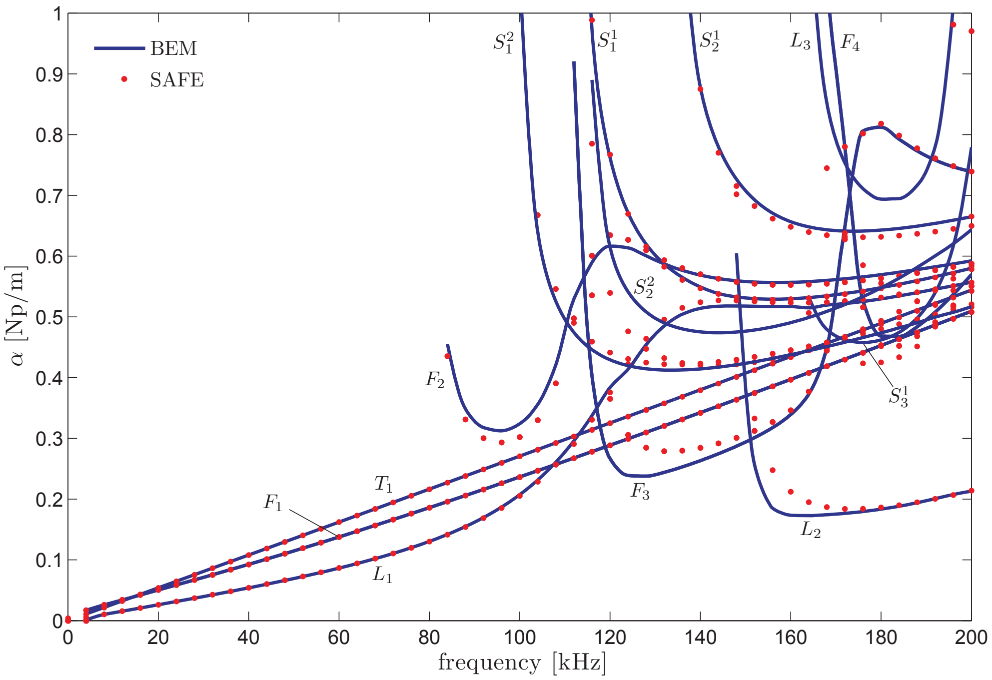

Figure 3.17: Attenuation dispersion curves for the viscoelastic steel square bar of 2.0 mm side length.

tained for a square cavity, where the normal modes appear to be grouped into families.

In line with other works [François et al., 2010; Rieckh et al., 2012], the proposed method could be equally used in the dispersion analysis of cavities embedded in layered media, providing that the fundamental solutions for the isotropic elastic full space are replaced by a numerically computed solution for a layered halfspace.

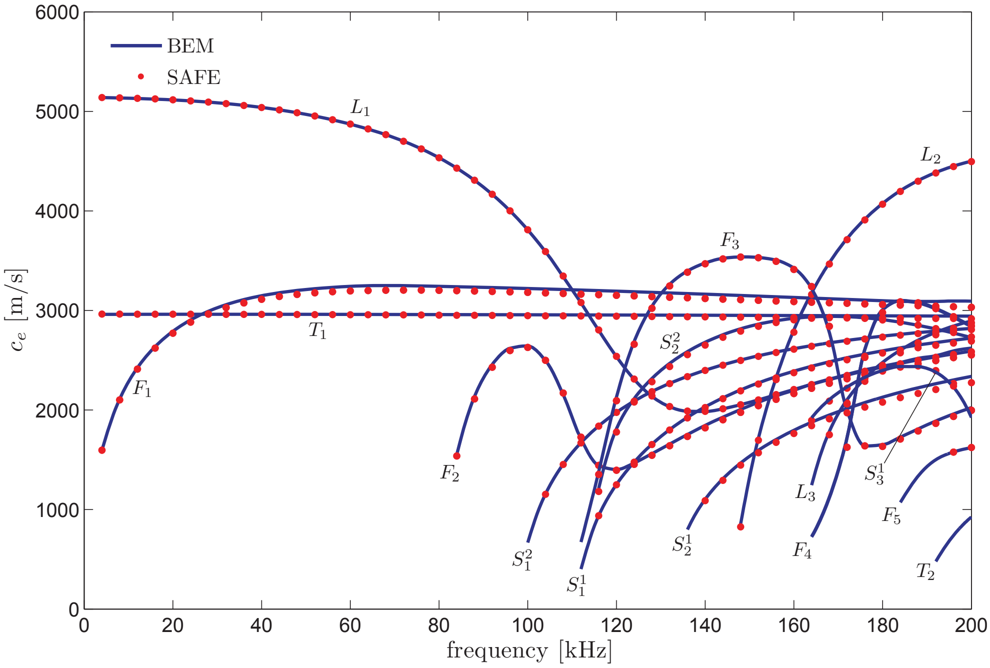

Figure 3.18: Energy velocity dispersion curves for the viscoelastic steel square bar of 2.0 mm side length.

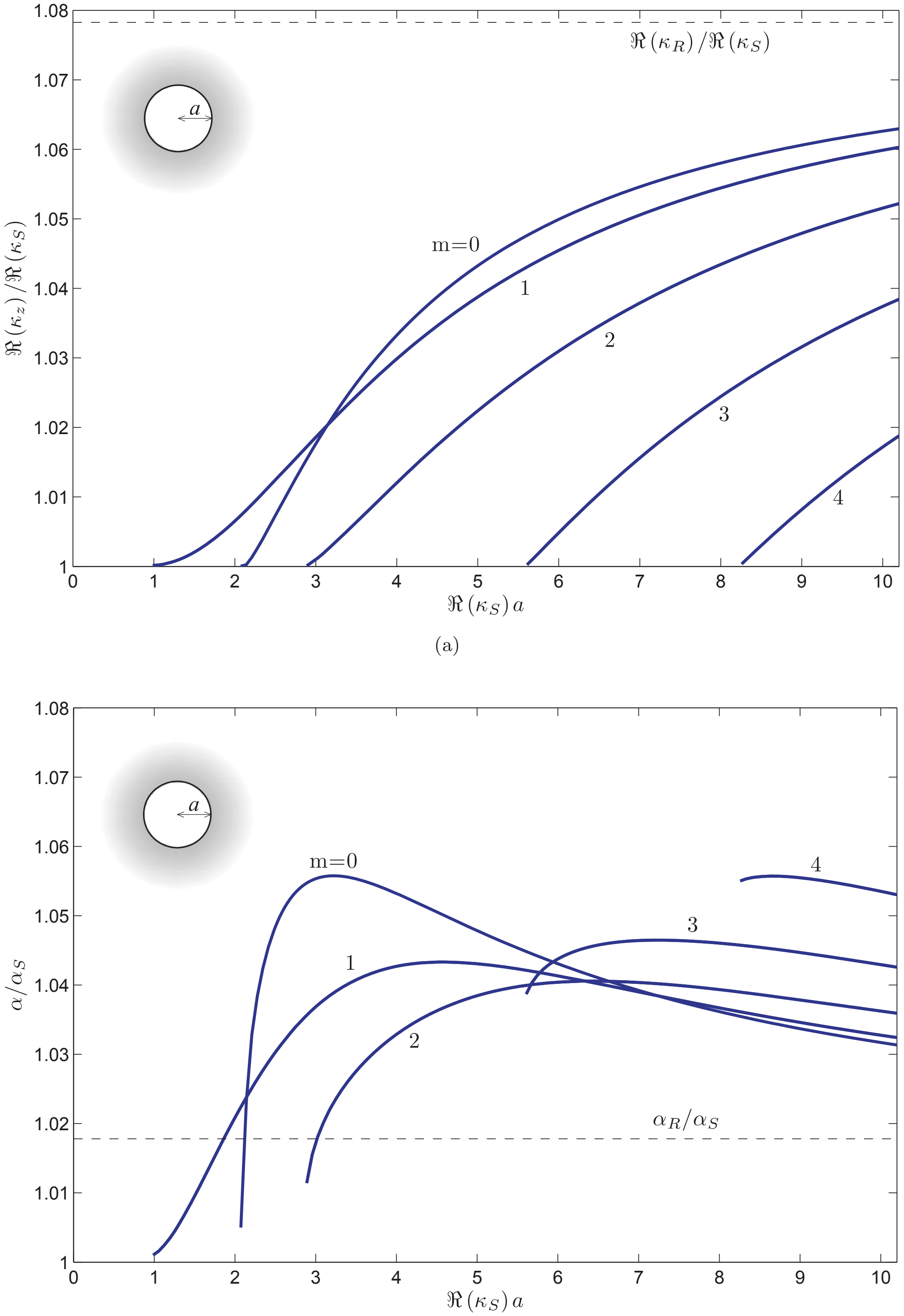

(a)

(b)

Figure 3.19: Dimensionless (a) real axial wavenumbers and (b) attenuations versus dimensionless frequency for $\tilde{\nu} = 0.3 - \mathrm{i}4.5 \times 10^{-}4$. The normal modes are identified as in Boström and Burden [1982].

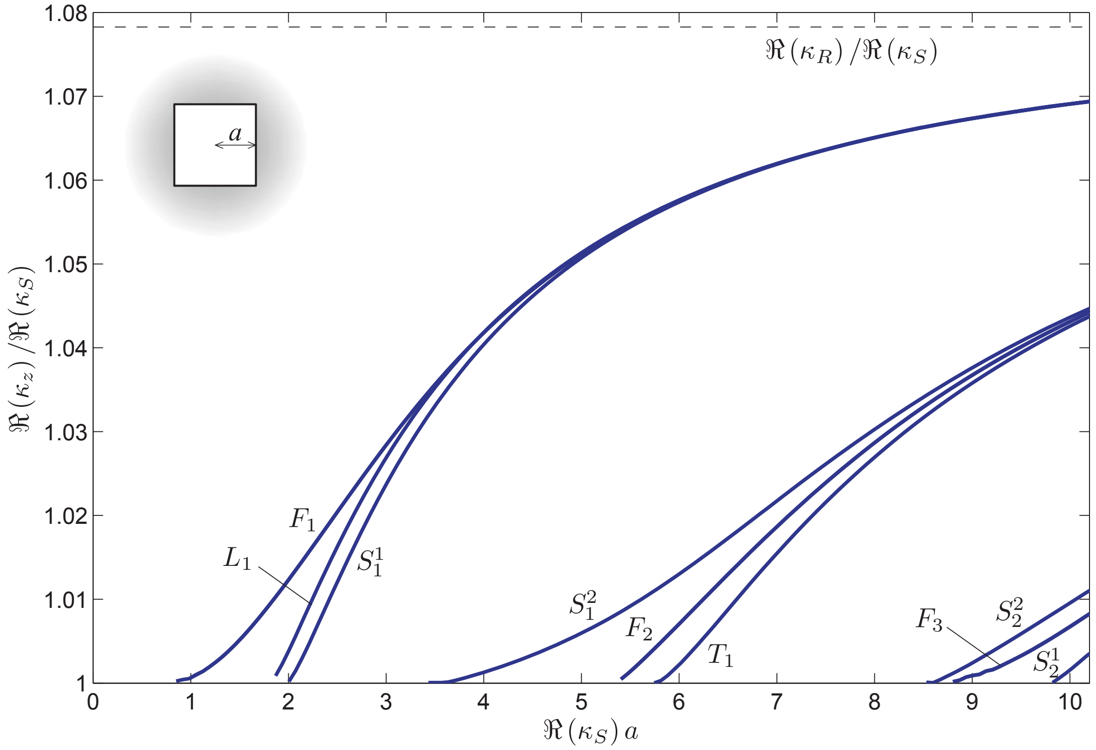

(a)

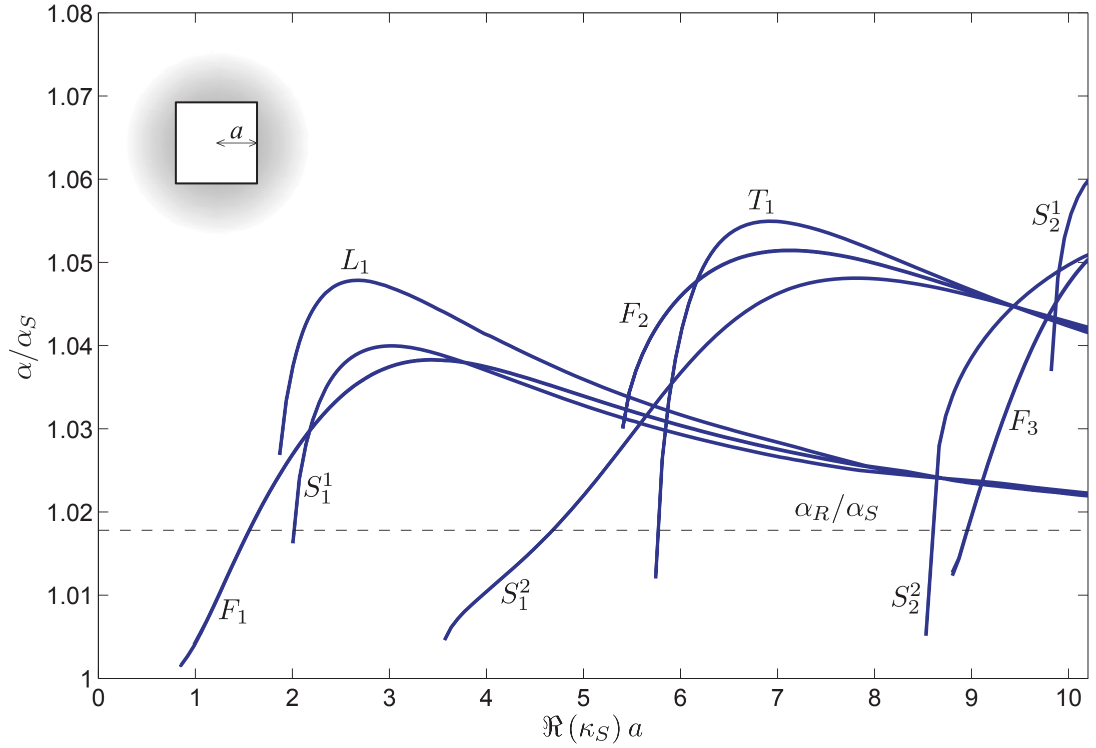

(b)

Figure 3.20: Dimensionless (a) real axial wavenumbers and (b) attenuations versus dimensionless frequency for $\tilde{\nu} = 0.3 - \mathrm{i}4.5 \times 10^{-4}$.

Chapter 4

Leaky Guided Waves in waveguides embedded in solid media: coupled SAFE-2.5D BEM formulation

4.1 Sommario

In questo capitolo viene presentata una formulazione accoppiata SAFE-2.5D BEM per il calcolo delle caratteristiche di dispersione di onde guidate che si propagano in guide d'onda viscoelastiche immerse in mezzi isotropi, viscoelastici ed infinitamente estesi (leaky guided waves).

La natura dispersiva delle leaky guided waves è stato studiato in letteratura utilizzando metodi analitici [Lowe, 1992; Pavlakovic, 1998; Simmons et al., 1992; Viens et al., 1994] e metodi semi-analitici agli elementi finiti accoppiati con metodi delle regioni di assorbimento [Castaings and Lowe, 2008], elementi semi-analitici infiniti [Jia et al., 2011] e Perfectly Matched Layers (PML) [Treyssède et al., 2012]. Tuttavia, mentre i metodi analitici sono applicabili solamente a guide d'onda di geometrie semplici, i metodi semi-analitici presentano delle difficoltà nella modellazione del campo irradiato a causa di riflessioni spurie (metodo delle regioni di assorbimento), arbitrarietà nella scelta delle funzioni di forma (elementi infiniti semi-analitici) o scelta delle funzioni di smorzamento (PML).

La formulazione accoppiata SAFE-2.5D BEM descritta in questo capitolo consente di superare i problemi dei metodi analitici e di quelli numerici sopra citati. Infatti, mentre il metodo SAFE consente di rappresentare guide d'onda immerse di geometrie e caratteristiche meccaniche complesse, mediante il BEM è possibile descrivere accuratamente il campo irradiato nel mezzo solido circostante.

In particolare, la formulazione SAFE differisce da quella descritta nel Capitolo 2 nell'utilizzo di elementi finiti quadratici in luogo di quelli lineari, mentre l'effetto di uno stato di stress iniziale non viene considerato. Poichè l'accoppiamento delle regioni SAFE e BEM prevede la compatibilit degli spostamenti e la continuit delle trazioni lungo all'interfaccia, anche nella formulazione BEM viene fatto uso di elementi quadratici. Inoltre, le funzioni di Green 2.5D utilizzate nel Capitolo 3 vengono sostituite da un set di funzioni simili ma che consentono un risparmio in termini di tempi computazionali. Le singolarità delle funzioni nucleo negli integrali di contorno vengono trattate utilizzando la procedura di regolarizzazione descritta nel Capitolo 3.

Poichè il numero di gradi di libertà del dominio discretizzato BEM generalmente inferiore a quello del dominio discretizzato SAFE, l'accoppiamento delle due formulazioni viene eseguito trasformando il dominio BEM in un singolo elemento finito avente lo stesso numero di gradi di libertà del dominio originale. La matrice di impedenza del mezzo circostante viene pertanto trasformata in una matrice di rigidezza dinamica equivalente, la quale è successivamente assemblata nel sistema SAFE.

L'equazione d'onda ottenuta si configura come un problema non lineare agli autovalori. Tale problema viene risolto utilizzando il metodo degli integrali di contorno proposto da Beyn [2012] e descritto nel Capitolo 3. Date le profonde differenze tra la natura delle onde guidate di tipo leaky e quelle che si propagano in guide d'onda immerse nel vuoto, una nuova analisi delle superfici di Riemann viene presentata, nella quale si tiene conto delle condizioni aggiuntive di interfaccia (legge di Snell generalizzata).

I risultati ottenuti con il metodo proposto vengono dapprima validati con due risultati noti in letteratura, nei quali solamente geometrie cilindriche vengono considerate. Infine, le potenzialità del metodo proposto vengono dimostrate attraverso tre esempi numerici di interesse pratico, presentati in letteratura per la prima volta.

4.2 Introduction and literature review

As discussed in previous chapters, the dispersion properties of guided waves in traction-free waveguides can be efficiently computed by means of analytical methods [Chaki and Bourse, 2009; Knopoff, 1964; Lowe, 1995; Pavlakovic et al., 1997; Pavlakovic, 1998; Shin and Rose, 1999] and finite element-based methods [Bartoli et al., 2006; Chen and Wilcox, 2007; Gavric, 1995; Hayashi et al., 2003, 2006; Loveday, 2009; Sorohan et al., 2011; Treyssède, 2008].

The 2.5D BEM formulation described in Chapter 3 also assumes that the boundary of the waveguide is in contact with vacuum, so that only reflection and mode conversion of bulk waves occur at the solid-vacuum interface.

However, in several circumstances waveguides are embedded in solid media. These are, for examples, the cases of tendons, foundation piles, buried pipes, railways or embedded fibers.

In these cases, guided modes traveling with phase speed greater than the bulk speed of the surrounding media radiates energy into it. As a consequence, inspection ranges are generally reduced since the energy radiated in the surrounding media causes high attenuation rates of the guided modes (leaky modes).

The knowledge of dispersion properties of leaky modes is therefore fundamental in NDE testing of civil, mechanical and aerospace structures and mathematical tools able to describe waveguides with different geometric and mechanical characteristics are needed. In this context, several studies can be found in literature involving simple geometries, i.e. plate and cylindrical structures, in which analytical methods have been extensively applied.

A comprehensive study of matrix techniques for the computation of dispersion curves in free, embedded and immersed plates can be found in the work of Lowe [1995]. The propagation of leaky Lamb waves in plates embedded in solids have been studied by Dayal and Kinra [1989, 1991] and Lowe [1992].

The propagation of non-leaky guided waves in elastic circular waveguides embedded in elastic media have been investigated by Parnes [1981, 1982] and Kleczewski and Parnes [1987]. Dispersion relations for leaky modes in elastic circular rods embedded in isotropic elastic solids have been extracted by Thurston [1978], Simmons et al. [1992] and Viens et al. [1994] using analytic dispersive equations. In their work, Nayfeh and Nagy [1996] have applied the Transfer Matrix Method to investigate the propagation of axisymmetric waves in coaxial layered anisotropic fibers embedded in solids and immersed in fluids. General studies on wave propagation in transversely isotropic and homogeneous anisotropic circular rods immersed in fluids have been conducted by Dayal [1993], Nagy [1995], Berliner and Solecki [1996a,b] and Ahmad [2001].

The dispersion properties of leaky guided waves in both embedded and immersed cylindrical structures have been in depth analyzed by Pavlakovic [1998] using the Global Matrix Method (GMM). This method has been used next to perform numerical analyses and support experimental investigations involving free pipes with defects [Lowe et al., 1998], buried pipes [Long et al., 2003b], embedded circular bars [Pavlakovic et al., 2001] and embedded tendons and bolts Beard et al. [2003]; Beard and Lowe [2003]. An analytical method has been proposed by Laguerre et al. [2007] to predict dispersion curves and to interpret the ultrasonic transient bounded-beam propagation in a solid cylindrical waveguide embedded in a solid medium.

Although very attractive for simple geometries, analytical approaches are generally unsuitable to extract dispersion properties for waveguides with irregular cross-section and, in these cases, one must resort to numerical methods.

Due to the capability to represent domains with different materials and arbitrary geometries while forming well posed polynomial eigenvalue problems, the SAFE method has been also extended in recent years to wave propagation problems involving unbounded domains. In their work, Castaings and Lowe [2008] have used a SAFE mesh to discretize both the waveguide and the embedding medium. The material surrounding the waveguide was simulated by introducing a finite absorbing region of length proportional to the largest radial wavelength of the existing leaky waves. The method eliminates the well known problem of non-physical reflections which would arise using a finite mesh to model the unbounded surrounding domain. However, this method may require very large meshes to properly model waves radiating in the surrounding media and guided modes with high rates of energy confined in the embedded cross-section need to be selected from a large set of eigensolutions.

A hybrid SAFE formulation has been proposed by Jia et al. [2011] to study double layer hollow cylinders embedded in infinite media. In this study, the unbounded medium has been discretized by means of infinite elements, which overcomes the problem of energy reflection. However, the capability of infinite elements to correctly represent the physics of leaky waves is strongly related to the choice of the elements shape functions. Moreover, complicated geometries, such as H shaped beams, may result difficult to treat.

In their work, Lin et al. [2011] have considered the presence of two isotropic elastic half spaces at the top and bottom interface of a SAFE-modeled layer by introducing appropriate analytical boundary conditions. The analytical boundary conditions have been adopted in order to satisfy the Snell's law for radiated longitudinal and shear waves. Only solutions relative to evanescent wavefields in the surrounding medium have been considered in this study.

A further numerical technique that allows to model radiated waves without reflections has been proposed by Treyssède et al. [2012] by coupling the SAFE method with the Perfectly Matched Layer (PML) method. Using the PML, leaky modes are defined through analytic extensions in terms of complex spatial coordinates. Although this method allows to preserve the original dimension of the problem as well as the nature of the dispersive wave equation, the radiation efficiency strictly depends on the choice of the complex-valued function used to represent geometric decay inside the PML domain.

A possible alternative is represented by the Boundary Element Method (BEM). Unlike FE-based formulations, the BEM allows to describe the unbounded surrounding domain by means of a boundary mesh only. Moreover, since the weight functions are represented by the fundamental solutions of the dynamic problem (Green's function), no approximations are introduced in the definition of the radiated wavefield.

In recent years, different coupled FEM-BEM formulations have been proposed to investigate the wave propagation in waveguide-like structures. Such formulations are sometimes referred in literature as the wavenumber finite-boundary element method [Sheng et al., 2005, 2006], the waveguide finite-boundary element method [Nilsson et al., 2009] or the 2.5D finite-boundary element method [Costa et al., 2012; François et al., 2010]. While most of these studies are focused on forced or induced vibrations problems, minor attention has been dedicated to the study of dispersive characteristics of guided waves, especially when attenuation is involved.

Some exceptions are represented by the work of Tadeu and Santos [2001] and Zengxi et al. [2007], which have adopted a 2.5D BEM for the computation of dispersion relations in fluid filled boreholes. However, attenuation information is not provided in these works. More recently, Nilsson et al. [2009] have proposed a waveguide FEM-BEM formulation to study the radiation efficiency of open and embedded rails. In such work, dispersion relations for radiating modes have been obtained by considering complex wavenumbers, thus taking into account the amplitude decay due to attenuation. However, since the acoustic impedance mismatch between the rail and the air was very high, the authors have considered in their model only the influence of the rail on the fluid vibrations and not the one of the air on the rail (the model is not fully coupled).

In this chapter, the SAFE method is coupled with the regularized 2.5D BEM to extract dispersion curves for viscoelastic waveguides of arbitrary cross-section embedded in viscoelastic isotropic materials. With respect to the SAFE formulations that use absorbing regions, infinite elements and PMLs, the proposed SAFE-2.5D BEM formulation represents exactly the radiated wavefield from waveguides of arbitrary cross-section while preserving the dimension of the SAFE problem and without the need of special complex functions. The complex axial wavenumbers and the corresponding wavestructures are computed from a nonlinear eigenvalue problem solved via a contour the Contour Integral Method proposed by [Beyn, 2012] and described in Sec. 3.8.1. The complex poles associated to leaky and evanescent modes are obtained by choosing the arguments of the wavenumbers in the embedding medium consistently with the nature of the radiated waves and removing points of singularities and discontinuities from the complex plane of the axial wavenumber.

The method is first validated against available results obtained, for embedded circular bars, by means of alternative approaches [Castaings and Lowe, 2008; Pavlakovic et al., 2001]. Next, dispersion curves are extracted for a viscoelastic square steel bar embedded in viscoelastic grout and for a viscoelastic HP200 steel pile embedded in a viscoelastic soil. To the best of author's knowledge, these cases are never been studied in literature. The proposed method can be useful to understand the physical behaviour of leaky guided waves as well as to design testing conditions in GUW-based inspections and experiments involving embedded beams or foundation piles.

4.3 Wave equation

In this section, the guided wave equation is derived for the system with translational invariant geometric and mechanical properties of Fig. 4.1. The wavenumber-frequency dependence is assumed in the form

$$\exp\left[\mathrm{i}\left(\kappa_z z - \omega t\right)\right], \tag{4.1}$$

from which, the following conditions

$$\mathrm{Re}\left(\kappa_z\right) = \left|\mathbf{k}_z^{\mathrm{Re}}\right| > 0, \qquad \mathrm{Im}\left(\kappa_z\right) = \left|\mathbf{k}_z^{\mathrm{Im}}\right| > 0, \tag{4.2}$$

must be satisfied in order to ensure the amplitude decay of guided modes propagating in the positive direction of the z-axis (cf. Sec. 2.6.1).

As seen in Chapter 2, the longitudinal invariance allows to describe the three-dimensional wave propagation problem in the $x - y$ plane, while the third dimension is accounted by contraction of any z-dependent scalar or vectorial field in the axial wavenumber domain through the spatial Fourier transform in Eq.2.35. In particular, the waveguide cross-section of area Ω_s is discretized using the SAFE method while the external medium of infinite extent Ω_b is modeled via a 2.5D regularized boundary integral formulation. The in-plane position vector $\mathbf{x} = [x,\ y]^{\mathrm{T}}$ ($\mathbf{x} \in \Omega_s \cup \Omega_b$) is used to denote a generic point located at the cross-section of axial coordinate $z = 0$.

The SAFE and BEM meshes are defined with coincident nodes and matching shape functions at the coupling interface

$$\partial\Omega = \partial\Omega_s = \partial\Omega_b,$$

where compatibility of displacements and equilibrium of tractions are enforced through the relationships

$$\mathbf{u}\left(\mathbf{x}, z, t\right)|_{\partial\Omega_s} = \mathbf{u}\left(\mathbf{x}, z, t\right)|_{\partial\Omega_b}, \tag{4.3}$$

$$\mathbf{t}\left(\mathbf{x}, z, t\right)|_{\partial\Omega_s} = -\mathbf{t}\left(\mathbf{x}, z, t\right)|_{\partial\Omega_b}, \tag{4.4}$$

denoting with $\mathbf{u}\left(\mathbf{x}, z, t\right) = [u_1,\ u_2,\ u_3]^{\mathrm{T}}$ the displacements vector and $\mathbf{t}\left(\mathbf{x}, z, t\right) = [t_1,\ t_2,\ t_3]^{\mathrm{T}}$ the tractions vector. The minus on the right hand side of Eq. (4.4) accounts for the opposite sign of the outward normals of the SAFE and BEM regions at the boundary point $\mathbf{x}$, i.e. $\mathbf{n}\left(\mathbf{x}\right)|_{\partial\Omega_s} = -\mathbf{n}\left(\mathbf{x}\right)|_{\partial\Omega_b}$ (see Fig. 4.1).

The equilibrium equation for a waveguide embedded in an infinite medium can be obtained in the wavenumber-frequency domain by following the same procedure described in Chapter 2. Under the hypotheses of (i) translational invariant mechanical characteristics, (ii) initial stress-free state and (iii), absence of body forces, the equilibrium equation (2.44) reduces to

$$\begin{aligned} &\omega^2 \int_{\Omega_s} \delta\mathbf{u}^{\mathrm{T}} \rho\left(\mathbf{x}\right) \mathbf{u} \mathrm{d}x\mathrm{d}y - \int_{\Omega_s} \left(\delta\boldsymbol{\epsilon}\left(\mathbf{u}\right)\right)^{\mathrm{T}} \tilde{\mathbf{C}}\left(\mathbf{x}, \omega\right) \boldsymbol{\epsilon}\left(\mathbf{u}\right) \mathrm{d}x\mathrm{d}y \\ &+ \int_{\partial\Omega_s} \delta\mathbf{u}^{\mathrm{T}} \left[\mathbf{t}_s\left(\mathbf{x}, \kappa_z, \omega\right) - \mathbf{t}_b\left(\mathbf{x}, \kappa_z, \omega\right)\right] \mathrm{d}s = 0, \end{aligned} \tag{4.5}$$

where $\rho\left(\mathbf{x}\right)$ is the material density at point $\mathbf{x} \in \Omega_s$, $\boldsymbol{\epsilon}\left(\mathbf{u}\right)$ is the vector of the independent linear strain components, defined in Eq. (2.7), and $\tilde{\mathbf{C}}\left(\mathbf{x}, \omega\right)$ is the fourth order tensor of complex moduli defined as in Eqs. (2.36) and (2.72). In the derivation of Eq. (4.5), the vector of surface loads $\mathbf{t}_c\left(\mathbf{x}, \kappa_z, \omega\right)$ appearing in Eq. (2.44) has been replaced by

$$\mathbf{t}_c\left(\mathbf{x}, z, \omega\right) = \mathbf{t}_s\left(\mathbf{x}, \omega\right) - \mathbf{t}_b\left(\mathbf{x}, z, \omega\right), \tag{4.6}$$

where $\mathbf{t}_s\left(\mathbf{x}, \kappa_z, \omega\right)$ is the vector of the external surface loads applied at the interface while $\mathbf{t}_b\left(\mathbf{x},\kappa_z,\omega\right)$ is the vector of the interface tractions resulting from the mutual interaction of the waveguide with the surrounding medium.

The strategy adopted to solve Eq. (4.5) is based on a SAFE discretization of the embedded waveguide and the computation of the vector of interface tractions $\mathbf{t}_b\left(\mathbf{x},\kappa_z,\omega\right)$ by means of a 2.5D BEM formulation. Compared to well stated analytical methods such as the Transfer Matrix Method (TMM) or the Global matrix Method (GMM), this approach allows to model embedded waveguides of any geometry and material through the SAFE. At the same time, the BEM allows to exactly compute the radiated wavefield, which is the main drawback of FE-based techniques.

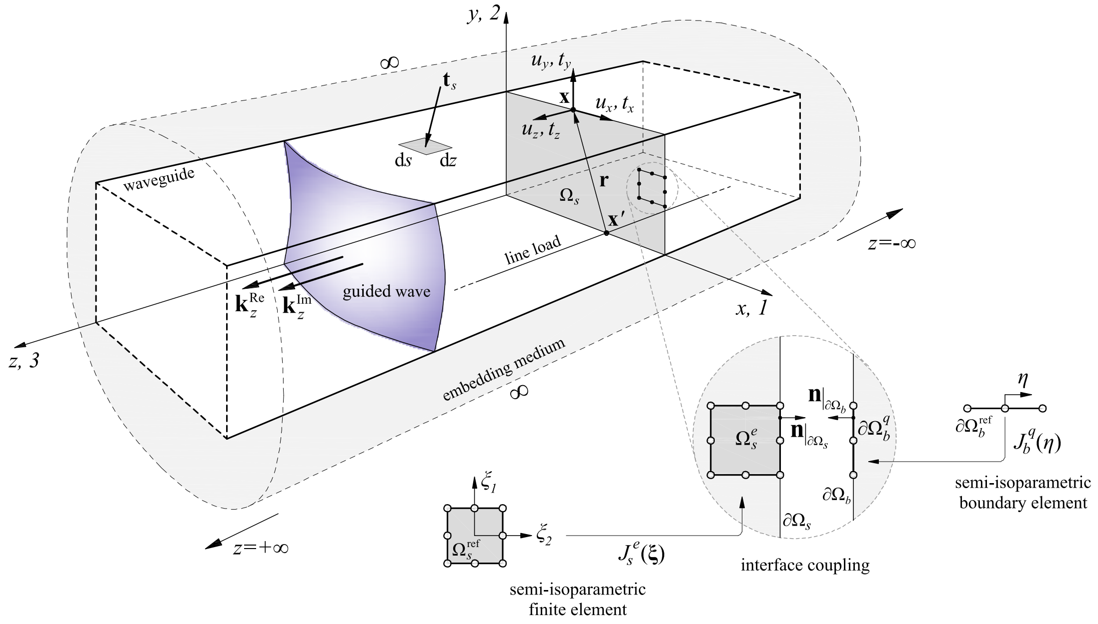

Figure 4.1: Analytical model of the embedded waveguide.

4.4 SAFE model of the embedded waveguide

The domain Ω_s is discretized into a number N_{el} of quadratic semi-isoparametric finite elements of area Ω_s^e, with 3 degrees of freedom per node associated to the three displacement components u_i. The displacement vector at point $\mathbf{x} \in (\Omega_s^e \cup \partial\Omega_s^e)$ is approximated as

$$\mathbf{u}(\boldsymbol{\xi}, z, t) = \mathbf{N}(\boldsymbol{\xi})\, \mathbf{q}^e(z, t)\,, \tag{4.7}$$

where $\mathbf{N}(\boldsymbol{\xi})$ is the matrix collecting the quadratic shape functions for the parent element of area Ω_s^{ref} in the natural reference system, $\boldsymbol{\xi} = [\,\xi_1,\, \xi_2\,]^{\mathrm{T}}$ is the vector of the natural coordinates defined on Ω_s^{ref}, and $\mathbf{q}^e(z, t)$ is the vector of nodal displacements. A list of various quadratic elements used in this study is given in Table4.1. From Eq. (4.7), using the space-time Fourier transform in Eq. (2.35) the vector of linear strain components $\boldsymbol{\epsilon}(\mathbf{u})$ in the (κ_z, ω) domain is obtained as (cf. Eq.2.49)

$$\boldsymbol{\epsilon}(\boldsymbol{\xi}, \kappa_z, \omega) = \left[\mathscr{B}_{xy}(\boldsymbol{\xi}) + \mathrm{i}\kappa_z \mathscr{B}_z(\boldsymbol{\xi})\right] \mathbf{q}^e(\kappa_z, \omega)\,, \tag{4.8}$$

in which the compatibility operators $\mathscr{B}_{xy}(\boldsymbol{\xi})$ and $\mathscr{B}_z(\boldsymbol{\xi})$ are expressed as in Eqs. (2.50) and (2.51).

Following the analysis in Chapter 3, the complex tensor of viscoelastic moduli $\tilde{\mathbf{C}}^e(\boldsymbol{\xi}, \omega)$ is defined so that the material attenuation vectors for both longitudinal and shear bulk waves in the embedded waveguide and surrounding medium are assumed perpendicular to their wavefronts. Physically, this means that the directions of propagation and maximum decay due to material damping are mutually parallel. The complex Lamé constants can be expressed as

$$\begin{gathered}\tilde{\lambda}(\omega) = \rho\left[\tilde{c}_L^2(\omega) - 2\tilde{c}_S^2(\omega)\right], \quad \tilde{\mu}(\omega) = \rho\tilde{c}_S^2(\omega)\,, \\ \tilde{c}_L(\omega) = \frac{c_L}{1 + \mathrm{i}\beta_L(\omega)/2\pi}, \quad \tilde{c}_S(\omega) = \frac{c_S}{1 + \mathrm{i}\beta_S(\omega)/2\pi},\end{gathered} \tag{4.9}$$

from which one derives $\tilde{C}^e_{ijkm}(\omega) = \tilde{\lambda}(\omega)\,\delta_{ij}\delta_{km} + \tilde{\mu}(\omega)\left(\delta_{ik}\delta_{jm} + \delta_{im}\delta_{jk}\right)$.
Substituting Eqs. (4.7), (4.8) into Eq. (4.5) and using Eq. (4.9), algebraic manipulations lead to the following N-dimensional linear system of equations in the (κ_z, ω) domain

$$\left[\kappa_z^2\mathbf{K}_3 + \mathrm{i}\kappa_z\left(\mathbf{K}_2 - \mathbf{K}_2^{\mathrm{T}}\right) + \mathbf{K}_1 - \omega^2\mathbf{M}\right]\mathbf{Q}(\kappa_z, \omega) + \mathbf{F}_b(\kappa_z, \omega) = \mathbf{F}_s(\kappa_z, \omega)\,, \tag{4.10}$$

where the different matrix operators, which result from the application of a finite element assembling procedure for all the N_{el} elements of the mesh, take the following

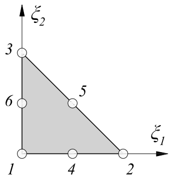	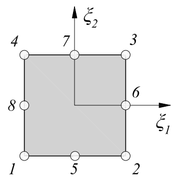	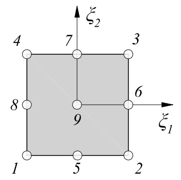
$N_1 = \zeta\left(2\zeta - 1\right)$	$N_1 = \frac{1}{4}\left(1-\xi_1\right)\left(1-\xi_2\right)\left(-\xi_1-\xi_2-1\right)$	$N_1 = \frac{1}{4}\left(\xi_1^2-\xi_1\right)\left(\xi_2^2-\xi_2\right)$
$N_2 = \xi_1\left(2\xi_1 - 1\right)$	$N_2 = \frac{1}{4}\left(1+\xi_1\right)\left(1-\xi_2\right)\left(\xi_1-\xi_2-1\right)$	$N_2 = \frac{1}{4}\left(\xi_1^2+\xi_1\right)\left(\xi_2^2-\xi_2\right)$
$N_3 = \xi_2\left(2\xi_2 - 1\right)$	$N_3 = \frac{1}{4}\left(1+\xi_1\right)\left(1+\xi_2\right)\left(\xi_1+\xi_2-1\right)$	$N_3 = \frac{1}{4}\left(\xi_1^2+\xi_1\right)\left(\xi_2^2+\xi_2\right)$
$N_4 = 4\xi_1\zeta$	$N_4 = \frac{1}{4}\left(1-\xi_1\right)\left(1+\xi_2\right)\left(-\xi_1+\xi_2-1\right)$	$N_4 = \frac{1}{4}\left(\xi_1^2-\xi_1\right)\left(\xi_2^2+\xi_2\right)$
$N_5 = 4\xi_1\xi_2$	$N_5 = \frac{1}{2}\left(1-\xi_2\right)\left(1+\xi_1\right)\left(1-\xi_1\right)$	$N_5 = \frac{1}{2}\left(\xi_2^2-\xi_2\right)\left(1-\xi_1^2\right)$
$N_6 = 4\xi_2\zeta$	$N_6 = \frac{1}{2}\left(1+\xi_1\right)\left(1+\xi_2\right)\left(1-\xi_2\right)$	$N_6 = \frac{1}{2}\left(\xi_1^2+\xi_1\right)\left(1-\xi_2^2\right)$
$\zeta = 1 - \xi - 1 - \xi_2$	$N_7 = \frac{1}{2}\left(1+\xi_2\right)\left(1+\xi_1\right)\left(1-\xi_1\right)$	$N_7 = \frac{1}{2}\left(\xi_2^2+\xi_2\right)\left(1-\xi_1^2\right)$
	$N_8 = \frac{1}{2}\left(1-\xi_1\right)\left(1+\xi_2\right)\left(1-\xi_1\right)$	$N_8 = \frac{1}{2}\left(\xi_1^2+\xi_1\right)\left(1-\xi_2^2\right)$
		$N_9 = \left(1-\xi_1^2\right)\left(1-\xi_2^2\right)$

Table 4.1: Shape functions for different quadratic isoparametric finite elements.

representations (cf. Eqs. (2.57)-(2.60))

$$\mathbf{K}_3 = \bigcup_{e=1}^{N_{el}} \int_{\Omega_s^{\mathrm{ref}}} \mathscr{B}_z^{\mathrm{T}}\left(\boldsymbol{\xi}\right)\tilde{\mathbf{C}}^e\left(\boldsymbol{\xi},\omega\right)\mathscr{B}_z\left(\boldsymbol{\xi}\right)J_s^e\left(\boldsymbol{\xi}\right)\mathrm{d}\xi_1\mathrm{d}\xi_2 \tag{4.11}$$

$$\mathbf{K}_2 = \bigcup_{e=1}^{N_{el}} \int_{\Omega_s^{\mathrm{ref}}} \left(\mathscr{B}_{xy}\left(\boldsymbol{\xi}\right)\right)^{\mathrm{T}}\tilde{\mathbf{C}}^e\left(\boldsymbol{\xi},\omega\right)\mathscr{B}_z\left(\boldsymbol{\xi}\right)J_s^e\left(\boldsymbol{\xi}\right)\mathrm{d}\xi_1\mathrm{d}\xi_2 \tag{4.12}$$

$$\mathbf{K}_1 = \bigcup_{e=1}^{N_{el}} \int_{\Omega_s^{\mathrm{ref}}} \left(\mathscr{B}_{xy}\left(\boldsymbol{\xi}\right)\right)^{\mathrm{T}}\tilde{\mathbf{C}}^e\left(\boldsymbol{\xi},\omega\right)\mathscr{B}_{xy}\left(\boldsymbol{\xi}\right)J_s^e\left(\boldsymbol{\xi}\right)\mathrm{d}\xi_1\mathrm{d}\xi_2 \tag{4.13}$$

$$\mathbf{M} = \bigcup_{e=1}^{N_{el}} \int_{\Omega_s^{\mathrm{ref}}} \rho_e\left(\boldsymbol{\xi}\right)\left(\mathbf{N}\left(\boldsymbol{\xi}\right)\right)^{\mathrm{T}}\mathbf{N}\left(\boldsymbol{\xi}\right)J_s^e\left(\boldsymbol{\xi}\right)\mathrm{d}\xi_1\mathrm{d}\xi_2 \tag{4.14}$$

in which $J_s^e\left(\boldsymbol{\xi}\right) = \det\left[\partial\mathbf{x}\left(\boldsymbol{\xi}\right)/\partial\boldsymbol{\xi}\right]$ represents the Jacobian of the isoparametric mapping in the $x - y$ plane for the eth semi-isoparametric finite element. The vectors of nodal displacements on $\Omega_s \cup \partial\Omega_s$, $\mathbf{Q}\left(\kappa_z,\omega\right)$, and nodal forces on $\partial\Omega_s$, $\mathbf{F}_s\left(\kappa_z,\omega\right)$ and $\mathbf{F}_b\left(\kappa_z,\omega\right)$, are expressed as

$$\mathbf{Q}\left(\kappa_z,\omega\right)=\bigcup_{e=1}^{N_{el}}\mathbf{q}^e\left(\kappa_z,\omega\right), \tag{4.15}$$

$$\mathbf{F}_s\left(\kappa_z,\omega\right)=\bigcup_{q=1}^{N_b}\int_{\partial\Omega_s^{\mathrm{ref}}}\left(\mathbf{N}\left(\boldsymbol{\xi}\left(\eta\right)\right)\right)^{\mathrm{T}}\mathbf{t}_s^q\left(\kappa_z,\omega\right)J_s^q\left(\boldsymbol{\xi}\left(\eta\right)\right)\mathrm{d}\eta, \tag{4.16}$$

$$\mathbf{F}_b\left(\kappa_z,\omega\right)=\bigcup_{q=1}^{N_b}\int_{\partial\Omega_s^{\mathrm{ref}}}\left(\mathbf{N}\left(\boldsymbol{\xi}\left(\eta\right)\right)\right)^{\mathrm{T}}\mathbf{t}_b^q\left(\kappa_z,\omega\right)J_s^q\left(\boldsymbol{\xi}\left(\eta\right)\right)\mathrm{d}\eta, \tag{4.17}$$

where $\boldsymbol{\xi}\left(\eta\right)$ is a coordinate transformation for the in-plane mapping of the edge of an element which nodes belong to $\partial\Omega_s$, $J_s^q\left(\boldsymbol{\xi}\left(\eta\right)\right)=\left|\left(\partial\mathbf{x}/\partial\boldsymbol{\xi}\right)\left(\partial\boldsymbol{\xi}/\partial\eta\right)\right|$ the corresponding Jacobian and N_b the total number of edges that discretize $\partial\Omega_s$.

It is worth noting that, while the matrix operators $\mathbf{K}_1$, $\mathbf{K}_2$ and $\mathbf{K}_3$ can be either dependent or independent on the frequency with varying rheological models (see the description given in Sec. 2.4), the vector $\mathbf{F}_b\left(\kappa_z,\omega\right)$ always depends on wavenumber and frequency since it accounts for the acoustic mechanical and geometric properties of the external medium. This vector is determined via a 2.5D BEM formulation, which is described in the next section.

4.5 BEM model of the surrounding medium

4.5.1 Regularized 2.5D boundary integral equation

The surrounding medium of unbounded domain Ω_b is assumed to be isotropic and linear viscoelastic, with mechanical properties defined by mass density ρ and complex bulk velocities $\tilde{c}_L$ and $\tilde{c}_S$. As shown in Chapter 3, the 2.5D boundary integral formulation is obtained from the corresponding integral representation theorem in which two different dynamic states are considered. The first state is represented by the unknown displacements $\mathbf{u}\left(\mathbf{x},\kappa_z,\omega\right)$ and tractions $\mathbf{t}\left(\mathbf{x},\kappa_z,\omega\right)$ at a receiver point $\mathbf{x}\in\partial\Omega_b$ (see Fig. 4.1). The second state is assumed as the state of fundamental solutions in the full space for the spatial and time harmonic problem, i.e. the dynamic Green's functions in terms of displacements and tractions at $\mathbf{x}$ due to a harmonic line load $\mathfrak{p}\left(\mathbf{x}',z',t\right)=\delta\left(\mathbf{x}-\mathbf{x}'\right)\exp\left[\mathrm{i}\left(\kappa_z z'-\omega t\right)\right]$ with plane coordinates $\mathbf{x}'\in\Omega_b$ (see Fig. 4.1). The procedure adopted to extend the boundary integral formulation to source points $\mathbf{x}'$ belonging to the boundary involves the limiting process $\mathbf{x}'\in\Omega_b\rightarrow\mathbf{x}'\in\partial\Omega_b$ and is described in Sec. 3.6.1. As a result, the boundary integrals are convergent in the

Cauchy Principal Value sense.

In Chapter 3 it has been illustrated how numerical difficulties in treating Cauchy principal value integrals and boundary corners can be overcome by using the so called rigid body motion technique [François et al., 2010; Lu et al., 2008b]. From Eq. (3.54), by posing $c_\infty = 0$, the regularized 2.5D boundary integral equation in the (κ_z, ω) domain for a source point $\mathbf{x}' \in \partial\Omega_b$ and in absence of body forces is expressed as

$$\begin{aligned} \mathbf{u}\left(\mathbf{x}', \kappa_z, \omega\right) = & \int_{\partial\Omega_b} \left[\mathbf{U}^D\left(r, \kappa_z, \omega\right) - \mathbf{U}^S\left(r\right)\right] \mathbf{t}\left(\mathbf{x}, \kappa_z, \omega\right) \mathrm{d}s\left(\mathbf{x}\right) \\ & + \int_{\partial\Omega_b} \mathbf{U}^S\left(r\right) \mathbf{t}\left(\mathbf{x}, \kappa_z, \omega\right) \mathrm{d}s\left(\mathbf{x}\right) \\ & - \int_{\partial\Omega_b} \left[\mathbf{T}^D\left(r, \kappa_z, \omega\right) \mathbf{u}\left(\mathbf{x}, \kappa_z, \omega\right) - \mathbf{T}^S\left(r\right) \mathbf{u}\left(\mathbf{x}', \kappa_z, \omega\right)\right] \mathrm{d}s\left(\mathbf{x}\right), \\ & \left(\mathbf{x}, \mathbf{x}'\right) \in \partial\Omega_b, \end{aligned} \tag{4.18}$$

where $r = |\mathbf{x} - \mathbf{x}'|$ is the source-receiver distance in the $z = 0$ plane (see Fig. 4.1). The different sign for the axial wavenumber κ_z in the arguments of the dynamic Green's functions between Eq. (3.54) and Eq. (4.18) follows directly from the assumptions in Eqs. (3.1) and (4.1), respectively.

The fundamental dynamic solutions $U_{ij}^D\left(r, \kappa_z, \omega\right)$ in Eq. (4.18) express the jth displacement component at $\mathbf{x}$ when the harmonic line load of plane coordinates $\mathbf{x}'$ is acting in the ith direction.

In this chapter, the dynamic Green's functions proposed by Li et al. [1992] for a homogeneous isotropic linear viscoelastic full space are adopted instead of those derived by Tadeu and Kausel [2000] and used in Chapter 3, since they present an advantage in terms of computational times. In fact, while the Green's functions proposed by Tadeu and Kausel [2000] require the evaluation of a set of four Hankel functions (in this case from order 0 to order 3), those proposed by Li et al. [1992] need only the evaluation of the zero and one order Hankel functions. In boundary element codes that operate with dynamic analyses, the evaluation of the Green's functions (and therefore of the Hankel functions) represent a time-consuming operation, especially for large meshes and large numbers of integration points, since the evaluation must be performed for several combinations of $\kappa_{\alpha,\beta} r$. The fundamental solution derived by Li et al. [1992] for the harmonic wave motion in time and space reads

$$\begin{aligned} U_{ij}^D\left(r, \kappa_z, \omega\right) = & \frac{\mathrm{i}}{4\tilde{\mu}} \left\{ H_0^{(1)}(\kappa_\beta r)\delta_{ij} + L_{ij} \left[H_0^{(1)}(\kappa_\beta r) - H_0^{(1)}(\kappa_\alpha r) \right] \right\}, \\ & i, j = 1, 2, 3 \end{aligned} \tag{4.19}$$

where

$$\kappa_\alpha = \sqrt{\kappa_L^2 - \kappa_z^2}, \tag{4.20}$$

$$\kappa_\beta = \sqrt{\kappa_S^2 - \kappa_z^2}, \tag{4.21}$$

are the wavenumbers normal to the interface $\partial\Omega$ and

$$\kappa_L = \frac{\omega}{\tilde{c}_L}, \tag{4.22}$$

$$\kappa_S = \frac{\omega}{\tilde{c}_L}, \tag{4.23}$$

denote the complex longitudinal and shear bulk wavenumbers. In Eq. (4.19), $H_0^{(1)}(\cdot)$ is the zero order Hankel function of first kind and

$$\begin{aligned} L_{ij} =& \frac{1}{\kappa_S^2}\left[\delta_{kj}\delta_{qi}\frac{\partial^2}{\partial x_k \partial x_q} - \mathrm{i}\kappa_z\left(\delta_{3j}\delta_{ki} + \delta_{3i}\delta_{kj}\right)\frac{\partial}{\partial x_k} - \kappa_z^2\delta_{3j}\delta_{3i}\right]. \\ & i, j, k, q = 1, 2, 3 \end{aligned} \tag{4.24}$$

Following Gunawan and Hirose [2005], the fundamental displacements in Eq. (4.19) can be further elaborated to give

$$\begin{aligned} U_{ij}^D(r,\kappa_z,\omega) &= \frac{1}{4\tilde{\mu}}\left[\left(Q_1 - \frac{P_2}{\kappa_S r}\right)\delta_{ij} - \left(P_3 - \frac{2P_2}{\kappa_S r}\right)\frac{\partial r}{\partial x_i}\frac{\partial r}{\partial x_j}\right] \quad i, j = 1, 2 \\ U_{i3}^D(r,\kappa_z,\omega) &= U_{3i}^D(r,\kappa_z,\omega) = \frac{-\kappa_z}{4\tilde{\mu}\kappa_S}P_2\frac{\partial r}{\partial x_i} \quad i = 1, 2 \\ U_{33}^D(r,\kappa_z,\omega) &= \frac{\mathrm{i}}{4\tilde{\mu}}\left(Q_1 - \frac{\kappa_z^2}{\kappa_S^2}P_1.\right) \end{aligned} \tag{4.25}$$

The second set of fundamental solutions, the tractions Green's functions $T_{ij}^D(r,\kappa_z,\omega)$, are obtained as

$$T_{ij}^D(r,\kappa_z,\omega) = \sigma_{ijk}^D(r,\kappa_z,\omega)\, n_k(\mathbf{x}), \quad i, jk = 1, 2, 3 \tag{4.26}$$

being $n_k(\mathbf{x})$ the kth component of the outward normal at $\mathbf{x} \in \partial\Omega_b$ and

$$\sigma_{ijk}^D(r,\kappa_z,\omega) = \tilde{\lambda}\varepsilon_{ill}^D(r,\kappa_z,\omega)\,\delta_{jk} + 2\tilde{\mu}\varepsilon_{ijk}^D(r,\kappa_z,\omega), \quad i, j, k, = 1, 2, 3 \tag{4.27}$$

the jkth component of the Cauchy stress tensor at $\mathbf{x}$ when the line load of projection

$\mathbf{x}'$ is acting in direction i, while

$$\varepsilon^D_{ijk}\left(r,\kappa_z,\omega\right)=\frac{1}{2}\left[\frac{\partial U^D_{ij}\left(r,\kappa_z,\omega\right)}{\partial x_k}+\frac{\partial U^D_{ik}\left(r,\kappa_z,\omega\right)}{\partial x_j}\right],\quad i,j,k,=1,2,3 \tag{4.28}$$

is the associated Green's tensor of linear strains. Substituting Eq. (4.25) into Eqs. (4.28), (4.27) and (4.26) leads to the following expressions for the fundamental tractions [Gunawan and Hirose, 2005]

$$\begin{aligned}
T^D_{ij}\left(r,\kappa_z,\omega\right)=&\frac{\mathrm{i}\kappa_S}{4}\left\{\left[\frac{\tilde{\lambda}}{\tilde{\mu}}\left(P_4-\frac{\kappa_\beta}{\kappa_S}Q_2+\frac{\kappa_z^2}{\kappa_S^2}P_2\right)+\frac{4P_2}{\left(\kappa_S r\right)^2}-\frac{2P_3}{\kappa_S r}\frac{\partial r}{\partial x_j}n_i\right]\right.\\
&+\left[-\frac{\kappa_\beta}{\kappa_S}Q_2+\frac{4P_2}{\left(\kappa_S r\right)^2}-\frac{2P_3}{\kappa_S r}\right]\left(\frac{\partial r}{\partial x_i}n_j+\frac{\partial r}{\partial x_j}n_i\right)\\
&\left.+\left[-\frac{16P_2}{\left(\kappa_S r\right)^2}+\frac{8P_3}{\kappa_S r}+2P_4\right]\frac{\partial r}{\partial x_i}\frac{\partial r}{\partial x_j}\frac{\partial r}{\partial n}\right\},\quad i,j=1,2\\
T^D_{i3}\left(r,\kappa_z,\omega\right)=&-\frac{\kappa_z}{4}\left\{\left[\frac{\tilde{\lambda}}{\tilde{\mu}}\left(P_3+\frac{\kappa_z^2}{\kappa_S^2}P_1-Q_1\right)+\frac{2P_2}{\kappa_S r}\right]n_i\right.\\
&\left.-2\left(\frac{2P_2}{\kappa_S r}-P_3\right)\frac{\partial r}{x_i}\frac{\partial r}{\partial n}\right\},\quad i=1,2\\
T^D_{3i}\left(r,\kappa_z,\omega\right)=&-\frac{\kappa_z}{4}\left[\left(\frac{2P_2}{\kappa_S r}-Q_1\right)n_i-2\left(\frac{2P_2}{\kappa_S r}-P_3\right)\frac{\partial r}{\partial x_i}\frac{\partial r}{\partial n}\right],\quad i=1,2\\
T^D_{33}\left(r,\kappa_z,\omega\right)=&\frac{\mathrm{i}\kappa_S}{4}\left(-\frac{\kappa_\beta}{\kappa_S}Q_2+\frac{2\kappa_z^2}{\kappa_S^2}P_2\right)\frac{\partial r}{\partial n},
\end{aligned} \tag{4.29}$$

in which

$$\begin{aligned}
&Q_1=H_0^{(1)}\left(\kappa_\beta r\right),\quad Q_2=H_1^{(1)}\left(\kappa_\beta r\right),\\
&P_1=H_0^{(1)}\left(\kappa_\beta r\right)-H_0^{(1)}\left(\kappa_\alpha r\right),\\
&P_2=\left(\frac{\kappa_\beta}{\kappa_S}\right)H_1^{(1)}\left(\kappa_\beta r\right)-\left(\frac{\kappa_\alpha}{\kappa_L}\right)H_1^{(1)}\left(\kappa_\alpha r\right),\\
&P_3=\left(\frac{\kappa_\beta}{\kappa_S}\right)^2H_0^{(1)}\left(\kappa_\beta r\right)-\left(\frac{\kappa_\alpha}{\kappa_L}\right)^2H_0^{(1)}\left(\kappa_\alpha r\right),\\
&P_4=\left(\frac{\kappa_\beta}{\kappa_S}\right)^3H_1^{(1)}\left(\kappa_\beta r\right)-\left(\frac{\kappa_\alpha}{\kappa_L}\right)^3H_1^{(1)}\left(\kappa_\alpha r\right).
\end{aligned} \tag{4.30}$$

The static fundamental displacements and tractions in Eq. (4.18), $U^S_{ij}\left(r\right)$ and $T^S_{ij}\left(r\right)$, respectively, correspond to the fundamental solutions for the in-plane line load problem in plane strain (cf. Eq. (3.40))

$$U_{ij}^{S}(r) = \frac{1}{8\pi \mathrm{Re}(\tilde{\mu})(1-\mathrm{Re}(\tilde{\nu}))}\left[(3-4\mathrm{Re}(\tilde{\mu}))\ln\left(\frac{1}{r}\right)\delta_{ij} + \frac{\partial r}{\partial x_i}\frac{\partial r}{\partial x_j}\right], \tag{4.31}$$

$$\begin{aligned} T_{ij}^{S}(r) = &- \frac{1}{4\pi(1-\mathrm{Re}(\tilde{\mu}))r}\left\{\frac{\partial r}{\partial x_k}n_k\left[\left(2\mathrm{Re}(\tilde{\mu})\delta_{ij} + 2\frac{\partial r}{\partial x_i}\frac{\partial r}{\partial x_j}\right)\right.\right. \\ &- \left.\left.(1-2\mathrm{Re}(\tilde{\mu}))\left(\frac{\partial r}{\partial x_i}n_j - \frac{\partial r}{\partial x_j}n_i\right)\right]\right\}, \quad i,j,k=1,2 \end{aligned} \tag{4.32}$$

and those for the anti-plane line load problem in plane strain (cf. Eq. (3.41))

$$U_{33}^{S}(r) = \frac{1}{2\pi\mathrm{Re}(\tilde{\mu})}\ln\left(\frac{1}{r}\right), \tag{4.33}$$

$$T_{33}^{S}(r) = -\frac{1}{2\pi r}\frac{\partial r}{\partial x_k}n_k. \quad k=1,2 \tag{4.34}$$

Since the asymptotic behaviour of the dynamic and static fundamental solutions correspond when $r \to 0$, the dominant singularities of the kernel functions in the first and last integral of Eq. (4.18) cancel each other out when the source point $\mathbf{x}'$ approaches the receiver point $\mathbf{x}$. Consequently, these integrals can be evaluated numerically using the standard Gauss-Legendre quadrature formula [Stroud and Secrest, 1996]. The second integral in Eq. (4.18) behaves asymptotically as $\ln(1/r)$ for $r \to 0$ and can be evaluated using the Gauss-Laguerre and Gauss-Legendre quadrature formulae (see Sec. 4.5.3).

4.5.2 Boundary element discretization

The boundary $\partial\Omega_b$ is subdivided into a number N_b of quadratic semi-isoparametric monodimensional elements with shape functions as indicated in Table4.2. In order to satisfy the compatibility conditions Eq. (4.3), the nodes of the generic boundary element $\partial\Omega_b^q$ are chosen to coincide with those belonging to one edge of an adjacent semi-analytical finite element Ω_s^e. The boundary geometry, displacements and tractions are interpolated as follows

$$\mathbf{x}(\eta) = \mathbf{N}(\eta)\mathbf{x}^q, \tag{4.35}$$

$$\mathbf{u}(\eta,\kappa_z,\omega) = \mathbf{N}(\eta)\mathbf{q}^q(\kappa_z,\omega), \tag{4.36}$$

$$\mathbf{t}(\eta,\kappa_z,\omega) = \mathbf{N}(\eta)\mathbf{h}^q(\kappa_z,\omega), \tag{4.37}$$

where $\mathbf{N}(\eta)$ is the matrix containing the quadratic shape functions in the natural coordinate $\eta \in \partial\Omega_b^{\mathrm{ref}}$ (see Table4.2), while $\mathbf{x}^q$, $\mathbf{q}^q(\kappa_z,\omega)$ and $\mathbf{h}^q(\kappa_z,\omega)$ are the vectors of nodal coordinates, displacements and tractions, respectively.

The regularized boundary integral formulation Eq. (4.18) is rewritten in discretized form by applying a point collocation scheme [Brebbia and Dominguez, 1989], where collocation points $\mathbf{x}'$ are assumed to be coincident with the nodes of the boundary element mesh. Denoting by $\mathbf{x}_c$ the cth collocation node and introducing Eqs. (4.36) and (4.37) into Eq. (4.18), the recursive collocation procedure over the total number of nodes $N_n = N_b \times 2$ of the boundary element leads to

$$\begin{aligned}
\bigcup_{c=1}^{N_n} \Bigg\{ & \bigcup_{q=1}^{N_b} \left[\mathbf{U}_1^q\left(r_c\left(\eta\right), \kappa_z, \omega\right) + \mathbf{U}_2^q\left(r_c\left(\eta\right)\right)\right] \mathbf{h}^q\left(\kappa_z, \omega\right) \\
& - \bigcup_{\substack{q=1 \\ (\mathbf{x}_c \notin \partial\Omega^q)}}^{N_b} \left[\mathbf{T}_1^q\left(r_c\left(\eta\right), \kappa_z, \omega\right) \mathbf{q}^q\left(\kappa_z, \omega\right)\right] - \bigcup_{\substack{q=1 \\ (\mathbf{x}_c \in \partial\Omega^q)}}^{N_b} \left[\mathbf{T}_2^q\left(r_c\left(\eta\right), \kappa_z, \omega\right) \mathbf{q}^q\left(\kappa_z, \omega\right)\right] \\
& + \bigcup_{\substack{q=1 \\ (\mathbf{x}_c \notin \partial\Omega^q)}}^{N_b} \left[\mathbf{T}_3^q\left(r_c\left(\eta\right)\right) \mathbf{u}_c\left(\kappa_z, \omega\right)\right] \Bigg\} = \bigcup_{c=1}^{N_n} \mathbf{u}_c\left(\kappa_z, \omega\right), \quad \left(\mathbf{x}, \mathbf{x}_c\right) \in \partial\Omega_b
\end{aligned} \tag{4.38}$$

where $\mathbf{u}_c\left(\kappa_z, \omega\right)$ is the displacement vector at $\mathbf{x}_c$ and

$$\mathbf{U}_1^q\left(r_c\left(\eta\right), \kappa_z, \omega\right) = \int_{\partial\Omega_b^{\text{ref}}} \left[\mathbf{U}^D\left(r_c\left(\eta\right), \kappa_z, \omega\right) - \mathbf{U}^S\left(r_c\left(\eta\right)\right)\right] \mathbf{N}\left(\eta\right) J_b^q\left(\eta\right) \mathrm{d}\eta, \tag{4.39}$$

$$\mathbf{U}_2^q\left(r_c\left(\eta\right)\right) = \int_{\partial\Omega_b^{\text{ref}}} \mathbf{U}^S\left(r_c\left(\eta\right)\right) \mathbf{N}\left(\eta\right) J_b^q\left(\eta\right) \mathrm{d}\eta, \tag{4.40}$$

$$\mathbf{T}_1^q\left(r_c\left(\eta\right), \kappa_z, \omega\right) = \int_{\partial\Omega_b^{\text{ref}}} \mathbf{T}^D\left(r_c\left(\eta\right), \kappa_z, \omega\right) \mathbf{N}\left(\eta\right) J_b^q\left(\eta\right) \mathrm{d}\eta, \tag{4.41}$$

$$\mathbf{T}_2^q\left(r_c\left(\eta\right), \kappa_z, \omega\right) = \int_{\partial\Omega_b^{\text{ref}}} \left[\mathbf{T}^D\left(r_c\left(\eta\right), \kappa_z, \omega\right) \mathbf{N}\left(\eta\right) - \mathbf{T}^S\left(r_c\left(\eta\right)\right) \mathbf{N}\left(\eta_c\right)\right] J_b^q\left(\eta\right) \mathrm{d}\eta, \tag{4.42}$$

$$\mathbf{T}_3^q\left(r_c\left(\eta\right)\right) = \int_{\partial\Omega_b^{\text{ref}}} \mathbf{T}^S\left(r_c\left(\eta\right)\right) J_b^q\left(\eta\right) \mathrm{d}\eta, \tag{4.43}$$

are influence operators, in which $r_c\left(\eta\right) = \left|\mathbf{x}\left(\eta\right) - \mathbf{x}_c\right|$ denotes the in-plane distance between the integration point $\mathbf{x}\left(\eta\right)$ and the collocation point $\mathbf{x}_c$, η_c is the adimensional coordinate evaluated at the element's node coincident with $\mathbf{x}_c$ and $J_b^q\left(\eta\right) = \left|\partial\mathbf{x}\left(\eta\right)/\partial\eta\right|$ is the Jacobian of the semi-isoparametric transformation.

From Eq. (4.38), by grouping the displacements and tractions operators into the global influence operators $\mathbf{U}_b\left(\kappa_z,\omega\right) = \bigcup_c \bigcup_q \sum_{j=1}^{2} \mathbf{U}_j^q\left(r_c,\kappa_z,\omega\right)$ and $\mathbf{T}_b\left(\kappa_z,\omega\right) = \bigcup_c \bigcup_q \sum_{j=1}^{3} \mathbf{T}_j^q\left(r_c,\kappa_z,\omega\right)$, and by assembling the displacements and tractions vectors into the global vectors $\mathbf{Q}_b\left(\kappa_z,\omega\right) = \bigcup_q \mathbf{q}^q\left(\kappa_z,\omega\right)$ and $\mathbf{H}_b\left(\kappa_z,\omega\right) = \bigcup_q \mathbf{h}^q\left(\kappa_z,\omega\right)$ according to the mesh topology, the following set of linear algebraic equations is obtained

$$\left[\mathbf{T}_b\left(\kappa_z,\omega\right) + \mathbf{I}\right]\mathbf{Q}_b\left(\kappa_z,\omega\right) = \mathbf{U}_b\left(\kappa_z,\omega\right)\mathbf{H}_b\left(\kappa_z,\omega\right), \quad (\mathbf{x},\mathbf{x}_c) \in \partial\Omega_b \tag{4.44}$$

which is defined only for source points $\mathbf{x}_c$ belonging to the boundary. Once the vectors of boundary displacements $\mathbf{Q}_b\left(\kappa_z,\omega\right)$ and tractions $\mathbf{H}_b\left(\kappa_z,\omega\right)$ have been determined from Eq. (4.44), the radiated wavefield $\mathbf{u}_d\left(\mathbf{x}',\kappa_z,\omega\right)$ at any $\mathbf{x}' \in \Omega_b$ can be computed using the 2.5D integral representation theorem in Eq. (3.16). The discretized form of the 2.5D integral representation theorem is given in Eq. (3.71) and is repeated here for convenience

$$\mathbf{u}_d\left(\mathbf{x}',\kappa_z,\omega\right) = \mathbf{U}_d\left(\kappa_z,\omega\right)\mathbf{H}_b\left(\kappa_z,\omega\right) - \mathbf{T}_d\left(\kappa_z,\omega\right)\mathbf{Q}_b\left(\kappa_z,\omega\right), \quad \mathbf{x}' \in \Omega_b, \tag{4.45}$$

where the influence operators $\mathbf{U}_d\left(\kappa_z,\omega\right)$ and $\mathbf{T}_d\left(\kappa_z,\omega\right)$ result from the following element assembling procedure

$$\mathbf{U}_d\left(\kappa_z,\omega\right) = \bigcup_{q=1}^{N_b} \int_{\partial\Omega_q^{\mathrm{ref}}} \mathbf{U}^D\left(r'\left(\eta\right),\kappa_z,\omega\right)\mathbf{N}\left(\eta\right)J_b^q\left(\eta\right)\mathrm{d}\eta, \tag{4.46}$$

$$\mathbf{T}_d\left(\kappa_z,\omega\right) = \bigcup_{q=1}^{N_b} \int_{\partial\Omega_q^{\mathrm{ref}}} \mathbf{T}^D\left(r'\left(\eta\right),\kappa_z,\omega\right)\mathbf{N}\left(\eta\right)J_b^q\left(\eta\right)\mathrm{d}\eta, \tag{4.47}$$

in which $r'\left(\eta\right) = \left|\mathbf{x}\left(\eta\right) - \mathbf{x}'\right|$. Since the dynamic Green's functions are nonsingular for $\mathbf{x}' \in \Omega_b$, the integrals in Eqs. (4.46) and (4.47) can be evaluated numerically using the standard Gauss-Legendre quadrature formula.

4.5.3 Evaluation of weakly singular integrals

As can be noted from Eqs. (4.31) and (4.33), the displacement kernels in Eq. (4.40) are weakly singular of order $\ln\left(1/r\right)$. Following [Gao and Davies, 2001], the strategy adopted in this case is to isolate the logarithmic singularity and integrate it using the Gauss-Laguerre quadrature rule, while the nonsingular residual can be integrated using the Gauss-Legendre quadrature rule. For the quadratic element of Table4.2 three cases need to be considered because the source point $\mathbf{x}_c = [x_c,\ y_c]^{\mathrm{T}}$ may be located at

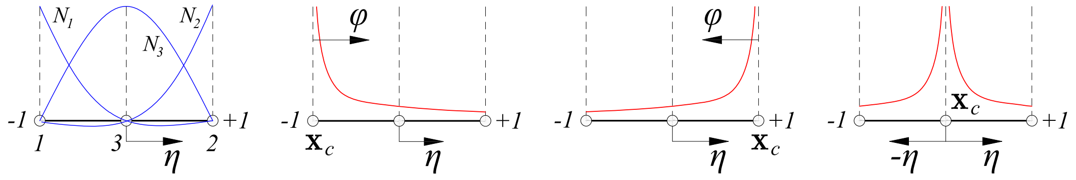

$N_1 = \frac{1}{2}\eta\,(\eta - 1)$ $N_2 = \frac{1}{2}\eta\,(\eta + 1)$ $N_3 = 1 - \eta^2$	$\mathbf{x}_c = \mathbf{x}_1^q$	$\mathbf{x}_c = \mathbf{x}_2^q$	$\mathbf{x}_c = \mathbf{x}_3^q$

Table 4.2: Shape functions for the quadratic monodimensional boundary element and logarithmic singularities for various configurations of the source point.

the initial node (node 1) of coordinates $\mathbf{x}_1^q = [x_1,\ y_1]^{\mathrm{T}}$, at the end node (node 2) of coordinates $\mathbf{x}_2^q = [x_2,\ y_2]^{\mathrm{T}}$ or the mid-side node (node 3), of coordinates $\mathbf{x}_3^q = [x_3,\ y_3]^{\mathrm{T}}$. The distance $r_c\,(\eta)$ between an arbitrary point of coordinates $\mathbf{x}\,(\eta)$ (see Eq. (4.35)) and the source $\mathbf{x}_c$ is obtained from the equation

$$r_c\,(\eta) = [x\,(\eta) - x_c]^2 - [y\,(\eta) - y_c]^2\,. \tag{4.48}$$

If $\mathbf{x}_c$ is located at node 1, the substitution of Eq. (4.35) into Eq. (4.48) along with the quadratic shape functions given in Table4.2 leads to the following expression

$$\begin{aligned} r_c^2 = \left[\frac{1}{2}\,(1+\eta)\right]^2 & \Big\{\left[-\,(2-\eta)\,x_1^q + \eta x_2^q + 2\,(1-\eta)\,x_3^q\right]^2 \\ & + \left[-\,(2-\eta)\,y_1^q + \eta y_2^q + 2\,(1-\eta)\,y_3^q\right]^2\Big\} \end{aligned} \tag{4.49}$$

Similarly, if $\mathbf{x}_c$ is located at node 2, one obtains

$$\begin{aligned} r_c^2 = \left[\frac{1}{2}\,(1+\eta)\right]^2 & \Big\{\left[-\,(2+\eta)\,x_1^q - \eta x_2^q + 2\,(1+\eta)\,x_3^q\right]^2 \\ & + \left[-\,(2+\eta)\,y_1^q - \eta y_2^q + 2\,(1+\eta)\,y_3^q\right]^2\Big\} \end{aligned} \tag{4.50}$$

Eqs. (4.49) and (4.50) can be expressed in the unified form

$$r_c^2 = \varphi^2\left[f_1^2 + f_2^2\right] \tag{4.51}$$

where φ is an adimensional coordinate with origin at the same point in which the source point is located, obtained via the change of variables

$$\varphi = \frac{1}{2}\left(1 - \eta_c \eta\right) \tag{4.52}$$

in which $\eta_c = -1$ if the source point $\mathbf{x}_c$ is located at node 1 of the element $\partial\Omega^q$ and $\eta_c = +1$ if it is located at node 2. The functions f_1 and f_2 in Eq. (4.51) are then

$$\begin{aligned} f_1 &= -\left(2 + \eta_c \eta\right) x_a - \eta_c \eta x_b + 2\left(1 + \eta_c \eta\right) x_3, \\ f_2 &= -\left(2 + \eta_c \eta\right) y_a - \eta_c \eta y_b + 2\left(1 + \eta_c \eta\right) y_3, \end{aligned} \tag{4.53}$$

where $a = 1$, $b = 2$ when the collocation point is located at node 1, and $a = 2$, $b = 1$ when it is located at node 2. For the case when the collocation point is located at the mid-side node $\mathbf{x}_3^q$, one obtains

$$r_c^2 = \eta^2 \left[g_1^2 + g_2^2\right] \tag{4.54}$$

where the functions g_1 and g_2 take the following representation

$$\begin{aligned} g_1 &= \frac{1}{2}\left[\left(\eta - 1\right) x_1 + \left(\eta + 1\right) x_2\right] - \eta x_3, \\ g_2 &= \frac{1}{2}\left[\left(\eta - 1\right) y_1 + \left(\eta + 1\right) y_2\right] - \eta y_3, \end{aligned} \tag{4.55}$$

Taking the logarithm of Eq. (4.51), the following expression can be obtained

$$\ln\left(\frac{1}{r_c}\right) = \underbrace{\ln\left(\frac{1}{\varphi}\right)}_{Gauss-Laguerre} - \underbrace{\frac{1}{2}\ln\left[f_1^2\left(\eta\right) + f_2^2\left(\eta\right)\right]^2}_{Gauss-Legendre} \tag{4.56}$$

The expression for the logarithm given in Eq. (4.56) can be substituted into Eqs. (4.31) and (4.33), and then into Eq. (4.40). The resulting integral can be subdivided into a singular part, containing the first term on the right hand side of Eq. (4.56), and the regular part, containing the second term. The singular and regular integral are evaluated numerically using the Gauss-Laguerre and Gauss-Legendre quadrature formulae, respectively. An expression equivalent to Eq. (4.56) can be obtained from Eq. (4.54), valid for the case in which the source point is located in the mid-side node of the element.

Finally, the boundary integrals in Eqs. (4.39), (4.41), (4.42) and (4.43) are evaluated by means of the Gauss-Legendre quadrature formula, since they are nonsingular.

4.6 SAFE-BE coupling

The coupling between the SAFE and the BEM regions is established via the compatibility conditions in Eqs. (4.3) and (4.4), and is carried out in a finite element sense [Andersen, 2006]. On these bases, the infinite boundary element domain is converted into a single, wavenumber and frequency dependent, finite element-like domain with N_n nodes. The dynamic stiffness matrix of this pseudo finite element, relating nodal tractions to nodal displacements, is obtained by recasting Eq. (4.44) in the following form

$$\mathbf{H}_b\left(\kappa_z,\omega\right)=\mathbf{K}_b\left(\kappa_z,\omega\right)\mathbf{Q}_b\left(\kappa_z,\omega\right), \tag{4.57}$$

where the dynamic stiffness matrix relating the nodal displacements and tractions

$$\mathbf{K}_b\left(\kappa_z,\omega\right)=\mathbf{U}_b^{-1}\left(\kappa_z,\omega\right)\left[\mathbf{T}_b\left(\kappa_z,\omega\right)+\mathbf{I}\right] \tag{4.58}$$

is complex and non symmetric. The nodal tractions are then converted into nodal forces by following the procedure indicated by Andersen [2006], which uses the equivalence between the virtual work done by the integral of the surface tractions over the boundary for the virtual displacements and the virtual work resulting from the application of the equivalent nodal forces for the same virtual displacements. The work done by the surface tractions $\mathbf{t}\left(\mathbf{x},\kappa_z,\omega\right)$ over the boundary in applying a virtual displacement $\delta\mathbf{u}\left(\mathbf{x},\kappa_z,\omega\right)$ is given as

$$\delta\mathscr{W}_b=\int_{\partial\Omega_b}\left[\delta\mathbf{u}\left(\mathbf{x},\kappa_z,\omega\right)\right]^{\mathrm{T}}\mathbf{t}\left(\mathbf{x},\kappa_z,\omega\right)\mathrm{d}s\left(\mathbf{x}\right). \tag{4.59}$$

Using the element shape functions to interpolate the displacements and the tractions, the field quantities at any point $\mathbf{x}\in\partial\Omega_b$ remains determined from Eqs. (4.36) and (4.37), respectively. Substituting these equations into Eq. (4.59) and applying the discretization procedure lead to

$$\delta\mathscr{W}_b=\bigcup_{q=1}^{N_b}\left\{\left[\delta\mathbf{q}^q\left(\kappa_z,\omega\right)\right]^{\mathrm{T}}\int_{\partial\Omega_b^{\mathrm{ref}}}\left(\boldsymbol{\mathcal{N}}\left(\eta\right)\right)^{\mathrm{T}}\boldsymbol{\mathcal{N}}\left(\eta\right)J_b^q\left(\eta\right)\mathrm{d}\eta\,\mathbf{h}^q\left(\kappa_z,\omega\right)\right\}. \tag{4.60}$$

Since the work done by the surface tractions for the qth element is equal to the work done by the equivalent nodal forces $\mathbf{f}_b^q\left(\kappa_z,\omega\right)$ for the same virtual displacement, the following relation holds

$$\delta \mathscr{W}_b = \bigcup_{q=1}^{N_b} \left[\delta \mathbf{q}^q \left(\kappa_z, \omega\right)\right]^{\mathrm{T}} \mathbf{f}_b^q \left(\kappa_z, \omega\right). \tag{4.61}$$

Combining Eqs. (4.60) and (4.61), the following relationship is derived

$$\mathbf{F}_b \left(\kappa_z, \omega\right) = \mathbf{T}_b \mathbf{H}_b \left(\kappa_z, \omega\right), \tag{4.62}$$

where

$$\mathbf{T}_b \left(\kappa_z, \omega\right) = \bigcup_{q=1}^{N_b} \int_{\partial\Omega_b^{\mathrm{ref}}} \left(\mathbf{N}\left(\eta\right)\right)^{\mathrm{T}} \mathbf{N}\left(\eta\right) J_b^q \left(\eta\right) \mathrm{d}\eta. \tag{4.63}$$

is a distribution matrix that relates the nodal tractions to nodal forces on the boundary. Substituting Eq. (4.57) in Eq. (4.63) leads to the following relation between nodal displacements and nodal forces

$$\mathbf{F}_b \left(\kappa_z, \omega\right) = \mathbf{T}_b \mathbf{K}_b \left(\kappa_z, \omega\right) \mathbf{Q}_b \left(\kappa_z, \omega\right). \tag{4.64}$$

Introduction of Eq. (4.64) in Eq. (4.10) gives the following complex and nonsymmetric N-dimensional linear system

$$\begin{split} \Big\{ \kappa_z^2 \mathbf{K}_3 + \mathrm{i}\kappa_z \left(\mathbf{K}_2 - \mathbf{K}_2^{\mathrm{T}}\right) + \mathbf{K}_1 \\ + \mathscr{L}_b^{\mathrm{T}} \left[\mathbf{T}_b \mathbf{K}_b \left(\kappa_z, \omega\right)\right] \mathscr{L}_b - \omega^2 \mathbf{M} \Big\} \mathbf{Q}\left(\kappa_z, \omega\right) = \mathbf{F}_s \left(\kappa_z, \omega\right), \end{split} \tag{4.65}$$

in which

$$\mathbf{Q}_b \left(\kappa_z, \omega\right) = \mathscr{L}_b \mathbf{Q}\left(\kappa_z, \omega\right) \tag{4.66}$$

is a matrix that collocates the global vector of nodal displacements on the boundary into the global vector of nodal displacements of the SAFE mesh. The displacement field at any $\mathbf{x} \in \left(\Omega_s \cup \partial\Omega_s\right)$ can be obtained by solving the $N \times N$ linear system Eq. (4.65) in the unknown nodal displacements $\mathbf{Q}\left(\kappa_z, \omega\right)$ and using the interpolation in Eq. (4.7). In addition, substituting Eq. (4.57) into Eq. (4.45) leads to the following $3 \times N$ linear system of equations

$$\mathbf{u}_d \left(\mathbf{x}', \kappa_z, \omega\right) = \left[\mathbf{U}_d \left(\kappa_z, \omega\right) \mathbf{K}_b \left(\kappa_z, \omega\right) - \mathbf{T}_d \left(\kappa_z, \omega\right)\right] \mathscr{L}_b \mathbf{Q}\left(\kappa_z, \omega\right), \quad \mathbf{x}' \in \Omega_b \tag{4.67}$$

which allows to compute the radiated displacement wavefield at any source point belonging to the surrounding domain.

4.7 Dispersion analysis

The dispersion properties of guided modes are determined in terms of complex wavenumbers $\kappa_z(\omega)$ for any fixed $\omega > 0$ in absence of external forces applied at the interface $\partial\Omega_s$. Substituting $\mathbf{F}_s(\kappa_z, \omega) = \mathbf{0}$ in Eq. (4.65), the dispersive equation for the unbounded waveguide of domain $\Omega_s \cup \Omega_b$ results in the following nonlinear eigenvalue problem in $\kappa_z(\omega)$

$$\mathbf{Z}(\kappa_z, \omega)\,\mathbf{Q}(\kappa_z, \omega) = \mathbf{0}, \tag{4.68}$$

where

$$\begin{aligned}\mathbf{Z}(\kappa_z, \omega) = \Big\{&\kappa_z^2\mathbf{K}_3 + \mathrm{i}\kappa_z\left(\mathbf{K}_2 - \mathbf{K}_2^{\mathrm{T}}\right) + \mathbf{K}_1 \\ &+ \mathscr{L}_b^{\mathrm{T}}\left[\mathbf{T}_b\mathbf{K}_b(\kappa_z, \omega)\right]\mathscr{L}_b - \omega^2\mathbf{M}\Big\}, \quad \in \mathbb{C}^{N,N}\end{aligned} \tag{4.69}$$

is the dynamic stiffness matrix of the coupled SAFE-2.5D BEM model. As shown in Chapter 3 the Contour Integral Method proposed by Beyn [2012] can be applied to transform the nonlinear eigenvalue problem Eq. (4.68) into a linear one inside a simple closed curve $\Gamma(\kappa_z) \in \mathbb{C}$ where poles of the guided modes must be sought.

Since the algorithm described in Sec. 3.8.1 remains unchanged and requires only the substitution of $\mathbf{Z}(\kappa_z,)$ with the expression in Eq. (4.69), the procedure will not be repeated here. On the other hand, the analysis of Sec. 3.8.2 is no longer valid for the case of embedded waveguides, and the single-valued definition of the dynamic stiffness matrix Eq. (4.69) must be revised.

4.7.1 Single-valued definition of the dynamic stiffness matrix

The procedure reported in Sec. 3.8.2 allows to extract all the eigenvalues for a holomorphic problem $\mathbf{Z}(\kappa_z, \omega) \in H(\Omega^*, \mathbb{C}^{K,K})$, where Ω^* denotes the region of the complex κ_z-plane enclosed by $\Gamma(\kappa_z)$. However, this condition is not generally satisfied as $\mathbf{Z}(\kappa_z, \omega)$ is singular and multivalued due to the properties of the Hankel functions $H_n^{(1)}(\cdot)$ as well as the two wavenumbers $\kappa_\alpha = \pm(\kappa_L^2 - \kappa_z^2)^{1/2}$ and $\kappa_\beta = \pm(\kappa_S^2 - \kappa_z^2)^{1/2}$. Before performing the contour integration in Eqs. (3.75) and (3.76), the operator $\mathbf{Z}(\kappa_z, \omega)$ must be made single valued and analytic everywhere inside Ω^*. This task is accomplished by choosing the phase of κ_α and κ_β consistently with the nature of the existing partial bulk waves in the surrounding medium, and by removing points of singularity and discontinuity in the κ_z-plane.

The signs of the wavenumbers normal to the interface, with reference to the more

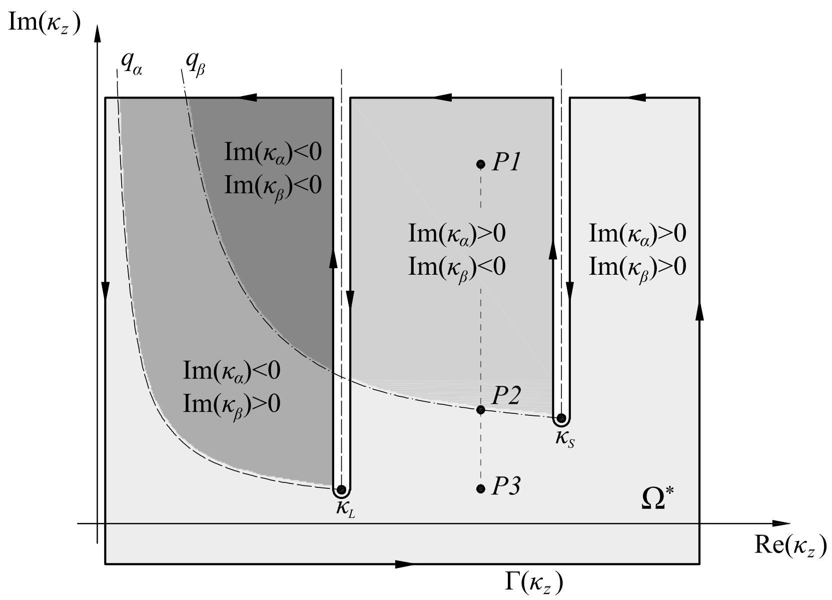

Figure 4.2: Complex κ_z-plane with bulk wavenumbers, vertical branch cuts and integration path for an external isotropic viscoelastic medium. The signs of κ_α and κ_β on Ω^* and along $\Gamma(\kappa_z)$ are determined by imposing the conditions on their imaginary parts as indicated in the different regions.

general viscoelastic case of Fig. 4.2, are established as in the following:

- for $\mathrm{Re}(\kappa_z) > \mathrm{Re}(\kappa_S)$, the Snell-Descartes law [Borcherdt, 2009; Rose, 2004] enforces a total reflection, with possible mode conversion at the interface, of the longitudinal and shear bulk waves traveling inside the waveguide (non-leaky region). In this case, the particles motion in the surrounding medium remains confined in proximity of the interface, with amplitude decaying exponentially in the direction normal to the interface [Auld, 1973; Pavlakovic, 1998]. Since the propagation process is represented by the Hankel functions $H_n^{(1)}(\kappa_\alpha r)$ and $H_n^{(1)}(\kappa_\beta r)$ and assumes a dependence $\exp[\mathrm{i}(\kappa_z z - \omega t)]$, in order to have outgoing waves satisfying the radiation condition at infinity, the signs of κ_α and κ_β must be chosen so that $\mathrm{Im}(\kappa_\alpha) > 0$ and $\mathrm{Im}(\kappa_\beta) > 0$.

- In the range $\mathrm{Re}(\kappa_L) < \mathrm{Re}(\kappa_z) < \mathrm{Re}(\kappa_S)$, the longitudinal bulk waves are still totally reflected at the interface, and the sign of κ_α is then selected in order to preserve the positiveness of its imaginary component, which satisfies the radiation condition at infinity. On the other hand, shear bulk waves are also refracted at some leakage angle $\vartheta_S^{Leak} = \sin^{-1}\left[\frac{\mathrm{Re}(\kappa_z)}{\mathrm{Re}(\kappa_S)}\right]$ with respect to the normal at the

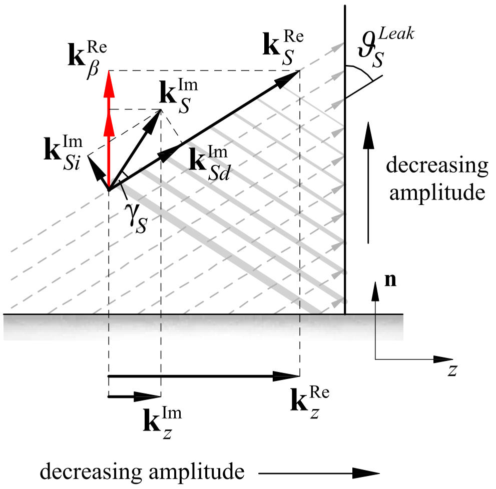

Figure 4.3: Wave vectors configurations for the point $P3$ of Fig. 4.2. The propagation vector $\mathbf{k}_S^{\mathrm{Re}}$ is oriented along the radiation direction (dashed gray lines), while the attenuation vector $\mathbf{k}_S^{\mathrm{Im}}$ is perpendicular to equi-amplitude lines (solid gray lines) and oriented in the direction of maximum decay. Magnitude of displacements is proportional to the thickness of equi-amplitude lines.

interface [Auld, 1973; Castaings and Lowe, 2008] and therefore, for the properties of the nth order Hankel function of the first kind, $\mathrm{sgn}(\kappa_\beta)$ must be chosen in order to satisfy the condition $\mathrm{Re}(\kappa_\beta) > 0$.

Regarding the imaginary component of κ_β, it must be observed that for any fixed positive $\mathrm{Re}(\kappa_z) \in [0, \mathrm{Re}(\kappa_S)]$, $\mathrm{Im}(\kappa_\beta)$ changes monotonically as a function of $\mathrm{Im}(\kappa_z)$ and vanishes for values of $\mathrm{Im}(\kappa_z) = \mathrm{Re}(\kappa_S)\mathrm{Im}(\kappa_S)/\mathrm{Re}(\kappa_z)$, which define a branch of hyperbola passing through the point κ_S. This branch of hyperbola, indicated with q_β in Fig. 4.2, determines the transition between an outgoing growing ($\mathrm{Im}(\kappa_\beta) < 0$) and an outgoing decaying ($\mathrm{Im}(\kappa_\beta) > 0$) shear waves wavefield along the orthogonal direction to the interface. These physical states are represented by points $P1$ and $P3$ in Fig. 4.2, respectively, while the transition state ($\mathrm{Im}(\kappa_\beta) = 0$) is represented by point $P2$ on q_β.

The wavevector configurations for points $P1$, $P2$ and $P3$ for a planar interface, are shown in Figs. 4.5-4.3 in terms of propagation and attenuation vectors, $\mathbf{k}_S^{\mathrm{Re}}$ and $\mathbf{k}_S^{\mathrm{Im}}$, respectively, with $|\mathbf{k}_S^{\mathrm{Re}}||\mathbf{k}_S^{\mathrm{Im}}|\cos(\gamma_S) = \mathbf{k}_S^{\mathrm{Re}} \cdot \mathbf{k}_S^{\mathrm{Im}}$ and $0 < \gamma_S < \pi/2$ [Carcione et al., 1988; Caviglia et al., 1990]. The attenuation vector is given by $\mathbf{k}_S^{\mathrm{Im}} = \mathbf{k}_{Sd}^{\mathrm{Im}} + \mathbf{k}_{Si}^{\mathrm{Im}}$, where $\mathbf{k}_{Sd}^{\mathrm{Im}}$ is the component due to material damping (homogeneous component), parallel to $\mathbf{k}^{\mathrm{Re}}$ according to the material damping

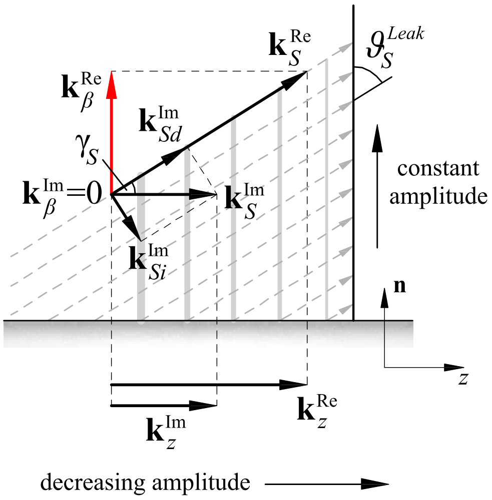

Figure 4.4: Wave vectors configurations for the point $P2$ of Fig. 4.2. The propagation vector $\mathbf{k}_S^{\mathrm{Re}}$ is oriented along the radiation direction (dashed gray lines), while the attenuation vector $\mathbf{k}_S^{\mathrm{Im}}$ is perpendicular to equi-amplitude lines (solid gray lines) and oriented in the direction of maximum decay. Magnitude of displacements is proportional to the thickness of equi-amplitude lines.

model of Eq. (4.9), and $\mathbf{k}_{Si}^{\mathrm{Im}}$ is the component associated to energy radiation (inhomogeneous component), which is normal to $\mathbf{k}_S^{\mathrm{Re}}$ [Cervený and Pšencík, 2011]. All the wavenumber vectors lie on the plane containing the z-axis and the outward normal $\mathbf{n}$ at the interface.

For any κ_z above q_β (point $P1$), imposition of $\mathrm{Re}(\kappa_\beta) > 0$ implies that $\mathrm{Im}(\kappa_\beta) < 0$ and the propagation and attenuation vectors normal to the interface, $\mathbf{k}_\beta^{\mathrm{Re}}$ and $\mathbf{k}_\beta^{\mathrm{Im}}$, respectively, result in opposite directions (Fig. 4.5). Since $\mathbf{k}^{\mathrm{Im}}$ is perpendicular to the lines of constant amplitudes in the $z - \mathbf{n}$ plane and is oriented in the direction of the maximum decay of amplitude [Cervený and Pšencík, 2011], a well known characteristic of leaky waves can be observed: while material damping (homogeneous component) causes the amplitude of the partial shear wave to decrease along the radiation direction (dashed lines), due to the inhomogeneous component the wave amplitude increases in direction $\mathbf{n}$. This behaviour can be observed from the intersections of the equi-amplitude lines (solid lines) with the normal to the interface and has been already discussed by different authors [Simmons et al., 1992; Viens et al., 1994; Vogt et al., 2003] in the special case of isotropic elastic open waveguides, for which $\mathbf{k}_S^{\mathrm{Im}} = 0$ and $\gamma_S = \pi/2$ [Carcione et al., 1988; Caviglia et al., 1990].

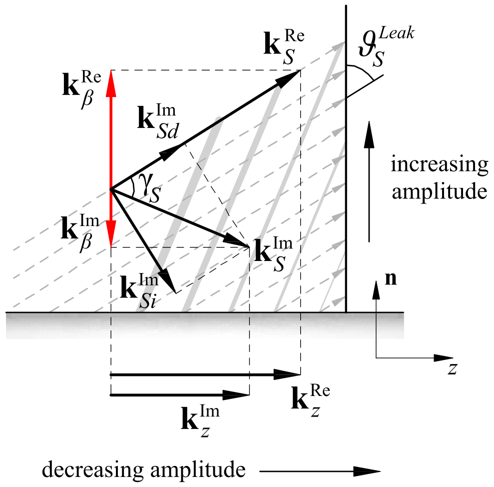

Figure 4.5: Wave vectors configurations for the point $P1$ of Fig. 4.2. The propagation vector $\mathbf{k}_S^{\mathrm{Re}}$ is oriented along the radiation direction (dashed gray lines), while the attenuation vector $\mathbf{k}_S^{\mathrm{Im}}$ is perpendicular to equi-amplitude lines (solid gray lines) and oriented in the direction of maximum decay. Magnitude of displacements is proportional to the thickness of equi-amplitude lines.

If κ_z lies below q_β (point $P3$), then $\mathrm{Re}(\kappa_\beta) > 0$ implies that $\mathrm{Im}(\kappa_\beta) > 0$, and $H_n^{(1)}(\kappa_\beta r)$ is therefore convergent. In this case, the shear wave amplitude decreases along both the radiation direction and the direction normal to the interface (Fig. 4.3).

- Analogous considerations apply in the range $\mathrm{Re}(\kappa_z) < \mathrm{Re}(\kappa_L)$, where both longitudinal and shear bulk waves are radiated in the surrounding medium.

Once the signs for κ_α and κ_β have been determined, the operator $\mathbf{Z}(\kappa_z, \omega)$ results single-valued everywhere on Ω^*. To make it also analytical, it is necessary to remove points corresponding to singularities and discontinuities. In this study, an approach similar to the Vertical Branch Cut Integration (VBCI) method [He and Hu, 2010; Kurkjian, 1985; Liu and Chang, 1996; Zhang et al., 2009] has been adopted.

For the given choices of $\mathrm{sgn}(\kappa_\alpha)$ and $\mathrm{sgn}(\kappa_\beta)$, points of discontinuities are represented by the two vertical lines departing from $\kappa_L = \omega/\tilde{c}_L$ and $\kappa_S = \omega/\tilde{c}_S$ and extending along the positive direction of the imaginary axis (see Fig. 4.2). These lines delimit zones of Ω^* where κ_α and κ_β change sign in both their real and imaginary components. The two vertical cuts are therefore introduced to remove these discontinuities. These cuts also include the bulk wavenumbers, since $H_n^{(1)}(\kappa_{\alpha,\beta} r)$ are not defined for $\kappa_z \to \kappa_{\alpha,\beta}$. The last branch cut is represented by the whole negative real axis, which

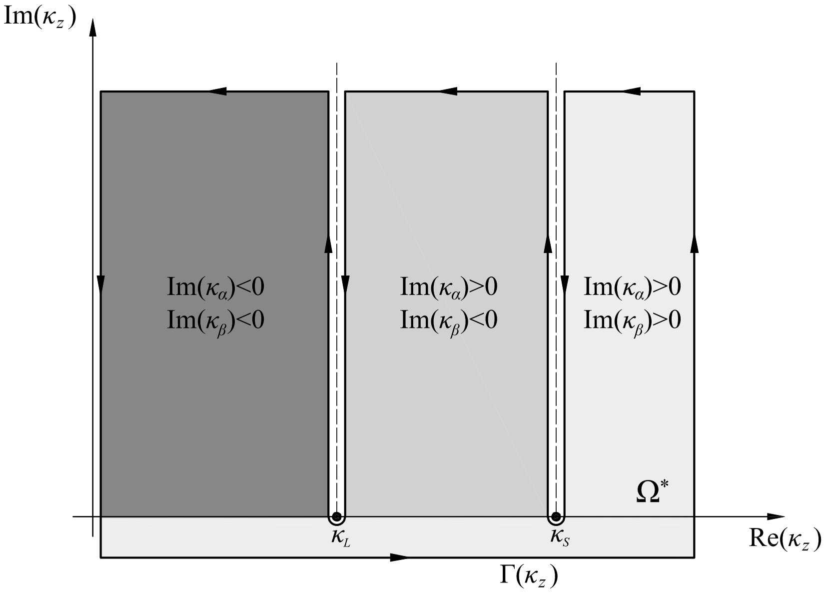

Figure 4.6: Complex κ_z-plane with bulk wavenumbers, vertical branch cuts and integration path for an external isotropic elastic medium. The signs of κ_α and κ_β on Ω^* and along $\Gamma(\kappa_z)$ are determined by imposing the conditions on their imaginary parts as indicated in the different regions.

is a branch cut of the Hankel function, and is easily avoided by restricting the contour $\Gamma(\kappa_z)$ only to positive real values of the axial wavenumbers (right propagating waves).

The integral path in Fig. 4.6 represents a special case of that in Fig. 4.2 when an isotropic elastic surrounding medium is considered. In this case, κ_L and κ_S are purely real and the hyperbolic lines q_α and q_β collapse on the positive imaginary axis and part of the real axis. Since in this case $\mathbf{k}^{\mathrm{Im}}_{L,S} = 0$, lines of constant amplitude become parallel to the radiation direction ($\gamma_{L,S} = \pi/2$), causing the displacement field to grow with distance in the direction normal to the interface [Vogt et al., 2003].

4.7.2 Dispersion characteristics extraction

Once the complete set of eigensolutions $[\kappa_z^m(\omega), \mathbf{Q}^m(\omega)]$ has been determined from Eq. (4.68) for the frequency of interest, the dispersion characteristics for the mth guided mode are computed as

$$c_p^m(\omega) = \frac{\omega}{\mathrm{Re}[\kappa_z^m(\omega)]}, \tag{4.70}$$

$$\alpha^m(\omega) = \mathrm{Im}[\kappa_z^m(\omega)], \tag{4.71}$$

$$c_e^m(\omega) = \frac{\frac{\omega}{2}\mathrm{Im}\left\{\int_{\Omega_s} [\mathbf{u}^m(\omega)]^{\mathrm{H}} \mathscr{L}_z^{\mathrm{T}} \tilde{\mathbf{C}}(\omega)\, \boldsymbol{\epsilon}^m(\omega)\, \mathrm{d}x\mathrm{d}y\right\}}{\frac{1}{4}\mathrm{Re}\left\{\int_{\Omega_s} \omega^2 \rho\, [\mathbf{u}^m(\omega)]^{\mathrm{H}} \mathbf{u}^m(\omega) + [\boldsymbol{\epsilon}^m(\omega)]^{\mathrm{H}} \tilde{\mathbf{C}}(\omega)\, \boldsymbol{\epsilon}^m(\omega)\, \mathrm{d}x\mathrm{d}y\right\}}, \tag{4.72}$$

where the displacements $\mathbf{u}^m(\omega)$ and strains $\boldsymbol{\epsilon}^m(\omega)$ on Ω_s are recovered from $\mathbf{Q}^m(\omega)$ using the interpolations Eq. (4.7) and the strain-displacement relations Eq. (4.8), respectively. It should be noted that Eq. (4.72) does not represent the exact expression of the energy velocity for leaky guided modes. In this case, energy flow curves bend away from the waveguide into the surrounding medium, determining an axial component of the energy flow on Ω_b [Auld, 1973; Castaings and Lowe, 2008; Molz and Beamish, 1996; Simmons et al., 1992]. In such circumstances, the domain integrals in Eq. (4.72) should be rigorously evaluated on $\Omega_s \cup \Omega_b$, which has infinite extension. However, Eq. (4.72) is commonly accepted as sufficiently accurate in GUW applications [Pavlakovic, 1998; Pavlakovic and Lowe, 2003] and becomes exact for non-leaky modes ($\mathrm{Re}(\kappa_z) > \mathrm{Re}(\kappa_S)$), being the wavefield on Ω_b constituted by evanescent waves [Auld, 1973]. In this case there is no energy flux through Ω_b, with the total energy remaining confined within Ω_s and flowing parallel to the interface.

4.8 Numerical applications

In this section, five numerical applications are presented. The first two, which have been studied in literature using the Global Matrix Method and the SAFE method with absorbing regions, are used as validation cases, while the remaining three applications are proposed to show the unique capabilities of the coupled SAFE-2.5D BEM formulation to compute dispersive properties of leaky waves in embedded waveguides of arbitrary cross-section. The material properties used in the analyses are listed in Tab. 4.3. Since only the Maxwell rheological model is considered in this study, the material constants are independent from frequency [Bartoli et al., 2006]. The settings of the contour algorithm have been defined on the basis of single analysis performed at few frequencies, by changing the parameters (N_p, tol_{rank} and tol_{res}) until a stable trend was observable in the separation of the singular values as well as the relative residuals of eigensolutions.

material	i	ρ^i (Kg/m^3)	c_L^i (m/s)	c_S^i (m/s)	β_L^i (Np/wavelength)	β_S^i (Np/wavelength)
steel [1]	st	7932	5960	3260	0.003	0.008
concrete [2]	co	2300	4222.1	2637.5	-	-
grout [1]	gr	1600	2810	1700	0.043	0.100
soil [3]	so	1750	1000	577	0.126	0.349

[1] Pavlakovic et al. [2001]
[2] Castaings and Lowe [2008]
[3] Ketcham et al. [2001]

Table 4.3: Materials constants used for the numerical analyses in Sec. 4.8

4.8.1 Elastic steel bar of circular cross section embedded in elastic concrete

In the first example, the coupled SAFE-BEM formulation is validated with respect to the FEM solution proposed by Castaings and Lowe [2008] for a 20 mm diameter elastic steel (st) bar embedded in elastic concrete (co). The SAFE mesh used in the analysis is composed of 48 six-node triangular elements and 32 nine-node quadrilateral elements, as shown in Fig. 4.7. The BEM mesh matches the SAFE mesh at the interface and is composed of 32 three-node monodimensional elements. The steel longitudinal and shear bulk wave attenuations listed in Tab. 4.3, β_L^{st} and β_S^{st}, respectively, are neglected. The dispersion curves, represented in Figs. 4.8-4.10 in terms of phase velocity, attenuation and energy velocity, have been obtained by considering the upper limit of the integration path in Fig. 4.6 equal to 200 Np/m (1737.18 dB/m), while the horizontal extension has been limited to $\mathrm{Re}(\kappa_S^{co})$ at each frequency step. The attenuation value has been added to the phase and energy velocity curves filling the circular markers with different blue levels. Light and dark levels denote higher and lower values of the attenuations, respectively.

The results for the $L(0,1)$, $F(1,1)$ and $F(1,2)$ modes are in very good agreement with those in Ref. [Castaings and Lowe, 2008]. Of the remaining modes, it is interesting to observe the global behaviour of the $F(2,1)$, which experiences three discontinuities in the range $0 - 200$ kHz. The first discontinuity is located at about 40 kHz, where the mode becomes leaky ($c_p^{F(2,1)} > c_S^{co}$). Moreover, the energy velocity in the frequency

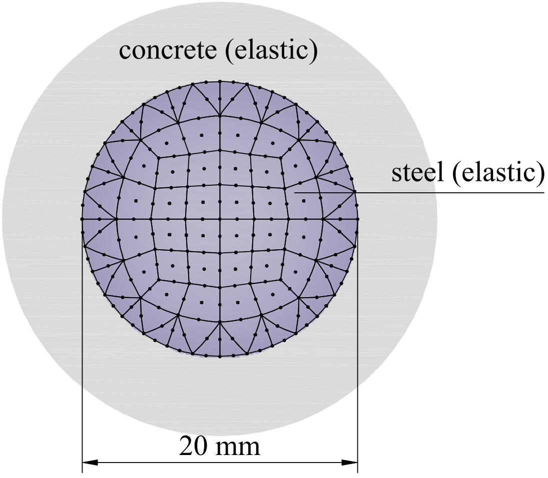

Figure 4.7: SAFE-BEM mesh of the elastic steel bar of circular cross section embedded in elastic concrete.

range corresponding to $c_S^{co} < c_p^{F(2,1)} < c_L^{co}$ is negative. The second discontinuity occurs when the mode crosses the longitudinal bulk velocity of the concrete. In the frequency range $82-130$ kHz, where the mode is indicated as $F(2,1)'$, both longitudinal and shear bulk waves are leaked in the concrete. The third discontinuity occurs in the frequency range $130-136$ kHz, where the phase velocity becomes lower than the longitudinal bulk velocity of the concrete, thus corresponding to radiation of shear bulk waves only.

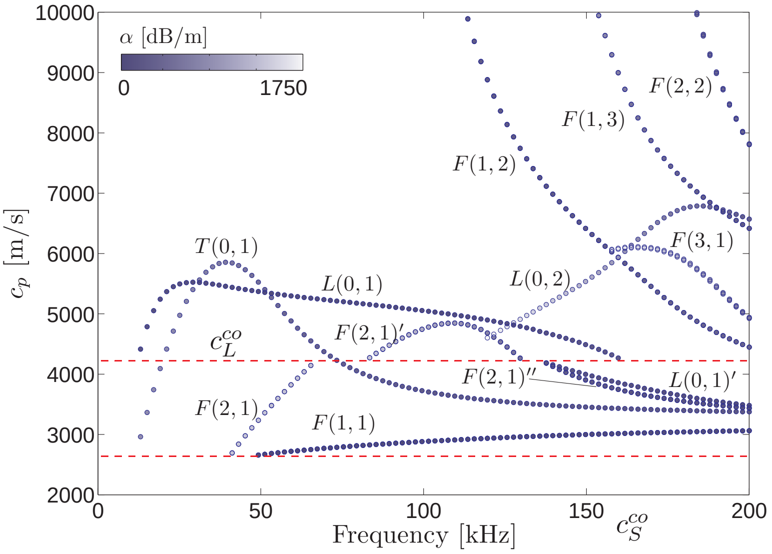

Figure 4.8: Phase velocity dispersion curves for the elastic steel bar of circular cross section embedded in elastic concrete of Fig. 4.7. Modes are indicated as in Ref. [Castaings and Lowe, 2008].

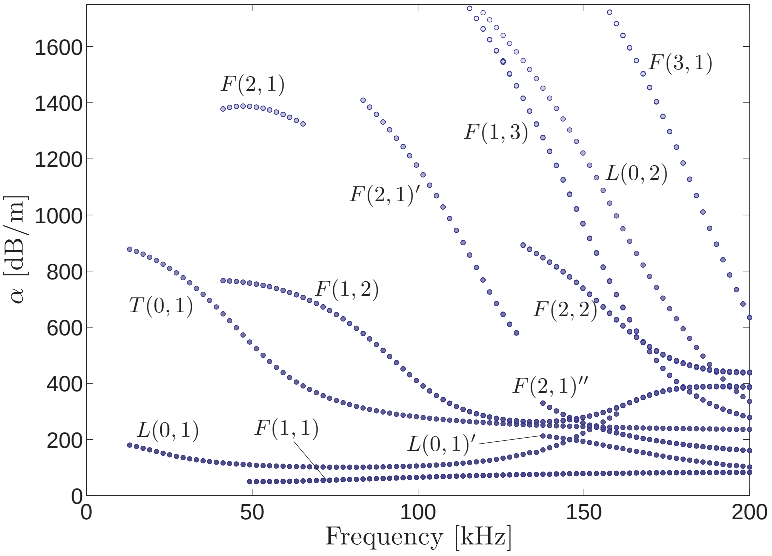

Figure 4.9: Attenuation dispersion curves for the elastic steel bar of circular cross section embedded in elastic concrete of Fig. 4.7. Modes are indicated as in Ref. [Castaings and Lowe, 2008].

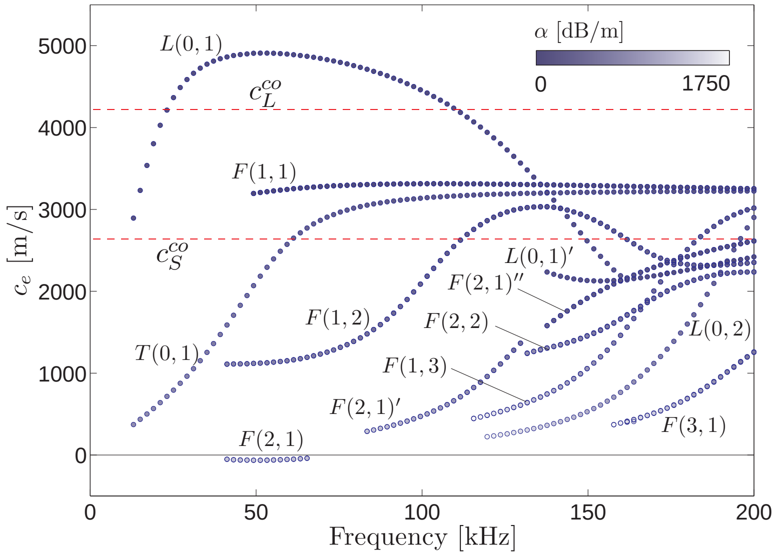

Figure 4.10: Energy velocity dispersion curves for the elastic steel bar of circular cross section embedded in elastic concrete of Fig. 4.7. Modes are indicated as in Ref. [Castaings and Lowe, 2008].

4.8.2 Viscoelastic steel bar of circular cross section embedded in viscoelastic grout

In the second example, a 20 mm diameter viscoelastic steel bar (st) embedded in viscoelastic grout (gr) is considered. This example is used to validate the proposed SAFE-BEM formulation for a case in which all the materials are viscoelastic. The cross section is discretized with the same type and number of elements used in Sec. 4.8.1. The obtained dispersion curves, shown in Figs. 4.12-4.13, are very similar to those in Ref. [Pavlakovic et al., 2001], in which the same problem has been solved by using the software DISPERSE [Pavlakovic et al., 1997]. In the analysis, the imaginary part of the integral path in Fig. 4.2 has been limited to 200 Np/m (1737.18 dB/m). The dispersion curves for the fundamental longitudinal mode, $L(0,1)$, and fundamental flexural mode, $F(1,1)$, are in very good agreement with those in the Ref. [Pavlakovic et al., 2001]. It is also worth noting that the contour integral method is able to detect the portion of the $F(1,1)$ mode in the frequency range $0-15$ kHz, although the non-leaky poles lie in this case very close to κ_S^{gr}. As indicated by Beyn [2012], the contour integral method is indeed able to detect the roots if they lie outside but close to the contour, although the accuracy becomes strongly dependent on the number of integration points used in proximity of the same roots. Since $\mathbf{Z}(\kappa_z, \omega)$ is not defined for $\kappa_z \rightarrow \kappa_S^{gr}$, the solutions provided by the contour integral method can be inaccurate. In fact, some of these solutions have been found to lie in the non-leaky region, while Pavlakovic et al. [2001] have excluded the existence of the $F(1,1)$ mode in this region. Therefore, to get precise and reliable solutions for $\kappa_z \rightarrow \kappa_S^{gr}$, the roots obtained by the contour integral method were improved by using them as initial guesses in the Muller's root finding algorithm [Press et al., 1992].

As in the elastic case of Sec. 4.8.1, discontinuities occur when the modes cross the bulk velocities of the external medium. The discontinuities for the $F(1,1)$ mode in the phase velocity spectra are mild compared with those of the $F(2,1)$ mode. The corresponding jumps in attenuation are clearly observable. As for the $F(2,1)$ mode in Sec. 4.8.1, the branch of the mode that satisfies the condition $c_S^{gr} < c_p^{F(2,1)} < c_L^{gr}$ shows a negative energy velocity.

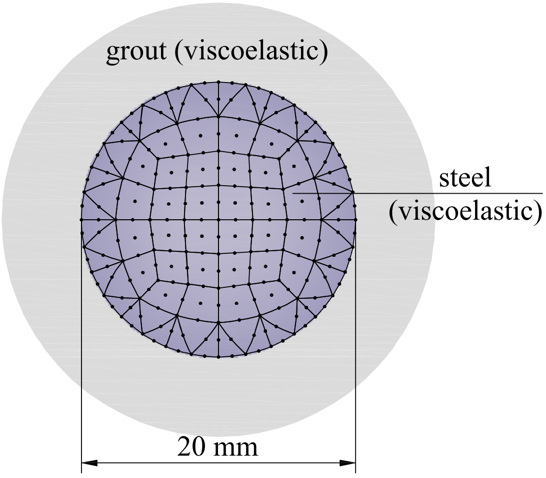

Figure 4.11: SAFE-BEM mesh of the viscoelastic steel bar of circular cross section embedded in viscoelastic grout.

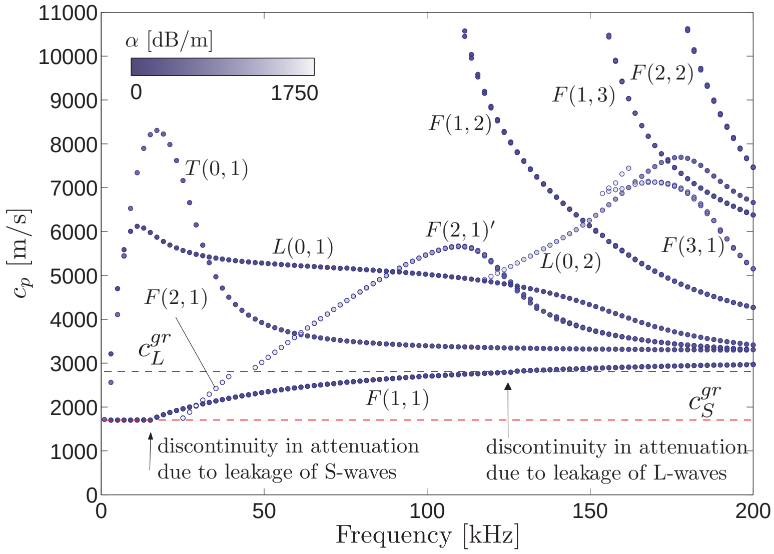

Figure 4.12: Phase velocity dispersion curves for the viscoelastic steel circular bar embedded in viscoelastic grout of Fig. 4.11. Modes are indicated as in Ref. [Pavlakovic et al., 2001].

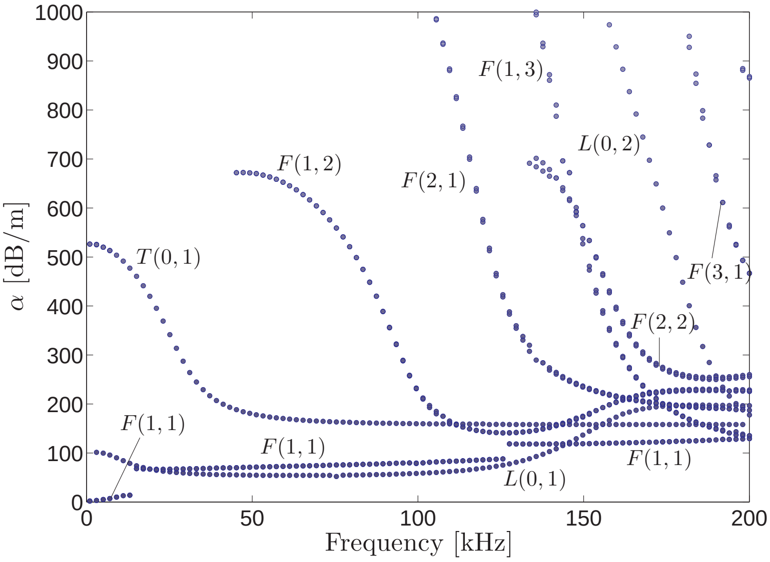

Figure 4.13: Attenuation dispersion curves for the viscoelastic steel circular bar embedded in viscoelastic grout of Fig. 4.11. Modes are indicated as in Ref. [Pavlakovic et al., 2001].

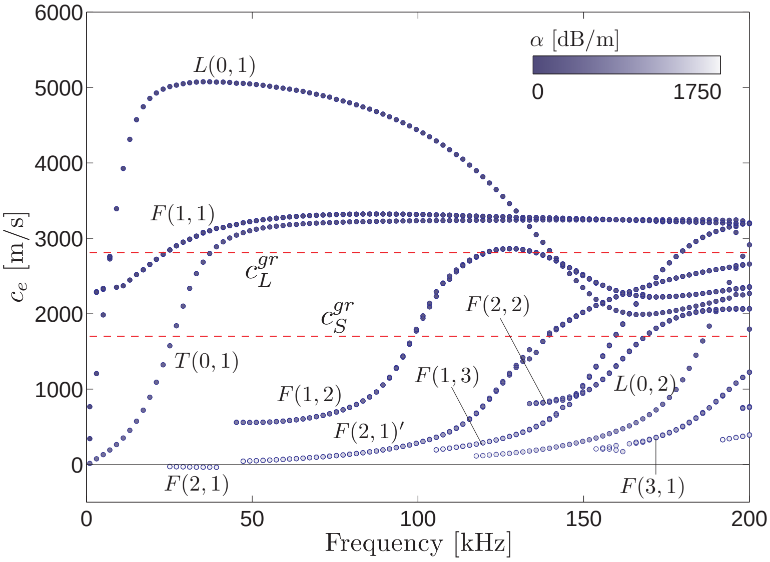

Figure 4.14: Energy velocity dispersion curves for the viscoelastic steel circular bar embedded in viscoelastic grout of Fig. 4.11. Modes are indicated as in Ref. [Pavlakovic et al., 2001].

4.8.3 Viscoelastic steel bar of square cross section embedded in viscoelastic grout

The third example considers a square viscoelastic steel bar (st), of 20 mm side length, embedded in viscoelastic grout (gr) (see Fig. 4.15). Actually, in the considered frequency range the steel does not generally exhibit material damping, thus, to test the presented method a small damping was artificially added by considering the material as viscoelastic. The bar is discretized with 100 eight-node quadrilateral elements, while a boundary mesh of 40 three-node monodimensional elements is adopted to model the surrounding space. A maximum attenuation of 200 Np/m (1737.18 dB/m) has been considered in the analysis. The modes in the dispersion spectra of Fig. 4.16-4.18 have been labeled as in Ref. [Gunawan and Hirose, 2005], where a square waveguide in vacuum was considered. It can be observed that, in the frequency range $0 - 13$ kHz, the first flexural mode, F_1, behaves similarly to the $F(1,1)$ mode for the circular bar in Sec. 4.8.2. Also in this case the Muller's method has been applied to improve the accuracy of these solutions. It is also interesting noting the existence of a non-leaky section for the two skew modes S_1^1 and S_1^2. Similarly to the $F(2,1)$ mode in both the examples of Secs. 4.8.1 and 4.8.2, the energy velocity of these modes becomes positive for values of $c_p^{S_1^1} > c_L^{gr}$ and $c_p^{S_1^2} > c_L^{gr}$.

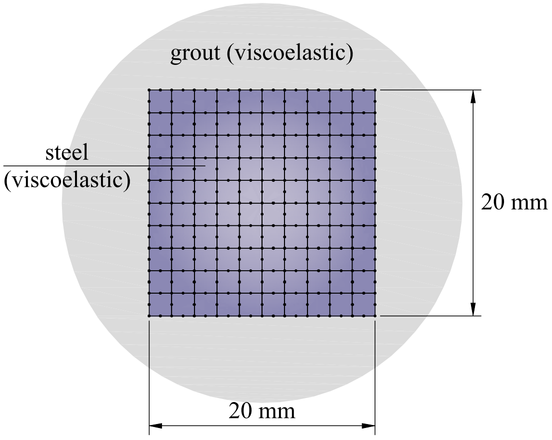

Figure 4.15: SAFE-BEM mesh of the viscoelastic steel bar of square cross-section embedded in viscoelastic grout.

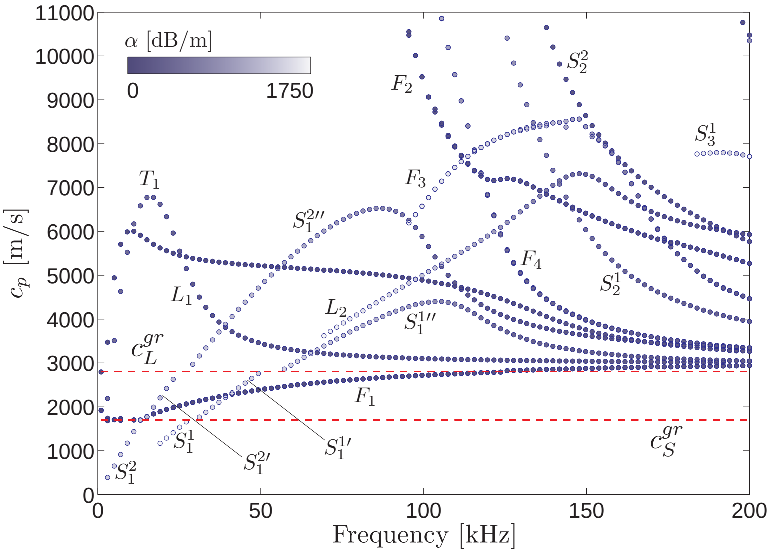

Figure 4.16: Phase velocity dispersion curves for the viscoelastic steel square bar embedded in viscoelastic grout of Fig. 4.15. Modes are indicated as in Ref. [Gunawan and Hirose, 2005], where a square bar in vacuum was considered.

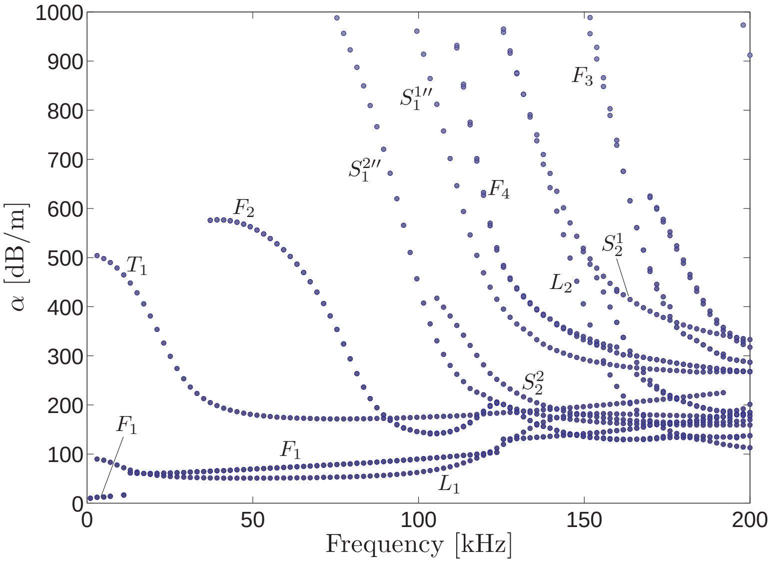

Figure 4.17: Attenuation dispersion curves for the viscoelastic steel square bar embedded in viscoelastic grout of Fig. 4.15. Modes are indicated as in Ref. [Gunawan and Hirose, 2005], where a square bar in vacuum was considered.

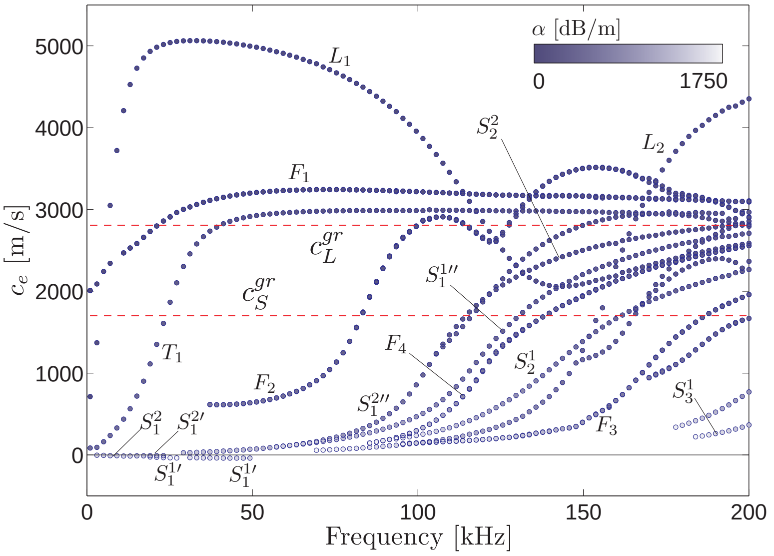

Figure 4.18: Energy velocity dispersion curves for the viscoelastic steel square bar embedded in viscoelastic grout of Fig. 4.15. Modes are indicated as in Ref. [Gunawan and Hirose, 2005], where a square bar in vacuum was considered.

4.8.4 Viscoelastic steel HP200 beam embedded in viscoelastic soil

Despite the fact that non-destructive evaluation of pile-integrity is an important topic in geotechnical engineering [Ding et al., 2011; Liu, 2012; Ni et al., 2008], dispersion analyses of guided waves propagating in foundation piles seem to be limited in literature to simple geometries [Finno and Chao, 2005; Finno et al., 2001]. In this example, the proposed formulation is exploited to predict the dispersion curves for an HP200 steel (st) pile embedded in soil (so). Both steel and surrounding soil are treated as linear viscoelastic materials. The attenuations of L and S waves in soils have been investigated by Ketcham et al. [2001] and are reported in Tab. 4.3 for a surface soil layer. The pile is discretized with 52 eight-node quadrilateral elements and 2 six-node triangular elements, as shown in Fig. 4.19. The BEM mesh is composed of 108 three-node monodimensional elements. Since only the first low order modes are of interest in practical applications, the analysis has been carried out by considering a maximum attenuation of 9.2 Np/m (80.86 dB/m), where these modes have been found to exist in the frequency range $0 - 1000$ Hz. The low order modes are indicated with $m1$, $m2$, $m3$ and $m4$. It can be noted that all these modes are discontinuous in correspondence of the soil bulk velocities. The flexural-like mode $m4$, which is indicated with $m4'$ for $c_p^{m4'} > c_S^{so}$ and with $m4''$ for $c_p^{m4''} > c_L^{so}$, exists in both the two leaky zones of the spectra in the frequency range $600 - 870$ Hz. The longitudinal-like mode $m1$ becomes almost non-dispersive in the frequency range $700 - 1000$ Hz, while its attenuation remains almost constant in the frequency range corresponding to $c_p^{m1} > c_L^{so}$. Since this mode also shows the highest energy velocity combined with the minimum attenuation if compared to the remaining low order modes, it can be particularly suitable in practical inspection applications.

The behaviour of the radiated wavefield for the flexo-torsional $m2$ mode is examined with reference to the analysis of Sec. 4.7.1. From Fig. 4.21, it can be noted that the attenuation of this mode is always greater than the attenuations of both longitudinal and shear bulk waves, $\alpha_L^{so}(\omega) = \mathrm{Im}[\kappa_L^{so}(\omega)]$ and $\alpha_S^{so}(\omega) = \mathrm{Im}[\kappa_S^{so}(\omega)]$, respectively. It is therefore expected that the amplitudes of both longitudinal and shear waves in their corresponding leaky zones must increase with distance along the direction normal to the boundary. On the other hand, for $c_p^{m2} < c_S^{so}$, the radiated wavefield must decay with distance from the pile-soil interface. These behaviours can be observed in Fig. 4.23, where the wavestructures $\mathbf{Q}^{m2}(\omega)$ of the $m2$ mode at various frequencies have been substituted in Eq. (4.67) to compute the radiated wavefield at the nodes $\mathbf{x}'$ of an external mesh. As can be noted, the wavefield in soil for the $m2$ mode at 88.38 Hz

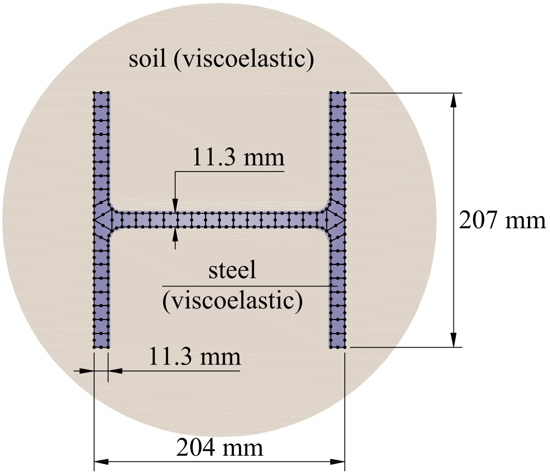

Figure 4.19: SAFE-BEM mesh of the HP200 viscoelastic steel beam embedded in viscoelastic soil.

decays rapidly away from the interface, while the wavefield amplitudes for the $m2'$ mode at 616.16 Hz (radiated S waves) and the $m2''$ mode at 952.02 Hz (radiated S and L waves) increase with distance from the interface.

It should be kept in mind that the modes attenuations resulting from the present analysis are probably overestimated due to the assumptions in Eq. (4.3). Lower and more realistic attenuations could be predicted by inserting an appropriate thin layer between the two media as previously done by Nayfeh and Nagy [Nayfeh and Nagy, 1996] and by Pavlakovic [Pavlakovic, 1998].

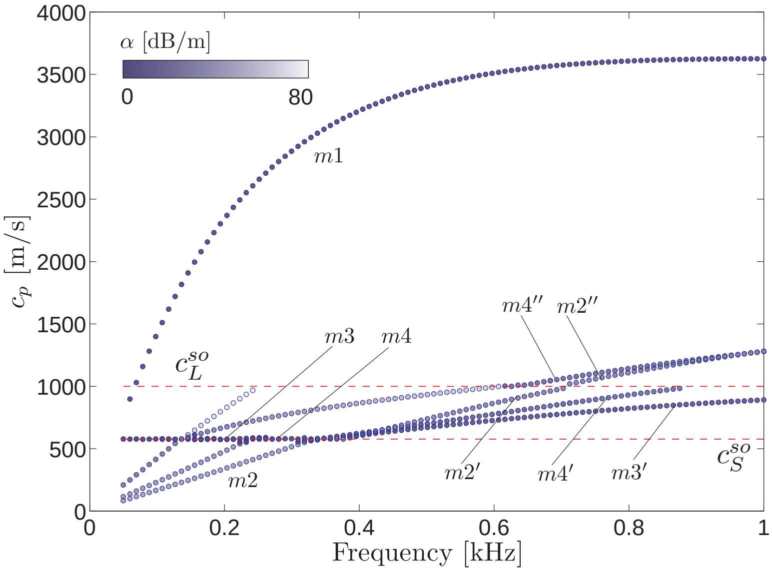

Figure 4.20: Phase velocity velocity dispersion curves for the viscoelastic steel HP200 beam embedded in viscoelastic soil of Fig. 4.19.

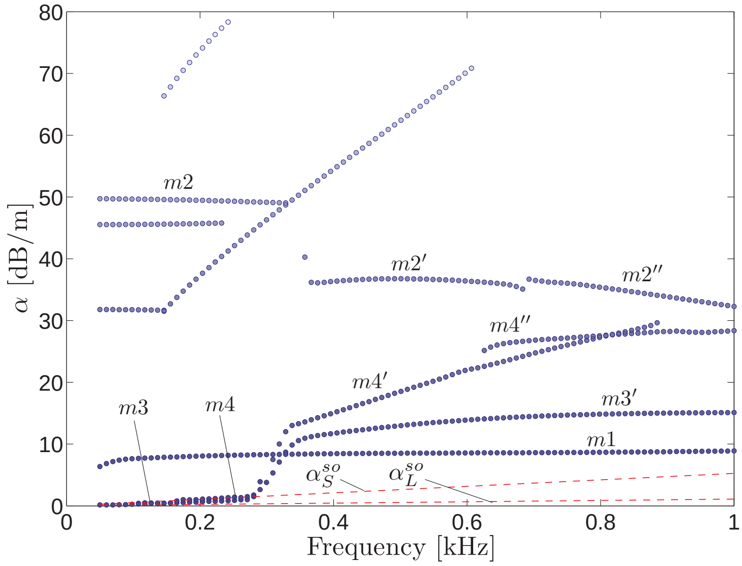

Figure 4.21: Attenuation dispersion curves for the viscoelastic steel HP200 beam embedded in viscoelastic soil of Fig. 4.19.

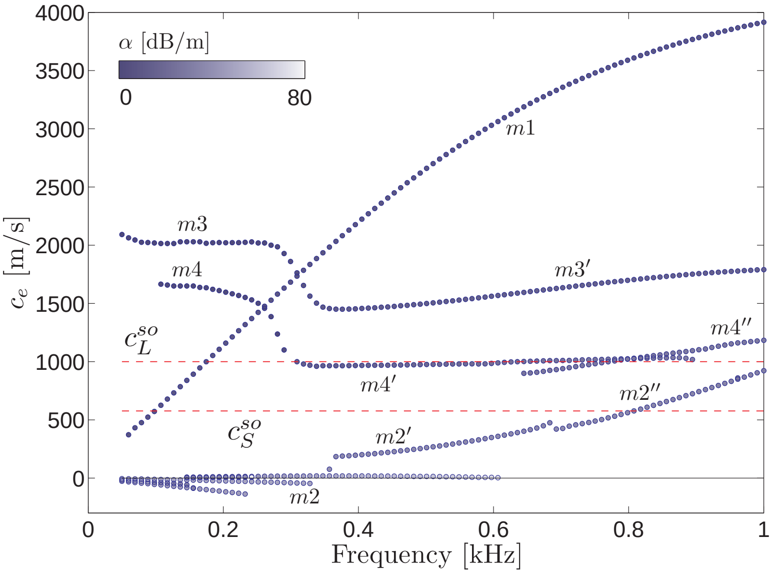

Figure 4.22: Energy velocity dispersion curves for the viscoelastic steel HP200 beam embedded in viscoelastic soil of Fig. 4.19.

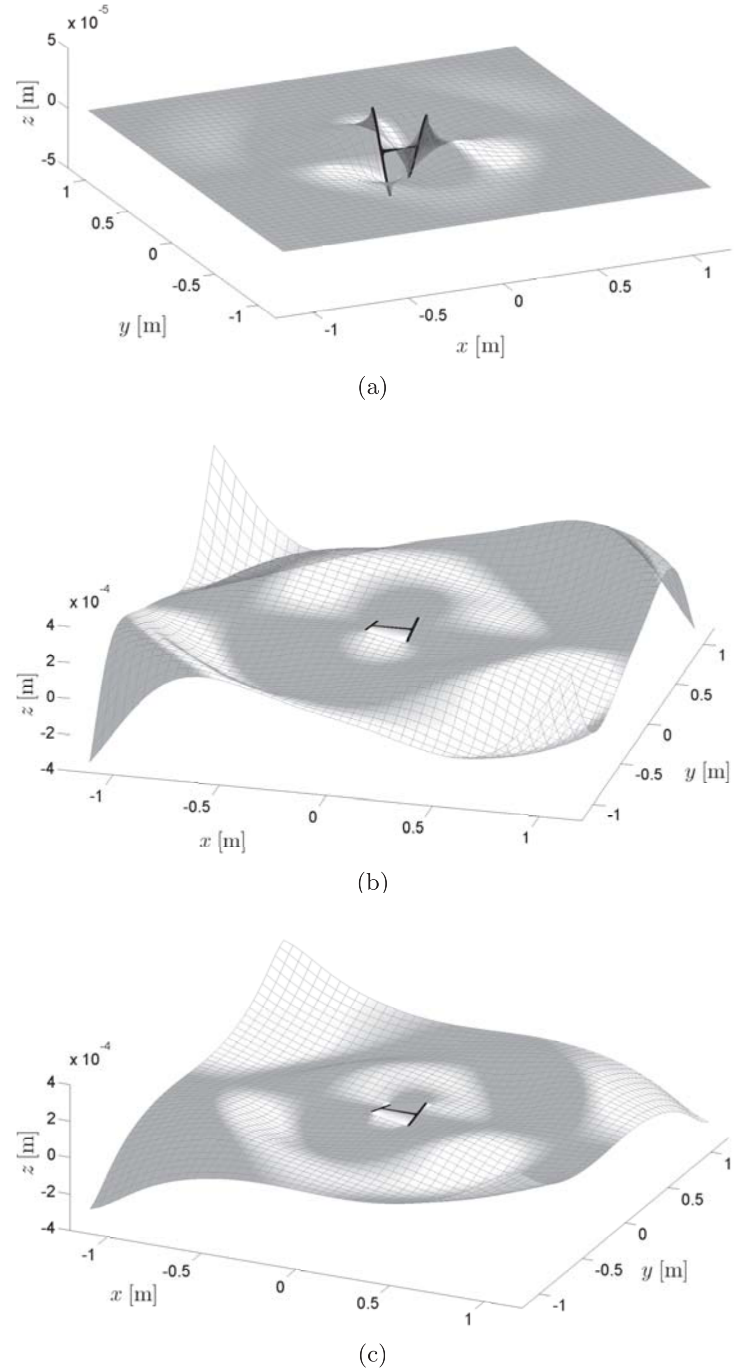

(a)

(b)

(c)

Figure 4.23: Mode shapes and wavefield in soil for (a) mode $m2$ at 88.38 Hz, (b) mode $m2'$ at 616.16 Hz and (c) mode $m2''$ at 952.02 Hz.

4.8.5 Rectangular HSS40×20×2 viscoelastic steel tube embedded in viscoelastic grout

The last numerical example considers the rectangular HSS40×20×2 viscoelastic steel tube embedded in viscoelastic grout of Fig. 4.24.

The cross-section is discretized using a mesh of 36 eight-nodes quadratic elements for the steel section and a boundary element mesh of 36 three-nodes monodimensional elements for the surrounding grout.

The dispersion curves, represented in Fig. 4.25 in terms of real wavenumber, phase velocity, attenuation and energy velocity, are extracted in the frequency range $0 \div 35$ kHz by considering modes with attenuation lower than 903.33 dB/m, i.e. by limiting the contour $\Gamma(\kappa_z)$ to values of κ_z with imaginary component $\mathrm{Im}(\kappa_z) \leq 104$ Np/m at each frequency step.

The first four fundamental modes are identified with $m1$ (longitudinal-like mode), $m2$ (torsional-like mode), $m3$ (first flexural-like mode) and $m4$ (second flexural-like mode). From the inspection of the dispersive spectra of real wavenumbers (Fig. 4.25(a)) it can be noted that when the real part of a guided mode crosses the lines $\mathrm{Re}[\kappa^{gr}_{L,S}(\omega)] = \omega/\mathrm{Re}(\tilde{c}^{gr}_{L,S})$ a jump in both the real and imaginary part of the mode is observed, which reflects into a jump in the phase velocity, attenuation and energy velocity. The existence of such jumps has been explained by Pavlakovic [1998] and it's essentially due to the different amount of energy radiated while passing from the non-leaky to the leaky regime or between two leaky regimes.

From a physical point of view, their existence may indicate the presence of some modes with different wavenumbers at the same frequency (backward jumps) or that the phase velocity of the mode correspond to the bulk phase velocity of the surrounding material. However, as noted by Pavlakovic [1998], sections of curves corresponding to jumps are unsuitable in non-destructive testing because of the unstable characteristics of the corresponding guided modes. Moreover, a mathematical link between different branches of the same mode is generally difficult to obtain, since the dynamic stiffness matrix $\mathbf{K}_b(\kappa_z, \omega)$ is numerically unstable for values of κ_z close to the two bulk wavenumbers of the surrounding medium. Besides the fact that the bulk wavenumbers of the surrounding medium are excluded by the integration path of Fig. 4.2, the contour integral method has however the additional capability to extract roots located outside the contour but close to it [Beyn, 2012]. The accuracy depends in this case on the number of integration points used to discretize the contour near the bulk wavenumbers. An example is given by the second flexural mode $m4$ in the frequency range $0 \div 8$ kHz. In

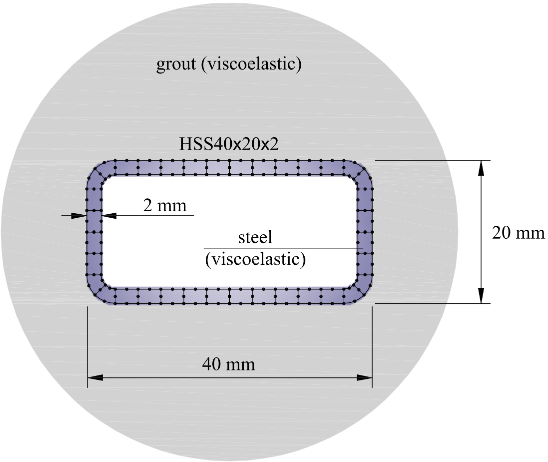

Figure 4.24: SAFE-BEM mesh of the embedded HSS40×20×2 rectangular steel tube
.

this range, the phase velocity of the mode is almost equal to the shear bulk velocity in the cement grout and therefore the Hankel function $H_n^{(1)}(\kappa_\beta r)$ is divergent, leading to the numerical instability. A root searching analysis has been performed in this frequency range by comparing the performances of the contour integral method with those of the Muller's algorithm [Press et al., 1992], which uses a quadratic interpolation to find the minimum of $\det\left[\mathbf{Z}\left(\kappa_z, \omega\right)\right]$. Both the algorithms are able to extract complex roots, but the Muller's algorithm leads to more inaccurate results due to the numerical instabilities in the computation of the determinant. On the other hand, the contour integral method can extract the roots more accurately by performing the integration along the non-singular path around the bulk wavenumbers. However, from the energy velocity spectra of Fig. 4.25(d) it can be noted that the computation of eigenvectors for the mode $m4$ in the frequency range $0 \div 8$ kHz should be further improved in order to obtain acceptable results. This can be achieved by increasing the number of integration points along the integration path in proximity of the bulk wavenumbers. The frequency range $8 \div 24$ kHz corresponds to a gap in the mode $m4$, while in the frequency range $24 \div 35$ kHz the phase velocity of the mode decreases and the mode becomes non-leaky. The first fundamental pseudo-flexural mode $m3$ shows a phase velocity always bounded between the two bulk velocities of the grout in the frequency range $11 \div 35$ kHz. Although not shown in the dispersion spectra, the behaviour of this mode in the frequency range $0 \div 11$ kHz is expected to be similar to that of the $m4$ mode, with the phase velocity almost equal to the shear bulk velocity of the grout.

The fundamental pseudo-torsional mode $m2$ behaves similarly to the mode $m3$, although it can be noted that in the frequency range $20 \div 35$ kHz both its phase velocity and attenuation are almost constant, thus showing a nearly-nondispersive characteristic. This mode, represents therefore a particularly suitable guided mode for nondestructive testing, along with the pseudo-longitudinal mode $m1$.

The latter shows in fact the highest phase velocity and is weakly dispersive in the frequency range $30 \div 35$ kHz, where it also shows the highest energy velocity. However, from the attenuation spectra of Fig. 4.25(c) it can be noted that in the above frequency range the mode $m2$ has a lower attenuation.

The remaining modes of the spectra correspond to higher order modes, some of which are not shown in Figs. 4.25(b) and 4.25(c) for representative reasons. As can be noted, higher order modes generally present several jumps and are characterized by higher attenuation values compared with the fundamental modes.

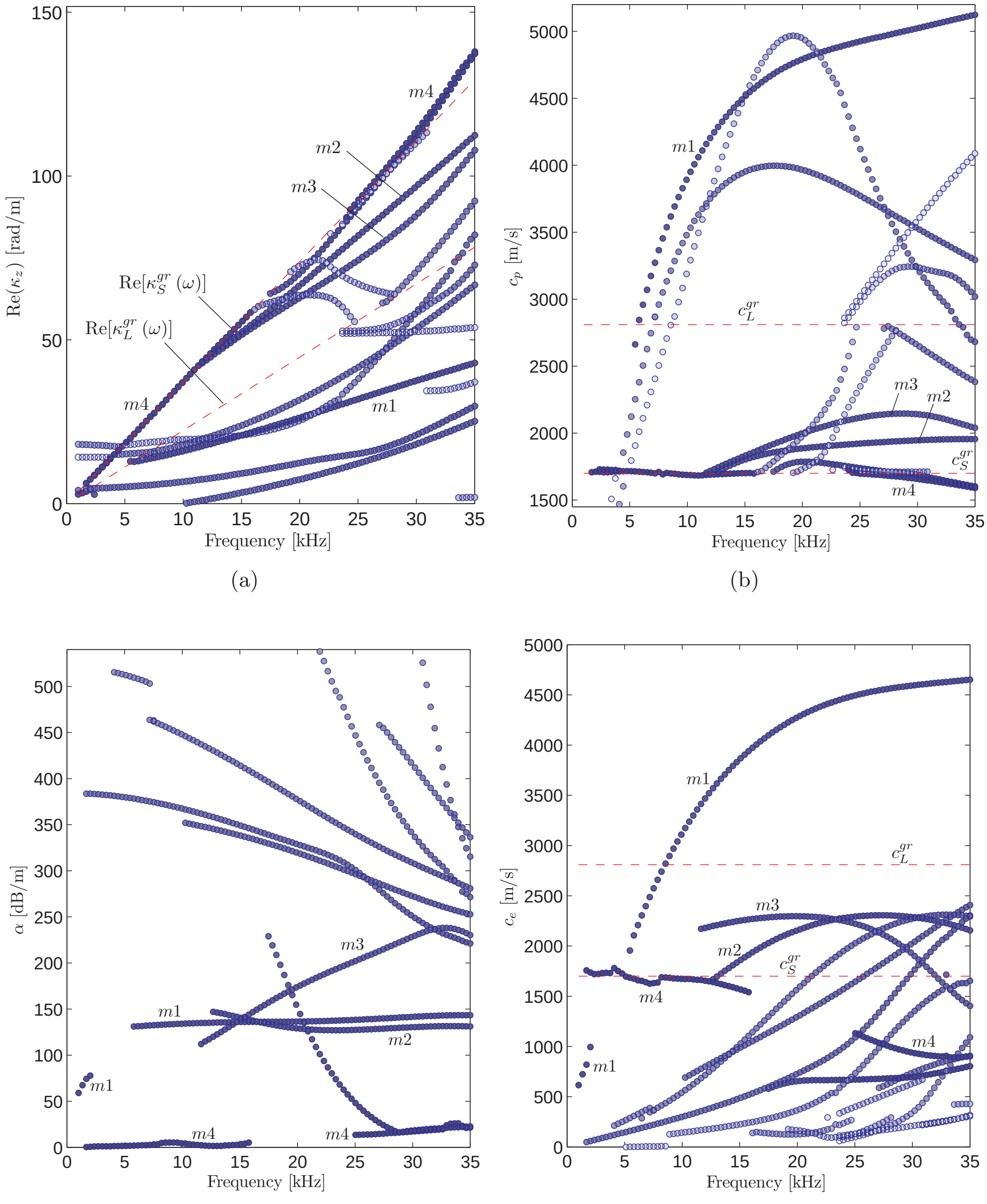

(a) (b)

(c) (d)

Figure 4.25: Dispersion curves for the viscoelastic HSS40×20×2 steel section embedded in viscoelastic grout of Fig. 4.24.

4.9 Conclusions

In this chapter, a Semi-Analytical Finite Element (SAFE) method coupled with a regularized 2.5D Boundary Element Method (BEM) has been applied to derive the dispersive equation for a viscoelastic waveguide of arbitrary cross-section embedded in a viscoelastic isotropic unbounded medium. The coupling between the SAFE and BEM domains has been established in a finite element sense, by converting the infinite BEM domain into a single, wavenumber and frequency dependent, SAFE-like element. The discretized wave equation, which is configured as a nonlinear eigenvalue problem in the complex axial wavenumber, has been solved using a Contour Integral Method. In order to fulfill the requirement of holomorphicity of the dynamic stiffness matrix $\mathbf{Z}\left(\kappa_z, \omega\right)$ inside the complex contour, the phase of the wavenumbers normal to the interface have been chosen consistently with the nature of the waves existing in the surrounding medium.

The method has been first validated against literature results for an elastic circular steel bar embedded in elastic concrete and a viscoelastic circular steel bar embedded in viscoelastic grout, for which results relative to some modes were available. In both cases, a very good agreement between the solutions has been observed.

Next, four new cases have been investigated. The dispersion curves obtained for a viscoelastic steel bar of square cross section embedded in viscoelastic grout show some analogies with those of the viscoelastic steel bar of circular cross section embedded in viscoelastic grout, especially for the longitudinal, torsional and flexural modes. The dispersion analysis performed for a HP200 viscoelastic steel beam embedded in viscoelastic soil show that the first longitudinal mode is the most suitable in practical guided waves-based inspections. The dispersion curves for a rectangular HSS40×20×2 viscoelastic steel tube embedded in viscoelastic grout have been extracted in the $0 \div 35$ kHz frequency range. The results show that the fundamental torsional mode is almost nondispersive in the frequency range $25 \div 35$ kHz and can be therefore suitable for nondestructive testings. The fundamental longitudinal mode presents similar characteristics in the same frequency range, with similar values of attenuation and higher values of energy velocity, but with a more pronounced dispersive behavior compared to the torsional guided mode. The coupled SAFE-2.5D BEM formulation can be further extended to problems with embedded thin walled sections [Shah et al., 2001], immersed waveguides [Godinho et al., 2003], poroelastic surrounding media Lu et al. [2008a,b] and waveguides embedded in both isotropic and layered half spaces [François et al., 2010; Rieckh et al., 2012].

Chapter 5

Leaky Guided Waves in waveguides immersed in perfect fluids: coupled SAFE-2.5D BEM formulation

5.1 Sommario

Una formulazione accoppiata SAFE-2.5D BEM viene proposta per lo studio delle caratteristiche di dispersione di guide d'onda viscoelastiche immerse in fluidi ideali. Il metodo semi-analitico agli elementi finiti è utilizzato per modellare la guida d'onda immersa, mentre la formulazione spettrale agli elementi di contorno, impiegata per modellare il fluido circostante di estensione infinita, consente di superare il problema delle riflessioni spurie tipico di altre tecniche basate sulla discretizzazione del dominio [Fan et al., 2008].

Contrariamente al caso elastodinamico descritto nei Capitoli 3 e 4, le singolarità asintotiche delle soluzioni fondamentali per il problema di Helmholtz non corrispondono quando i punti sorgente e ricevente risultano infinitamente vicini sul contorno. Tuttavia, una formulazione regolarizzata risulta comunque possibile e gli integrali di contorno possono pertanto essere valutati con tecniche di quadratura numerica convenzionali.

In maniera simile a quanto fatto nel Capitolo 4, l'accoppiamento delle regioni SAFE e BEM viene eseguito nel senso degli elementi finiti trasformando le matrici di impedenza della regione BEM in una matrice di rigidezza dinamica equivalente, la quale risulta dipendente dal numero d'onda e dalla frequenza.

Pur ammettendo soluzione unica in linea teorica, risulta ben noto dalla letteratura [Bonnet, 1999; Schenck, 1968] che il problema esterno di Helmholtz modellato con gli elementi di contorno soffre di non unicità della soluzione per specifici autovalori di un corrispondente problema interno. Questo problema, di tipo puramente numerico, si manifesta in maniera maggiore alle alte frequenze, dove lo spettro di dispersione risulta più popolato. L'effetto delle frequenze fittizie viene mitigato usando il metodo CHIEF proposto da [Schenck, 1968], il quale consiste nella scrittura di un sistema di equazioni sovradeterminato che viene in seguito risolto nel senso dei minimi quadrati.

L'equazione d'onda ottenuta dal sistema accoppiato SAFE-2.5D BEM si configura come un problema non lineare agli autovalori, dal quale i numeri d'onda complessi sono per diverse fissate frequenze utilizzando il metodo degli integrali di contorno. Un'analisi delle superfici di Riemann viene descritta in maniera analoga a quella del Capitolo 4, nella quale si tiene conto della legge di Snell-Descartes all'interfaccia solido-fluido.

La formulazione proposta viene dapprima validata confrontando i risultati ottenuti con quelli generati dal software DISPERSE [Pavlakovic and Lowe, 2011] per una barra circolare di titanio immersa nell'olio. Infine, vengono mostrati i risultati relativi ad una barra quadrata di ed una barra ad L di acciaio immerse nell'acqua.

5.2 Introduction and literature review

Guided Ultrasonic Waves (GUW) are widely used as an efficient tool for the non-destructive diagnostic and ultrasonic characterization of fluid-loaded waveguides [Aristégui et al., 2001; Fan et al., 2008; Fan, 2010; Kažys et al., 2010; Long et al., 2003a,c; Lowe, 1992; Ma, 2007; Pavlakovic, 1998; Siqueira et al., 2004; Zernov et al., 2011]. As in the embedded case discussed in Chapter 4, guided waves propagating in immersed waveguides are referred as trapped or leaky. If the phase velocity of the guided wave is lower than the bulk velocity of the surrounding fluid, its energy is totally reflected and mode-converted at the interface and the wave remains trapped within the waveguide. Therefore, the attenuation of such a wave is due only to material damping mechanisms. On the other hand, if the phase velocity of the guided wave exceeds the bulk velocity of the surrounding fluid, its mechanical energy is only partially reflected and mode-converted at the interface. The remaining part is refracted and travels away in the fluid medium in form of bulk waves. Such mechanism, also known as energy leakage, causes the leaky guided waves to be generally highly attenuated, with significant reduction of inspection ranges.

The knowledge of the attenuation of guided waves, as well as their phase and energy velocity, is of paramount importance in guided ultrasonic applications. To this end, dispersion characteristics of immersed waveguides of regular cross-section (plates, rods, cylinders) have been investigated in depth in recent years by means of analytical methods. The behaviour of immersed plate-like structures has been analyzed using analytical expressions by Nayfeh and Chimenti [1988] for the case of fiber-reinforced composite immersed plates and by Ahmad et al. [2002] in the case of fluid-loaded transversely isotropic plates. In their studies, Belloncle et al. [2003, 2004] have extracted the dispersion properties of poroelastic plates immersed in fluids. Guided waves in circular rods immersed in fluids have been studied by several researchers [Ahmad, 2001; Berliner and Solecki, 1996a,b; Dayal, 1993; Honarvar et al., 2011; Nagy, 1995; Nagy and Nayfeh, 1996].

For multilayered cylindrical and plate-like systems, the matrix family methods have been widely applied in the literature for the dispersion analysis of both embedded and immersed waveguides. A comparison between the Transfer Matrix Method (TMM) [Haskell, 1953; Thomson, 1950] and the Global Matrix Method (GMM) [Knopoff, 1964; Randall, 1967] applied to free, embedded and immersed plates can be found in the work of Lowe [1995]. Using the Transfer Matrix Method, Nayfeh and Nagy [1996] have investigated the propagation of axisymmetric waves in coaxial layered anisotropic fibers embedded in solids and immersed in fluids. The Global Matrix Method for plate-like structures has been used by Lowe [1992] for the detection of a brittle layer in diffusion bonded titanium and by Bernard et al. [2001] to study the energy velocity in non-absorbing plates immersed fluids. In his work, Pavlakovic [1998] has applied the GMM to study free, embedded and immersed multilayered cylindrical systems. This method has also been used for the numerical analyses and experimental investigations of fluid-filled pipes surrounded by fluids [Aristégui et al., 2001] and buried water pipes [Long et al., 2003a,c].

In the context of numerical methods, and in particular spectral Finite Element Methods, Hladky-Hennion et al. [1997, 1998] have proposed a finite element formulation enriched with a non-reflective boundary condition applied on the perimeter of the fluid domain. More recently, Fan et al. [2008] have proposed a SAFE formulation in which absorbing regions are used to simulate the unbounded surrounding fluid. The absorbing region has been modeled considering the same mass density of the fluid, but increasing damping properties with increasing distance from the central axis of the waveguide. The two methods above present the advantages that only small changes are required in existing FEM/SAFE codes, while the discrete dispersive equation remains formulated as a polynomial eigenvalue problem, which can be solved by standard routines. However, due to the large number of elements required, the dimension of the problem increases considerably, thus leading to a large set of eigensolutions from which only meaningful guided modes with energy concentrated in the waveguide must be filtered. Other hybrid SAFE formulations have been proposed in literature for waveguides embedded in solid media, which use infinite elements [Jia et al., 2011] and Perfectly Matched Layers (PML) [Treyssède et al., 2012]. Although these formulations could be equally extended to the case of infinite surrounding fluids, they suffer of some drawbacks. For instance the wave attenuation is described by user-defined shape functions in infinite elements, while in the PML is defined by analytical continuation of the equilibrium equations into the complex spatial coordinates, which is introduced by an arbitrary complex function.

On the contrary, a Boundary Element Method (BEM) approach allows for a more natural description of the radiation problem.

The 2.5D BEM has been used by different authors for the extraction of dispersion curves of fluid-filled boreholes in solid formations [Tadeu et al., 2002a; Tadeu and Santos, 2001; Zengxi et al., 2007] and submerged cylindrical solids with irregular cross-section geometry [Godinho et al., 2003; Pereira et al., 2002]. However, attenuation spectra are not obtained in these works.

In this chapter, a coupled SAFE-2.5D BEM formulation to model guided waves in immersed waveguides is proposed, in which the SAFE method is used to model the viscoelastic waveguide while the BEM is used to account for surrounding infinite inviscid fluids. The formulation described in this chapter is the natural extension of that proposed in Chapter 4.

In the case of sourronding fluids, the well known problem of spurious solutions due to the non-uniqueness of the external Helmholtz boundary integrals is addressed by means of the CHIEF method [Schenck, 1968]. Numerical results obtained for a titanium bar immersed in oil are in perfect agreement with those obtained using the GMM [Pavlakovic and Lowe, 2011], while new results are presented for viscoelastic steel bars with square and L-shaped cross-section immersed in water.

5.3 Discretized wave equation

5.3.1 Problem statement

The equation governing the wave propagation problem under consideration is obtained for the translational invariant system of Fig. 5.1, in which Ω_s denotes the cross-section of the immersed waveguide in the $x-y$ plane, while Ω_f is used to indicate the cross-section of the infinite surrounding fluid. The in-plane fluid-structure interface is denoted by $\partial\Omega = \partial\Omega_s = \partial\Omega_f$.

The geometric an and mechanical parameters used to describe the waveguide are assumed as in Sec. 4.3, and will not be repeated here. Since only non-viscous ideal fluids are considered, the acoustic properties of the surrounding liquid are identified by the mass density ρ^f and the phase speed of the longitudinal bulk wave, c_L^f.

Finally, the wave propagation process is assumed with a wavenumber-frequency dependence of any scalar and vectorial field of the form $\exp\left[\mathrm{i}\left(\kappa_z z - \omega t\right)\right]$.

5.3.2 SAFE model of the waveguide

The equilibrium equation of the fluid-loaded waveguide can be obtained from Eq. (4.5) in absence of externally applied surface loads. By letting $\mathbf{t}_s\left(\mathbf{x}, \kappa_z, \omega, \right) = \mathbf{0}$, the following integral equation is obtained

$$\begin{aligned}\omega^2 \int_{\Omega_s} \delta\mathbf{u}^{\mathrm{T}} \rho\left(\mathbf{x}\right) \mathbf{u} \mathrm{d}x\mathrm{d}y - \int_{\Omega_s} \left(\delta\boldsymbol{\epsilon}\left(\mathbf{u}\right)\right)^{\mathrm{T}} \tilde{\mathbf{C}}\left(\mathbf{x}, \omega\right) \boldsymbol{\epsilon}\left(\mathbf{u}\right) \mathrm{d}x\mathrm{d}y \\ - \int_{\partial\Omega_s} \delta\mathbf{u}^{\mathrm{T}} \mathbf{t}_b\left(\mathbf{x}, \kappa_z, \omega\right) \mathrm{d}s = 0,\end{aligned} \tag{5.1}$$

where the various terms are defined as in Sec. 4.3. Following the procedure described in Sec. 4.4, the discretization of the immersed waveguide is carried out at the cross-section level by using semi-isoparametric quadratic finite elements. The displacement within the eth SAFE element is interpolated as

$$\mathbf{u}^e\left(\mathbf{x}, z, t\right) = \mathbf{N}\left(\boldsymbol{\xi}\right)\mathbf{q}^e\left(z, t\right) \tag{5.2}$$

which can be substituted in the compatibility relations Eq. (4.8) and then in Eq. (5.1). After applying the usual standard finite element assembling procedure, the wave equation results in the following expression

$$\left\{\kappa_z^2\mathbf{K}_3 + \mathrm{i}\kappa_z\left[\mathbf{K}_2 - \mathbf{K}_2^{\mathrm{T}}\right] + \mathbf{K}_1 - \omega^2\mathbf{M}\right\}\mathbf{Q}\left(\kappa_z, \omega\right) + \mathbf{F}_b\left(\kappa_z, \omega\right) = \mathbf{0}, \tag{5.3}$$

where the operators inside the braces are defined as in Eqs. (4.11)-(4.14). In Eq. (5.3), $\mathbf{Q}\left(\kappa_z, \omega\right)$ represents the global vector of nodal displacements while $\mathbf{F}_b\left(\kappa_z, \omega\right)$ is the vector of nodal forces at the fluid-structure interface, which is derived in the following sections via a boundary element formulation.

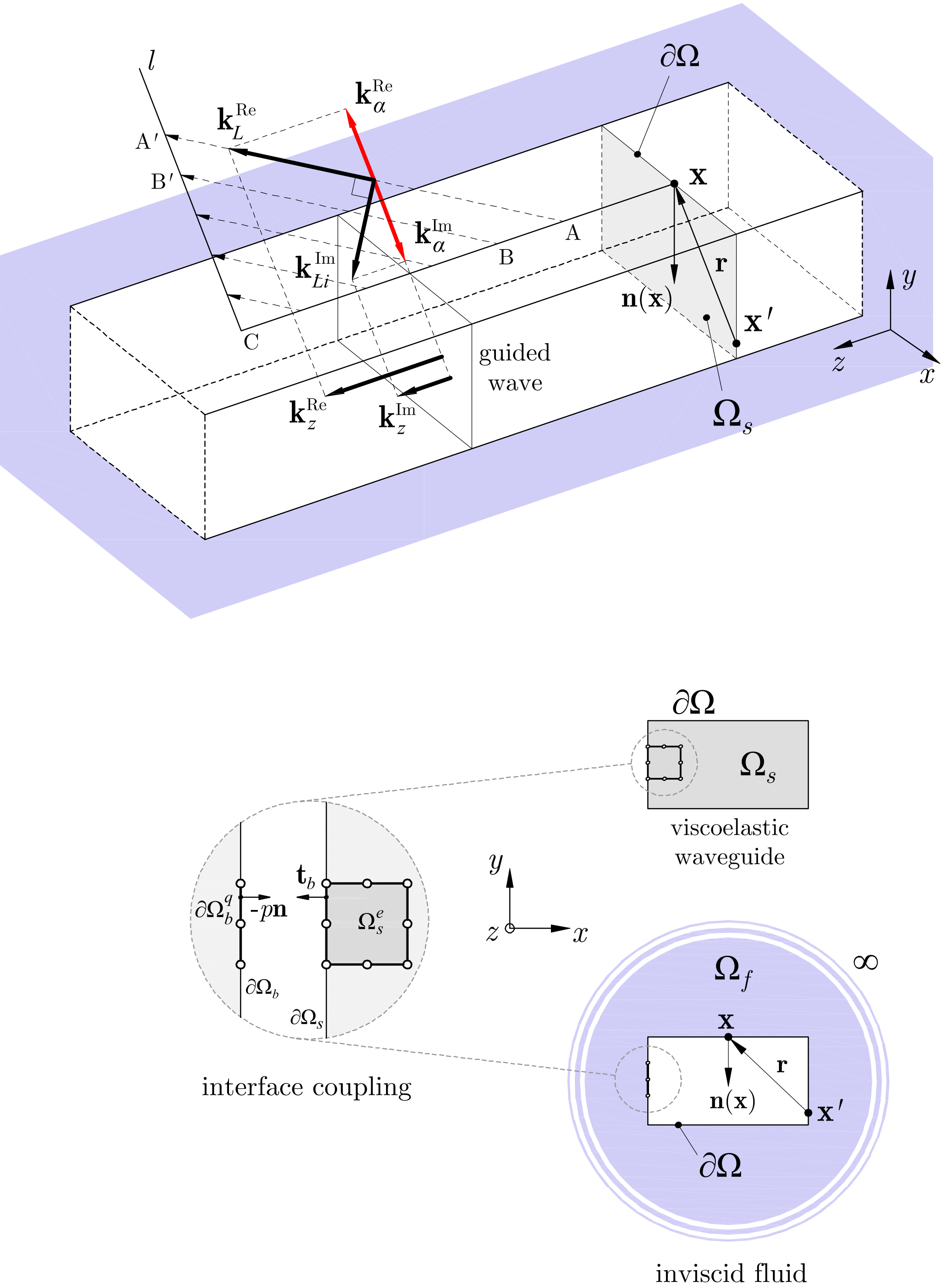

Figure 5.1: Analytical model of the immersed waveguide.

5.3.3 2.5D BEM model of the fluid domain

The linear acoustic problem in the translational invariant fluid domain is governed by the 2.5D Helmholtz equation. As shown in other works [Nilsson et al., 2009; Tadeu et al., 2012], this equation can be readily obtained from the three-dimensional case by applying the space Fourier transform along the longitudinal coordinate (z-coordinate). The resulting espression is formally indentical to the Helmholtz equation in three dimensions, providing that the 3D Laplace operator is substituded by the corresponding 2D one and the bulk wavenumber of the fluid is substituted by the wavenumber normal to the interface. The 2.5D Helmholtz equation then becomes

$$\left(\frac{\partial^2}{\partial x^2}+\frac{\partial^2}{\partial y^2}\right)p\left(\mathbf{x},\kappa_z,\omega\right)+\kappa_\alpha^2 p\left(\mathbf{x},\kappa_z,\omega\right)=0, \quad \mathbf{x}\in\Omega_f \tag{5.4}$$

where $p\left(\mathbf{x},\kappa_z,\omega\right)$ is the acoustic pressure in the fluid and $\kappa_\alpha=\pm[(\kappa_L^f)^2-\kappa_z^2]^{1/2}$ denotes the wavenumber in the $x-y$ plane, being $\kappa_L^f=\omega/c_L^f$ the real wavenumber of the longitudinal wave in the fluid medium. The equilibrium of normal tractions and continuity of normal displacements are prescribed via the boundary conditions [Fan et al., 2008]

$$-p\left(\mathbf{x},\kappa_z,\omega\right)\mathbf{n}\left(\mathbf{x}\right)=\mathbf{t}_b\left(\mathbf{x},\kappa_z,\omega\right), \tag{5.5}$$

$$\frac{\partial p}{\partial \mathbf{n}}\left(\mathbf{x},\kappa_z,\omega\right)=\rho^f\omega^2 u_{\mathbf{n}}\left(\mathbf{x},\kappa_z,\omega\right), \quad \mathbf{x}\in\partial\Omega \tag{5.6}$$

where $\partial(\cdot)/\partial\mathbf{n}$ denotes the directional derivative along the outward pointing normal to the fluid domain $\mathbf{n}\left(\mathbf{x}\right)$ and

$$u_{\mathbf{n}}\left(\mathbf{x},\kappa_z,\omega\right)=\mathbf{u}\left(\mathbf{x},\kappa_z,\omega\right)\cdot\mathbf{n}\left(\mathbf{x}\right) \tag{5.7}$$

is the normal displacement component at the same point.

The boundary integral equation can be derived from the Green's second identity applied to an unknown physical state

$$\left[p\left(\mathbf{x},\kappa_z,\omega\right),\frac{\partial p\left(\mathbf{x},\kappa_z,\omega\right)}{\partial\mathbf{n}}\right]$$

and the state of the fundamental solutions

$$\left[P^D\left(r,\kappa_z,\omega\right),\frac{\partial P^D\left(r,\kappa_z,\omega\right)}{\partial\mathbf{n}}\right]$$

that satisfy the 2.5D Helmholtz equation in the full space when a unitary line load

$\mathfrak{p}\left(x', y', z', t\right) = \delta\left(\mathbf{x} - \mathbf{x}'\right) \exp\left[\mathrm{i}\left(\kappa_z z' - \omega t\right)\right]$ is acting at a fixed point $\mathbf{x}'$ [Bonnet, 1999]. Using the Green's second identity and Eq. (5.6), the integral representation theorem for source points $\mathbf{x}' \in \Omega_f$ results [Zengxi et al., 2007]

$$\begin{aligned} c\left(\mathbf{x}'\right) p\left(\mathbf{x}', \kappa_z, \omega\right) =& \rho^f \omega^2 \int_{\partial\Omega} P^D\left(r, \kappa_z, \omega\right) u_{\mathbf{n}}\left(\mathbf{x}, \kappa_z, \omega\right) \mathrm{d}s\left(\mathbf{x}\right) \\ & - \int_{\partial\Omega} \frac{\partial P^D\left(r, \kappa_z, \omega\right)}{\partial \mathbf{n}} p\left(\mathbf{x}, \kappa_z, \omega\right) \mathrm{d}s\left(\mathbf{x}\right), \\ & \mathbf{x}' \in \Omega_f,\ \mathbf{x} \in \partial\Omega \end{aligned} \tag{5.8}$$

where $r = \left|\mathbf{x} - \mathbf{x}'\right|$ is the usual in-plane source-receiver distance while $c\left(\mathbf{x}'\right)$ is equal to 1 when $\mathbf{x}' \in \Omega_f$ and 0 otherwise. The dynamic fundamental solutions $P^D\left(r, \kappa_z, \omega\right)$ and $\partial P^D\left(r, \kappa_z, \omega\right) / \partial \mathbf{n}$ represent, respectively, the pressure and flux at $\mathbf{x}$ when the harmonic line source passes through $\mathbf{x}'$. These solutions can be recovered from the corresponding 3D solutions (see, for example, [Bonnet, 1999; Brebbia and Dominguez, 1989]) by applying the space Fourier transform in the z-coordinate. The resulting expressions are formally identical to those of the 3D case, but require the substitution of the bulk wavenumber κ_L^f with the radial wavenumber κ_α, leading to

$$P^D\left(r, \kappa_z, \omega\right) = \frac{\mathrm{i}}{4} H_0^{(1)}\left(\kappa_\alpha r\right), \tag{5.9}$$

$$\frac{\partial P^D\left(r, \kappa_z, \omega\right)}{\partial \mathbf{n}} = -\frac{\mathrm{i}}{4} \kappa_\alpha H_1^{(1)}\left(\kappa_\alpha r\right) \frac{\partial r}{\partial x_k} n_k. \quad k = 1, 2 \tag{5.10}$$

In order to extend Eq. (5.8) to source points $\mathbf{x}'$ located on the boundary $\partial\Omega$, the limiting process $\mathbf{x}' \in \Omega_f \rightarrow \mathbf{x}' \in \partial\Omega$ can be followed, in which boundary integrals involving the fundamental fluxes are convergent in the Cauchy Principal Value sense [Bonnet, 1999; Chen et al., 2005].

A regularized boundary integral equation can be obtained by applying the so called equi-potential condition for external domains, which reads [Brebbia and Dominguez, 1989; Tomioka and Nishiyama, 2010]

$$c\left(\mathbf{x}'\right) = -\int_{\partial\Omega} \frac{P^S\left(r\right)}{\partial \mathbf{n}} \mathrm{d}s\left(\mathbf{x}\right) + 1 \tag{5.11}$$

where

$$P^S\left(r\right) = P^D\left(r, \kappa_z = 0, \omega = 0\right), \tag{5.12}$$

is the fundamental solution of the 2D Laplace equation.

Substituting Eq. (5.11) into Eq. (5.8) and making use of the subtraction-addition technique proposed by Lu et al. [2008b] for weakly singular integrals, the following boundary integral equation is obtained

$$\begin{aligned} p\left(\mathbf{x}', \kappa_z, \omega\right) =& \rho^f \omega^2 \int_{\partial\Omega} \left[P^D\left(r, \kappa_z, \omega\right) - P^S\left(r\right)\right] u_{\mathbf{n}}\left(\mathbf{x}, \kappa_z, \omega\right) \mathrm{d}s\left(\mathbf{x}\right) \\ &+ \rho^f \omega^2 \int_{\partial\Omega} P^S\left(r\right) u_{\mathbf{n}}\left(\mathbf{x}, \kappa_z, \omega\right) \mathrm{d}s\left(\mathbf{x}\right) \\ &- \int_{\partial\Omega} \left[\frac{\partial P^D\left(r, \kappa_z, \omega\right)}{\partial \mathbf{n}} p\left(\mathbf{x}, \kappa_z, \omega\right) - \frac{\partial P^S\left(r\right)}{\partial \mathbf{n}} p\left(\mathbf{x}', \kappa_z, \omega\right)\right] \mathrm{d}s\left(\mathbf{x}\right), \\ &\left(\mathbf{x}', \mathbf{x}\right) \in \partial\Omega \end{aligned} \tag{5.13}$$

where the fundamental solutions of the 2D potential problem are defined as [Brebbia and Dominguez, 1989]

$$P^S\left(r\right) = \frac{1}{2\pi} \ln \frac{1}{r}, \tag{5.14}$$

$$\frac{\partial P^S\left(r\right)}{\partial \mathbf{n}} = -\frac{1}{2\pi r} \frac{\partial r}{\partial x_k} n_k. \quad k = 1, 2 \tag{5.15}$$

Since $P^D\left(r, \kappa_z, \omega\right)$ and $P^S\left(r\right)$ behave asymptotically as $\ln 1/r$ for $r \to 0$, the kernel in the first boundary integral of Eq. (5.13) is nonsingular with the highest order term of $O\left(1\right)$, while the kernel in the second boundary integral has a weak singularity of order $\ln 1/r$. Therefore, the first and second boundary integrals in Eq. (5.13) can be evaluated numerically using the Gauss-Legendre and Gauss-Laguerre quadrature formulas, respectively [Gao and Davies, 2001; Stroud and Secrest, 1996].

From the inspection of Eqs. (5.10) and (5.15) it can be noted that the asymptotic singularities of the dynamic and static fundamental solutions do not correspond when the source point approaches the receiver point. This is in contrast with the 2.5D elastodynamic case of Chapters 3 and 4.

However, Eq. (5.13) still represents a regular boundary integral equation [Tomioka and Nishiyama, 2010]. In fact, the kernels in the last boundary integral can be rewritten as (superscripts D and S omitted)

$$\frac{\partial P}{\partial \mathbf{n}} = \frac{\partial P}{\partial r} \mathbf{e}_r \cdot \mathbf{n}, \tag{5.16}$$

in which

$$\mathbf{e}_r = \frac{\mathbf{x} - \mathbf{x}'}{\left|\mathbf{x} - \mathbf{x}'\right|}. \tag{5.17}$$

is the unit vector between the receiver and source points. Since $\mathbf{e}_r \perp \mathbf{n}$ for $r \to 0$, the inner vector product becomes zero and the strong singularities in Eqs. (5.10) and (5.15) vanish. Therefore, the last boundary integral in Eq. (5.13) is nonsingular and can be evaluated by means of the Gauss-Legendre quadrature formula.

5.3.4 Boundary element discretization

The fluid-structure interface $\partial\Omega$ is discretized with N_b quadratic monodimensional elements with nodes coincident to the boundary nodes of the SAFE mesh. Pressures and normal displacements are interpolated within the generic qth boundary element of domain $\partial\Omega_b^q$ as follows

$$p^q\left(\eta,\kappa_z,\omega\right) = \mathbf{N}\left(\eta\right)\mathbf{p}^q\left(\kappa_z,\omega\right) \tag{5.18}$$

$$u_{\mathbf{n}}^q\left(\eta,\kappa_z,\omega\right) = \mathbf{N}\left(\eta\right)\mathbf{q}_{\mathbf{n}}^q\left(\kappa_z,\omega\right) \tag{5.19}$$

where $\mathbf{N}\left(\eta\right)$ is the matrix of shape functions in the natural coordinate η, while $\mathbf{p}^q\left(\kappa_z,\omega\right)$ and $\mathbf{q}_{\mathbf{n}}^q\left(\kappa_z,\omega\right)$ are vectors of nodal pressures and normal displacements, respectively. Applying a point collocation scheme in which collocation points are assumed coincident with the nodes of the boundary element mesh and making use of Eqs. (5.18) and (5.19), the boundary integral Eq. (5.13) is recasted in the following discretized form

$$\mathbf{W}_b\left(\kappa_z,\omega\right)\mathbf{P}_b\left(\kappa_z,\omega\right) = \rho^f\omega^2\mathbf{G}_b\left(\kappa_z,\omega\right)\mathbf{Q}_b^{\perp}\left(\kappa_z,\omega\right), \tag{5.20}$$

where $\mathbf{G}_b\left(\kappa_z,\omega\right)$ and $\mathbf{W}_b\left(\kappa_z,\omega\right)$ are influence operators involving the fundamental pressures and fluxes, respectively, $\mathbf{P}_b\left(\kappa_z,\omega\right)$ denotes the global vector of nodal pressures and $\mathbf{Q}_b^{\perp}\left(\kappa_z,\omega\right)$ represents the global vector of normal displacements at the boundary nodes. The acoustic pressure at any $\mathbf{x}' \in \Omega_f$ can be computed from the discrete representation of Eq. (5.8)

$$c\left(\mathbf{x}'\right)p_d\left(\mathbf{x}',\kappa_z,\omega\right) = \rho^f\omega^2\mathbf{G}_d\left(\kappa_z,\omega\right)\mathbf{Q}_b^{\perp}\left(\kappa_z,\omega\right) - \mathbf{W}_d\left(\kappa_z,\omega\right)\mathbf{P}_b\left(\kappa_z,\omega\right), \tag{5.21}$$

where $\mathbf{G}_d\left(\kappa_z,\omega\right)$ and $\mathbf{W}_d\left(\kappa_z,\omega\right)$ are influence operators that are built on a element-by-element basis for the given source point $\mathbf{x}' \in \Omega_f$.

5.3.5 Non-uniqueness problem

As well known [Schenck, 1968], the operator $\mathbf{W}_b\left(\kappa_z,\omega\right)$ in Eq. (5.20) may become ill-conditioned for wavenumbers close to the resonance wavenumbers of the corresponding internal problem, thus leading to an inaccurate representation of the impedance of the surrounding fluid.

As shown by Nilsson et al. [2009], this numerical problem can be overcome by means of the so-called CHIEF method [Schenck, 1968]. The method uses Eq. (5.8) with $\mathbf{x}' \in \Omega_s$ as additional constraint that must be satisfied along with the surface Helmholtz integral in Eq. (5.13). Since $c(\mathbf{x}') = 0$ for source points located outside Ω_f, an additional zero-pressure condition is obtained from Eq. (5.21) and added to Eq. (5.20) to form an over-determined system. A unique solution can then be obtained in a least square sense, providing that the CHIEF points are not distributed over modal lines of the internal eigenstructures.

5.4 Fluid-structure coupling

The coupling between the SAFE and BEM regions is established in a finite element sense [Andersen, 2006], i.e. by transforming the discretized BEM domain into an equivalent single finite element that relates nodal forces to nodal displacements at the fluid-structure interface. The pressure values at the boundary nodes can be obtained in terms of normal displacements by inverting Eq. (5.20) as follows

$$\mathbf{P}_b(\kappa_z, \omega) = \rho^f \omega^2 \mathbf{W}_b^{-1}(\kappa_z, \omega)\, \mathbf{G}_b(\kappa_z, \omega)\, \mathbf{Q}_b^{\perp}(\kappa_z, \omega). \tag{5.22}$$

in which a least square procedure can be used when CHIEF points are adopted.

The relation between nodal pressures $\mathbf{P}_b(\kappa_z, \omega)$ in the fluid and nodal forces $\mathbf{F}_b(\kappa_z, \omega)$ on the waveguide is obtained by using Eq. (5.5) and the Principle of Virtual Displacements over the fluid-structure interface [Schneider, 2008]

$$\int_{\partial\Omega} \delta\mathbf{u}^{\mathrm{T}}(\mathbf{x}, \kappa_z, \omega) \left[\mathbf{t}_b(\mathbf{x}, \kappa_z, \omega) + p(\mathbf{x}, \kappa_z, \omega)\, \mathbf{n}(\mathbf{x})\right] \mathrm{d}s(\mathbf{x}) = 0. \tag{5.23}$$

Eq. (5.23) is rewritten in discretized form using the interpolations in Eqs. (5.2) and (5.18), leading to

$$\mathbf{F}_b(\kappa_z, \omega) = -\mathbf{R}_P \mathbf{P}_b(\kappa_z, \omega), \tag{5.24}$$

where $\mathbf{R}_P$ is a distribution matrix deriving from the following finite element assembling procedure

$$\mathbf{R}_P = \bigcup_{q=1}^{N_b} \int_{\partial\Omega_b^q} \mathbf{N}^{\mathrm{T}}(\boldsymbol{\xi}(\eta))\, \mathbf{n}(\eta)\, \mathfrak{N}(\eta)\, J_b^q(\eta)\, \mathrm{d}\eta, \tag{5.25}$$

in which $J_b^q(\eta)$ is the Jacobian of the in-plane mapping for the qth semi-isoparametric boundary element.

The relation between nodal displacements $\mathbf{Q}_b(\kappa_z,\omega)$ and their normal components $\mathbf{Q}_b^{\perp}(\kappa_z,\omega)$ can be obtained from the energy balance of the fluxes at the fluid-structure interface

$$\rho^f\omega^2\int_{\partial\Omega}\delta p(\mathbf{x},\kappa_z,\omega)\left[u_{\mathbf{n}}(\mathbf{x},\kappa_z,\omega)-\mathbf{u}(\mathbf{x},\kappa_z,\omega)\cdot\mathbf{n}(\mathbf{x})\right]\mathrm{d}s(\mathbf{x})=0. \tag{5.26}$$

Using Eqs. (5.2), (5.18) and (5.19), the discretized form of Eq. (5.26) is derived as

$$\mathbf{Q}_b^{\perp}(\kappa_z,\omega)=\mathbf{T}_b^{-1}\mathbf{R}_P^{\mathrm{T}}\mathbf{Q}_b(\kappa_z,\omega) \tag{5.27}$$

where the matrix $\mathbf{T}_b$ is obtained from the following finite element assembling procedure (cf. Eq. (4.63))

$$\mathbf{T}_b=\bigcup_{q=1}^{N_b}\int_{\partial\Omega_b^q}\mathbf{N}^{\mathrm{T}}(\eta)\,\mathbf{N}(\eta)\,J_b^q(\eta)\,\mathrm{d}\eta. \tag{5.28}$$

Substituting Eq. (5.24) into Eq. (5.22) and introducing the resulting expression into Eq. (5.27) lead to the following equivalent dynamic stiffness matrix for the fluid domain

$$\mathbf{F}_b(\kappa_z,\omega)=-\rho^f\omega^2\mathbf{K}_b(\kappa_z,\omega)\,\mathbf{Q}_b(\kappa_z,\omega) \tag{5.29}$$

where

$$\mathbf{K}_b(\kappa_z,\omega)=\mathbf{R}_P\mathbf{W}_b^{-1}(\kappa_z,\omega)\,\mathbf{G}_b(\kappa_z,\omega)\,\mathbf{T}_b^{-1}\mathbf{R}_P^{\mathrm{T}} \tag{5.30}$$

Eq. (5.29) is finally substituted into Eq. (5.3) to form the following homogeneous system

$$\Big\{\kappa_z^2\mathbf{K}_3+\mathrm{i}\kappa_z\Big[\mathbf{K}_2-\mathbf{K}_2^{\mathrm{T}}\Big]+\mathbf{K}_1-\omega^2\Big[\mathbf{M}+\rho^f\mathscr{L}_b^{\mathrm{T}}\mathbf{K}_b(\kappa_z,\omega)\,\mathscr{L}_b\Big]\Big\}\mathbf{Q}(\kappa_z,\omega)=\mathbf{0} \tag{5.31}$$

where $\mathscr{L}_b$ is a collocation matrix so that $\mathbf{Q}_b(\kappa_z,\omega)=\mathscr{L}_b\mathbf{Q}(\kappa_z,\omega)$. The operator inside the braces in Eq. (5.31) represents the wavenumber and frequency dependent dynamic stiffness matrix for a waveguide that is immersed in an infinite inviscid fluid.

The nodal displacements $\mathbf{Q}(\kappa_z,\omega)$ that represent the nontrivial solution of Eq. (5.31) for a fixed couple (κ_z,ω) can be used to extract the pressure at any point $\mathbf{x}'\in\Omega_f$. Recalling Eqs. (5.22) and (5.30), Eq. (5.21) can be rewritten as follows

$$p_d\left(\mathbf{x}',\kappa_z,\omega\right)=\rho^f\omega^2\left[\mathbf{G}_d(\kappa_z,\omega)-\mathbf{W}_d(\kappa_z,\omega)\,\mathbf{R}_p^{-1}\mathbf{K}_b(\kappa_z,\omega)\right]\mathscr{L}_b\mathbf{Q}(\kappa_z,\omega), \tag{5.32}$$

which is valid only for $\mathbf{x}'\in\Omega_f$.

5.5 Single valued definition of the dynamic stiffness matrix

The dynamic stiffness matrix in Eq. (5.31) is multivalued due to the possible signs of the radial wavenumber $\kappa_\alpha = \pm[(\kappa_L^f)^2 - \kappa_z^2]^{1/2}$. Poles corresponding to leaky and trapped modes can be determined by imposing the Snell-Descartes law at the fluid-structure interface, i.e. by imposing the continuity of $\mathrm{Re}\,(\kappa_z)$ and $\mathrm{Im}\,(\kappa_z)$, and by choosing the sign of κ_α according to the characteristics of the partial wave in the fluid medium.

For $\mathrm{Re}\,(\kappa_z) > \kappa_L^f$ (non-leaky region) the angle of incidence formed by the longitudinal bulk wave in the immersed waveguide with the normal at the interface is larger than the critical angle, resulting into a total internal energy reflection [Rose, 2004]. The partial wave in the fluid medium is thus evanescent and its amplitude decays exponentially in the $x-y$ plane. Being the wave propagation process in the fluid medium represented by the Hankel function of the first kind, the sign of κ_α is chosen to satisfy $\mathrm{Im}\,(\kappa_\alpha) > 0$. Since all the energy remains confined within the waveguide, the attenuation of guided modes in the non-leaky region is due only to the material damping of the waveguide.

In the wavenumber range $0 \leq \mathrm{Re}\,(\kappa_z) < \kappa_L^f$ (leaky region) the angle of incidence of the longitudinal bulk wave is lower than the critical angle and the wave is partially reflected and mode-converted at the interface, while a longitudinal bulk wave is also refracted in the fluid medium. Therefore, part of the wave energy leaks from the waveguide into the fluid, which causes the guided wave that exhibit an in-plane displacement component to be attenuated even in the case of non-dissipative materials.

In absence of external sources, the propagation process in the fluid field corresponds to a longitudinal wave that propagates away at a leakage angle $\vartheta_L^{Leak} = \sin^{-1}[\mathrm{Re}(\kappa_z)/\kappa_L^f]$ with respect to the $x-y$ plane. In order for $H_n^{(1)}(\kappa_\alpha r)$ to represent such a process, the sign of κ_α must be chosen so that $\mathrm{Re}\,(\kappa_\alpha) > 0$. This implies in turn $\mathrm{Im}(\kappa_\alpha) \leq 0$ for any $\mathrm{Re}\,(\kappa_z) \in [0, \kappa_L^f]$ and $\mathrm{Im}\,(\kappa_z) > 0$, i.e. the far field amplitude of the radial wave increases with distance from the interface.

The corresponding configuration of the wavenumber vectors in the $z - \mathbf{r}$ plane is shown in Fig. 5.1, where $\mathbf{k}_L^{\mathrm{Re}}$ and $\mathbf{k}_{Li}^{\mathrm{Im}}$ represent the propagation vector and the inhomogeneous attenuation vector, respectively, while l denotes the intersection line of the $x-y$ plane with the $z-\mathbf{r}$ plane. Since the fluid is non dissipative, $\mathbf{k}_L^{\mathrm{Re}}$ and $\mathbf{k}_{Li}^{\mathrm{Im}}$ are orthogonal and the partial longitudinal wave propagates along leaky rays (dashed lines in Fig. 5.1) without attenuation [Hladky-Hennion et al., 2000]. As it can be observed, in order to have a guided mode that is attenuated in the propagation direction and that satisfies the Snell-Descartes law at the fluid-structure interface, the attenuation component of the radial wavenumber in the fluid medium ($\mathbf{k}_\alpha^{\mathrm{Im}}$) must be necessarily oriented in the opposite direction of the propagation component ($\mathbf{k}_\alpha^{\mathrm{Re}}$).

Due to the continuous energy loss along the positive z-direction, the wave amplitude along a generic internal leaky ray, e.g. the line B-B′, is always lower than the amplitude along an external leaky ray, for example A-A′; consequently, an increasing amplitude along the line l can be observed. Similar considerations can also be found in different journal articles Hladky-Hennion et al. [1998, 2000]; Mozhaev and Weihnacht [2002]; Simmons et al. [1992]; Vogt et al. [2003] and textbooks [Caviglia and Morro, 1992].

It can be noted that the radial wavefield obtained from the modal analysis keeps growing to infinity while moving along the line l, which would imply that leaky bulk waves with infinite amplitude are radiated at $z = -\infty$. This unphysical behaviour derives from the assumption of translational invariance in the mathematical model. In reality, the phenomenon starts at a precise location, e.g. section A, where a leaky wave with the largest but finite amplitude ϕ_A is radiated in the surrounding fluid. Therefore, for any considered distance $r >$ A′ along the line l, no leaky bulk waves with amplitude greater than ϕ_A can be found.

From the energetic point of view, the presence of a radial wavefield that grows while propagating away from the interface does not violate thermodynamics. In fact, the total energy carried through the fluid domain Ω_f at a generic distance z from the origin is given by the sum of the energy previously radiated through the lateral surface $\partial\Omega \times [-\infty, z]$, so that the energy balance is preserved.

5.6 Eigenvalue analysis

Once the admissible signs of the radial wavenumber κ_α have been determined for the non-leaky and leaky regions, the N-dimensional nonlinear eigenvalue problem in Eq. (5.31) can be solved in terms of complex wavenumbers and associated wavestructures for any fixed real positive frequency.

As in Chapters 3 and 4, also in this case the Contour Integral Method proposed by Beyn [2012] is adopted. The requirement of holomorphicity for the dynamic stiffness matrix in Eq. (5.31) is fulfilled by deforming the contour in the complex plane in order to avoid points of singularity or discontinuity that do not correspond to poles of guided modes. If the contour is limited only to the first and fourth quadrants of the complex κ_z-plane, these points are represented by the longitudinal wavenumber κ_L^f, in correspondence of which $H_n^{(1)}(\kappa_\alpha r)$ is not defined, and the vertical branch cut $\kappa_L^f + \mathrm{i}\mathrm{Im}(\kappa_z)$ ($\mathrm{Im}(\kappa_z) > 0$), along which the dynamic Green's functions show a jump

material	i	ρ^i (Kg/m^3)	c_L^i (m/s)	c_S^i (m/s)	β_L^i (Np/wavelength)	β_S^i (Np/wavelength)
titanium	ti	4460	6060	3230	-	-
steel	st	7932	5960	3260	0.003	0.008
oil	oi	870	1740	-	-	-
water	wt	998.2	1478	-	-	-

Table 5.1: Materials constants used in Sec. 5.7 (from Pavlakovic and Lowe [2003]).

related to the abrupt change of phase in κ_α. After the contour integration has been carried out numerically, the SVD decomposition followed by the rank test is performed to separate physical from spurious eigensolutions. The accuracy of the eigenvalues computation is finally checked by means of the residual test.

Once the full set of eigensolutions $[\kappa_z^m(\omega), \mathbf{Q}_b^m(\omega)]$ $(m = 1, .., M)$ has been obtained for the frequency of interest, the phase velocity (c_p), attenuation (α) and energy velocity (c_e) for the mth guided mode can be obtained as described in Sec. 4.7.2.

5.7 Numerical examples

In this section, some numerical applications are performed on waveguides with geometries typically encountered in NDE tests. The different materials considered are reported in Table 5.1, where only the Maxwell rheological model is considered.

The optimal set of parameters of the contour integral algorithm, i.e. the number of integration points, the rank test tolerance and the residual test tolerance Beyn [2012], have been determined on the basis of single analyses performed at few frequencies. At the same frequencies, the complex contour $\Gamma(\kappa_z)$ has been designed to include only guided modes with moderate attenuations. Both the contour integral method parameters and the extension of the complex contour have been assumed to vary with frequency.

Due to the low frequency ranges and number of modes considered in the different examples, the eigenvalues computation has always proved to be numerically stable even without the use of CHIEF points. However, if dispersion data are needed at higher frequencies, the use of CHIEF points can substantially improve the condition number of the boundary element matrices, which in turn results into a better separation of the singular values and facilitate the distinction between physical and spurious eigensolutions.

5.7.1 Validation case: elastic titanium bar of circular cross-section immersed in oil

The SAFE-2.5D BEM formulation is first validated for the case of a 10 mm diameter titanium (ti) bar immersed in oil (oi), for which the obtained solution is compared with that given by the software DISPERSE (evaluation copy) [Pavlakovic and Lowe, 2011]. The SAFE mesh used in the analysis, shown in Fig. 5.2, is composed of 48 six-nodes triangular elements plus 32 nine-node quadrilateral elements for the embedded (SAFE) section and 32 three-nodes monodimensional elements for the external fluid domain (BEM).

The real wavenumber, phase velocity, attenuation and energy velocity dispersion curves in the frequency range $0-500$ kHz are shown in Figs. 5.2-5.5. For the comparison with DISPERSE, only the modes $L(0,1)$, $L(0,2)$, $F(1,1)$, $F(1,2)$ and $F(1,3)$ have been considered (dashed lines). As can be noted, the SAFE-2.5D BEM solutions (continuous lines) are in good agreement with the DISPERSE predictions.

The behaviour of immersed circular bars has been analyzed by different authors [Ahmad, 2001; Fan et al., 2008; Pavlakovic et al., 1997; Pavlakovic, 1998] and it is not reexamined here. However, it is worth mentioning that some high order modes with phase velocity greater than the oil bulk velocity experience zero attenuation values at certain frequencies. These are the cases of the $F(1,3)$ and $L(0,2)$ modes at about 330 kHz and 465 kHz, respectively, for which the radial displacements at the interface vanish. An analogous behaviour of the same modes in a elastic steel bar embedded in water has been previously observed by Pavlakovic et al. [1997].

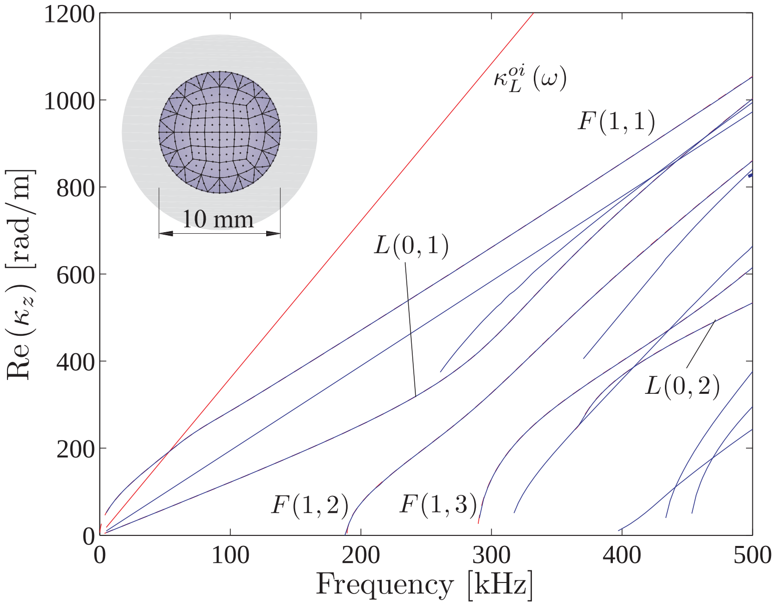

Figure 5.2: Real wavenumber dispersion curves for the elastic steel bar of circular cross section immersed in oil.

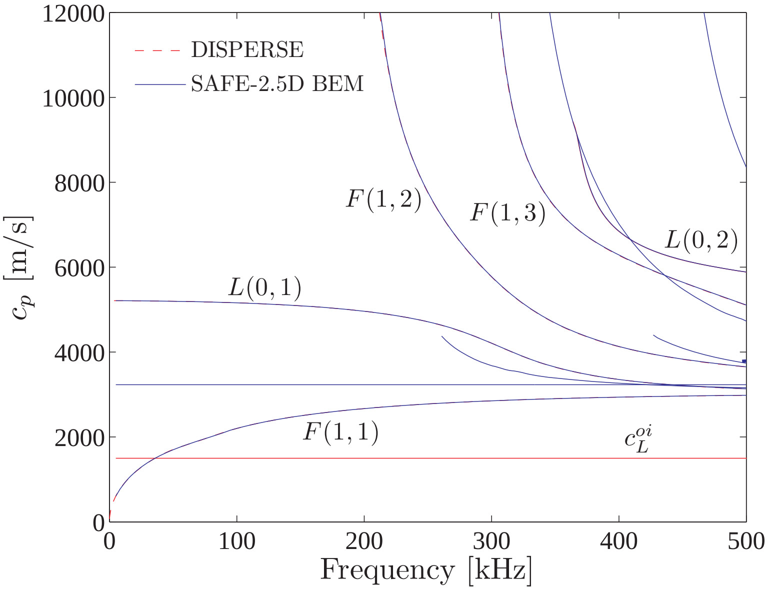

Figure 5.3: Phase velocity dispersion curves for the elastic steel bar of circular cross section immersed in oil.

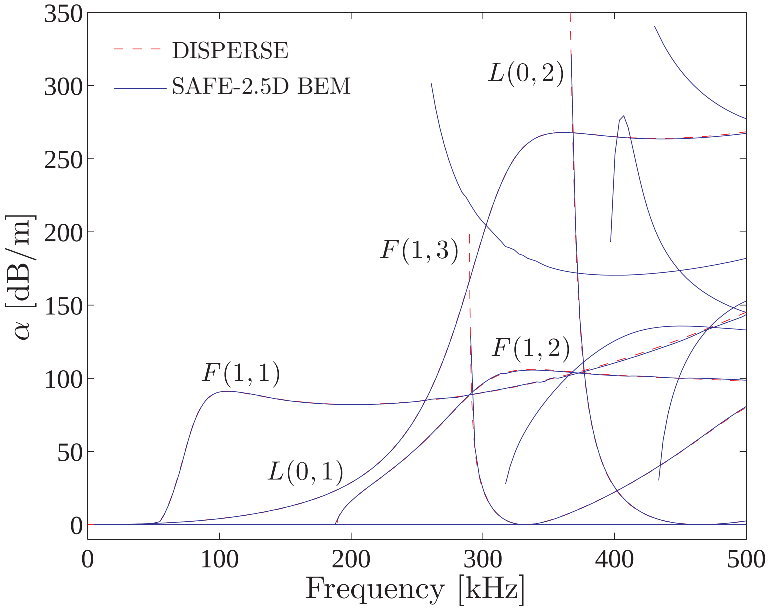

Figure 5.4: Attenuation dispersion curves for the elastic steel bar of circular cross section immersed in oil.

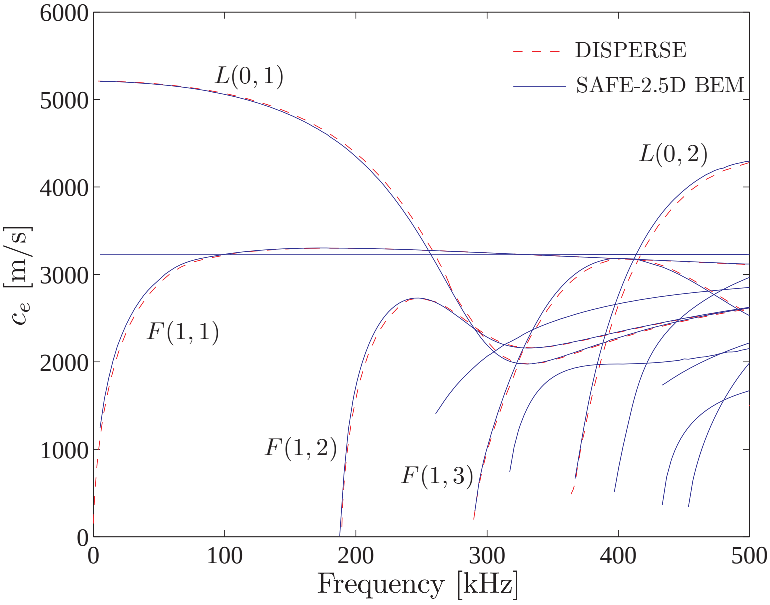

Figure 5.5: Energy velocity dispersion curves for the elastic steel bar of circular cross section immersed in oil.

5.7.2 Viscoelastic steel bar of square cross-section immersed in water

The following example considers a 10mm wide square bar immersed in water (wt). The bar is assumed to be made of steel (st) and small material damping component is considered (see Table 5.1). The mesh used for the solid region is composed of 100 eight-nodes quadrilateral elements, while the fluid region has been modeled by means of 40 three-nodes monodimensional boundary elements (see Fig. 5.6).

The dispersion spectra of the bar in the $0-400$ kHz frequency range are reported in Figs. 5.6-5.9, where the comparison between the immersed case (continuous blue lines) and the in-vacuum case (continuous gray lines) is also shown. The low order modes have been named as in Ref. [Gunawan and Hirose, 2005]. The second main difference with respect to the immersed circular bar is that the first torsional mode T_1 becomes slightly dispersive w.r.t. the in-vacuum case, whereas the $T(0,1)$ mode of the circular bar in both the immersed and in-vacuum cases remains non-dispersive. In particular, it can be observed that the phase velocity of the T_1 mode in the $0-200$ kHz frequency range is in the order of $50-150$ m/s lower with respect to the in-vacuum case (non-dispersive), while in the $200-400$ kHz the two phase velocities correspond.

Another distinction between the different behaviour of the fundamental torsional mode in the square and circular bars is that, while in the circular bar the torsional displacements are always orthogonal to the normal at the interface, in the square bar this condition is no longer verified. Since the displacement component along the normal causes the displacement of the fluid, the square (and, more generally, the non-circular sections) experiences attenuation due to leakage of bulk waves in the fluid.

Concerning the remaining low order modes, the first flexural (F_1) mode presents, similarly to the $F(1,1)$ in the circular bar, a non-leaky section in the frequency range $0-30$ kHz, in which the mode is non-attenuated. The phase velocity of the longitudinal mode L_1 is similar to the phase velocity of the corresponding in-vacuum mode, while in the $0-100$ kHz frequency range it also shows the lower attenuation and the highest energy velocity. Therefore, in this frequency range the L_1 mode is particularly suitable for guided ultrasonic applications.

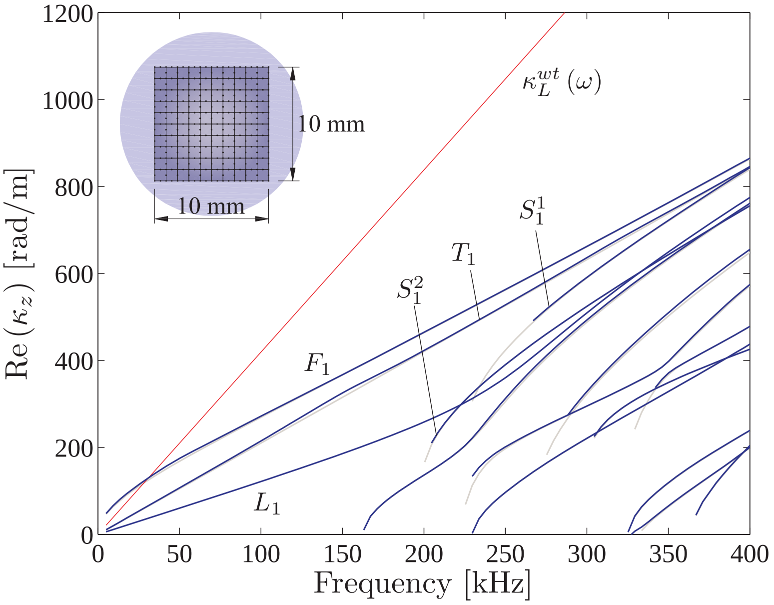

Figure 5.6: Real wavenumber dispersion curves for the viscoelastic steel square bar immersed in water. Guided modes are named as in Ref. [Gunawan and Hirose, 2005].

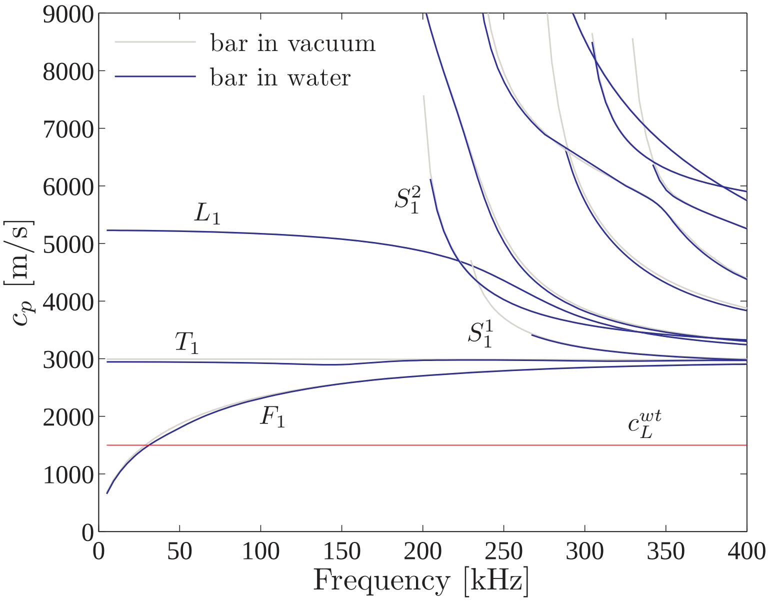

Figure 5.7: Phase velocity dispersion curves for the viscoelastic steel square bar immersed in water. Guided modes are named as in Ref. [Gunawan and Hirose, 2005].

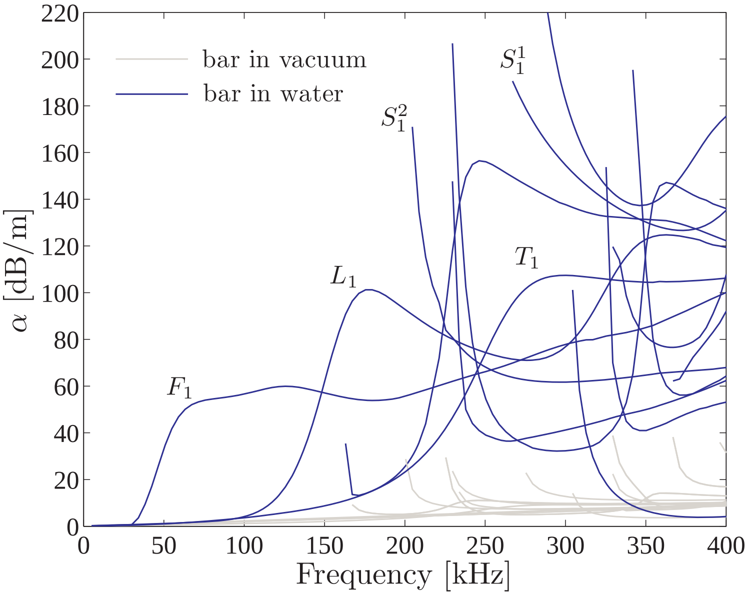

Figure 5.8: Attenuation dispersion curves for the viscoelastic steel square bar immersed in water. Guided modes are named as in Ref. [Gunawan and Hirose, 2005].

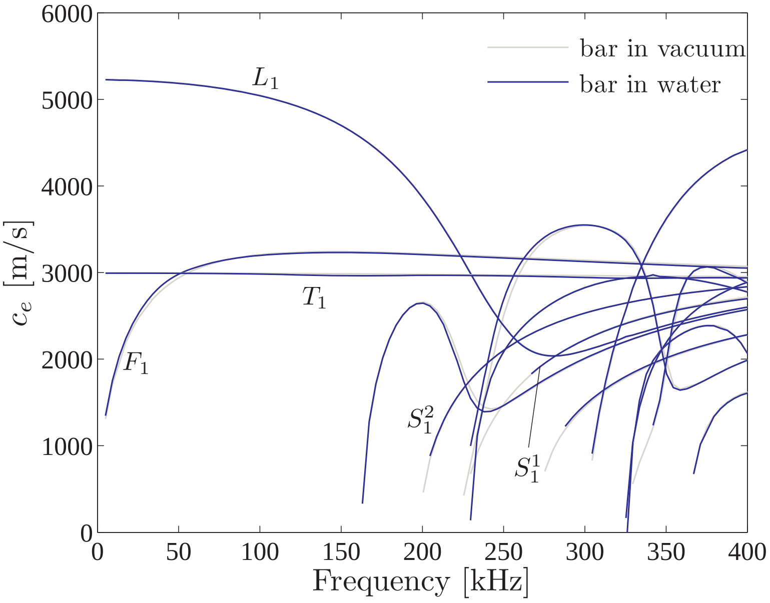

Figure 5.9: Energy velocity dispersion curves for the viscoelastic steel square bar immersed in water. Guided modes are named as in Ref. [Gunawan and Hirose, 2005].

5.7.3 L-shaped viscoelastic steel bar immersed in water

In the third example, a L-shaped bar with dimensions 30×20×4 mm is considered. The bar is assumed to be made of viscoelastic steel and immersed in water. The bar cross-section is discretized by means of 32 eight-nodes quadrilateral elements and 2 six-nodes triangular elements, while the surrounding water is represented through a boundary element mesh of 36 three-nodes monodimensional elements (see Fig. 5.10).

The dispersion curves for the in-vacuum case (continuous gray lines) and the immersed case (continuous blue lines) are shown in Figs. 5.10-5.13. The first four fundamental modes are indicated in the spectra with $m1$ (longitudinal mode), $m2$ (first pseudo-flexural mode), $m3$ (second pseudo-flexural mode) and $m4$ (pseudo-torsional mode).

In this case, a substantial modification of the dispersion curves for the immersed configuration with respect to the in-vacuum case is observed. The $m1$ no longer shows the jump at about 29.5 kHz, but couples with the high order modes $h2$ and $h3$ at 26.7 kHz and 51.2 kHz, respectively. A similar phenomenon has been observed in plate waves due to the addition of material damping [Bartoli et al., 2006; Bernard et al., 2001; Ma, 2007; Simonetti and Cawley, 2004]. As it can be noted from Fig. 5.13, at such frequencies the $m1$ mode shows local minima of energy velocity as well as local maxima of attenuation. The normalized in-plane displacement and pressure fields for the $m1$ and $m3$ modes at 51.2 kHz are depicted in Figs. 5.14(a) and 5.14(b), respectively, showing that the mode shapes and pressure fields of the two modes are very similar at this frequency. In the frequency range $51.2 - 57$ kHz, the attenuation of the $m1$ mode increases rapidly whereas its phase and energy velocities decreases. The maximum peak of attenuation occurs at about 77.0 kHz, which corresponds to the minimum value of the energy velocity and therefore to the frequency of maximum radiation for this mode. The normalized in-plane displacement and pressure at this frequency are shown in Fig. 5.15. Since the entity of the in-plane displacements decreases in the frequency range $77 - 120$ kHz, the attenuation of the mode drops while its energy velocity increases. The $m1$ mode appears as the most suitable for NDT applications, in particular in the $0 - 48$ kHz frequency range, where it is almost non-dispersive and characterized by high values of the energy velocity and low values of attenuation.

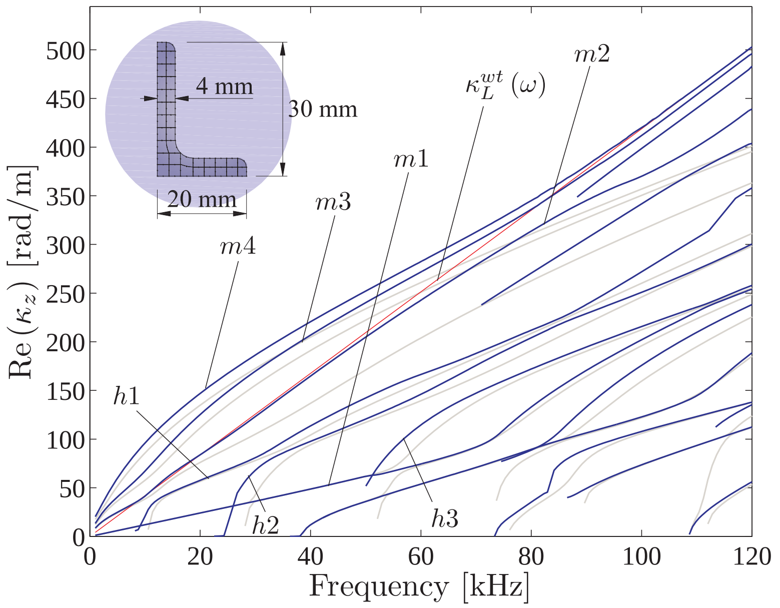

Figure 5.10: Real wavenumber dispersion curves for the L-shaped viscoelastic steel bar immersed in water.

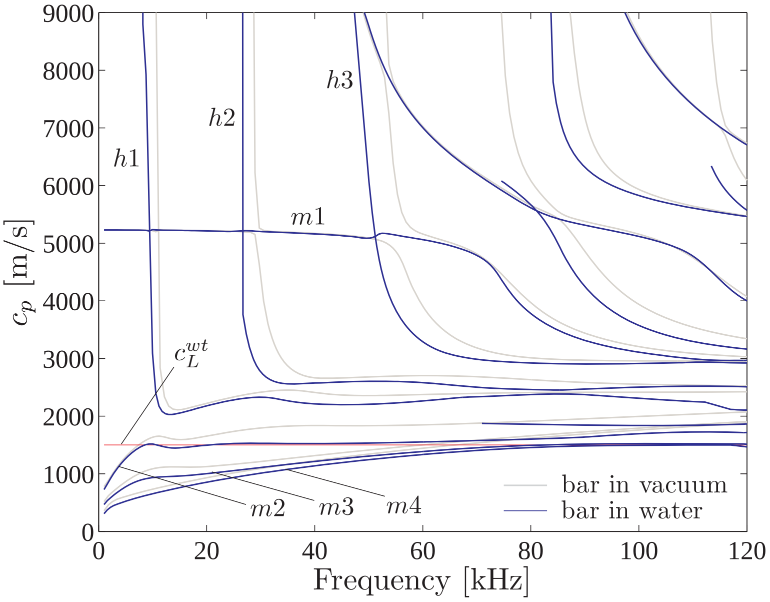

Figure 5.11: Phase velocity dispersion curves for the L-shaped viscoelastic steel bar immersed in water.

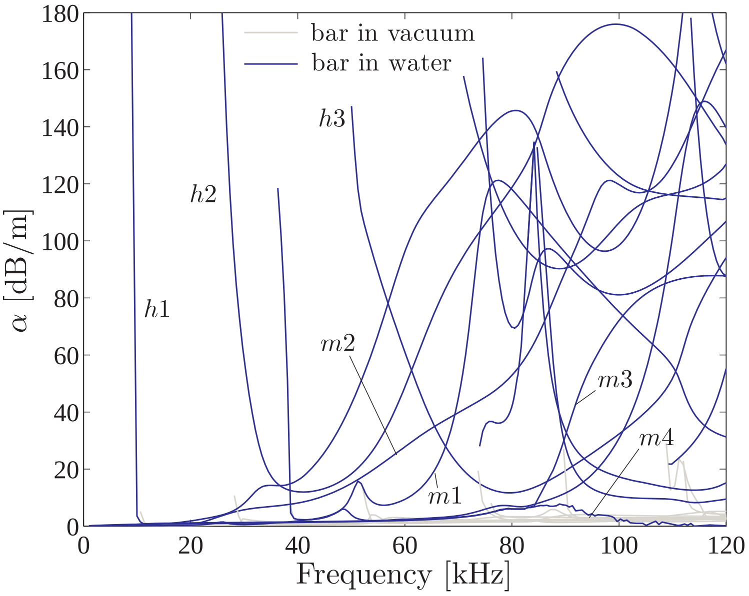

Figure 5.12: Attenuation dispersion curves for the L-shaped viscoelastic steel bar immersed in water.

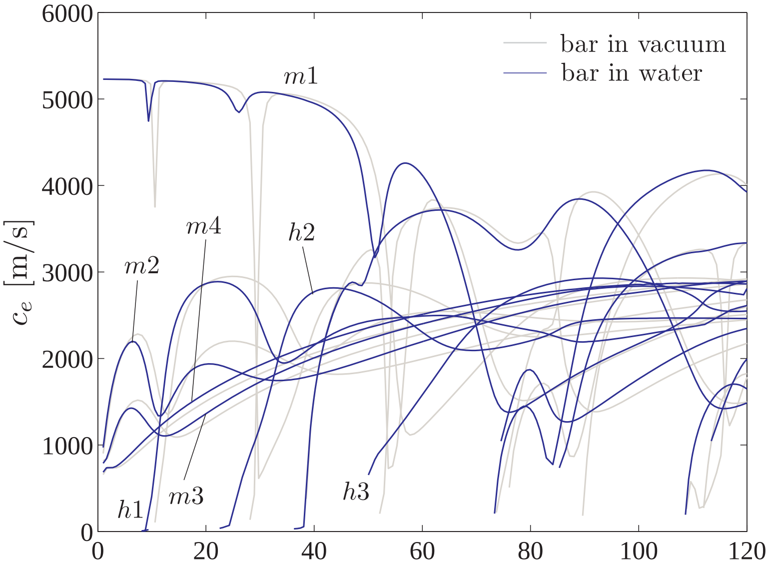

Figure 5.13: Energy velocity dispersion curves for the L-shaped viscoelastic steel bar immersed in water.

Due to their complexity, the $m2$, $m3$ and $m4$ modes may be of less interest for ultrasonic applications. However, they show some noteworthy features. The $m2$ mode shows alternate frequency intervals with radiating and non-radiating properties. The mode is first non-leaky ($0 - 8.5$ kHz), with attenuation only due to the small material damping of the steel. Then it becomes leaky in the frequency range $8.5 - 11$ kHz.

In Fig. 5.16, the normalized in-plane displacements and pressure wavefields for the $m2$ mode at 9.7 kHz are represented on the $x - y$ plane at different scales (the normalization is the same in both figures). From Fig. 5.16(a) it can be noted that, near the interface, the partial wave behaves similarly to an evanescent wave, i.e. the amplitude decreases almost exponentially away from the interface. However, in Fig. 5.16(b) it can be observed that at about 10.0 m the radial wave reaches an amplitude comparable to the maximum amplitude in Fig. 5.16(a) (near field). An explanation of this behaviour can be given by observing first that $c_p^{m2}(9.7 \text{ kHz}) = 1520$ m/s, from which a leakage angle of $\vartheta_L^{m2}(9.7 \text{ kHz}) \simeq 80$ deg is defined with respect to the $x - y$ plane. Therefore, the propagation vector of the partial wave in the fluid medium lies close to the interface, which correspond to a configuration similar to that of an evanescent wave. Moreover, from the computed axial wavenumber $\kappa_z^{m2}(9.7 \text{ kHz}) = 40.09 \text{ rad/m} + \text{i}0.047 \text{ Np/m}$, the radial bulk wavenumber in the water results $\kappa_\alpha^{wt}(9.7 \text{ kHz}) = 6.62 \text{ rad/m} - \text{i}0.28 \text{ Np/m}$. The small propagation component in the radial direction and the large angle of radiation determine a radial wavelength approximately equal to 0.95 m, which can be directly observed in Fig. 5.16(b), while the small negative attenuation component determines a slow increasing amplitude with the distance from the waveguide. Other than the leaky section discussed above, the $m2$ mode becomes non-leaky in the frequency range $11 - 20$ kHz and then again leaky in the frequency range $20 - 120$, in which is weakly dispersive with attenuation increasing monotonically to reach the value of about 168 dB/m at 120 kHz.

The second pseudo-flexural mode $m3$ and the flexo-torsional mode $m4$ show similar characteristics. Both modes have large non-leaky branches characterized by a strongly evanescent wavefield in the fluid. For example, in Figs. 5.17(a) and 5.17(b) the normalized in-plane displacement and pressure fields are reported for the two modes at 40 kHz. The mode $m3$ crosses the phase bulk velocity of the water at about 84 kHz, from which its attenuation increases drastically (see Fig. 5.12) since leakage of longitudinal bulk waves occurs. In the $84 - 120$ kHz range ($c_p^{m3} \simeq c_L^{wt}$), the imaginary component of κ_z^{m4} shows a slight numerical instability. Physically, such mode branch corresponds to a transition zone, which would not be suitable for experimental or application purposes due to its unstable behaviour.

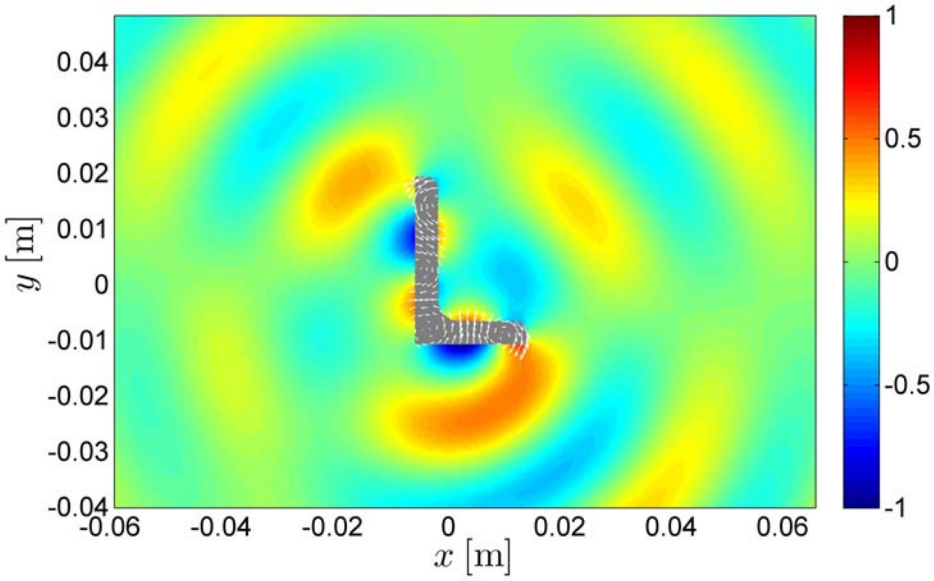

(a)

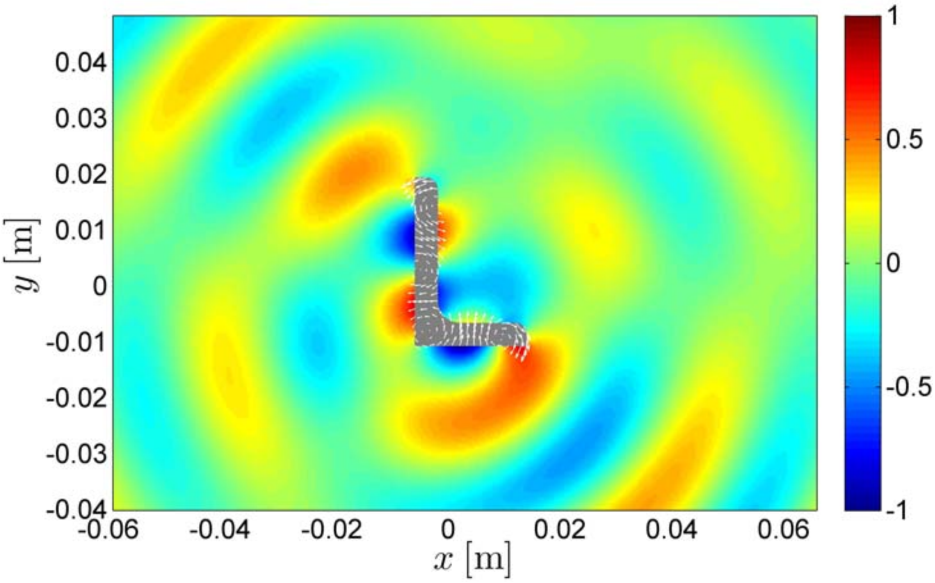

(b)

Figure 5.14: Normalized in-plane displacement and pressure fields for (a) the $m1$ mode and (b) the $h3$ mode at 51.2 kHz.

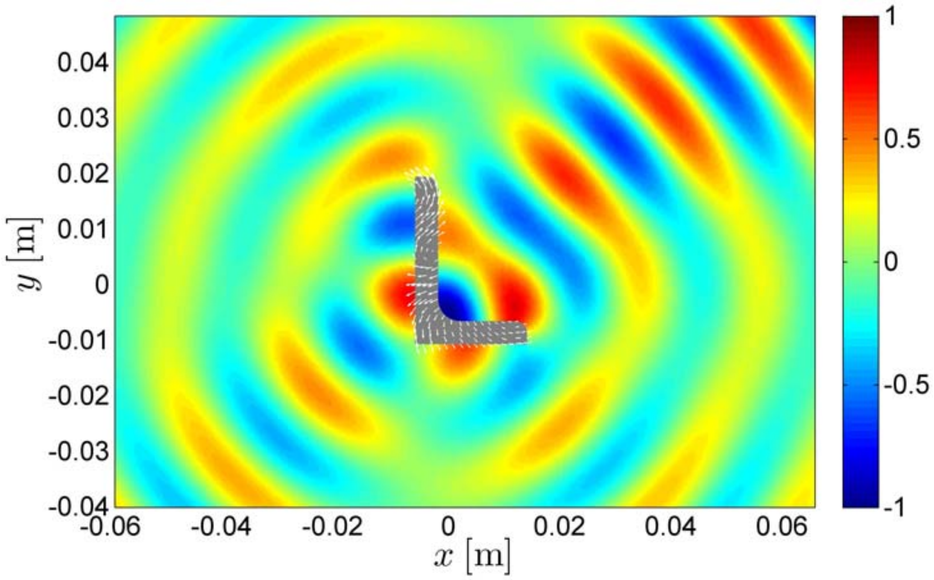

Figure 5.15: Normalized in-plane displacement and pressure fields for the $m1$ mode at 77.0 kHz.

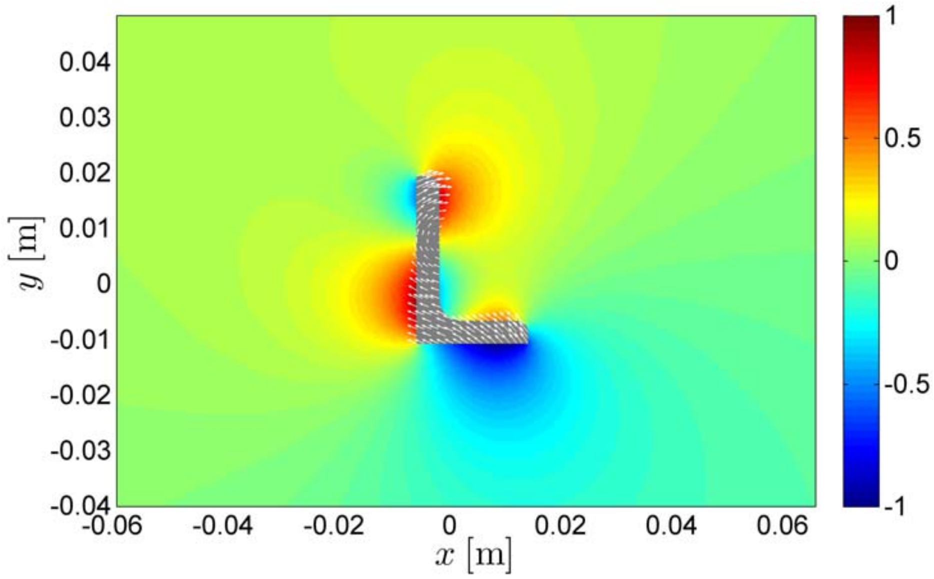

(a)

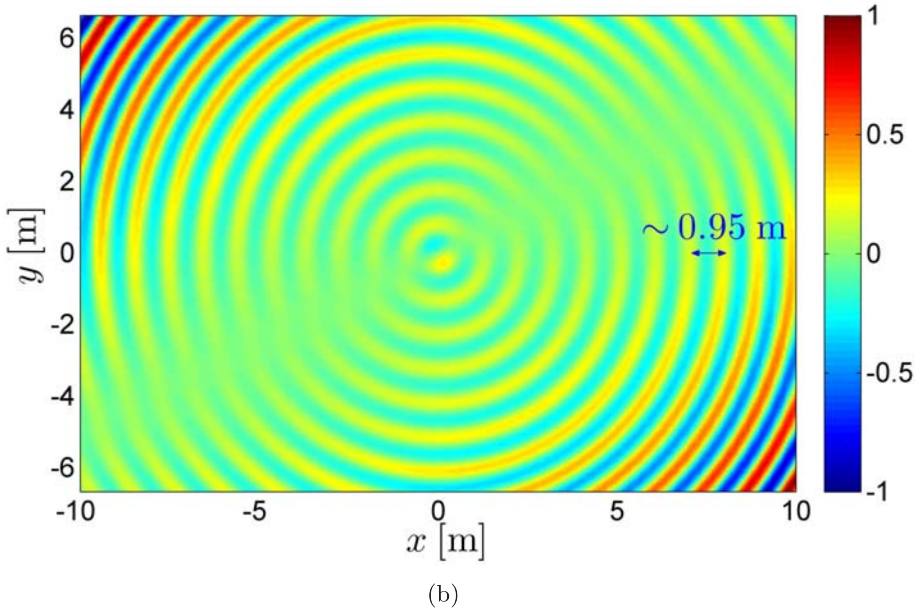

(b)

Figure 5.16: Normalized in-plane displacement and pressure fields for the $m2$ mode at 9.7 kHz in (a) the near field and (b) the far field (the normalized scale is the same in (a) and (b)).

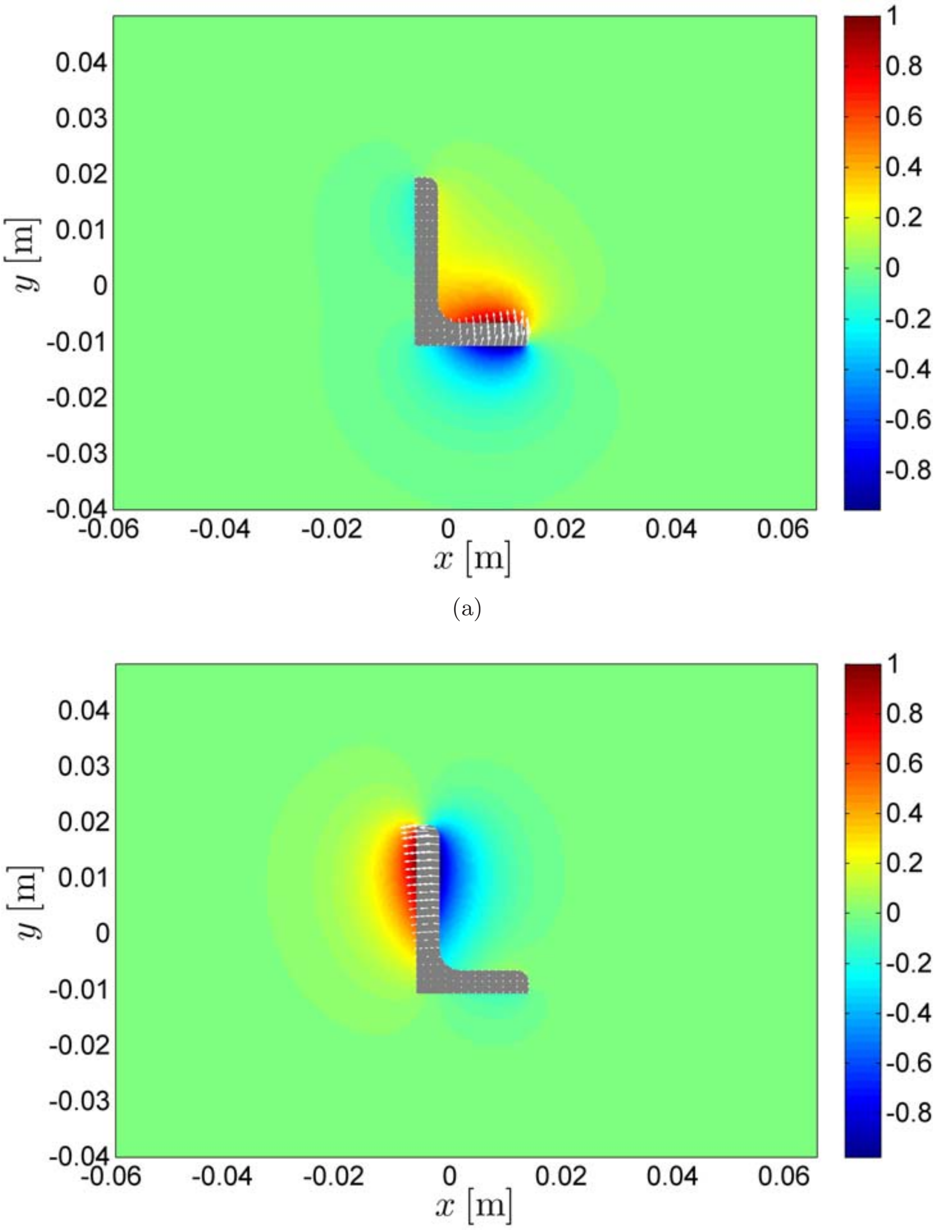

(a)

(b)

Figure 5.17: Normalized in-plane displacement and evanescent pressure fields for (a) the $m3$ and (b) the $m4$ mode at 40 kHz.

5.8 Conclusions

In this Chapter, a fully coupled SAFE-2.5D BEM formulation has been proposed for the computation of dispersion curves for viscoelastic waveguides immersed in inviscid fluids. The solid region has been modeled via a standard SAFE procedure, while a regularized 2.5D BEM formulation has been used for the fluid region, which allows to treat implicitly boundary corners as well as singular integrals. The dispersive equation is configured as a nonlinear eigenvalue problem, which has been solved by means of a contour integral algorithm. Complex poles for leaky and trapped modes can be obtained by imposing the correct phase of the radial wavenumber in the fluid medium, which must represent a radially decaying field in the non-leaky region ($\kappa_z > \kappa_L^f$) and a radially growing field in the leaky region ($\kappa_z < \kappa_L^f$).

Numerical experiments have been performed for waveguides of different geometries, for which the BEM matrices involving fundamental fluxes have proven to be numerically stable even without the use of CHIEF points. However, for computations in frequency ranges higher than those used in the numerical examples, the use of CHIEF points could improve the numerical stability and the separation of the singular values for the reduced linear problem inside the complex contour.

The comparison between the dispersion curves obtained using software DISPERSE (evaluation copy) [Pavlakovic and Lowe, 2011] and the SAFE-2.5D BEM formulation for a circular titanium bar immersed in oil are in excellent agreement. The dispersion curves for a square steel bar immersed in water show that the first torsional mode becomes slightly dispersive, while for the in-vacuum case the same mode is non-dispersive. This behaviour is not observed in the immersed circular bar and is mainly due to the square geometry, which allows for the coupling of the in-plane displacements with the fluid medium. Therefore, the first torsional mode in the square bar is also attenuated, whereas it is not in the immersed circular bar. The dispersion curves of a L-shaped viscoelastic steel bar immersed in water show a more noticeable shift in the phase velocity of the different modes. In particular, the longitudinal mode does not present a clear jump as in the in-vacuum case and also shows a nearly non-dispersive behaviour in a wider frequency range compared to the in-vacuum case.

As shown in other works Fan et al. [2008]; Fan [2010], the proposed method can be extended to the case of surrounding viscous fluids.

Chapter 6

Conclusions

6.1 Sommario

In questa tesi sono stati presentati tre differenti metodi numerici per lo studio delle caratteristiche di dispersione di onde guidate ultrasoniche che si propagano in guide d'onda di geometria complessa.

Lo scopo principale della ricerca svolta è stato quello di sviluppare delle formulazioni in grado di superare i problemi classici dei metodi utilizzati in letteratura per lo studio dei fenomeni di propagazione e il calcolo delle curve di dispersione. Come descritto nel Capitolo 1, i metodi analitici [Haskell, 1953; Knopoff, 1964; Lowe, 1992; Pavlakovic, 1998; Simmons et al., 1992; Thomson, 1950], a fronte di risultati tipicamente molto accurati, non consento lo studio di guide d'onda aventi geometrie complesse. Quest'ultime sono generalmente studiate in letteratura utilizzando tecniche basate su elementi finiti di tipo spettrale [Bartoli et al., 2006; Gavric, 1995; Hayashi et al., 2006; Sorohan et al., 2011], le quali tuttavia non sono in grado di rappresentare correttamente fenomeni di propagazione che coinvolgono domini illimitati [Castaings and Lowe, 2008; Fan et al., 2008; Jia et al., 2011; Treyssède et al., 2012].

Pertanto, si rende necessaria la disponibilità di modelli in grado di rappresentare accuratamente alcune situazioni d'interesse pratico e scientifico, come ad esempio i fenomeni di propagazione in guide d'onda complesse soggette a stati di stress iniziale non nulli ed i fenomeni di radiazione dell'energia in guide d'onda immerse in mezzi solidi o fluidi.

Nel Capitolo 2, l'effetto di uno stato di stress iniziale è stato studiato mediante un'estensione del metodo Semi-Analitico agli Elementi Finiti (SAFE) in descrizione Lagrangiana aggiornata, È stata inoltre derivata una nuova formula modale per il calcolo della velocità dell'energia e nuovi risultati di interesse pratico sono stati proposti.

Il Capitolo 3 è stato dedicato all'applicazione di un metodo spettrale (2.5D) agli elementi di contorno (BEM) come alternativa al metodo SAFE e per lo studio delle caratteristiche di dispersione in domini illimitati.

Nei Capitoli 4 e 5 due formulazioni accoppiate SAFE-2.5D BEM sono state proposte per lo studio delle leaky guided waves in guide d'onda generiche immerse in mezzi solidi e fluidi.

I risultati ottenuti in questa tesi possono risultare utili nella comprensione della natura dei fenomeni propagativi ed in molte applicazioni reali basate sull'utilizzo di onde guidate, per le quali la conoscenza dei parametri di dispersione risulta di fondamentale importanza.

6.2 Conclusions and future works

This thesis focuses on the development of numerical tools for the dispersion analysis of guided waves in complex translational invariant systems. As discussed in Chapter 1, the knowledge of the dispersion curves in terms of phase velocity, attenuation and group/energy velocity, is of crucial importance in nondestructive evaluation testing and structural health monitoring strategies based on guided waves.

In particular, the phase velocity spectra shows the changes in velocity of existing modes at various frequencies, thus revealing the dispersive nature of the wave propagation process.

The attenuation spectra gives an information on the amplitude decay per unit distance traveled. In Chapters 4 and 5 it has been shown that the attenuation can increase of one or more orders of magnitude if the waveguide is surrounded by solid or fluid media, depending on the interface conditions and the specific mode considered. Since the energy losses cause the signal to be attenuated while propagating, it is easily argued the importance of the attenuation information in practical applications.

The third dispersive parameter, the group velocity, describes the rate at which packets of waves at infinitely close frequency propagates along the waveguide. Although this parameter has been discussed in Chapter 2 for elastic prestressed waveguides, it as not been considered in the rest of the thesis, being replaced by the more general energy velocity concept. The energy velocity expresses the rate at which the energy carried by a wave moves along the propagation direction. A generalized formula for the energy velocity computation has been given in Chapter 2. However, as shown in Chapters 4 and 5, such formula is approximated for leaky modes in embedded or immersed waveguides, while still retains its general validity for trapped modes.

At the beginning of each chapter, the advantages and drawbacks of available analytical and numerical tools have been discussed in relation to specific problems. The basic characteristics of these methods can be summarized as follows: analytical methods, although very accurate, are limited to simple geometries, whereas numerical finite element-based techniques, in particular the SAFE method, fail in the description of unbounded domains.

In order to overcome such problems, three different numerical tools have been described throughout Chapters 2-5. The major novelties and results of each chapter are summarized in the following, along with some suggestions and purposes for future works.

In Chapter 2 a classical SAFE formulation for viscoelastic waveguide has been extended to include the effect of a three-dimensional initial stress with translational invariant properties along the propagation direction. SAFE formulations proposed in literature [Loveday, 2009] account for initial axial stresses only and consider elastic materials. The effect of pressure-type nonconservative loads have also been taken into account, which was never been treated in literature. Since stresses due to ultrasonic pulses are orders of magnitude lower than those commonly produced by service loads, the wave equation has been derived in linearized incremental form within an Updated Lagrangian framework. Given the dissipative properties of the materials considered, an energy velocity formula based on the Umov's definition and the balance of energy in material description has been proposed. Changes in the dispersion curves have been shown for residual stresses in rails due to roller-straightening processes and initial stresses in pipelines due to the presence of gradients of pressure along the pipe walls. The study proposed in this chapter can be further extended to plasticized waveguides, for which a fully-nonlinear Lagrangian framework is needed.

In Chapter 3 the drawback of finite element-based techniques in representing infinite domains has been addressed by using a 2.5D BEM formulation. The well known analytical and numerical difficulties presented by the BEM in treating singular integrals and non-smooth boundary geometries have been overcome using a regularization procedure. The main novelty introduced with respect to other works proposed in literature [Gunawan and Hirose, 2005] is the introduction of material damping and the use of the Contour Integral Method [Beyn, 2012] to solve the resulting nonlinear eigenvalue problem. It has been shown how the presence of the material damping influences the choice of appropriate Riemann sheets as well as the contour integration path. The method, validated against a reliable SAFE formulation, has been used to compute for the first time the dispersion curves for surface guided waves along cavity of arbitrary cross-section. The method proposed in this chapter can be further extended to the cases of cavities embedded in layered media, in which a numerically computed solution for a half space can be used [François et al., 2010], and poroelastic materials [Lu et al., 2008a,b].

Chapter 4 has been dedicated to the study of leaky guided waves in viscoelastic waveguides of arbitrary cross-section embedded in viscoelastic media. To this end, a coupled SAFE-2.5D BEM formulation has been proposed, exploits the capability of the SAFE to model geometrically and mechanically complex waveguides and the unique capability of the BEM to correctly model the radiated wavefield. The major novelty introduced is in the definition of the interface conditions for the complex wavevectors, which must satisfy the Snell-Descartes law. This in turn leads to the definition of the proper phases of the wavenumbers normal to the interface, which are fundamental in the extraction of leaky poles. The integration path used in the Contour Integral Method has been defined as generally assumed in the Vertical Branch Cut Integration (VBCI) method [Kurkjian, 1985]. The obtained results for waveguides of simple geometry have been validated against those obtained in literature using the Global Matrix Method (GMM) Pavlakovic [1998]; Pavlakovic and Lowe [2003] and the SAFE method with absorbing regions Castaings and Lowe [2008], while new results have been proposed for a square, an H-shaped and a hollow rectangular beams. As suggested for the method in Chapter 3, also the SAFE-2.5D BEM formulation can be extended to the case of surrounding layered media. Moreover, the effect of an initial stress can be included by exploiting the method proposed in Chapter 2 and defining appropriate interface conditions. Such a method could be particularly useful for the dispersion analysis of pre-tensioned or post-tensioned embedded cables and strands.

Finally, in Chapter 5 attention has been focused on the dispersion properties of guided waves in immersed viscoelastic waveguides, for which a SAFE formulation coupled with a regularized 2.5D BEM formulation, used to represent the exterior 2.5D Helmholtz problem, has been proposed. In addition to the analysis of Chapter 4, the CHIEF method has been implemented to avoid numerical instabilities due to the non-uniqueness problem [Schenck, 1968]. The complex leaky poles have been found by means of the Contour Integral Method after the imposition of the correct phase of the wavenumbers normal to the interface. The numerical results for immersed waveguides of circular cross-section have been compared with those obtained using well-stated softwares [Pavlakovic and Lowe, 2011], while new results have been presented for a square and a L-shaped bar. The method proposed in this chapter can be further extended to the case of viscous fluids. Moreover, the effect of the initial pressure could be added following the analysis of Chapter 2, which can be useful for the design of guided waves-based inspections of subsea transportation pipelines.

Appendix A

List of publications

Journal papers

M. Mazzotti, A. Marzani, I. Bartoli, "Dispersion analysis of leaky guided waves in fluid-loaded waveguides of generic shape", submitted to Ultrasonics, 2013.

M. Mazzotti, I. Bartoli, A. Marzani, E. Viola, "A 2.5D Boundary Element formulation for modeling damped waves in arbitrary cross-section waveguides and cavities", Journal of Computational Physics, 2013.

M. Mazzotti, I. Bartoli, A. Marzani, E. Viola, "A coupled SAFE-2.5D BEM approach for the dispersion analysis of damped leaky guided waves in embedded waveguides of arbitrary cross-section", Ultrasonics, accepted for publication, 2013.

C. Gentilini, A. Marzani, **M. Mazzotti**, "Nondestructive characterization of tie-rods by means of dynamic testing, added masses and genetic algorithms", Journal of Sound and Vibration, 332(1), 2012, pp. 76-101

M. Mazzotti, A. Marzani, I. Bartoli, E. Viola, "Guided waves dispersion analysis for prestressed viscoelastic waveguides by means of the SAFE method", International Journal of Solids and Structures, 49(18), 2012, pp. 2359-2372

A. Marzani, **M. Mazzotti**, E. Viola, P. Vittori, I. Elishakoff, "FEM formulation for dynamic instability of fluid-conveying pipe on non-uniform elastic foundation", Mechanics Based Design of Structures and Machines, 40(1), 2012, pp. 83-95

Conference proceedings

M. Mazzotti, A. Marzani, I. Bartoli, E. Viola, "A coupled SAFE-BEM formulation for modeling leaky waves in waveguides of arbitrary cross-section surrounded by isotropic media", Proceedings of

SPIE, Vol. 8695 .

M. Mazzotti, I. Bartoli, A. Marzani, E. Viola, "A Boundary Element formulation for the computation of damped Guided Waves", Review of progress In Quantitative Nondestructive Evaluation- AIP Conference Proceedings, 1511(1), 2013, pp. 113-120

M. Mazzotti, A. Marzani, I. Bartoli, E. Viola, "A SAFE formulation for modeling stress waves in elastic waveguides subjected to an initial 3D prestress", Proceedings of the 20th Conference of the Italian Association for Theoretical and Applied Mechanics - AIMETA 2011, Bologna, Italy, 12-15 September 2011, pp. 1-10

M. Miniaci, **M. Mazzotti**, A. Marzani, E. Viola, "Mechanical waves in simply and multiply connected thin-walled beams", Proceedings of the 20th Conference of the Italian Association for Theoretical and Applied Mechanics - AIMETA 2011, Bologna, Italy, 12-15 September 2011, pp. 1-10

C. Gentilini, **M. Mazzotti**, A. Marzani, "Nondestructive characterization of tie-rods by means of dynamic testing, added masses and Genetic Algorithms", Proceedings of the 20th Conference of the Italian Association for Theoretical and Applied Mechanics - AIMETA 2011, Bologna, Italy, 12-15 September 2011, pp. 1-10

A. Marzani, **M. Mazzotti**, E. Viola, L. De Marchi, N. Speciale, P. Rizzo, "A Genetic Algorithm based procedure for the constitutive characterization of composite plates using dispersive guided waves data" in: , Advances in Structural Engineering, Mechanics and Computation, LEIDEN, CRC Press/Balkema, 2010, pp. 305 - 308 (4th International Conference on Structural Engineering, Mechanics and Computation - SEMC 2010, Cape Town, South Africa, 6-8 September 2010)

Bibliography

J. D. Achenbach. *Wave Propagation in Elastic Solids*. North-Holland Pub. Co., Amsterdam, 1973. 34

F. Ahmad, N. Kiyani, F. Yousaf, and M. Shams. Guided waves in a fluid-loaded transversely isotropic plate. *Mathematical Problems in Engineering*, 8(2):151 – 159, 2002. 157

Faiz Ahmad. Guided waves in a transversely isotropic cylinder immersed in a fluid. *The Journal of the Acoustical Society of America*, 109(3):886–890, 2001. 108, 157, 171

T. Amako, Y. Yamamoto, and Shao-Liang Zhang. A large-grained parallel algorithm for nonlinear eigenvalue problems and its implementation using omnirpc. In *Cluster Computing, 2008 IEEE International Conference on*, pages 42–49, 2008. 59, 80

Lars Andersen. *Linear Elastodynamic Analysis*. Aalborg University. Department of Civil Engineering, 2006. 62, 63, 73, 125, 166

C. Aristégui, M.J.S. Lowe, and P. Cawley. Guided waves in fluid-filled pipes surrounded by different fluids. *Ultrasonics*, 39(5):367 – 375, 2001. 157, 158

J. Asakura, T. Sakurai, H. Tadano, T. Ikegami, and K. Kimura. A numerical method for nonlinear eigenvalue problems using contour integrals. *JSIAM Letters*, 52:52–55, 2009. 59, 80

B. A. Auld. *Acoustic Fields and Waves in Solids. Volume 2*. John Wiley & Sons, Inc., New York, 1973. 128, 129, 133

S. A. Badsar, M. Schevenels, W. Haegeman, and G. Degrande. Determination of the material damping ratio in the soil from sasw tests using the half-power bandwidth method. *Geophysical Journal International*, 182(3):1493–1508, 2010. 59

P. K. Banerjee. *Boundary Element Methods in Engineering Science*. McGraw-Hill-Book Co. (UK), New York, 1981. 71

I. Bartoli, A. Marzani, F. Lanza di Scalea, and E. Viola. Modeling wave propagation in damped waveguides of arbitrary cross-section. *Journal of Sound and Vibration*, 295:685 – 707, 2006. ix, 3, 10, 14, 39, 41, 57, 59, 90, 107, 133, 177, 187

Ivan Bartoli, Stefano Coccia, Robert Phillips, Ankit Srivastava, Francesco Lanza di Scalea, and Salvatore Salamone. Stress dependence of guided waves in rails. In Tribikram Kundu, editor, *Health Monitoring of Structural and Biological Systems 2010*, volume 7650 of *Proc. SPIE*, pages 765021–1 – 765021–10, 2010. 10, 38

Klaus-Jürgen Bathe. *Finite Element Procedures*. Prentice Hall, Upper Saddle River, New Jersey 07458, 1996. 12, 17

Zdeněk P. Bažant and Luigi Cedolin. *Stability of Structures: Elastic, Inelastic, Fracture and Damage Theories*. Oxford University Press, New York, 1991. 12, 15

M. Beard, M. Lowe, and P. Cawley. Ultrasonic guided waves for inspection of grouted tendons and bolts. *Journal of Materials in Civil Engineering*, 15(3):212–218, 2003. 108

M.D. Beard and M.J.S. Lowe. Non-destructive testing of rock bolts using guided ultrasonic waves. *International Journal of Rock Mechanics and Mining Sciences*, 40(4):527 – 536, 2003. 108

G. Belloncle, H. Franklin, F. Luppé, and J. M. Conoir. Normal modes of a poroelastic plate and their relation to the reflection and transmission coefficients. *Ultrasonics*, 41(3):207 – 216, 2003. 157

G. Belloncle, F. Luppé, H. Franklin, and J. M. Conoir. Influence of the slow wave on the relation between the angular resonances and the leaky guided modes properties for a poroelastic plate embedded in water. *Ultrasonics*, 42(19):511 – 514, 2004. 157

Marilyn J. Berliner and Roman Solecki. Wave propagation in fluid-loaded, transversely isotropic cylinders. part i. analytical formulation. *The Journal of the Acoustical Society of America*, 99(4):1841–1847, 1996a. 108, 157

Marilyn J. Berliner and Roman Solecki. Wave propagation in fluid-loaded, transversely isotropic cylinders. part ii. numerical results. *The Journal of the Acoustical Society of America*, 99(4):1848–1853, 1996b. 108, 157

A. Bernard, M. J. S. Lowe, and M. Deschamps. Guided waves energy velocity in absorbing and non-absorbing plates. *The Journal of the Acoustical Society of America*, 110(1):186–196, 2001. 158, 177

W.-J. Beyn. An integral method for solving nonlinear eigenvalue problems. *Linear Algebra and its Applications*, 436(10):3839 – 3863, 2012. 59, 80, 81, 82, 99, 106, 110, 127, 138, 149, 169, 170, 189

Atul Bhaskar. Waveguide modes in elastic rods. *Proceedings: Mathematical, Physical and Engineering Sciences*, 459(2029):175 – 194, 2003. 9

C. Betegán Biempica, J.J. del Coz Díaz, P.J. García Nieto, and I. Peñuelas Sánchez. Nonlinear analysis of residual stresses in a rail manufacturing process by fem. *Applied Mathematical Modelling*, 33(1): 34 – 53, 2009. 43

M. A. Biot. Propagation of elastic waves in a cylindrical bore containing a fluid. *Journal of Applied Physics*, 23(9):997–1005, 1952. 92, 94, 95

M. A. Biot. General theorems on the equivalence of group velocity and energy transport. *Phys. Rev.*, 105(4):1129 – 1137, 1957. 9, 34

Maurice A. Biot. The influence of initial stress on elastic waves. *Journal of Applied Physics*, 11(8):522 – 530, 1940. 9

Maurice A. Biot. *Mechanics of Incremental Deformations*. John Wiley & Sons, Inc., New York, 1965. 9

Javier Bonet and Richard D. Wood. *Nonlinear Continuum Mechanics for Finite Element Analysis*. Cambridge University Press, New York, 2008. 11, 12, 13, 15, 25, 34, 35

M. Bonnet. *Boundary Integral Equation Methods for Solids and Fluids*. John Wiley & Sons Ltd, Chichester, 1999. 62, 63, 67, 70, 71, 156, 163

R. D. Borcherdt. *Viscoelastic Waves in Layered Media*. Cambridge University Press, Cambridge CB2 8RU, UK, 2009. 128

Anders Boström and Anthony Burden. Propagation of elastic surface waves along a cylindrical cavity and their excitation by a point force. *The Journal of the Acoustical Society of America*, 72(3): 998–1004, 1982. x, 92, 94, 96, 102

B. J. Botter and J. van Arkel. Circumferential propagation of acoustic boundary waves in boreholes. *The Journal of the Acoustical Society of America*, 71(4):790–795, 1982. 94

C.A. Brebbia and J. Dominguez. *Boundary Elements: An Introductory Course*. Computational Mechanics Publications and Elsevier Applied Science, Southampton, United Kingdom, 1989. 71, 73, 75, 76, 121, 163, 164

L. Brillouin. *Wave Propagation and Group Velocity*. Academic Press, New York, 1960. 34

A.D. Burden. The null-field approach and the propagation of elastic surface waves along cylindrical cavities. *Applied Scientific Research*, 42:333–346, 1985a. ISSN 0003-6994. 93

A.D. Burden. The propagation of elastic surface waves along cylindrical cavities of general cross section. *Wave Motion*, 7(2):153 – 168, 1985b. 93

José M. Carcione, Dan Kosloff, and Ronnie Kosloff. Wave propagation simulation in a linear viscoelastic medium. *Geophysical Journal*, 95(3):597–611, 1988. 129, 130

Michel Castaings and Michael Lowe. Finite element model for waves guided along solid systems of arbitrary section coupled to infinite solid media. *The Journal of the Acoustical Society of America*, 123(2):696–708, 2008. xi, xii, 4, 105, 108, 110, 129, 133, 134, 136, 137, 187, 190

Igor Castro and António Tadeu. Coupling of the bem with the mfs for the numerical simulation of frequency domain 2-d elastic wave propagation in the presence of elastic inclusions and cracks. *Engineering Analysis with Boundary Elements*, 36(2):169 – 180, 2012. 69

G. Caviglia and A. Morro. *Inhomogeneous Waves in Solids and Fluids*. World Scientific Publishing Co. Pte. Ltd., Farrer Road, Singapore, 1992. 10, 169

G. Caviglia and A. Morro. Energy flux and dissipation in pre-stressed solids. *Acta Mechanica*, 128:209 – 216, 1998. ISSN 0001-5970. 10

Giacomo Caviglia, Angelo Morro, and Enrico Pagani. Inhomogeneous waves in viscoelastic media. *Wave Motion*, 12(2):143 – 159, 1990. 129, 130

V. Cervený and I. Pšencík. Boundary attenuation angles for inhomogeneous plane waves in anisotropic dissipative media. *Geophysics*, 76(3):WA51–WA62, 2011. 130

S. Chaki and G. Bourse. Guided ultrasonic waves for non-destructive monitoring of the stress levels in prestressed steel strands. *Ultrasonics*, 49(2):162 – 171, 2009. 10, 107

Y.C. Chang and Bong Ho. The poynting theorem of acoustic wave propagating in an inhomogeneous moving medium. *Journal of Sound and Vibration*, 184(5):942 – 945, 1995. 34

Feng Chen and Paul D. Wilcox. The effect of load on guided wave propagation. *Ultrasonics*, 47(1-4): 111 – 122, 2007. 3, 9, 38, 49, 53, 107

Jeng-Tzong Chen, Tzong-Wey Lin, I-Lin Chen, and Yang-Jye Lee. Fictitious frequency for the exterior helmholtz equation subject to the mixed-type boundary condition using bems. *Mechanics Research Communications*, 32(1):75 – 92, 2005. 163

Y. Cho and J. L. Rose. An elastodynamic hybrid boundary element study for elastic guided wave interactions with a surface breaking defect. *International Journal of Solids and Structures*, 37(30): 4103 – 4124, 2000. ISSN 0020-7683. 57

Younho Cho and Joseph L. Rose. A boundary element solution for a mode conversion study on the edge reflection of lamb waves. *The Journal of the Acoustical Society of America*, 99(4):2097–2109, 1996. 57

Richard M. Christensen. *Theory of Viscoelasticity: Second Edition*. Dover Publications, Inc., Mineola, N.Y., 2010. 16, 20, 61

L. Pamela Cook and Mark Holmes. Waves and dispersion relations for hydroelastic systems. *SIAM Journal on Applied Mathematics*, 41(2):271 – 287, 1981. 9

P. Alves Costa, R. Calçada, and A. Silva Cardoso. Trackground vibrations induced by railway traffic: In-situ measurements and validation of a 2.5d fem-bem model. *Soil Dynamics and Earthquake Engineering*, 32(1):111 – 128, 2012. 57, 109

M. Davidovich. On the electromagnetic energy density and energy transfer rate in a medium with dispersion due to conduction. *Technical Physics*, 55:630 – 635, 2010. 34, 36

Vinay Dayal. Longitudinal waves in homogeneous anisotropic cylindrical bars immersed in fluid. *The Journal of the Acoustical Society of America*, 93(3):1249–1255, 1993. 108, 157

Vinay Dayal and Vikram K. Kinra. Leaky lamb waves in an anisotropic plate. i: An exact solution and experiments. *The Journal of the Acoustical Society of America*, 85(6):2268–2276, 1989. 107

Vinay Dayal and Vikram K. Kinra. Leaky lamb waves in an anisotropic plate. ii: Nondestructive evaluation of matrix cracks in fiber-reinforced composites. *The Journal of the Acoustical Society of America*, 89(4):1590–1598, 1991. 107

G. Degrande, D. Clouteau, R. Othman, M. Arnst, H. Chebli, R. Klein, P. Chatterjee, and B. Janssens. A numerical model for ground-borne vibrations from underground railway traffic based on a periodic finite elementboundary element formulation. *Journal of Sound and Vibration*, 293(35):645 – 666, 2006. 93

A. D. Degtyar and S. I. Rokhlin. Stress effect on boundary conditions and elastic wave propagation through an interface between anisotropic media. *Journal of Acoustical Society of America*, 104(4): 1992 – 2003, 1998. 10

X. Ding, H. Liu, J. Liu, and Y. Chen. Wave propagation in a pipe pile for low-strain integrity testing. *Journal of Engineering Mechanics*, 137(9):598–609, 2011. 144

J. Dominguez. *Boundary Elements in Dynamics*. Computational Mechanics Publications and Elsevier Applied Science, Southampton, United Kingdom, 1993. 62, 71, 87

M.P. Ekstrom. Dispersion estimation from borehole acoustic arrays using a modified matrix pencil algorithm. In *Signals, Systems and Computers, 1995. 1995 Conference Record of the Twenty-Ninth Asilomar Conference on*, volume 1, pages 449 –453, 1995. 59

W. M. Ewing, W. S. Jardetzky, and F. Press. *Elastic Waves in Layered Media*. McGraw-Hill Book Company, Inc., New York, 1957. 83, 84

Z. Fan, M. J. S. Lowe, M. Castaings, and C. Bacon. Torsional waves propagation along a waveguide of arbitrary cross section immersed in a perfect fluid. *The Journal of the Acoustical Society of America*, 124(4):2002–2010, 2008. 4, 155, 157, 158, 162, 171, 185, 187

Zheng Fan. *Applications of guided Waves propagation on waveguides with arbitrary cross-section*. PhD thesis, Imperial College, London, UK, 2010. 157, 185

R. Finno and H. Chao. Guided waves in embedded concrete piles. *Journal of Geotechnical and Geoenvironmental Engineering*, 131(1):11–19, 2005. 144

R.J. Finno, J.S. Popovics, A.A. Hanifah, W.L. Kath, H.-C. Chao, and Y.-H. Hu. Guided wave interpretation of surface reflection techniques for deep foundations. *Rivista Italiana di Geotecnica*, (1): 76–91, 2001. 144

S. François, M. Schevenels, P. Galvín, G. Lombaert, and G. Degrande. A 2.5d coupled fe-be methodology for the dynamic interaction between longitudinally invariant structures and a layered halfspace. *Computer Methods in Applied Mechanics and Engineering*, 199(2324):1536 – 1548, 2010. 57, 59, 63, 71, 100, 109, 117, 153, 190

Ahmed Frikha, Fabien Treyssède, and Patrice Cartraud. Effect of axial load on the propagation of elastic waves in helical beams. *Wave Motion*, 48(1):83 – 92, 2011. 9

J. M. Galán and R. Abascal. Boundary element solution for the bidimensional scattering of guided waves in laminated plates. *Computers & Structures*, 83(1011):740 – 757, 2005. 57

José M Galán and Ramón Abascal. Remote characterization of defects in plates with viscoelastic coatings using guided waves. *Ultrasonics*, 42(19):877 – 882, 2004. 57

H. Gao, T. Matsumoto, T. Takahashi, and T. Yamada. Eigenvalue analysis for 2d acoustic problem by bem with block ss method. In *Transactions of JASCOME*, volume 11, 2011. 59

Xiao-Wei Gao and Trevor G. Davies. *Boundary Element Programming in Mechanics.* Cambridge University Press, New York, NY, USA, 2001. 122, 164

L. Gavric. Computation of propagative waves in free rail using a finite element technique. *Journal of Sound and Vibration*, 185(3):531 – 543, 1995. 3, 57, 90, 107, 187

Vladimir Gerasik and Marek Stastna. Complex group velocity and energy transport in absorbing media. *Phys. Rev. E*, 81:056602, 2010. 34

L. Godinho, A. Tadeu, and F.J. Branco. Wave scattering by infinite cylindrical shell structures submerged in a fluid medium. *Wave Motion*, 38(2):131 – 149, 2003. 57, 58, 153, 158

A. Gunawan and S. Hirose. Boundary element analysis of guided waves in a bar with an arbitrary cross-section. *Engineering Analysis with Boundary Elements*, 29(10):913 – 924, 2005. xii, xiii, 58, 71, 118, 119, 141, 142, 143, 174, 175, 176, 189

N. A. Haskell. The dispersion of surface waves on multilayered media. *Bulletin of the Seismological Society of America*, 43(1):17–34, 1953. 3, 157, 187

Takahiro Hayashi, Won-Joon Song, and Joseph L Rose. Guided wave dispersion curves for a bar with an arbitrary cross-section, a rod and rail example. *Ultrasonics*, 41(3):175 – 183, 2003. 3, 57, 90, 107

Takahiro Hayashi, Chiga Tamayama, and Morimasa Murase. Wave structure analysis of guided waves in a bar with an arbitrary cross-section. *Ultrasonics*, 44(1):17 – 24, 2006. 107, 187

M. Hayes. Wave propagation and uniqueness in prestressed elastic solids. *Proceedings of the Royal Society of London. Series A, Mathematical and Physical Sciences*, 274(1359):500 – 506, 1963. 9

Xiao He and Hengshan Hu. Borehole flexural modes in transversely isotropic formations: Low-frequency asymptotic velocity. *Geophysics*, 74(4):E149–E158, 2009. 83

Xiao He and HengShan Hu. Single-valued definition of the multivalued function for borehole acoustic waves in transversely isotropic formations. *SCIENCE CHINA Physics, Mechanics & Astronomy*, 53:1419–1426, 2010. ISSN 1674-7348. 83, 131

A.-C. Hladky-Hennion. Finite element analysis of the propagation of acoustic waves in waveguides. *Journal of Sound and Vibration*, 194(2):119 – 136, 1996. 3

A.-C. Hladky-Hennion, P. Langlet, and M. de Billy. Finite element analysis of the propagation of acoustic waves along waveguides immersed in water. *Journal of Sound and Vibration*, 200(4):519 – 530, 1997. 158

A.-C. Hladky-Hennion, P. Langlet, R. Bossut, and M. de Billy. Finite element modelling of radiating waves in immersed wedges. *Journal of Sound and Vibration*, 212(2):265 – 274, 1998. 158, 169

Anne-Christine Hladky-Hennion, Philippe Langlet, and Michel de Billy. Conical radiating waves from immersed wedges. *The Journal of the Acoustical Society of America*, 108(6):3079–3083, 2000. 168, 169

Gerhard A. Holzapfel. *Nonlinear Solid Mechanics*. John Wiley & Sons Ltd, Baffins Lane, Chichester, 2000. 34

F. Honarvar, E. Enjilela, and A. N. Sinclair. Correlation between helical surface waves and guided modes of an infinite immersed elastic cylinder. *Ultrasonics*, 51(2):238 – 244, 2011. 157

Y. Hua and T.K. Sarkar. Matrix pencil method for estimating parameters of exponentially damped/undamped sinusoids in noise. *Acoustics, Speech and Signal Processing, IEEE Transactions on*, 38(5):814 – 824, 1990. 59

Hua Jia, Mu Jing, and L. Rose Joseph. Guided wave propagation in single and double layer hollow cylinders embedded in infinite media. *The Journal of the Acoustical Society of America*, 129(2): 691–700, 2011. 4, 105, 108, 158, 187

Eduardo Kausel. *Fundamental Solutions in Elastodynamics*. first edition, 2006. 19, 66, 68

Rymantas Kažys, Renaldas Raišutis, Egidijus Žukauskas, Liudas Mažeika, and Alfonsas Vladišauskas. Air-coupled ultrasonic testing of cfrp rods by means of guided waves. *Physics Procedia*, 3(1):185 – 192, 2010. 157

J. Keller, M. B. Prime, D. Buttle, P. M. Mummery, P. J. Webster, J. Shackleton, and P. J. Withers. The measurement of residual stress in railway rails by diffraction and other methods. *Journal of Neutron Research*, 11(4):187 – 193, 2003. ix, 43, 45

S. A. Ketcham, R. J. Greenfield, M. L. Moran, T. S. Anderson, and S. O. Hestholm. Soil attenuation in seismic simulations; implications for vehicle tracking. In *Proc. 2001 Meeting of the Military Sensing Symposia (MSS)*, 2001. 134, 144

D. Kleczewski and R. Parnes. Torsional dispersion relations in a radially dual elastic medium. *The Journal of the Acoustical Society of America*, 81(1):30–36, 1987. 107

L. Knopoff. A matrix method for elastic wave problems. *Bulletin of the Seismological Society of America*, 54(1):431–438, 1964. 3, 107, 157, 187

S. Kobayashy. *Boundary Element Methods in Mechanics*. Elsevier Science Publisher B.V., 1987. 63

Andrew L. Kurkjian. Numerical computation of individual far-field arrivals excited by an acoustic source in a borehole. *Geophysics*, 50(5):852–866, 1985. 131, 190

Laurent Laguerre, Anne Grimault, and Marc Deschamps. Ultrasonic transient bounded-beam propagation in a solid cylinder waveguide embedded in a solid medium. *The Journal of the Acoustical Society of America*, 121(4):1924–1934, 2007. 108

Usik Lee and Hyungmi Oh. Dynamics of an axially moving viscoelastic beam subject to axial tension. *International Journal of Solids and Structures*, 42(8):2381 – 2398, 2005. ISSN 0020-7683. 16

Mickal Lematre, Guy Feuillard, Emmanuel Le Clézio, and Marc Lethiecq. Modeling of the influence of a prestress gradient on guided wave propagation in piezoelectric structures. *Journal of Acoustical Society of America*, 120:1964 – 1975, 2006. 9

Z. L. Li, J. D. Achenbach, I. Komsky, and Y. C. Lee. Reflection and transmission of obliquely incident surface waves by an edge of a quarter space: Theory and experiment. *Journal of Applied Mechanics*, 59(2):349–355, 1992. 65, 117

M. J. Lighthill. Group velocity. *Journal of the Institute of Mathematics and Its Applications*, 1:1 – 28, 1965. 34

Zhirong Lin, Akira Kasai, and Yoshito Itoh. Dispersion curves computation for waveguides buried in infinite space by semi-analytical finite element method. *Procedia Engineering*, 10(0):1615 – 1620, 2011. 108

Q. Liu and C. Chang. Compressional head waves in attenuative formations: Forward modeling and inversion. *Geophysics*, 61(6):1908–1920, 1996. 131

Sjia Sheng Liu. The application of elastic wave reflection method in the pile foundation inspection. *Advanced Materials Research*, 594 - 597:1109 – 1112, 2012. 144

R Long, P Cawley, and M Lowe. Acoustic wave propagation in buried iron water pipes. 459(2039): 2749–2770, 2003a. 157, 158

R. Long, M. Lowe, and P. Cawley. Attenuation characteristics of the fundamental modes that propagate in buried iron water pipes. *Ultrasonics*, 41(7):509 – 519, 2003b. 108

R. Long, M. Lowe, and P. Cawley. Attenuation characteristics of the fundamental modes that propagate in buried iron water pipes. *Ultrasonics*, 41(7):509 – 519, 2003c. 157, 158

Philip W. Loveday. Semi-analytical finite element analysis of elastic waveguides subjected to axial loads. *Ultrasonics*, 49(3):298 – 300, 2009. 10, 33, 38, 49, 107, 189

Philip W. Loveday and Paul D. Wilcox. Guided wave propagation as a measure of axial loads in rails. In Tribikram Kundu, editor, *Health Monitoring of Structural and Biological Systems 2010*, volume 7650 of *Proc. SPIE*, pages 765023–1 – 765023–8, 2010. 10, 38

M. J. S. Lowe. *Plate waves for the NDT of diffu sion bonded titanium.* PhD thesis, Imperial College, London, UK, 1992. 3, 38, 105, 107, 157, 158, 187

M.J.S. Lowe. Matrix techniques for modeling ultrasonic waves in multilayered media. *Ultrasonics, Ferroelectrics and Frequency Control, IEEE Transactions on*, 42(4):525 –542, july 1995. 57, 58, 59, 61, 107, 157

M.J.S. Lowe, D.N. Alleyne, and P. Cawley. Defect detection in pipes using guided waves. *Ultrasonics*, 36(15):147 – 154, 1998. 108

Jian-Fei Lu, Dong-Sheng Jeng, and Sally Williams. A 2.5-d dynamic model for a saturated porous medium: Part i. greens function. *International Journal of Solids and Structures*, 45(2):378 – 391, 2008a. ISSN 0020-7683. 65, 153, 190

Jian-Fei Lu, Dong-Sheng Jeng, and Sally Williams. A 2.5-d dynamic model for a saturated porous medium. part ii: Boundary element method. *International Journal of Solids and Structures*, 45(2): 359 – 377, 2008b. ISSN 0020-7683. 57, 59, 65, 71, 74, 75, 117, 153, 164, 190

Wei Luo and Joseph L. Rose. Phased array focusing with guided waves in a viscoelastic coated hollow cylinder. *The Journal of the Acoustical Society of America*, 121(4):1945–1955, 2007. 61

Jian Ma. *On-lines measurements of contents inside pipes using guided ultrasonics waves.* PhD thesis, Imperial College, London, UK, 2007. 157, 177

Chi-Sing Man. Hartig's law and linear elasticity with initial stress. *Inverse Problems*, 14(2):313 – 319, 1998. 12

Eric B. Molz and John R. Beamish. Leaky plate modes: Radiation into a solid medium. *The Journal of the Acoustical Society of America*, 99(4):1894–1900, 1996. 133

V.G. Mozhaev and M. Weihnacht. Subsonic leaky rayleigh waves at liquidsolid interfaces. *Ultrasonics*, 40(18):927 – 933, 2002. 169

Jing Mu and Joseph L. Rose. Guided wave propagation and mode differentiation in hollow cylinders with viscoelastic coatings. *Journal Acoustical Society of America*, 124:866 – 874, 2008. 10

Peter B. Nagy. Longitudinal guided wave propagation in a transversely isotropic rod immersed in fluid. *The Journal of the Acoustical Society of America*, 98(1):454–457, 1995. 108, 157

Peter B. Nagy and Adnan H. Nayfeh. Viscosity-induced attenuation of longitudinal guided waves in fluid-loaded rods. *The Journal of the Acoustical Society of America*, 100(3):1501–1508, 1996. 157

Adnan H. Nayfeh and D. E. Chimenti. Propagation of guided waves in fluid-coupled plates of fiber-reinforced composite. *The Journal of the Acoustical Society of America*, 83(5):1736–1743, 1988. 157

Adnan H. Nayfeh and Peter B. Nagy. General study of axisymmetric waves in layered anisotropic fibers and their composites. *The Journal of the Acoustical Society of America*, 99(2):931–941, 1996. 107, 145, 157

G. Neau. *amb waves in anisotropic viscoelastic plates. Study of the wave fronts and attenuation.* PhD thesis, L'Université Bordeux I, Bordeaux, France, 2003. 20

Sheng-Huoo Ni, Kuo-Feng Lo, Lutz Lehmann, and Yan-Hong Huang. Timefrequency analyses of pile-integrity testing using wavelet transform. *Computers and Geotechnics*, 35(4):600 – 607, 2008. 144

C.-M. Nilsson, C.J.C. Jones, D.J. Thompson, and J. Ryue. A waveguide finite element and boundary element approach to calculating the sound radiated by railway and tram rails. *Journal of Sound and Vibration*, 321(35):813 – 836, 2009. 109, 162, 166

A. V. Osetrov, H.-J. Fröhlich ans R. Koch, and E. Chilla. Acoustoelastic effect in anisotropic layered structures. *Physical Review B*, 62:13 963 – 13 969, 2000. 9

R. Parnes. Dispersion relations of waves in a rod embedded in an elastic medium. *Journal of Sound and Vibration*, 76(1):65 – 75, 1981. 107

R. Parnes. Torsional dispersion relations of waves in an infinitely long clad cylindrical rod. *The Journal of the Acoustical Society of America*, 71(6):1347–1351, 1982. 107

B. Pavlakovic, M. J. S. Lowe, D. N. Alleyne, and P. Cawley. Disperse: A general purpose program for creating dispersion curves. In D. O. Thompson and D. E. Chimenti, editors, *Review of Progress in Quantitative NDE*, volume 16, pages 185 – 192, New York, 1997. Plenum Press. 107, 138, 171

B. N. Pavlakovic. *Leaky guided ultrasonic waves in NDT.* PhD thesis, Imperial College, London, UK, 1998. 3, 31, 32, 105, 107, 108, 128, 133, 145, 149, 157, 158, 171, 187, 190

B. N. Pavlakovic and M. J. S. Lowe. *DISPERSE: A System for Generating Dispersion Curves. User's Manual*, 2003. 133, 170, 190

B. N. Pavlakovic, M. J. S. Lowe, and P. Cawley. High-frequency low-loss ultrasonic modes in imbedded bars. *Journal of Applied Mechanics*, 68(1):67–75, 2001. xii, 108, 110, 134, 138, 139, 140

B.N. Pavlakovic and M.J.S. Lowe. Disperse software ver. 2.0.16i (evaluation copy). `http://www3.imperial.ac.uk/nde/products%20and%20services/disperse`, 2011. 156, 159, 171, 185, 190

H. A. Pedersen, F. J. Sãnchez Sesma, and M. Campillo. Three-dimensional scattering by two-dimensional topographies. *Bulletin of the Seismological Society of America*, 84(4):1169–1183, 1994. 57, 65

Andreia Pereira, António Tadeu, and Julieta António. Influence of the cross-section geometry of a cylindrical solid submerged in an acoustic medium on wave propagation. *Wave Motion*, 36(1):23 – 39, 2002. 158

W. H. Press, S. A. Teukolsky, W. T. Vetterling, and B. P. Flannery. *Numerical Recipes in Fortran 77, Second Edition. Volume 1: The Art of Scientific Computing.* Cambridge University Press, New York, NY, USA, 1992. 138, 150

M. J. Randall. Fast programs for layered half-space problems. *Bulletin of the Seismological Society of America*, 57(6):1299–1315, 1967. 157

Georg Rieckh, Wolfgang Kreuzer, Holger Waubke, and Peter Balazs. A 2.5d-fourier-bem model for vibrations in a tunnel running through layered anisotropic soil. *Engineering Analysis with Boundary Elements*, 36(6):960 – 967, 2012. 57, 100, 153

Jonas W. Ringsberg and Torbjörn Lindbäck. Rolling contact fatigue analysis of rails inculding numerical simulations of the rail manufacturing process and repeated wheel-rail contact loads. *International Journal of Fatigue*, 25(6):547 – 558, 2003. 43

Joseph. L. Rose. *Ultrasonic Waves in Solid Media.* Cambridge University Press, Cambridge, 2004. 12, 20, 33, 95, 128, 168

Harry A. Schenck. Improved integral formulation for acoustic radiation problems. *The Journal of the Acoustical Society of America*, 44(1):41–58, 1968. 156, 159, 165, 166, 190

G Schleinzer and F.D Fischer. Residual stress formation during the roller straightening of railway rails. *International Journal of Mechanical Sciences*, 43(10):2281 – 2295, 2001. 43

S. Schneider. Fe/fmbe coupling to model fluid-structure interaction. *International Journal for Numerical Methods in Engineering*, 76(13):2137–2156, 2008. 166

A. H. Shah, W. Zhuang, N. Popplewell, and J. B. C. Rogers. Guided waves in thin-walled structural members. *Journal of vibration and acoustics*, 123(3):376–382, 2001. 3, 153

Li-Hua Shen, Yue-Min Wang, and Feng-Rui Sun. Study on feasibility of pressure pipe guided wave ndt based on magnetostrictive effect. In *Ultrasonics Symposium, 2008. IUS 2008. IEEE*, pages 1897 – 1900, 2008. 10

X Sheng, C.J.C Jones, and D.J Thompson. Modelling ground vibration from railways using wavenumber finite- and boundary-element methods. *Proceedings of the Royal Society A: Mathematical, Physical and Engineering Science*, 461(2059):2043 – 2070, 2005. 57, 65, 71, 109

X. Sheng, C.J.C. Jones, and D.J. Thompson. Prediction of ground vibration from trains using the wavenumber finite and boundary element methods. *Journal of Sound and Vibration*, 293(35):575 – 586, 2006. ISSN 0022-460X. 57, 109

Hyeon Jae Shin and Joseph L. Rose. Guided waves by axisymmetric and non-axisymmetric surface loading on hollow cylinders. *Ultrasonics*, 37(5):355 – 363, 1999. 107

John A. Simmons, E. Drescher-Krasicka, and H. N. G. Wadley. Leaky axisymmetric modes in infinite clad rods. i. *The Journal of the Acoustical Society of America*, 92(2):1061–1090, 1992. 105, 107, 130, 133, 169, 187

Francesco Simonetti and Peter Cawley. On the nature of shear horizontal wave propagation in elastic plates coated with viscoelastic materials. *Proceedings of the Royal Society of London. Series A: Mathematical, Physical and Engineering Sciences*, 460(2048):2197–2221, 2004. 177

M.H.S. Siqueira, C.E.N. Gatts, R.R. da Silva, and J.M.A. Rebello. The use of ultrasonic guided waves and wavelets analysis in pipe inspection. *Ultrasonics*, 41(10):785 – 797, 2004. ISSN 0041-624X. 157

Stefan Sorohan, Nicolae Constantin, Mircea Gavan, and Viorel Anghel. Extraction of dispersion curves for waves propagating in free complex waveguides by standard finite element codes. *Ultrasonics*, 51 (4):503 – 515, 2011. 3, 107, 187

A. H. Stroud and D. Secrest. *Gaussian Quadrature Formulas*. Prentice-Hall, Englewood Cliffs, NJ, USA, 1996. 27, 75, 120, 164

A. Tadeu, J. António, and L. Godinho. Green's function for two-and-a-half dimensional elastodynamic problems in a half-space. *Computational Mechanics*, 27:484–491, 2001. ISSN 0178-7675. 65

A. Tadeu, J. António, L. Godinho, and P. Amado Mendes. Simulation of sound absorption in 2d thin elements using a coupled bem/tbem formulation in the presence of fixed and moving 3d sources. *Journal of Sound and Vibration*, 331(10):2386 – 2403, 2012. 162

A.J.B. Tadeu and E. Kausel. Green's functions for two-and-a-half-dimensional elastodynamic problems. *Journal of Engineering Mechanics*, 126(10):1093–1096, 2000. 57, 65, 66, 68, 70, 117

António Tadeu, Luiís Godinho, and Paulo Santos. Wave motion between two fluid-filled boreholes in an elastic medium. *Engineering Analysis with Boundary Elements*, 26(2):101 – 117, 2002a. 158

António J.B. Tadeu and Paulo F.A. Santos. 3-d wave propagation in fluid-filled irregular boreholes in elastic formations. *Soil Dynamics and Earthquake Engineering*, 21(6):499 – 517, 2001. 58, 109, 158

António J.B. Tadeu, Julieta M.P. António, and Eduardo Kausel. 3d scattering of waves by a cylindrical irregular cavity of infinite length in a homogeneous elastic medium. *Computer Methods in Applied Mechanics and Engineering*, 191(2728):3015 – 3033, 2002b. 93

Kazumi Tanuma and Chi-Sing Man. Perturbation formula for phase velocity of rayleigh waves in prestressed anisotropic media. *Journal of Elasticity*, 85:21–37, 2006. ISSN 0374-3535. URL `http://dx.doi.org/10.1007/s10659-006-9067-z`. 10.1007/s10659-006-9067-z. 9

William T. Thomson. Transmission of elastic waves through a stratified solid medium. *Journal of Applied Physics*, 21(2):89–93, 1950. 3, 157, 187

R. N. Thurston. Elastic waves in rods and clad rods. *The Journal of the Acoustical Society of America*, 64(1):1–37, 1978. 107

Satoshi Tomioka and Shusuke Nishiyama. Analytical regularization of hypersingular integral for helmholtz equation in boundary element method. *Engineering Analysis with Boundary Elements*, 34(4):393 – 404, 2010. 163, 164

Fabien Treyssède. Elastic waves in helical waveguides. *Wave Motion*, 45(4):457 – 470, 2008. ISSN 0165-2125. 10, 36, 107

Fabien Treyssède, Khac-Long Nguyen, Anne-Sophie Bonnet-BenDhia, and Christophe Hazard. On the use of a safe-pml technique for modeling two-dimensional open elastic waveguides. Acoustics 2012, Nantes, 2012. 4, 105, 109, 158, 187

K. N. van Dalen, G. G. Drijkoningen, and D. M. J. Smeulders. On wavemodes at the interface of a fluid and a fluid-saturated poroelastic solid. *The Journal of the Acoustical Society of America*, 127 (4):2240–2251, 2010. 83, 84

M. Viens, Y. Tsukahara, C. K. Jen, and J. D. N. Cheeke. Leaky torsional acoustic modes in infinite clad rods. *The Journal of the Acoustical Society of America*, 95(2):701–707, 1994. 105, 107, 130

T. Vogt, M. Lowe, and P. Cawley. The scattering of guided waves in partly embedded cylindrical structures. *The Journal of the Acoustical Society of America*, 113(3):1258–1272, 2003. 130, 132, 169

Shen Wang, Songling Huang, and Wei Zhao. Simulation of lamb waves interactions with transverse internal defects in an elastic plate. *Ultrasonics*, 51(4):432 – 440, 2011. 57

G. Whitam. *Linear and Nonlinear Waves*. Wiley, New York, 1974. 34

R. A. Williams and L. E. Malvern. Harmonic dispersion analysis of incremental waves in uniaxially prestressed plastic and viscoplastic bars, plates, and unbounded media. *Journal of Applied Mechanics*, 36(1):59 – 64, 1969. 9

Peter Wriggers. *Nonlinear Finite Element Methods*. Springer-Verlag Berlin Heidelberg, Berlin, Heidelberg, 2008. 12, 13, 15, 25, 27, 34, 35

T. W. Wu. *Boundary Element Acoustics: Fundamentals and Computer Codes*. WIT Press, Ashurst Lodge, Ashurst, Southampton, UK, 2000. 58

Yeong-Bin Yang and Shyng-Rong Kuo. *Nonlinear Framed Structures*. Prentice Hall, New York, 1994. 12

Ge Zengxi, W. Canyun, L. Ting, and C. Xiaofei. 2.5d boundary element simulation of wave propagation in a vertical fluid-filled borehole with irregular shape. *Applied Geophysics*, 4(3):155 – 163, 2007. 59, 109, 158, 163

V. Zernov, L. Fradkin, and P. Mudge. Guided waves in a monopile of an offshore wind turbine. *Ultrasonics*, 51(1):57 – 64, 2011. 157

XiuMei Zhang, HaiLan Zhang, and XiuMing Wang. Acoustic mode waves and individual arrivals excited by a dipole source in fluid-filled boreholes. *Science in China Series G: Physics Mechanics and Astronomy*, 52:822–831, 2009. ISSN 1672-1799. 83, 84, 131

Xiaoliang George Zhao and Joseph L. Rose. Boundary element modeling for defect characterization potential in a wave guide. *International Journal of Solids and Structures*, 40(11):2645 – 2658, 2003. 57

Chris Zimmerman and M. Stern. Boundary element solution of 3-d wave scatter problems in a poroelastic medium. *Engineering Analysis with Boundary Elements*, 12(4):223 – 240, 1993. 71, 75